

Nuclear Modification of J/Ψ and Ψ' Production at 120 GeV at E906 / SeaQuest

by

Noah B. Wuerfel

A dissertation submitted in partial fulfillment
of the requirements for the degree of
Doctor of Philosophy
(Physics)
in The University of Michigan
2023

Doctoral Committee:

Professor Wolfgang Lorenzon, Chair
Professor Christine Aidala
Professor Timothy Chupp
Professor Ryan McBride
Professor Aaron Pierce

Noah B. Wuerfel

nwuerfel@umich.edu

ORCID iD: 0000-0001-9872-5330

© Noah B. Wuerfel 2023

For Alex Patel.

Acknowledgements

While the text in this document is mine, the work could not have been completed without the labor and support of a large number of people. I have profound gratitude for the mentoring, patience, and endless support provided by my advisor, Wolfgang Lorenzon, who has, on several occasions, provided me the space and resources I needed to continue my studies, despite personal and professional challenges. He has not given up on me, even in times where I may have given up on myself. Likewise, Kun Liu has been a persistent guiding figure in my academic life, helping me to transition from Ann Arbor to Fermilab and providing a wealth of knowledge about the SpinQuest and SeaQuest experiments. Many challenges in this analysis were solved thanks to his thoughtful insights during our weekly conversations. Ching Him Leung has been my primary collaborator, saving me from many evenings of banging my head on the table with precise and clear answers to my SeaQuest analysis questions- often responding within minutes, even in the middle of the night. I owe him immensely for his assistance in this work.

I am thankful to all members of the SeaQuest collaboration for allowing me to perform this analysis using their hard-taken data. In particular I would like to thank Donald Geesaman, Paul Reimer, Jen-Chieh Peng, Stephen Pate, Kenichi Nakano, Arun Tadepalli, Shivangi Prasad, Marshall Scott, and Kei Nagai for their useful feedback during analysis presentations in this last year. I am also thankful for the SpinQuest collaborators who made my time at Fermilab enjoyable, particularly Minjung Kim, Zhaohuizi Ji, Zong-Wei Zhang, and Forhad Hossain who were there in

the early days of SpinQuest development. None of the work at Fermilab would be possible without our site contact, Rick Tesarek, who has taken on the monolithic task of organizing the experiment and keeping SpinQuest safety standards up to par.

I also want to thank the older graduate students who have mentored me during my research. Ethan Cline showed me the ropes on the MUSE experiment, took me around Switzerland during my first two years, and continues to be a friendly face at conferences. Ievgen Lavrukhin also took me under his wing during my time working on the MUSE experiment and later joined our group as a post-doc during SpinQuest development. In the last few years he has spent countless hours with me, working on the SpinQuest trigger system and taking smoko outside of NM4. It has been a pleasure to work with him on several projects and I have learned a great deal from him. Marshall Scott and Daniel Morton both reached out to me as a new student in the Lorenzon group and took me to celebrate after completing my preliminary exam, making me feel like a real member of the community.

Several individuals from Harvard saw potential in me and encouraged me to pursue my dream of studying physics. Jene Golovchenko was my first research advisor during my undergraduate studies and selected me for a special research course that provided me my first physics experience. He continued to support my studies and wrote recommendation letters for me throughout college, including my graduate school applications. I did not believe that I had the capacity to participate in physics until Jene invested in me. Jene's post-doc, Ryan Rollings, spent hours with me each day in lab, patiently explaining all of the parts of his experiment. His graduate student, Tamas Szalay, brought me to graduate events like Friday pizza hour and introduced me to many people in the department. The experiences I had in Golovchenko lab built my confidence to apply to graduate school and I dearly wish that I could present him with this dissertation. John Huth also supported my studies as my research advisor during my final year of college and it is likely that I would not be at UM without his

recommendation. Melissa Franklin provided priceless advice about graduate schools and research programs and she (brutally) reviewed my application letters, despite not being my advisor. Without her assistance and kindness, it is unlikely that I would have made it to graduate school. Margo Seltzer and James Mickens taught me everything I know about computers and programming and welcomed me into the computer science department, where I met my close friend Alexander Patel. Alex and I lived together, wrote our graduate school applications together, and studied for our GREs together. Without him I would not have been able to buckle down and prepare all the materials needed to apply to graduate school. He constantly built me up and gave me the confidence to think of myself as an academic. It is my greatest sadness to not be able to share the completion of this work with him.

Finally, the support and emotional labor provided by family is the single largest contributor to this work. My parents, Jim and Neva, have supported me in every capacity, through every challenge in my life. Words do not exist to describe the ways that they have enabled this journey. They have supported my studies and have never pressured me to take on additional jobs or pursue a life inconsistent with my values. They have provided me with endless opportunities to make mistakes and the grace to persist in whatever path I desire. My extended family have all supported me through this process, never complaining when I have missed some holidays for study or work. Without them, I would have nothing.

Table of Contents

Dedication	ii
Acknowledgements	iii
List of Figures	ix
List of Tables	xviii
Abstract	xxii
Chapter	
I. Introduction	1
1.1 A Brief History of Nuclear Structure Studies	1
1.2 Quantum Chromodynamics	3
1.3 Factorization	7
1.4 The Drell-Yan Process	9
1.5 Parton Distribution Functions	10
1.6 The \bar{d}/\bar{u} Ratio	11
1.7 The E906/SeaQuest Experiment	13
1.8 J/Ψ Production at SeaQuest	14
1.9 J/Ψ in Cold Nuclear Matter	16
1.10 Quark Gluon Plasma	18
II. Experimental Setup	21
2.1 Structure of the Main Injector Beam	21
2.2 SeaQuest Targets	22
2.3 SeaQuest Spectrometer	24
2.4 Tracking Detectors	25
2.4.1 Hodoscopes	26
2.4.2 Drift Chambers	27
2.4.3 Proportional Tubes	29

III. Trigger and Tracking	31
3.1 Data Acquisition Systems	31
3.2 FPGA and NIM Based Triggers	33
3.3 Muon track Reconstruction with kTracker	38
3.3.1 EventReducer	39
3.3.2 kFastTracking	41
3.3.3 kVertex	42
3.4 SpinQuest Trigger and Tracking Upgrades	43
3.4.1 SpinQuest Trigger System	43
3.4.2 A Multithreaded Extension of kTracker	48
IV. Data Analysis	59
4.1 Extracting J/Ψ and Ψ' Yields in SeaQuest Data	60
4.2 Data Selections	65
4.3 Monte Carlo Simulation	68
4.4 Monte Carlo p_T Reweighting	70
4.4.1 Drell-Yan MC	72
4.4.2 J/Ψ and Ψ' MC	75
4.5 Mixed Background Emulation	77
4.6 Chamber Occupancy Effects on kTracker 'Efficiency'	78
4.7 Acceptance Corrections	79
4.8 R_{pA} Results	81
4.9 Systematic Sources of Uncertainty	87
4.10 Unbinned Results	88
4.11 Binned Results in p_T and x_F	91
4.12 Comparison with Theory	92
4.12.1 J/Ψ in the Color Evaporation Model	93
4.12.2 Nuclear Modification of Parton Densities	94
4.12.3 Absorption by the Nucleus	95
4.12.4 k_T Broadening	95
4.12.5 Intrinsic Charm Contributions	96
4.12.6 Comparison With SeaQuest R_{pA} Results	97
4.13 Discussion	98
V. Conclusions	106
5.1 Summary	106
5.2 Future Outlook	109
Appendix	111

Bibliography 168

List of Figures

Figure

1.1	Feynman diagram for the quark self-energy at leading order. The quark emits a photon (or gluon) and reabsorbs it shortly afterwards.	5
1.2	Feynman diagram for the Drell-Yan process at leading order. A quark and antiquark from two colliding hadrons annihilate through a photon (or Z) which decays to a dilepton final state. Often, Drell-Yan experiments focus on measuring muonic final states.	10
1.3	Recently published results from the SeaQuest experiment show a value of $\bar{d}(x)/\bar{u}(x) > 1$ over the whole kinematic range. The NuSea data is also shown, with a pronounced tension in the large x region. Figure taken from ref. [45].	14
1.4	Feynman diagrams for (Left) Quark anti-quark annihilation through a photon to a charmed final state. (Center) Gluon-gluon fusion through a three gluon vertex. (Right) Gluon-Quark channel, predicted to contribute the least in SeaQuest kinematics [46].	15
1.5	Predictions from the Color Evaporation Model for contributions to the J/Ψ production cross sections over SeaQuest Kinematic range in (Left) x_F and (Right) p_T from gluon-gluon fusion (solid), quark-antiquark annihilation (dashed), and the quark-gluon channel (dotted). Reproduced as published in ref. [46]	15
1.6	$R_{pA} = \sigma_{pA}/\sigma_{pN}$ measured by NuSea on carbon, calcium, iron, and tungsten targets compared with deuterium. The extracted value of α is 0.92 and a surprising similarity in the fall-off for the J/Ψ and Ψ' particles is observed.	17
1.7	Cartoons depicting possible sources of charmonium suppression suspected by the E772 collaboration, reproduced as published in ref. [57].	18

1.8	Cartoon showing the survival probability, $S_{J/\Psi}$, of the J/Ψ as a function of energy density ε , reproduced as published in ref. [61]. Deconfinement in Quark Gluon Plasma is expected to generate discontinuities in $S_{J/\Psi}$, while the nuclear absorption effect grows stronger, continuously, at higher energy densities.	20
2.1	A schematic view of the Beam Intensity Monitor. Beam enters from left to right and generates Cerenkov radiation which is directed by mirrors into a photomultiplier tube. Reproduced as published in ref. [62].	23
2.2	A schematic view of the SeaQuest mobile target assembly. The target assembly is free to move vertically in the plane of the image and places the desired target in line with the beam which enters from the left. Figure taken from ref. [62].	23
2.3	A schematic of the SeaQuest spectrometer with labeled components, beam comes from left side. Figure from ref. [62].	25
2.4	A schematic diagram of the proportional tubes used in the SeaQuest experiment as seen from the top, interaction point on the left and muons traveling to the right. Figure published in ref. [62].	30
3.1	A flowchart showing the path of detector information through the FPGA boards which formed the trigger logic.	35
3.2	Trigger acceptance for the data used in this analysis, from ref. [67]. Reproduced as published, mass is in units of GeV/c^2	37
3.3	Data processing stages in the kTracker algorithm.	39
3.4	Cartoon showing local triplet formation in kFastTracking, with solid lines representing hit wires and dotted lines showing the search window for the next hit. First, a hit wire, colored red, is found in the X plane. Then a search is performed in the search window shown in blue in the U plane. Finally, a smaller search window, shown in red, is used to look for a matching hit in the V plane.	41
3.5	A cartoon showing the SpinQuest trigger teststand.	46
3.6	(Left) Two-dimensional histogram showing the frequency of TDC hits, with time in the vertical direction and input channel in the horizontal and an initial time delay of zero. A bright horizontal line should be observed when the channel timings are correctly aligned. (Right) The same histogram after the automatic alignment process has completed and an identifiable horizontal line is apparent.	48

3.7	Data flow in the multithreaded tracking algorithm. fReader handles memory inputs from the disk and schedules multiple instances of the kTracker software on free computer cores as they become available. fReaper collects each completed tracking instance, deleting the associated working thread and writing the results to disk.	50
3.8	A cartoon showing a single fWorker thread attempting to access the circular buffer of eventReducers via synchronous queue operations, 'put' and 'fetch'. Two of the EventReducers are in use by workers, but a third is available and will be acquired by the fWorker thread on 'fetch' and later returned with 'put'	53
3.9	Ratio of wall-clock time to the computation time as a function of threads in the multithreaded tracking algorithm the four core laptop model. . .	55
3.10	Ratio of wall-clock time to the computation time as a function of threads in the multithreaded tracking algorithm in the desktop installation in all thirty two cores.	56
3.11	Ratio of computation time in N threads to a single thread showing a maximum computation time 20% longer than the single thread case, though the wall clock time is still strictly 1/32 of this value.	57
3.12	Flowchart showing the automatic process by which the multithreaded tracking algorithm is applied to data each spill.	58
4.1	The mass-fit results of TFractionFitter, showing data from the liquid hydrogen target along with the scaled Monte Carlo samples which comprise it. The integrated yields are shown for each component and used in the cross section ratio calculation.	64
4.2	Selection on χ^2 of finding the track vertex in the target or dump from ref. [76]. Dotted blue lines show a nontrivial overlap region which is avoided by the selection.	68
4.3	Probability distribution used to select NIM3 events as a function of chamber 1 occupancy, D1, reproduced as published in ref. [76]. An incorrect normalization is shown, but the shape is correct.	71
4.4	p_T , x_F dependence observed in E615 pion-induced Drell-Yan dimuons. Figure reproduced as published in ref. [83].	72

4.5	Parameter p_1 , used in the Drell-Yan Monte Carlo reweighting, as a linear interpolation in x_F for the liquid hydrogen target. In the information box, p_0 and p_1 are distinct from $p_1(x_F)$, and represent the parameters of the linear fit.	74
4.6	J/Ψ yield from liquid hydrogen target, plotted in p_T and fit with Kaplan form to extract parameter p_1	76
4.7	kTracker efficiency for the J/Ψ as a function of chamber occupancy in stations 1, 2, and 3 for the liquid hydrogen target. The efficiency is computed as a ratio of messy and clean Monte Carlo samples. The efficiency as a function of D1 occupancy is chosen to correct the yields for all processes.	80
4.8	Acceptance results for J/Ψ in p_T for all targets. Small differences between targets are observed, particularly in the lowest bin, which are included in the cross section ratio calculation.	82
4.9	R_{pA} results for the hydrogen target in red, compared to E772 results in black from ref. [54]. The exponential fit, corresponding to $\alpha = 0.883$, is shown as a red curve for the J/Ψ , while the E772 value of $\alpha = 0.92$ used to describe both the J/Ψ and Ψ' is shown in dotted black. While the J/Ψ and Ψ' suppression is similar in the E772 data, the SeaQuest Ψ' ratio is consistent with unity.	89
4.10	R_{pA} results for the deuterium target in red, compared to hydrogen results reported by E772 in black from ref. [54]. The exponential fit, corresponding to $\alpha = 0.877$, is shown as a red curve for the J/Ψ . While the J/Ψ and Ψ' suppression is similar in the E772 data, the SeaQuest Ψ' ratio is consistent with unity.	90
4.11	R_{pA} results of this analysis compared to the predictions of ref. [46] for J/Ψ from the carbon target, binned in p_T . Horizontal errors represent bin widths, with markers placed at bin averages. Red error bars represent statistical error and the combined statistical and systematic error is shown in black. The magenta, cyan, and black curves include all nuclear effects, including enhanced nuclear k_T broadening, and correspond to a 0.1%, 0.31%, and 1% probability for intrinsic charm production, respectively. Prediction values are placed at bin centers rather than averages and use central values of the EPPS16 nPDF set.	99

4.12	R_{pA} results of this analysis compared to the predictions of ref. [46] for J/Ψ from the iron target, binned in p_T . Horizontal errors represent bin widths, with markers placed at bin averages. Red error bars represent statistical error and the combined statistical and systematic error is shown in black. The magenta, cyan, and black curves include all nuclear effects, including enhanced nuclear k_T broadening, and correspond to a 0.1%, 0.31%, and 1% probability for intrinsic charm production, respectively. Prediction values are placed at bin centers rather than averages and use central values of the EPPS16 nPDF set.	100
4.13	R_{pA} results of this analysis compared to the predictions of ref. [46] for J/Ψ from the tungsten target, binned in p_T . Horizontal errors represent bin widths, with markers placed at bin averages. Red error bars represent statistical error and the combined statistical and systematic error is shown in black. The magenta, cyan, and black curves include all nuclear effects, including enhanced nuclear k_T broadening, and correspond to a 0.1%, 0.31%, and 1% probability for intrinsic charm production, respectively. Prediction values are placed at bin centers rather than averages and use central values of the EPPS16 nPDF set.	101
4.14	R_{pA} results of this analysis compared to the predictions of ref. [46] for J/Ψ from the carbon target, binned in x_F . Horizontal errors represent bin widths, with markers placed at bin averages. Red error bars represent statistical error and the combined statistical and systematic error is shown in black. The magenta, cyan, and black curves include all nuclear effects, including enhanced nuclear k_T broadening, and correspond to a 0.1%, 0.31%, and 1% probability for intrinsic charm production, respectively. Prediction values are placed at bin centers rather than averages and use central values of the EPPS16 nPDF set.	102
4.15	R_{pA} results of this analysis compared to the predictions of ref. [46] for J/Ψ from the iron target, binned in x_F . Horizontal errors represent bin widths, with markers placed at bin averages. Red error bars represent statistical error and the combined statistical and systematic error is shown in black. The magenta, cyan, and black curves include all nuclear effects, including enhanced nuclear k_T broadening, and correspond to a 0.1%, 0.31%, and 1% probability for intrinsic charm production, respectively. Prediction values are placed at bin centers rather than averages and use central values of the EPPS16 nPDF set.	103

4.16	R_{pA} results of this analysis compared to the predictions of ref. [46] for J/Ψ from the tungsten target, binned in x_F . Horizontal errors represent bin widths, with markers placed at bin averages. Red error bars represent statistical error and blue error bars represent the systematic errors and the combined error is shown in black. The magenta, cyan, and black curves include all nuclear effects, including enhanced nuclear k_T broadening, and correspond to a 0.1%, 0.31%, and 1% probability for intrinsic charm production, respectively. Prediction values are placed at bin centers rather than averages and use central values of the EPPS16 nPDF set.	104
A.1	Kaplan fit for Drell-Yan reweighting in increasing x_F bins, hydrogen target.	112
A.2	Kaplan fit for Drell-Yan reweighting in increasing x_F bins, deuterium target.	113
A.3	Kaplan fit for Drell-Yan reweighting in increasing x_F bins, carbon target.	114
A.4	Kaplan fit for Drell-Yan reweighting in increasing x_F bins, iron target. .	115
A.5	Kaplan fit for Drell-Yan reweighting in increasing x_F bins, tungsten target.	116
A.6	Kaplan parameter p_1 as a linear interpolation in x_F used to reweight the Drell-Yan Monte Carlo. (Top) liquid hydrogen results (Bottom) liquid deuterium results.	118
A.7	Kaplan parameter p_1 as a linear interpolation in x_F used to reweight the Drell-Yan Monte Carlo. (Top) carbon results (Middle) iron results (Bottom) tungsten results.	119
A.8	Acceptance corrected J/Ψ yield, fit with the Kaplan form to determine p_1 , used in the Monte Carlo reweighting. (Top) liquid hydrogen results (Bottom) liquid deuterium results. Horizontal error bars are not considered in the fit and represent the standard deviation of each p_T bin.	121
A.9	Acceptance corrected J/Ψ yield, fit with the Kaplan form to determine p_1 , used in the Monte Carlo reweighting. (Top) carbon results (Middle) iron results (Bottom) tungsten results. Horizontal error bars are not considered in the fit and represent the standard deviation of each p_T bin. . .	122
A.10	Acceptance corrected Ψ' yield, fit with the Kaplan form to determine p_1 , used in the Monte Carlo reweighting. (Top) liquid hydrogen results (Bottom) liquid deuterium results. Horizontal error bars are not considered in the fit and represent the standard deviation of each p_T bin.	123

A.11	Acceptance corrected Ψ' yield, fit with the Kaplan form to determine p_1 , used in the Monte Carlo reweighting. (Top) carbon results (Middle) iron results (Bottom) tungsten results. Horizontal error bars are not considered in the fit and represent the standard deviation of each p_T bin. . . .	124
A.12	(Top) Drell-Yan acceptance in p_T . (Bottom) The acceptance in x_F	126
A.13	(Top) J/Ψ acceptance in p_T . (Bottom) The acceptance in x_F	127
A.14	(Top) Ψ' acceptance in p_T . (Bottom) The acceptance in x_F	128
A.15	Mass-fit plots and uncorrected yields for the unbinned data. (Top) hydrogen target (Bottom) deuterium target.	130
A.16	Mass-fit plots and uncorrected yields for the unbinned data. (Top) carbon target (Middle) iron target (Bottom) tungsten target.	131
A.17	Mass-fit plots for the p_T binned data, LH2 target.	133
A.18	Mass-fit plots for the p_T binned data, LD2 target.	134
A.19	Mass-fit plots for the p_T binned data, carbon target.	135
A.20	Mass-fit plots for p_T binned data, iron target.	136
A.21	Mass-fit plots for the p_T binned data, tungsten target.	137
A.22	Mass-fit plots for the x_F binned data, LH2 target.	138
A.23	Mass-fit plots for the x_F binned data, LD2 target	139
A.24	Mass-fit plots for the x_F binned data, carbon target.	140
A.25	Mass-fit plots for the x_F binned data, iron target.	141
A.26	Mass-fit plots for the x_F binned data, tungsten target.	142
A.27	R_{pA} for Drell-Yan from the hydrogen target, binned in p_T . (Top) results for carbon. (Middle) results for iron. (Bottom) results for tungsten. Horizontal error bars represent bin widths and markers are placed at bin averages. Red errors represent statistical uncertainty and black error bars represent the combined systematic and statistical error, summed in quadrature. A clear p_T broadening effect is observed.	154

A.28	<i>R_{pA}</i> for J/Ψ from the hydrogen target, binned in p_T . (Top) results for carbon. (Middle) results for iron. (Bottom) results for tungsten. Horizontal error bars represent bin widths and markers are placed at bin averages. Red errors represent statistical uncertainty and black error bars represent the combined systematic and statistical error, summed in quadrature. . .	155
A.29	<i>R_{pA}</i> for Ψ' from the hydrogen target, binned in p_T . (Top) results for carbon. (Middle) results for iron. (Bottom) results for tungsten. Horizontal error bars represent bin widths and markers are placed at bin averages. Red errors represent statistical uncertainty and black error bars represent the combined systematic and statistical error, summed in quadrature. . .	156
A.30	<i>R_{pA}</i> for Drell-Yan from the deuterium target, binned in p_T . (Top) results for carbon. (Middle) results for iron. (Bottom) results for tungsten. Horizontal error bars represent bin widths and markers are placed at bin averages. Red errors represent statistical uncertainty and black error bars represent the combined systematic and statistical error, summed in quadrature.	157
A.31	<i>R_{pA}</i> for J/Ψ from the deuterium target, binned in p_T . (Top) results for carbon. (Middle) results for iron. (Bottom) results for tungsten. Horizontal error bars represent bin widths and markers are placed at bin averages. Red errors represent statistical uncertainty and black error bars represent the combined systematic and statistical error, summed in quadrature. Theory curves from ref. [46] are overlayed for the 0.01%, 0.31%, and 1% intrinsic charm production probabilities respectively. . .	158
A.32	<i>R_{pA}</i> for Ψ' from the deuterium target, binned in p_T . (Top) results for carbon. (Middle) results for iron. (Bottom) results for tungsten. Horizontal error bars represent bin widths and markers are placed at bin averages. Red errors represent statistical uncertainty and black error bars represent the combined systematic and statistical error, summed in quadrature. . .	159
A.33	<i>R_{pA}</i> for Drell-Yan from the hydrogen target, binned in x_F . (Top) results for carbon. (Middle) results for iron. (Bottom) results for tungsten. Horizontal error bars represent bin widths and markers are placed at bin averages. Red errors represent statistical uncertainty and black error bars represent the combined systematic and statistical error, summed in quadrature.	160
A.34	<i>R_{pA}</i> for J/Ψ from the hydrogen target, binned in x_F . (Top) results for carbon. (Middle) results for iron. (Bottom) results for tungsten. Horizontal error bars represent bin widths and markers are placed at bin averages. Red errors represent statistical uncertainty and black error bars represent the combined systematic and statistical error, summed in quadrature. . .	161

A.35	<i>R_{pA}</i> for Ψ' from the hydrogen target, binned in x_F . (Top) results for carbon. (Middle) results for iron. (Bottom) results for tungsten. Horizontal error bars represent bin widths and markers are placed at bin averages. Red errors represent statistical uncertainty and black error bars represent the combined systematic and statistical error, summed in quadrature. . .	162
A.36	<i>R_{pA}</i> for Drell-Yan from the deuterium target, binned in x_F . (Top) results for carbon. (Middle) results for iron. (Bottom) results for tungsten. Horizontal error bars represent bin widths and markers are placed at bin averages. Red errors represent statistical uncertainty and black error bars represent the combined systematic and statistical error, summed in quadrature.	163
A.37	<i>R_{pA}</i> for J/Ψ from the deuterium target, binned in x_F . (Top) results for carbon. (Middle) results for iron. (Bottom) results for tungsten. Horizontal error bars represent bin widths and markers are placed at bin averages. Red errors represent statistical uncertainty and black error bars represent the combined systematic and statistical error, summed in quadrature. Theory curves from ref. [46] are overlayed for the 0.01%, 0.31%, and 1% intrinsic charm production probabilities respectively. . .	164
A.38	<i>R_{pA}</i> for Ψ' from the deuterium target, binned in x_F . (Top) results for carbon. (Middle) results for iron. (Bottom) results for tungsten. Horizontal error bars represent bin widths and markers are placed at bin averages. Red errors represent statistical uncertainty and black error bars represent the combined systematic and statistical error, summed in quadrature. . .	165

List of Tables

Table

2.1	Details about the dimensions, placement, and efficiencies of the hodoscope paddles used in SeaQuest data taking.	26
2.2	Naming convention and usage history of the drift chambers used during SeaQuest data taking.	28
2.3	Performance metrics of the drift chambers used during SeaQuest data taking showing position resolution and detection efficiencies matching experimental requirements.	28
3.1	Trigger requirements of the NIM and FPGA based triggers used at SeaQuest, along with prescale factors.	34
3.2	Estimated signal and background acceptances for each roadset used in this analysis as published in [67]. Random data from Run 3 is used for the background estimate.	38
3.3	Maximum occupancy selections on each detector during the EventReducer.	40
3.4	Cosmic ray FPGA trigger logic used for data taking while awaiting beam.	49
4.1	A table showing the dates and roadsets associated with Run 2 and 3 data.	60
4.2	Spill-level cuts applied to SeaQuest data, from ref. [77]. For a detailed description of each variable, see text.	66
4.3	Track-level cuts applied to SeaQuest data during track reconstruction.	66
4.4	Dimuon selections applied to reconstructed dimuon pairs in SeaQuest data.	67

4.5	Target and dump separation requirements for SeaQuest data. Nontrivial overlap of dimuons originating in the dump and the target is shown in fig. 4.2, motivating the selection.	68
4.6	x_F bins used in the Drell-Yan Monte Carlo reweighting.	73
4.7	Results of target gas analysis from ref. [88] showing a small fraction of hydrogen contamination in the deuterium targets used in data taking Run 2 and 3.	84
4.8	Constant values used to calculate the cross section ratios, $R_{pA}^{(D/H)}$, in this analysis.	86
4.9	x_F and p_T bins used in the analysis.	92
A.1	Systematic errors for each x_F bin in the Drell-Yan cross section ratio for carbon compared to the hydrogen target.	144
A.2	Systematic errors for each x_F bin in the Drell-Yan cross section ratio for iron compared to the hydrogen target.	144
A.3	Systematic errors for each x_F bin in the Drell-Yan cross section ratio for tungsten compared to the hydrogen target.	144
A.4	Systematic errors for each x_F bin in the J/Ψ cross section ratio for carbon compared to the hydrogen target.	144
A.5	Systematic errors for each x_F bin in the J/Ψ cross section ratio for iron compared to the hydrogen target.	145
A.6	Systematic errors for each x_F bin in the J/Ψ cross section ratio for tungsten compared to the hydrogen target.	145
A.7	Systematic errors for each x_F bin in the Ψ' cross section ratio for carbon compared to the hydrogen target.	145
A.8	Systematic errors for each x_F bin in the Ψ' cross section ratio for iron compared to the hydrogen target.	145
A.9	Systematic errors for each x_F bin in the Ψ' cross section ratio for tungsten compared to the hydrogen target.	146
A.10	Systematic errors for each x_F bin in the Drell-Yan cross section ratio for carbon compared to the deuterium target.	146

A.11	Systematic errors for each x_F bin in the Drell-Yan cross section ratio for iron compared to the deuterium target.	146
A.12	Systematic errors for each x_F bin in the Drell-Yan cross section ratio for tungsten compared to the deuterium target.	146
A.13	Systematic errors for each x_F bin in the J/Ψ cross section ratio for carbon compared to the deuterium target.	147
A.14	Systematic errors for each x_F bin in the J/Ψ cross section ratio for iron compared to the deuterium target.	147
A.15	Systematic errors for each x_F bin in the J/Ψ cross section ratio for tungsten compared to the deuterium target.	147
A.16	Systematic errors for each x_F bin in the Ψ' cross section ratio for carbon compared to the deuterium target.	147
A.17	Systematic errors for each x_F bin in the Ψ' cross section ratio for iron compared to the deuterium target.	148
A.18	Systematic errors for each x_F bin in the Ψ' cross section ratio for tungsten compared to the deuterium target.	148
A.19	Systematic errors for each p_T bin in the Drell-Yan cross section ratio for carbon compared to the hydrogen target.	148
A.20	Systematic errors for each p_T bin in the Drell-Yan cross section ratio for iron compared to the hydrogen target.	148
A.21	Systematic errors for each p_T bin in the Drell-Yan cross section ratio for tungsten compared to the hydrogen target.	149
A.22	Systematic errors for each p_T bin in the J/Ψ cross section ratio for carbon compared to the hydrogen target.	149
A.23	Systematic errors for each p_T bin in the J/Ψ cross section ratio for iron compared to the hydrogen target.	149
A.24	Systematic errors for each p_T bin in the J/Ψ cross section ratio for tungsten compared to the hydrogen target.	149
A.25	Systematic errors for each p_T bin in the Ψ' cross section ratio for carbon compared to the hydrogen target.	150

A.26	Systematic errors for each p_T bin in the Ψ' cross section ratio for iron compared to the hydrogen target.	150
A.27	Systematic errors for each p_T bin in the Ψ' cross section ratio for tungsten compared to the hydrogen target.	150
A.28	Systematic errors for each p_T bin in the Drell-Yan cross section ratio for carbon compared to the deuterium target.	150
A.29	Systematic errors for each p_T bin in the Drell-Yan cross section ratio for iron compared to the deuterium target.	151
A.30	Systematic errors for each p_T bin in the Drell-Yan cross section ratio for tungsten compared to the deuterium target.	151
A.31	Systematic errors for each p_T bin in the J/Ψ cross section ratio for carbon compared to the deuterium target.	151
A.32	Systematic errors for each p_T bin in the J/Ψ cross section ratio for iron compared to the deuterium target.	151
A.33	Systematic errors for each p_T bin in the J/Ψ cross section ratio for tungsten compared to the deuterium target.	152
A.34	Systematic errors for each p_T bin in the Ψ' cross section ratio for carbon compared to the deuterium target.	152
A.35	Systematic errors for each p_T bin in the Ψ' cross section ratio for iron compared to the deuterium target.	152
A.36	Systematic errors for each p_T bin in the Ψ' cross section ratio for tungsten compared to the deuterium target.	152

Abstract

The E906/SeaQuest experiment at Fermi National Accelerator Laboratory took scattering data with the 120 GeV Main Injector Proton beam on liquid hydrogen and deuterium targets, along with carbon, iron, and tungsten targets. Within the data are a significant number of muons coming from the decay of J/Ψ and Ψ' particles. In this thesis, I present a study of the suppression of these light, charmed particles by cold nuclear media at SeaQuest. The data are divided into two analyses: first, the cross sections for charmonia production on the carbon, iron, and tungsten targets is compared with the cross section on the hydrogen and deuterium targets to study the cross section ratio as a function of the atomic mass of the target; and second, each of the carbon, iron, and tungsten targets' effects on charmonia production are studied as a function of the transverse momentum and Feynman-x kinematic dimensions in the ranges $0.0 \leq p_T < 1.5$ GeV and $0.4 \leq x_F < 0.95$. Finally, the unbinned results are compared with previous results from the E772 experiment and the binned results are compared to theoretical predictions from the Color Evaporation Model.

Chapter I

Introduction

The E906 / SeaQuest experiment used the Fermilab 120 GeV Main Injector proton beam to take scattering data on hydrogen, deuterium, carbon, iron, and tungsten targets from November 2013 through July 2017. While the experiment's primary physics goal was a determination of the ratio of light anti-quarks in the nuclear sea, a rich set of scattering data from nuclear targets provides insight into the difference between single nucleon and bound nuclear states. In particular, a comparison of charmonia production from the various targets can be made to explore the potential suppression of J/Ψ and Ψ' production by cold nuclear matter. In this section, the SeaQuest experiment is contextualized and motivated with a short discussion of the history of nuclear structure studies, recent SeaQuest results published in Nature, and charmonia produced at E906.

1.1 A Brief History of Nuclear Structure Studies

The discovery of the proton and neutron by 1932 had essentially proven Bohr's atomic model [1] and it seemed that nearly all matter was comprised of these indivisible units. Still, the strong force that binds protons and neutrons together in the nucleus remained a mystery. The next twenty years of inquiry revealed an immense number of new particles, observed in cosmic rays and scattering experiments. Work-

ing to categorize this new “zoo” of particles, Zweig and Gell-Mann independently proposed a set of three new constituent particles in 1964: the up, down, and strange quarks [2, 3]. Extensions to the quark model were quick to follow and Glashow and Bjorken predicted the existence of the charm quark within the same year [4]. An early challenge to the quark model was the observation of the Δ^{++} baryon, which was described as three up quarks with parallel spin. This arrangement of spin-1/2 quarks would violate the Pauli exclusion principle and suggested that the quarks must have an additional quantum number. By 1965, Greenberg and the team of Han and Nambu had independently proposed an additional gauge degree of freedom in the SU(3) symmetry group to resolve this problem [5, 6]. Later, Gell-Mann would coin the term “color” for this extra quantum number. Gell-Mann, Han, and Nambu already noted that the theory introduced an octet of vector gauge bosons that might mediate interactions amongst the quarks, an early prediction of the existence of the gluon. The quark model served as a controversial organizational tool with little physical evidence until 1968, when a SLAC-MIT experiment produced electron beam energies large enough to shatter the proton and probe its internal structure. These deeply inelastic scattering (DIS) experiments led to the observation of two important phenomena: 1) the inelastic scattering cross-section was larger than expected by an order of magnitude and had weak dependence on the squared momentum transfer, Q^2 , from the electron to the proton and 2) the structure functions of the proton also had weak dependence on Q^2 despite a measured dependence in previous elastic scattering experiments. This second observation was predicted by Bjorken in 1966 and is often called “Bjorken Scaling” [7]. Feynman introduced the parton model to explain the SLAC-MIT data, suggesting that these observations could be explained if the proton was comprised of three point-like, spin 1/2 constituents [8]. Feynman’s partons were not immediately identified with Zweig and Gell-Mann’s quarks and it would take nearly a decade of additional theory work to unify these ideas under the

quark parton model. By 1970, Glashow, Iliopolis, and Maiani [9] had presented a theoretical model which required the charm quark earlier proposed by Glashow and Bjorken, and in 1973 Kobayashi and Maskawa [10] proposed the current total of six quarks to explain the observation of CP violation first made by Wu [11]. As theoretical applications of the quark model grew, a sudden jolt of experimental clarity came in 1974, with the simultaneous and independent production of charm quarks by Richter’s team at SLAC [12] and Ting’s team [13] at Brookhaven National Laboratory. The newly discovered J/Ψ meson was a bound state of charm and anti-charm quarks and solidified the quark model’s validity in the community. In 1977, the bottom quark was observed at Fermilab by Lederman’s group [14] and within a year the gluon had been observed at DESY [15]. The long awaited discovery of the top quark was provided by the CDF [16] and D0 [17] collaborations at Fermilab in 1995 providing the final experimental proof of the quark model.

1.2 Quantum Chromodynamics

By the early 1970’s, a mathematical formalism had emerged to describe the strong force. Yang and Mill’s 1954 work on non-Abelian gauge theories [18] was further refined by Fritzsche, Gell-Mann and Leutwyler [19], and came to be known as Quantum Chromodynamics (QCD). QCD is a non-Abelian gauge theory based on the $SU(3)$ symmetry group and bears some similarities to Quantum Electrodynamics, the field theory describing electromagnetic reactions. Instead of electric charge, the quarks carry an $SU(3)$ color charge and similar to the photon’s role in mediating the electromagnetic force, the gluon serves as the mediator of the strong force. All dynamics of strong interactions are governed by the QCD Lagrangian, written as

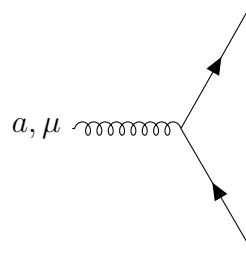
$$\mathcal{L} = \sum_{q=1}^{n_f} \bar{\psi}_i^q i\gamma^\mu (\partial_\mu \delta_{ij} - g_s t_{ij}^a A_\mu^a - m_q \delta_{ij}) \psi_j^q - \frac{1}{4} F_{\mu\nu}^a F^{a\mu\nu}. \quad (1.1)$$

Here, ψ^a are the Dirac spinor quark fields, q represents quark flavors, and i and j are color indices from 1 to $N_c = 3$. A_μ^a is the four potential of the gluon field, where a counts from 1 to $N_c^2 - 1 = 8$. $g_s = \sqrt{4\pi\alpha_s}$ is the coupling constant of the strong interaction and t_{ij}^a are the Gell-Mann matrices, which span the Lie algebra of the SU(3) symmetry group. $F_{\mu\nu}^a$ is the field strength tensor,

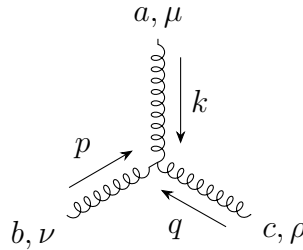
$$F_{\mu\nu}^a = \partial_\mu A_\nu^a - \partial_\nu A_\mu^a + g_s f^{abc} A_\mu^b A_\nu^c, \quad (1.2)$$

with f^{abc} being the structure constants of SU(3).

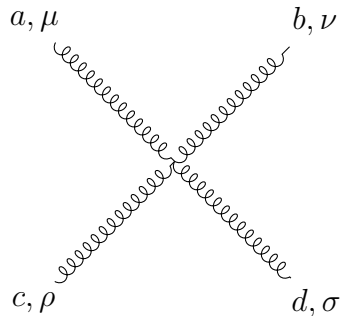
The QCD Lagrangian dictates the interactions of the strong force, with Feynman rules from ref. [20], given as



$$= ig_s \gamma^\mu t^a \quad (1.3)$$



$$= g_s f^{abc} [g^{\mu\nu} (k - p)^\rho + g^{\nu\rho} (p - q)^\mu + g^{\rho\mu} (q - k)^\nu] \quad (1.4)$$



$$= -ig_s^2 [f^{abc} f^{cde} (g^{\mu\rho} g^{\nu\sigma} - g^{\mu\sigma} g^{\nu\rho}) + f^{ace} f^{bde} (g^{\mu\nu} g^{\rho\sigma} - g^{\mu\sigma} g^{\nu\rho}) + f^{ade} f^{bce} (g^{\mu\nu} g^{\rho\sigma} - g^{\mu\rho} g^{\nu\sigma})], \quad (1.5)$$

which represent the interactions of a quark-antiquark pair with a gluon, a three

gluon vertex, and a four gluon vertex, respectively, and where $g^{\mu\nu}$ is the metric tensor. Writing out and computing scattering processes with Feynman diagrams is perturbative, with more complex diagrams contributing less to the overall scattering amplitude. This procedure is remarkably successful in QED, where the coupling is small and the expansion converges quickly. In QCD, the size of the coupling constant, even at large values of exchanged momentum Q^2 , requires several orders of perturbation theory to get good accuracy. As the order of computation grows, so does its complexity, making QCD calculations extremely demanding. A large class of these high order diagrams also give rise to seemingly unphysical infinities. One of these “ultraviolet” divergences appears in the computation of the quark self-energy, which at leading order evaluates the Feynman diagram in fig. 1.1 and diverges to

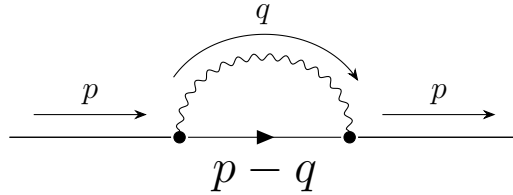


Figure 1.1: Feynman diagram for the quark self-energy at leading order. The quark emits a photon (or gluon) and reabsorbs it shortly afterwards.

infinity logarithmically.

The mathematical tool used to deal with these infinities is called renormalization and introduces a scale μ . In all renormalizable field theories, the coupling constant becomes a function of this renormalization scale - referred to as the “running” of the coupling. For QCD, at one loop order, the coupling constant runs as

$$\alpha_s(\mu^2) = \frac{g_s^2(\mu)}{4\pi} = \frac{4\pi}{\left(\frac{11N_c}{3} - \frac{2n_f}{3}\right) \ln\left(\frac{\mu^2}{\Lambda_{QCD}^2}\right)}, \quad (1.6)$$

where Λ_{QCD} is the QCD scale near 200 MeV, at which the perturbative calculation of QCD observables diverges. The renormalization scale μ is chosen to be close to

the scale of physics processes, such as Q , the momentum transfer of a scattering process. It is clear from Eq. 1.6 that the strength of the QCD coupling decreases logarithmically at higher energy scales, corresponding to short distance interactions. The remarkable discovery that short distance scattering in the strong force can be calculated perturbatively is called “asymptotic freedom”.

't Hooft, Gross, Politzer, and Wilzcek discovered this property in non-Abelian gauge field theories by application of the renormalization group method [21–23]. It was quickly shown by Coleman and Gross that asymptotic freedom is only present in non-Abelian field theories for four dimensional space-time [24]. By this time, Faddeev had already demonstrated the quantization of non-Abelian gauge theories [25] and 't Hooft had proven them to be renormalizable [21].

Asymptotic freedom separates QCD processes into two parts: a short distance, “hard” scattering event that is calculable using *perturbative* QCD (pQCD); and “soft” non-perturbative dynamics which bind hadrons together. To extract the short distance physics, the operator product expansion (OPE) is a powerful mathematical tool that writes the product of two fields as the sum of local fields. Using the OPE, one finds that Bjorken scaling is recovered at leading order in the parton picture, but divergent logarithms appear which spoil the perturbative calculation. Using the renormalization group equations, it was demonstrated that Bjorken scaling is indeed violated logarithmically [26, 27]. By 1975, slight deviations to Bjorken scaling were observed experimentally in DIS muon-nucleon scattering experiments such as EMC, CDHS, and BCDMS, [28] confirming the scaling violation computed in pQCD and solidifying belief in the theory.

By the end of the 1970's pQCD had become a mature field with several remarkable predictions. The calculation of next-to-leading-order effects in DIS had been completed, the OPE was generalized to explain a broader class of short-range phenomena, and new short distance processes such as the formation of quarkonium and

gluon jets had been introduced. The last 40 years of experimental work have continued to solidify confidence in pQCD, though many open questions remain in the study of hadron structure, jet formation, and quarkonium production.

1.3 Factorization

Factorization theorems address the fundamental problem of calculating high energy cross sections in pQCD. In a renormalized perturbation series, all physical quantities depend on three variables with dimensions of mass: the energy scale of the scattering, Q ; the masses of the particles, m ; and the renormalization scale, μ . Often the scale for renormalization is chosen to be close to the momentum exchange in the hard scattering process: $\mu \approx Q$. At n loops in this scale, the coupling appears in the combination $g^{2n}(Q) \ln^{an}(Q/m)$ where $a = 1$ or 2 [29]. Consequently, summing Feynman diagrams by order of the coupling is no longer an expansion in a small parameter. The presence of $\ln(Q/m)$ demonstrates the importance of long distance effects in QCD, where even the vanishing mass of the gluon becomes significant as $\ln(Q/m)$ becomes very large. Asymptotic freedom does not resolve these problems, either, as it is only a property of the coupling for short distances. So the cross section, generally, involves a combination of short and long distance dynamics and cannot be computed directly by pQCD.

Processes without hadrons in the initial state, such as the total cross section for e^+e^- scattering to hadrons or jets, can be computed perturbatively without worrying about long distance QCD effects. However, the vast majority of experimentally studied hadron-hadron and lepton-hadron collisions require special treatment to separate the long-distance and short-distance behavior when making predictions for these cross sections. Factorization theorems “factor” out the two scales into a “hard” scattering process and “soft” long range dynamics. This procedure is highly-nontrivial and required many decades of theory work. Factorization must be proved per-process

and serves as a necessary bridge between pQCD calculations of parton scattering and experimentally verifiable predictions.

Collins, Soper, and Sterman [29] have proven factorization for the following processes: deeply inelastic scattering, electron-positron annihilation, the Drell-Yan process, and inclusive hadron collisions, with the requirement that the invariants in each process be large and comparable. This means that factorization holds only for $Q^2 \approx s$ and that transverse momenta are either integrated out or are themselves comparable to Q .

Factorization theorems may be considered a field-theoretical realization of Feynman's parton model. As previously discussed, in the parton model, the hadrons are pictured as composite objects, formed by constituent partons and held together by the dynamics of these underlying constituents. It is assumed that the hadrons could be described by virtual parton states, but we do not have the knowledge to compute these states. We are capable, however, of calculating the scattering of "free" partons, e.g. by an electron. Here, "free" means we have ignored all surrounding parton-parton interactions. This is, of course, the separation of the "hard" and "soft" scales which comes from our ignorance of long-distance interactions and our knowledge of asymptotic freedom for short distances.

Intuitively, we might imagine ourselves in the center-of-mass frame of electron-hadron scattering. The hadron is Lorentz contracted along its longitudinal direction, like a pancake, and the interactions of its constituents are time dilated. As the center-of-mass (COM) energy increases, any virtual partonic state has its lifetime enhanced and the time scale of the electron scattering is shortened. If we imagine that the scattering time is much smaller than the lifetime of a virtual partonic state, the hadron will be in a single state, with a definite number of partons, for the entire length of the scattering event. Because the scattering happens very quickly, the interactions amongst partons are frozen and each can be considered to carry a well-

defined fraction of the total hadron momentum in the COM frame. This fraction, x , is often referred to, experimentally, as the Bjorken- x , and is expected to satisfy $0 < x < 1$ as it is unlikely that a parton is moving against the direction of the hadron.

Given all these assumptions, the high-energy, short-distance scattering process is essentially classical and the interactions amongst partons, which are time dilated and occur before or after the hard scattering event, cannot affect the electron-parton interaction. A parton distribution function, $f_{a/H}(\xi)$, is defined as the probability that the electron encounters a frozen parton of species a carrying fraction ξ of the hadron momentum. The Born cross section $\sigma_B(x/\xi, Q^2)$ is the electron-parton scattering cross section with momentum transfer Q^2 and the complete scattering cross section for deep inelastic scattering of a hadron by an electron in the parton model is

$$\sigma_{eH} = \sum_a \int_x^1 d\xi f_{a/H}(\xi) \sigma_B(x/\xi, Q^2). \quad (1.7)$$

This is the model for all factorization theorems. The cross section is written as a convolution of the short-distance cross section, calculated perturbatively by exploitation of asymptotic freedom, and the long-distance dynamics, which are abstracted into probability densities.

1.4 The Drell-Yan Process

Factorization extends to the Drell-Yan process: $A + B \rightarrow \mu^+ + \mu^- + X$, which is an important experimental probe of hadron structure shown in fig. 1.2. Drell and Yan first considered this parton model process to explain the production of high-mass lepton pairs observed in the inelastic collision of hadrons [30]. Two parton distributions are required in the factorization formula, one for each of the incoming hadrons. Drawing inspiration from eq. 1.7, the factorized parton model Drell-Yan

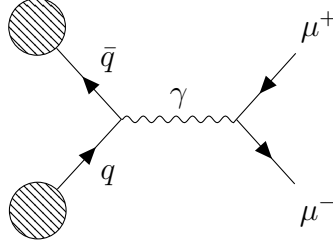


Figure 1.2: Feynman diagram for the Drell-Yan process at leading order. A quark and antiquark from two colliding hadrons annihilate through a photon (or Z) which decays to a dilepton final state. Often, Drell-Yan experiments focus on measuring muonic final states.

cross section is written as

$$\frac{d\sigma}{dQ^2 dy} = \sum_a \int_{x_A}^1 d\xi_A \int_{x_B}^1 d\xi_B f_{a/A}(\xi_A) f_{\bar{a}/B}(\xi_B) \sigma'_B(Q^2, y), \quad (1.8)$$

where q^μ is the momentum, $Q^2 = q^\mu q_\mu$ is the square of the mass, and

$$y = \frac{1}{2} \ln \left(\frac{q \cdot P_a}{q \cdot P_B} \right) \quad (1.9)$$

is the rapidity of the muon pair. To compute $\sigma'_B(Q^2, y)$, the Feynman diagram in fig. 1.2 is evaluated. The resulting cross section is a prediction of the parton model, not QCD. It is factorization theorems that connect them. A complete calculation of the Drell-Yan cross section to next-to-leading-order and discussion of the \overline{MS} renormalization scheme is given in ref. [29].

1.5 Parton Distribution Functions

Experimental knowledge of the parton distribution functions (PDFs) is an essential part of making predictions using the factorization formula. These distributions have been most commonly measured in fixed target and collider experiments through DIS or DY. Great effort, by large collaborations such as CTEQ, MSTW, GJR and NNPDF [31–34], has been dedicated to the extraction of the parton distributions from global

fits of experimental data across a wide range of energies and laboratory configurations. It is worth mentioning the increasing precision of lattice QCD calculations such as ref. [35] which may soon be given serious consideration in global fits. A rigorous development of the parton distributions is given in ref. [36] and a summary can be found in ref. [29]. There are two technical definitions of the parton distribution functions: the DIS definition, which privileges deeply inelastic scattering, and the more general \overline{MS} definition. The \overline{MS} definition itself can be constructed in several equivalent ways which are expanded in detail in ref. [37].

Key to experimental determination is that the PDFs are constructed to be universal. One should extract the same distributions in DIS and DY. The renormalization of the PDFs also introduces a scale dependence. The energy evolution of the PDFs is calculated via the Dokshizer-Gribov-Lipatov-Altarelli-Parisi (DGLAP) equation [38–40]. This allows experimental results to be compared across different energy scales.

In Gell-Mann and Zweig’s model, each particle is comprised of two or three quarks which are called the “valence quarks”. The proton, for example, is modeled as two up quarks and one down quark. Importantly, the probability distributions for finding other quarks inside the proton is non-vanishing due to virtual fermion loops, which appear in the gluon propagators that arise amongst strong interactions that bind the nucleon together. These other quarks are referred to as the “sea quarks” and heavier sea quarks may be resolved in hadron scattering experiments at higher energies. At SeaQuest kinematics, the dominant probability distributions of the proton belong to the up and down quarks, as well as the anti-up and anti-down quarks.

1.6 The \bar{d}/\bar{u} Ratio

Because the anti-up and anti-down quarks in the sea have nearly identical mass, which is much smaller than that of the proton, their distributions are expected to also be nearly identical. The New Muon Collaboration (NMC) measured deep inelastic

scattering of muons on hydrogen and deuterium in the range $0.004 < x < 0.8$ in the early 1990's and extracted the sea distributions of the \bar{d} and \bar{u} , published in ref. [41]. The NMC assumed that the integrals of the parton distributions for the proton and neutron are charge symmetric: $\int_0^1 u_p(x)dx = \int_0^1 d_n(x)dx$. Neglecting nuclear effects in deuterium, $F_2^D = F_2^p + F_2^n$, the NMC determined

$$\int_0^1 \frac{dx}{x} [F_2^p(x) - F_2^n(x)] = \frac{1}{3} + \frac{2}{3} \int_0^1 dx [\bar{u}(x) - \bar{d}(x)] = 0.235 \pm 0.026, \quad (1.10)$$

and therefore the integral of the $\bar{d}(x)$ distribution is larger than that of $\bar{u}(x)$

$$\int_0^1 dx [\bar{u}(x) - \bar{d}(x)] = 0.147 \pm 0.039. \quad (1.11)$$

To further investigate this surprising measurement, The NA51 collaboration at CERN was formed to study the NMC asymmetry using the Drell-Yan process and published results in ref. [42]. The experiment used a 450 GeV proton beam from the CERN-SPS to study muon pairs produced from interactions with a liquid hydrogen and liquid deuterium target. The p-n cross-section asymmetry for Drell-Yan is written

$$A_{DY} = \frac{\sigma^{pp} - \sigma^{pn}}{\sigma^{pp} + \sigma^{pn}}, \quad (1.12)$$

and, with simplifying assumptions, depends only on the quark and antiquark ratios: $\lambda_v(x) = u_v(x)/d_v(x)$ and $\lambda_s(x) = \bar{u}(x)/\bar{d}(x)$, where the subscript v indicates the valence distributions and s indicates the sea. NA51 reported a value

$$A_{DY} = -0.09 \pm 0.02(\text{stat}) \pm 0.025(\text{syst}). \quad (1.13)$$

Using previously measured values for the valence distributions, the final extrapolated result for the antiquark ratio at $x = 0.18$ was

$$\lambda_s = 0.51 \pm 0.04(\text{stat}) \pm 0.05(\text{syst}), \quad (1.14)$$

providing evidence from a Drell-Yan experiment to support the conclusions of the NMC experiment. The E866 “NuSea” experiment at Fermilab continued the spirit of NA51, measuring the cross section ratio of Drell-Yan production on deuterium and hydrogen targets with an 800 GeV proton beam. The cross section ratio almost directly measures the antiquark ratio as $\sigma_D/\sigma_H \approx (\sigma_p + \sigma_n)/\sigma_p \approx 1 + \bar{d}(x_T)/\bar{u}(x_T)$. Measurements were made in the kinematic regime of the target parton momentum, x_T , from $0.015 < x_T < 0.35$ and extrapolated to $x_T = 0$ and $x_T = 1$. A final reported value of $\int_0^1 dx[\bar{d}(x) - \bar{u}(x)] = 0.118 \pm 0.012$ is consistent with the NMC and NA51 results studied in ref. [43]. The HERMES collaboration published results consistent with NMC and NuSea shortly afterwards in ref. [44]. Notably, NuSea also observed a drop in the $\bar{d}(x)/\bar{u}(x)$ ratio for $x > 0.2$, with a value of $\bar{d}(x)/\bar{u}(x) = 0.35 \pm 0.40$ at $x = 0.31$.

1.7 The E906/SeaQuest Experiment

The E906 SeaQuest experiment was designed with a principal physics goal of investigating the NuSea flavor asymmetry at higher x_T using a newly constructed experimental apparatus. SeaQuest used the Fermilab Main Injector proton beam at 120 GeV to take scattering data on hydrogen, deuterium, carbon, iron, and tungsten targets from November 2013 through July 2017. The experiment was optimized to detect Drell-Yan muon pairs for the study of target antiquark distributions with x_T around 0.3, where NuSea observed a fall off in $\bar{d}(x)/\bar{u}(x)$. Recently, SeaQuest published results on the flavor asymmetry in Nature in ref. [45]. Their results for

the $\bar{d}(x)/\bar{u}(x)$ ratio are shown in fig. 1.3. A ratio larger than unity is observed over the entire range of x , and there is tension with the NuSea results in the high x data, where no drop off is observed.

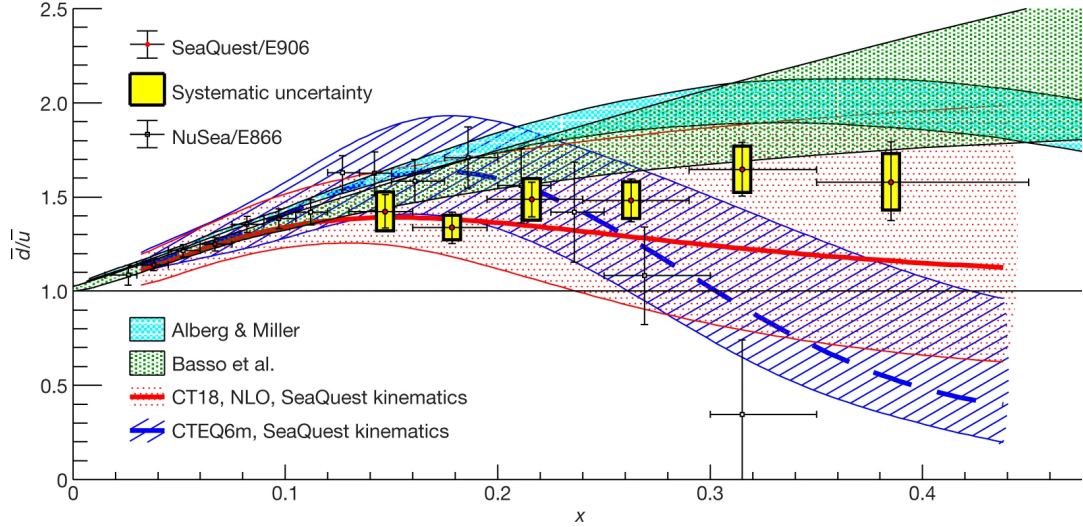


Figure 1.3: Recently published results from the SeaQuest experiment show a value of $\bar{d}(x)/\bar{u}(x) > 1$ over the whole kinematic range. The NuSea data is also shown, with a pronounced tension in the large x region. Figure taken from ref. [45].

1.8 J/ Ψ Production at SeaQuest

A rich set of muon pair data from SeaQuest still remain to be analyzed. Included in this data are muon pairs produced from the decay of light charmonia: the J/ Ψ and Ψ' . The J/ Ψ meson is the lightest bound state of charm and anticharm quarks, with a mass just over 3 GeV. In hadron-hadron collisions, the J/ Ψ is commonly produced at tree level through quark-antiquark annihilation and gluon-gluon fusion shown in fig. 1.4. The Ψ' is the first excited state of the J/ Ψ , with a mass near 3.6 GeV.

Theory predictions for J/ Ψ and Ψ' production at SeaQuest kinematics have been made by Vogt, shown in fig. 1.5 and published in ref. [46]. Here the kinematic dimensions are Feynman- x , the difference between the beam and target parton momenta $x_F = x_B - x_T$, and the transverse momentum of the muon pair, p_T . Quark anti-quark

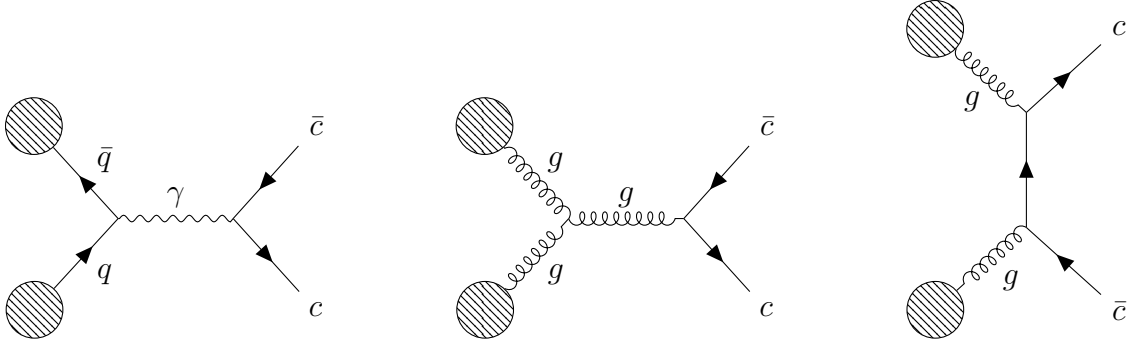


Figure 1.4: Feynman diagrams for (Left) Quark anti-quark annihilation through a photon to a charmed final state. (Center) Gluon-gluon fusion through a three gluon vertex. (Right) Gluon-Quark channel, predicted to contribute the least in SeaQuest kinematics [46].

annihilation provides a significant contribution, around 25% over the SeaQuest kinematic range. At larger energies, such as the NuSea experiment, gluon-gluon fusion contributes more than 95% (see ref. [46]) of the total J/Ψ cross section. This provides further motivation to investigate J/Ψ production at SeaQuest, as the effects of cold nuclear matter on charmonium production may differ depending on the production mechanism. The exact mechanism of J/Ψ production and suppression still poses a

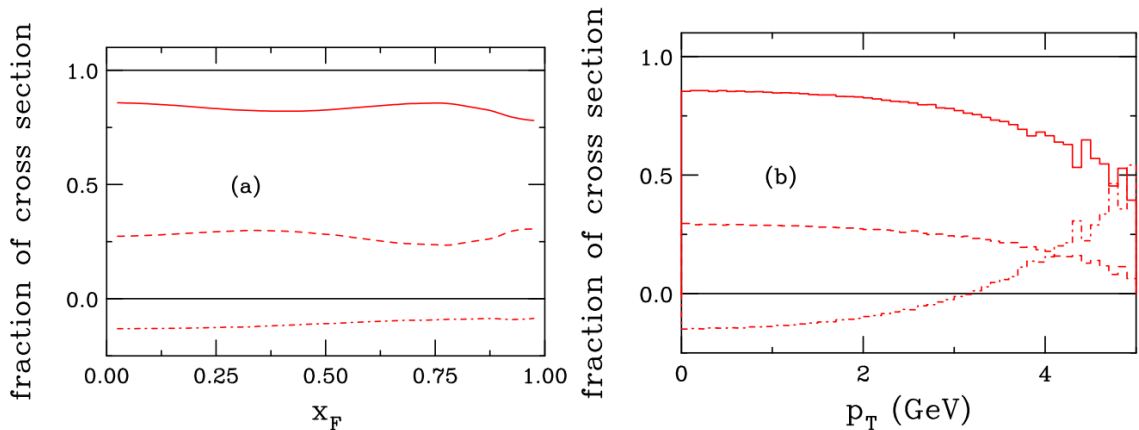


Figure 1.5: Predictions from the Color Evaporation Model for contributions to the J/Ψ production cross sections over SeaQuest Kinematic range in (Left) x_F and (Right) p_T from gluon-gluon fusion (solid), quark-antiquark annihilation (dashed), and the quark-gluon channel (dotted). Reproduced as published in ref. [46]

challenge to theory. Because the charm quark mass is large relative to Λ_{QCD} , its production should be calculable in perturbative QCD. However, the transition from $q\bar{q}$ to physical quarkonium states introduces a number of nonperturbative effects. A more thorough description of the theory is presented in comparison with the data in sec. 4.12.

It is fortuitous that the requirements of the flavor asymmetry analysis make the SeaQuest spectrometer an ideal tool for studying the production and decay of charmonium. The SeaQuest experiment stands out as a fixed-target experiment with lower incident proton energy than previous J/Ψ studies, allowing for an unprecedented forward coverage to probe partons carrying a large fraction of the beam momentum, x_B . Large coverage in x_B is of notable interest for theorists to set limits on the $c(x)$ and $\bar{c}(x)$ distributions of the proton wavefunction and has previously been suggested by Brodsky and collaborators [47, 48]. The low center-of-mass energy at SeaQuest is also desirable as charmonia production at collider energies often puts the high x partons outside detector coverage [46]. There are new proposals for fixed-target experiments and some have taken data, but all are higher energy than the SeaQuest data, such as those presented in refs. [49–51].

1.9 J/Ψ in Cold Nuclear Matter

Early studies of J/Ψ production by the NA3 [52] and NA38 [53] collaborations observed a dependence on the nuclear mass of the target and modeled this difference as a power law correction to the per-nucleon cross section, given by

$$\sigma_{pA} = \sigma_{pN} A^\alpha, \tag{1.15}$$

where A is the nuclear mass of the target, and σ_{pA} and σ_{pN} are the charmonium production cross sections for nuclear targets and nucleon targets respectively. Often

in experimental results, the value $R_{pA} = \sigma_{pA}/\sigma_{pN}$ is shown along with the extracted value of α . If the presence of the nucleus had no effect, the production cross section would be expected to grow linearly in A with $\alpha = 1$. Several experiments have published data with typical values of α between 0.9 and 1. The E772 NuSea experiment reported a value of $\alpha = 0.92$ in ref. [54] after taking scattering data on carbon, calcium, iron, and tungsten targets shown in fig. 1.6. Matsui and Satz had previously

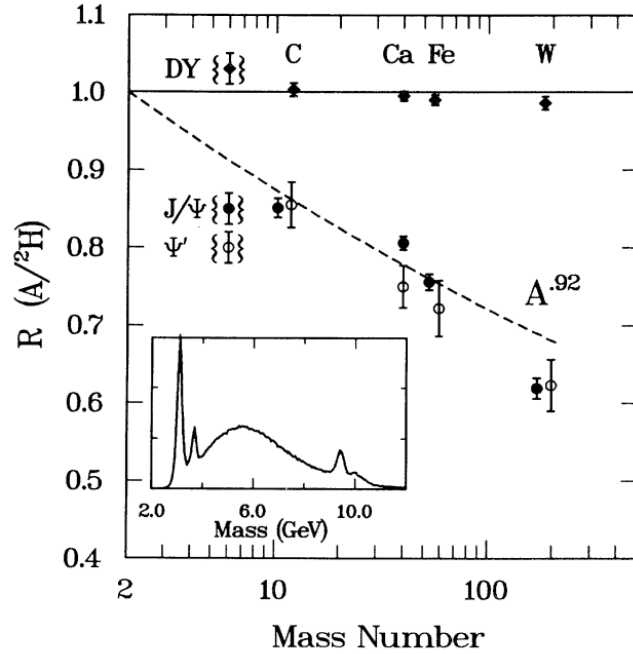


Figure 1.6: $R_{pA} = \sigma_{pA}/\sigma_{pN}$ measured by NuSea on carbon, calcium, iron, and tungsten targets compared with deuterium. The extracted value of α is 0.92 and a surprising similarity in the fall-off for the J/Ψ and Ψ' particles is observed.

predicted the suppression of the J/Ψ in p-A interactions and had interpreted the suppression as arising from the absorption of physical charmonium states in ref. [55]. However, the NuSea data excluded this interpretation as the Ψ' is four times larger than the J/Ψ , which would have had an observable effect in the nuclear absorption, noted in ref. [56]. Furthermore, multidimensional analysis has shown that α decreases as a function of x_F and grows as a function of p_T and neither effect can be explained via nuclear absorption in the E772 data. Multiple effects from “cold nuclear matter”

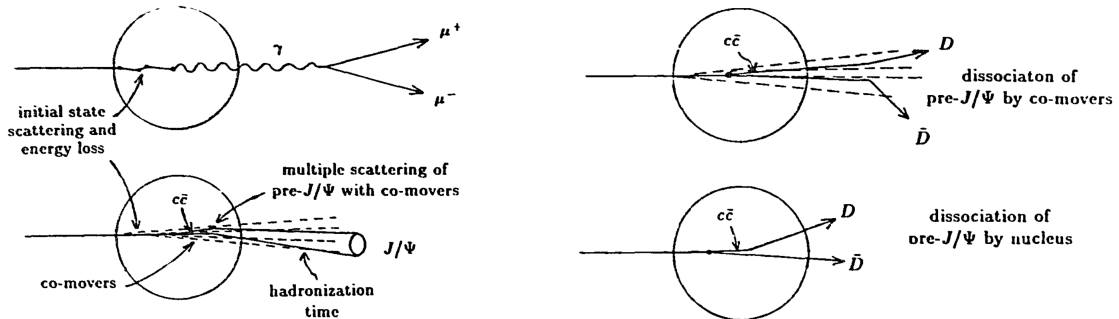


Figure 1.7: Cartoons depicting possible sources of charmonium suppression suspected by the E772 collaboration, reproduced as published in ref. [57].

could contribute to the dependence of α on x_F and p_T and a cartoon of some of these contributions suspected by the E772 collaboration is shown in fig. 1.7. Most notably, it is well known that the parton distributions of nucleons bound in a nucleus differ from those of free nucleons as studied in ref. [58]. It is also known that multiple scattering in the nuclear media causes energy loss and transverse momentum broadening and sometimes absorbs charmonia altogether, as published in ref. [59]. Models which only incorporate these cold nuclear matter effects still struggle to properly describe J/Ψ production in x_F and p_T . A concrete formulation of the cold nuclear matter effects is given, along with a comparison to the results of this analysis, in sec. 4.12.6.

1.10 Quark Gluon Plasma

In heavy ion collisions such as those performed at RHIC and the LHC, charmonium suppression is an important tool for identifying the formation of an extremely hot and dense state of matter known as Quark Gluon Plasma (QGP). In the QGP, free color charges are distributed over distances larger than the typical hadron size. Matsui and Satz predicted a QGP environment would screen the hadronization of $c\bar{c}$ pairs and proposed charmonium as an experimental probe of QGP formation [55]. The first experimental confirmation of charmonium suppression came from the CERN NA38 experiment, less than a year after Matsui and Satz published their prediction.

NA38 compared charmonium production in central and peripheral collisions of Oxygen and Uranium at the CERN SPS and reported a suppression of approximately 35% for charmonium in peripheral collisions compared with the central region [42]. Alternative causes of the suppression were quickly considered. Most notably, heavy ion collisions produce a substantial number of co-moving hadrons which can, themselves, cause disassociation of the $c\bar{c}$ as studied in ref. [60]. It was also understood that cold nuclear matter effects in $p - A$ collisions suppressed charmonium production. Together, the absorption by comovers and nuclear cold matter effects explained the NA38 data without the need for deconfinement in a QGP. Matsui and Satz then searched for a feature which could distinguish suppression from absorption via “co-movers” or cold nuclear effects and from disassociation in QGP. Satz points out that suppression from deconfinement should be a critical phenomenon, while absorption is always present and ought to increase gradually with nuclear density as shown in the cartoon of fig. 1.8. Data from low to medium energy experiments like SeaQuest are essential in profiling the absorption component of fig. 1.8, as there is no possibility of observing deconfinement effects at lower energies. Furthermore, fixed target experiments such as SeaQuest are capable of measuring the effect of the suppression at a range in other kinematic dimensions, such as high beam Bjorken- x , that would otherwise be outside of the acceptance of high energy collider experiments. In this work, J/Ψ and Ψ' suppression in SeaQuest data is studied to explore the effects of cold nuclear matter in this unique kinematic range.

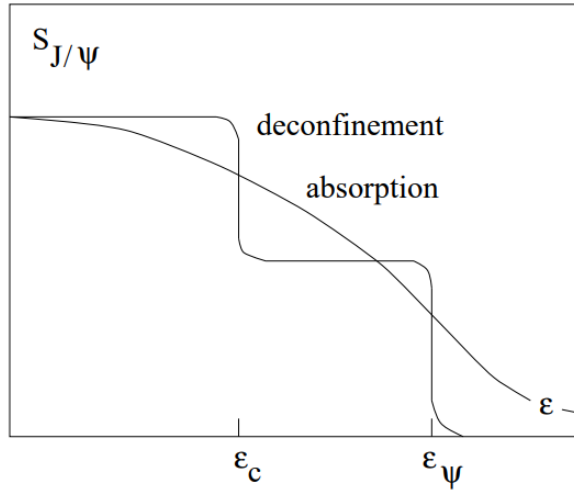


Figure 1.8: Cartoon showing the survival probability, $S_{J/\Psi}$, of the J/Ψ as a function of energy density ϵ , reproduced as published in ref. [61]. Deconfinement in Quark Gluon Plasma is expected to generate discontinuities in $S_{J/\Psi}$, while the nuclear absorption effect grows stronger, continuously, at higher energy densities.

Chapter II

Experimental Setup

The E906 SeaQuest experiment at Fermilab was designed to measure pairs of muons produced in the Drell-Yan process. In this chapter, I will provide an overview of the experimental layout of SeaQuest with a focus on key details in the structure of the beam, the design of the target, and the detector technology used in the muon spectrometer. A detailed description of the SeaQuest spectrometer has been published in ref. [62].

2.1 Structure of the Main Injector Beam

SeaQuest uses the 120 GeV Main Injector Proton Beam at Fermilab. The beam is delivered to the experimental hall in 4.5 second spills, with a 55.5 second downtime between. Each spill is further subdivided as the beam is bunched on a 53 MHz RF frequency. Each beam bucket is just over 1 nanosecond long, with gaps of 18.8 nanoseconds. The intensity of each bucket varied widely during SeaQuest data taking, containing between 0 and 80,000 protons. The SeaQuest flavor asymmetry analysis published in Nature in ref. [45] noted intensity-dependent effects as a dominant source of systematic uncertainty. For high-intensity buckets, the SeaQuest spectrometer was flooded with particles, making identification and tracking of associated muon pairs impossible against a background of single muons.

There are two primary beam monitors distributed along the beamline: ion chambers (ICs) and secondary emission monitors (SEMs). These detectors use mature technologies with decades of use in beam monitoring for experimental physics. At SpinQuest, the readout of the SEM in the G2 enclosure is used to monitor the intensity of beam spills and will appear as part of data selections in the analysis.

A “Beam Intensity Monitor” was designed and added in later production runs to provide additional veto power against high intensity bins, with greater than 95,000 protons, at trigger level. The monitor is shown in fig. 2.1 and consists of a gas Cerenkov counter and a charge (Q) Integration and Encoder module called the QIE. The gaseous Cerenkov detector uses a mixture of 80% Argon and 20% CO₂. As the beam passes through the monitor, Cerenkov radiation is collected and directed into a photo-multiplier tube, providing an estimate of the bunch intensity. The signal from the photo-multiplier is sent to the QIE, a custom integrated circuit which integrates charge signals and digitizes them. This charge sum, QIEsum, will also appear as part of the data selection.

2.2 SeaQuest Targets

SeaQuest took data on a total of 5 targets: two cryogenic liquid targets of hydrogen and deuterium, and three solid nuclear targets comprised of carbon, iron, and tungsten. In total the target had seven positions; one for each target, and then an empty cryogenic flask for background subtraction in the hydrogen and deuterium analysis and a “no target” position for background studies in the nuclear target analysis. The mobile target assembly is shown in fig. 2.2.

The liquid hydrogen and deuterium targets utilized a closed-circuit helium refrigeration system to condense ultra-high purity gas into the target cell. While the hydrogen used was purchased from a commercial source, the gas used in the deuterium target was initially sourced from old bubble chamber experiments at Fermilab. This

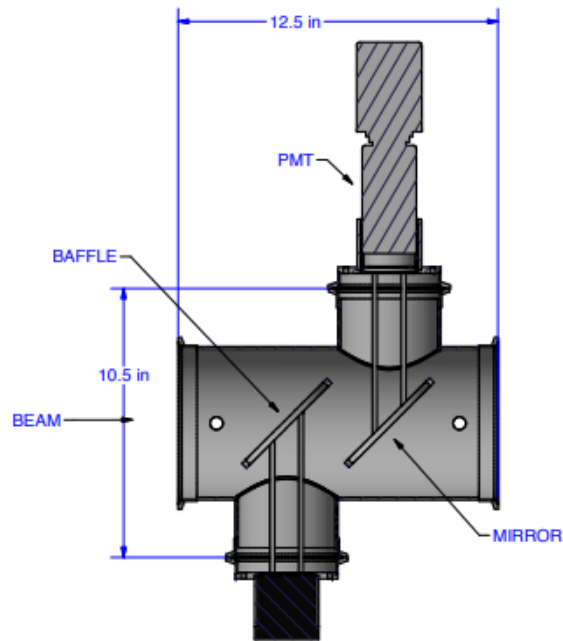


Figure 2.1: A schematic view of the Beam Intensity Monitor. Beam enters from left to right and generates Cerenkov radiation which is directed by mirrors into a photomultiplier tube. Reproduced as published in ref. [62].

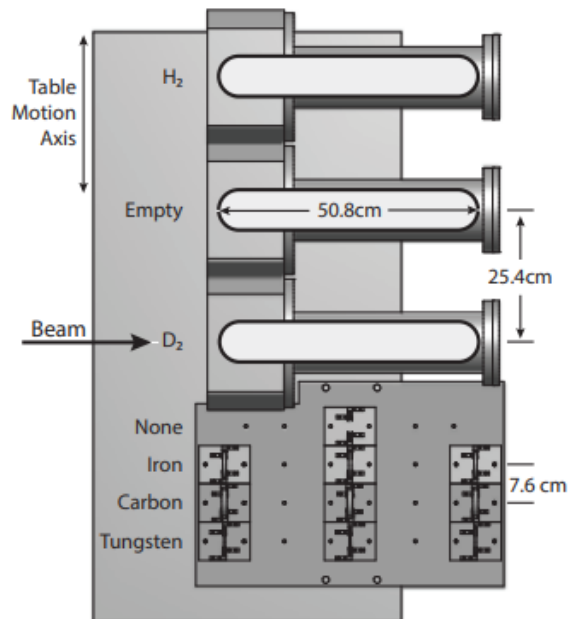


Figure 2.2: A schematic view of the SeaQuest mobile target assembly. The target assembly is free to move vertically in the plane of the image and places the desired target in line with the beam which enters from the left. Figure taken from ref. [62].

introduced hydrogen contamination in the target for the first production runs. A full list of runs and target information is given in table 4.7 of sec. 4.8. In the data analysis presented in this work, the target contamination is handled as a small term proportional to σ_{pp} added into the σ_{pd} cross section. Later production data used commercially available ultra-high purity gas for the deuterium target. Each of the liquid target flasks held a total of 2.2 liters of target material. The solid nuclear targets were each comprised of three, 2-inch diameter disks of either carbon, iron, or tungsten. The thickness of the disks were chosen to minimize differences in spectrometer acceptance from the targets.

2.3 SeaQuest Spectrometer

The SeaQuest spectrometer is shown in 2.3. Moving down the beamline, the target is 1.5 m upstream of the focusing magnet, FMag. The FMag is a solid iron focusing magnet, which serves as a primary hadron absorber and bends muon pairs produced in the target into the spectrometer acceptance using a 1.9 Tesla field. After FMag is the first station of tracking detectors. In total, four tracking stations are employed throughout the spectrometer, detailed in ref. [62]. In addition, hodoscopes located in each tracking system are used to form the NIM (Nuclear Instrument Modules) and FPGA (Field Programmable Gate Array) triggers detailed in the next chapter. Following station 1, a second, hollow-core magnet, KMag, is used to focus muon pairs into the spectrometer acceptance and applies an approximately 0.4 GeV kick via a 0.4 T field, which allows for a determination of the muon momentum via sagitta ratio. In a standard running configuration, both FMag and KMag bend the muons in the same direction. With the y axis vertically oriented in the lab and z being the direction of the beamline, the magnets are designed to bend muons in the x direction. Two more tracking detectors follow KMag along with a 1 meter thick iron wall placed just in front of the proportional tubes in station 4.

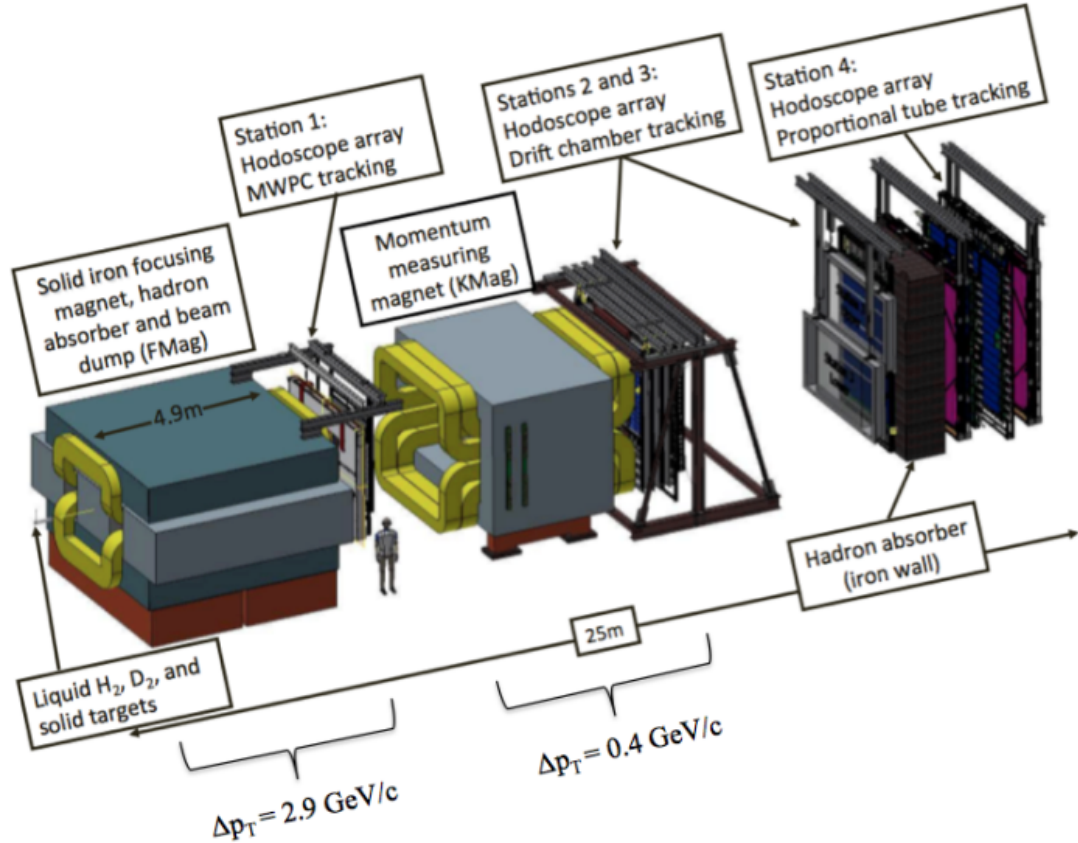


Figure 2.3: A schematic of the SeaQuest spectrometer with labeled components, beam comes from left side. Figure from ref. [62].

2.4 Tracking Detectors

SeaQuest is a simple counting experiment, measuring the ratios of muon pairs produced in various physics processes on various targets. The key experimental challenge is to properly identify muon pairs and determine their physical characteristics, such as the mass and transverse momentum, from a reconstruction of their paths through the spectrometer. The solid, 5-meter iron core of FMag prevents hadrons, such as pions and kaons, as well as electrons from reaching the spectrometer. The detector systems described in this section are used to record key information used in the reconstruction of the surviving muon tracks.

Plane	Number	Length (cm)	Width (cm)	Thickness (cm)	Array Width	Location (cm)	Avg. Efficiency
1Y	20 x 2	78.7	7.32	0.64	140	663	0.978
1X	23 x 2	69.9	7.32	0.64	161	653	
2Y	19 x 2	132.0	13.0	0.64	241	1403	
2X	16 x 2	152.0	13.0	0.64	203	1421	0.989
3X	16 x 2	167.6	14.3	1.3	224	1958	0.959
4Y1	16 x 2	152.4	23.16	1.3	366	2130 (L) 2146 (R)	Unmeasured
4Y2	16 x 2	152.4	23.16	1.3	366	2200 (L) 2217 (R)	Unmeasured
4X	16 x 2	182.9	19.33	1.3	305	2240	0.979

Table 2.1: Details about the dimensions, placement, and efficiencies of the hodoscope paddles used in SeaQuest data taking.

2.4.1 Hodoscopes

A total of four plastic scintillator hodoscope stations are used to form the primary physics trigger for the experiment. Stations 1 and 2 are located just downstream of FMag and KMag, respectively, and are recycled from the HERMES experiment with details in ref. [63]. Hodoscope stations 3 and 4 were constructed with new Eljen EJ-200 scintillator material for the experiment. As the bending plane of the magnets is oriented in the x direction, the primary hodoscopes used to form the trigger are oriented vertically. The scintillator bars in each station are split into a top and bottom half. Each bar has a slight overlap (2-3mm) with its neighbors. This improves the efficiency of the trigger, but overlapping the bars also reduces the ability of the trigger to reject background. Overlapping effectively widens the trigger acceptance and makes it easier for single muons to be misidentified as pairs. The number and sizes of scintillators in each plane is given in table 2.1.

Each scintillator bar is connected to a readout photomultiplier tube (PMT), with the exception of scintillators in station 4 which are readout by two PMTs, one on top and one on the bottom of the paddle. The PMT signals are sent to discriminating electronics and then to a time to digital converter. Per-plane timing was roughly adjusted with short cable delays and then fine adjustments on the order of 1 ns were made inside of the FPGA trigger, discussed in more detail in chapter 3.

The trigger efficiency was optimized by individually adjusting the PMTs on a channel-per-channel basis. Because the absolute value of the PMT signal is not recorded by the readout electronics, the gain adjustment was made by measuring PMT count rates as a function of PMT voltage. The operating voltage was selected in the plateau of the voltage vs. count rate curve. Each counter's efficiency was then evaluated by using tracks reconstructed without requiring a hit in the given counter shown in table 2.1.

2.4.2 Drift Chambers

Drift chambers are used to detect muons traversing stations 1, 2 and 3. In each of these stations, two wire planes are used to measure the x-position and an additional two planes are used for each of the left and right stereo angles at $\pm 14^\circ$ from horizontal, though the configuration of the chambers changed slightly during data taking. The position resolution of each plane is less than $400 \mu\text{m}$, which corresponds to a momentum resolution of $\Delta p/p(\%) = 0.03 * p(\text{GeV}/c)$. To maintain a track reconstruction efficiency greater than 90%, the single plane efficiency was required to be at least 95%.

The drift chambers used at SeaQuest are named “DC” followed by the station number, such as DC3 in station 3. During data taking runs 1-3, a smaller chamber, DC1.1, was installed in station 1. A larger station, DC1.2, replaced DC1.1 as it was expected to have a better high rate capability for data runs 4-6. Later, DC1.1 was reinstalled upstream of its original position for data runs 5-6. During this period, both DC1.1 and DC1.2 were located in station 1. In Station 3, separate drift chambers are used in the top and bottom halves of the detector and are labeled “DC3p” and “DC3m” respectively. During data taking, DC3m was upgraded to DC3m.1 and later replaced by a new detector, DC3m.2. Other than DC1.2, all chambers were filled with $\text{Ar}:\text{CH}_4:\text{CF}_4$ gas mixture at a ratio of 88:8:4. DC1.2 used a mixture of

Run	Dates	Live Protons (10^{17})	Chambers	Changes
1	Mar. - Apr. 2012		DC1.1; DC2; DC3p-m.1	Commissioning
2	Nov. 2013 - Sep. 2014	2.0	DC1.1; DC2; DC3p-m.2	New station 3 lower drift chamber New station 1 and 2 photomultiplier bases
3	Nov. 2014 - Jul. 2015	6.1	DC1.1; DC2; DC3p-m.2	
4	Nov. 2015 - Feb. 2016	0.8	DC1.2; DC2; DC3p-m.2	New station 1 drift chamber (DC1.2)
5	Mar. 2016 - Jul. 2016	2.5	DC1.1; DC1.2; DC2; DC3p-3m.2	DC1.1 and DC1.2 installed in station 1
6	Nov. 2016 - Jul. 2017	2.3	DC1.1; DC1.2; DC2; DC3p-3m.2	DAQ upgrade

Table 2.2: Naming convention and usage history of the drift chambers used during SeaQuest data taking.

Chamber	Max. drift (ns)	Position Resolution (μm)	Detection Efficiency (min. - max.)
DC1.1	100	225	99 - 100 %
DC2	260	325	96 - 99 %
DC3p	220	240	95 - 98 %
DC3m.2	210	246	97 - 98 %

Table 2.3: Performance metrics of the drift chambers used during SeaQuest data taking showing position resolution and detection efficiencies matching experimental requirements.

Ar:CF₄:C₄H₁₀:C₃H₈O₂ with a ratio of 81:5:12:2.

The DC2 and DC3m chambers were inherited from the completed Fermilab experiment E605 and DC1.1 had been constructed for use in the E866/NuSea experiment. DC3p and DC3m.2 were designed and built for SeaQuest to meet large acceptance requirements in Station 3. Details of the chambers, including their active data runs are given in table 2.2.

During data taking, the chamber performance was evaluated by measuring the probability of detecting a hit in the chambers where the reconstructed muon track crosses the plane. The position resolution was also determined by the distance between a recorded hit and the reconstructed track. Each station meets the requirements for efficiency, greater than 95%, and position resolution, with uncertainty in the x -position less than 400 μm . The performance of the drift chambers in Run 6 is given in table 2.3.

2.4.3 Proportional Tubes

In station 4, tracking and muon identification is accomplished with four layers of proportional tube planes. The proportional tubes are inherited from a project at Los Alamos National Laboratory which had published results and characteristics of the tubes in ref. [64]. The primary purpose of the proportional tubes is to identify final state muons by measuring a characteristic, momentum-dependent deflection in particle tracks passing through the 1 meter thick iron wall between station 3 and station 4. Each plane contains 9 tube modules which are themselves each comprised of 16 proportional tubes. Each tube has a length of 3.66 m and a diameter of 5.08 cm with a wall thickness of 0.16 cm. The first and fourth planes are oriented horizontally to measure the y-positions of the muons, while the second and third planes are oriented vertically to measure the x-positions as shown in fig. 2.4. The proportional tubes use the same gas mixture as the chambers in this experiment. The average position resolution was 0.5 mm which was sufficiently precise to identify muons during data collection.

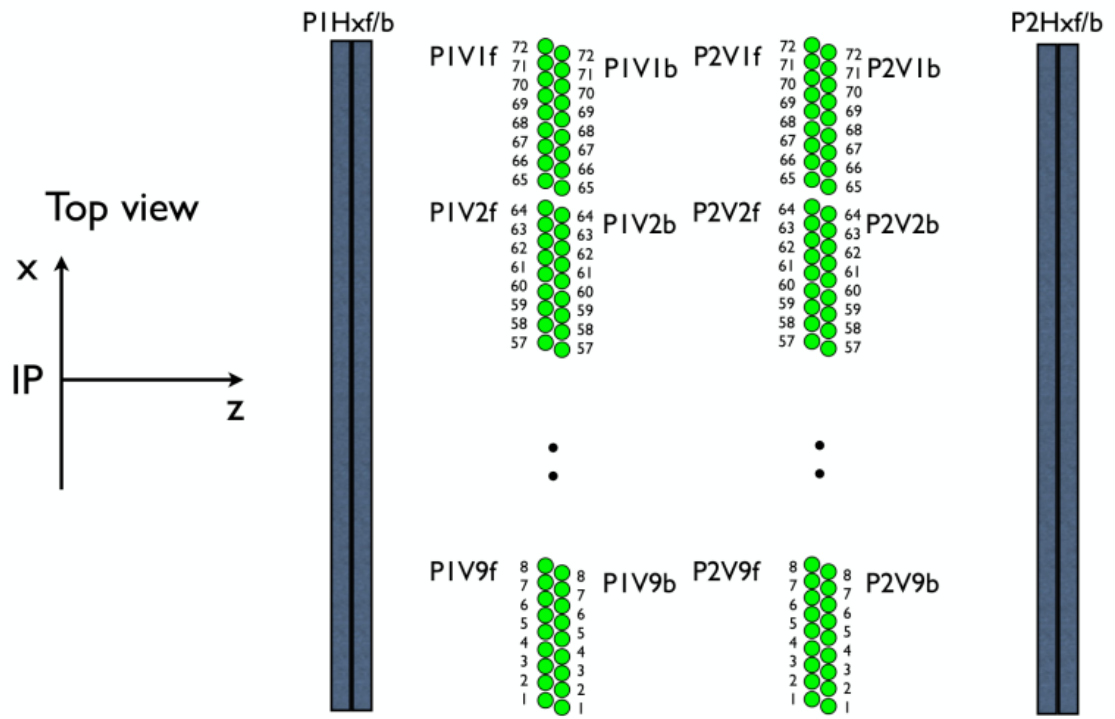


Figure 2.4: A schematic diagram of the proportional tubes used in the SeaQuest experiment as seen from the top, interaction point on the left and muons traveling to the right. Figure published in ref. [62].

Chapter III

Trigger and Tracking

The J/Ψ produced at SeaQuest may decay into muon pairs which are measured in the spectrometer along with muons from the Drell-Yan process. A system to read out the detector data, logic to select interesting detector patterns in the spectrometer, and an algorithmic approach to reconstructing the muon tracks were implemented and published in refs. [62, 65]. In this chapter, the SeaQuest data acquisition systems and trigger logic are described. Finally, the “kTracker” program, which reconstructs muon pairs from the recorded detector data, is detailed.

3.1 Data Acquisition Systems

SeaQuest utilized three data acquisition (DAQ) systems to meet timing and bandwidth requirements. The “Event DAQ” recorded primary detector information upon receiving the trigger, while the “Scaler DAQ” read out scalers on a fixed 7.5 kHz clock. The final system, the “Beam DAQ”, recorded information from Cerenkov detectors in the beam line to tag events with unusually high beam intensity. The Event and Scaler DAQs both utilized the VME-based CEBAF Online Data Acquisition (CODA) system developed at Thomas Jefferson National Accelerator Facility [66].

The Event DAQ was responsible for coordinating the readout of all detectors, grouping their data into events, and encoding the data to binary data. Each detector

system was connected to VME modular electronics crates where signals from the front end detectors were digitized. Inside of each crate was a Trigger Interface (TI) electronics card, along with a Motorola VME processor which served as a Readout Controller (ROC) in CODA, time to digital converters (TDC), and other detector-specific readout modules. All of the trigger interface modules were connected to a singular, central Trigger Supervisor (TS) module, which was connected to the trigger logic.

After receiving a trigger, the TS distributed a signal to all TI modules which stopped TDCs and began a data transfer from readout modules, over VME backplane, to the ROC. Data was read from all ROCs via gigabit Ethernet on a private data network. Simultaneously, the TS signal was sent to the QIE presented in chapter 2 to read out beam intensity data in a 20 ns window around the initial trigger signal. During data taking, the primary source of deadtime arose from data transfer over VME backplanes. On average, readout during data taking for Runs 1-6 took 150 μ s. Though the data is not included in this analysis, an experimental upgrade which added a buffered readout scheme to the TDCs was added after Run 6 and, during a short Run 7, demonstrated a reduced deadtime of 30 μ s [62].

The Scaler DAQ allowed the experiment to monitor trigger, beam, and spectrometer status irrespective of the status of Event DAQ. The system was controlled by a single ROC comprised of a VME crate with four scalars. The first scalar was triggered by an external 7.5 kHz signal and sampled two uncorrelated hodoscope channels to estimate the beam duty factor. All three other scalars are controlled by Beginning of Spill (BOS) and End of Spill (EOS) signals sent from Accelerator Division, correlating with the window of active beam in the experimental hall, and record spill-level information. Important information recorded at Scaler DAQ included beam intensity, rates in the hodoscope detectors, and number of triggers sent to Event DAQ.

Finally, the Beam DAQ monitored the Cerenkov detectors in the beamline which

recorded the per-bunch beam intensity measurements at 53 MHz. The duty factor of the beam, $\langle I \rangle^2 / \langle I^2 \rangle$, was the primary measurement of incoming beam quality at the experimental hall and a useful figure for Accelerator Division. The QIE board in the Beam DAQ measured four kinds of incoming data: the per-bunch beam intensity, the number of protons missed during detector read out, the number of protons marked by the QIE inhibit signal in particularly intense bunches, and a sum of the beam intensity and its square to compute the duty factor. When the Beam DAQ received the EOS signal, it read data through three separate Ethernet cables to a computer where the data was analyzed and posted to a public web-page to display per-spill updates during data taking.

3.2 FPGA and NIM Based Triggers

The trigger system uniquely identified physics events at SeaQuest and generated a readout signal which propagated to all detector systems. SeaQuest used two different technologies to produce two sets of triggers used in data taking. The primary physics trigger in the experiment utilized field programmable gate array (FPGA) technology and its details are have been published in refs. [65, 67]. A secondary trigger was constructed using nuclear instrument module (NIM) electronics to implement simple combinatorial logic. The NIM trigger was never used for primary physics data taking, but was used as a sanity check during commissioning and data taking. Each trigger used discriminated signals from the hodoscope detectors in each station, previously detailed in table 2.1, as their primary input.

To identify detector patterns which correlate to physics events of interest, muon pairs from Drell-Yan or charmonium decay were generated by a phenomenological model and propagated through a simulation of the SeaQuest detector geometry using the Geant4 software package [68–70]. Patterns of four detector hits, each from a hodoscope in station 1-4, were grouped together as “roads”, which were sorted by

frequency and associated with muon charge. During data taking, roads with higher than expected trigger rates were considered “hot” and removed from the trigger logic to balance event acceptance with noise suppression. Several roadsets were utilized during the SeaQuest data taking as the trigger logic evolved. Each road set was implemented in a look-up table in the FPGA firmware. The FPGAs used in this experiment had sufficient memory to fit between 300-400 roads in a typical roadset.

The hodoscopes used to form the trigger were oriented vertically in the lab and split into a top and bottom half. Triggers were formed based on the coincidence of muon tracks, charges, and which half of the detector the tracks were found in, presented in table 3.1. The primary physics trigger required muon tracks of opposite charges in opposite halves of the detector.

Name	Trigger Requirements	Prescale Factor
NIM 1	Hits in y hodoscopes in all four stations.	N/A
NIM 2	Hits in x hodoscopes in all four stations.	N/A
NIM 3	7.5 kHz “random” trigger.	N/A
FPGA 1	Two muon tracks of opposite charge in opposite halves of the detector.	1
FPGA 2	Two muon tracks of opposite charge in the same half of the detector.	1000
FPGA 3	Two muon tracks of the same charge in opposite halves of the detector.	123
FPGA 4	Any single muon track.	25461
FPGA 5	Any single muon track in a “high p_t ” subset of the roadset.	2427

Table 3.1: Trigger requirements of the NIM and FPGA based triggers used at SeaQuest, along with prescale factors.

Splitting the roads into a top and bottom half was necessary to reduce the large backgrounds observed in the same-side trigger, FPGA 2, resulting from the interference of unassociated muons in the central spectrometer. Near the center of the spectrometer, muons with small transverse momenta may have crossed tracks by the time they have reached station 4. This results in some central roads differing by a single hodoscope paddle in the final station. Therefore, it was possible to satisfy the trigger requirement of two muon roads in the same half with only five hodoscope hits. A single muon from a true pair would generate four hits on its own, allowing any stray, unassociated muon to generate a trigger. By contrast, the primary physics

trigger requirement of tracks in opposite halves of the detector can only be satisfied by eight hodoscope hits.

The FPGA trigger was comprised of nine CAEN v1495 VME modules, which each mounted an EP1C20F400C6 FPGA chip from Altera, along with a “Trigger Supervisor” VME module, and “Trigger Interface” modules for each detector system to read out. Each v1495 FPGA board was loaded with custom firmware, developed by Jinyuan Wu at Fermilab, which implemented the trigger logic and a TDC module to record hodoscope hit times for cross-comparison with Event DAQ data. Details on the firmware and development of the trigger have been published in reference [65].

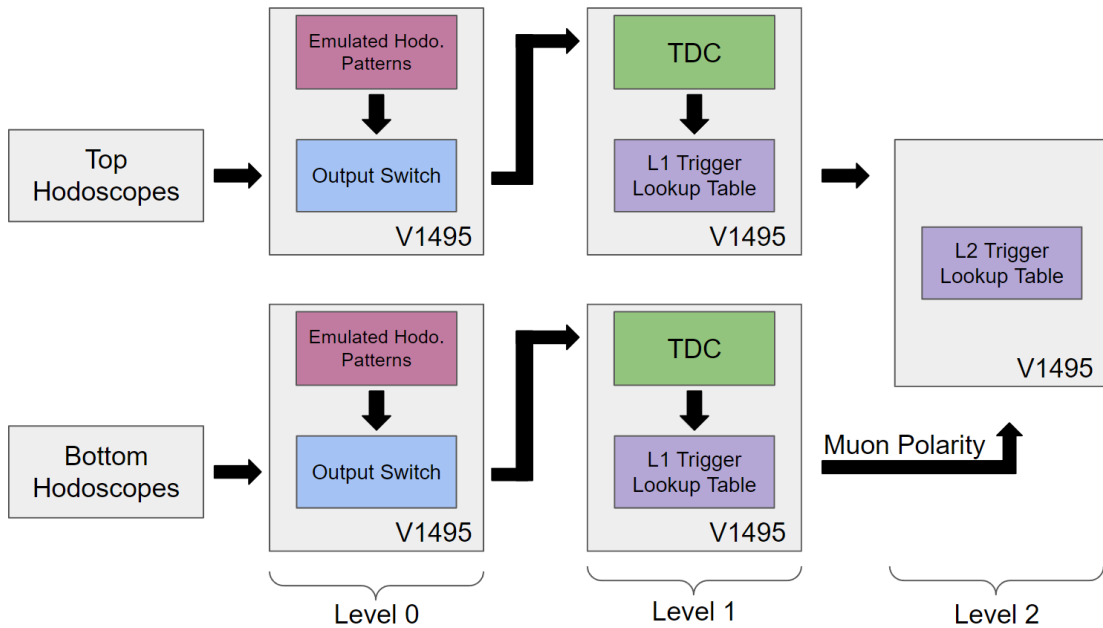


Figure 3.1: A flowchart showing the path of detector information through the FPGA boards which formed the trigger logic.

A block diagram of the trigger data flow is shown in fig. 3.1 for the vertical hodoscopes used to form the trigger. The trigger logic was divided amongst three layers, “Levels 0, 1, and 2”. Level 0 and Level 1 were each comprised of four FPGA boards, analyzing hodoscope data from the top, bottom, left, and right halves of the hodoscope planes. In practice, only the vertical hodoscopes, measuring the x -

positions of muon tracks, were used in the trigger logic during production data taking. Each FPGA board was capable of taking input from a maximum of 96 hodoscope detectors. As a result, there were two input paths matching the top and bottom halves of the detector. During development and testing of the trigger, Level 0 was used to generate signals to emulate hodoscopes of known patterns to test the trigger firmware in Level 1. However, during production data taking, the Level 0 boards simply forwarded hodoscope information to Level 1. In the Level 1 boards, hodoscope signals could be adjusted at a resolution of 1 ns to correct for cable length differences coming from the readout electronics in each station. Incoming hodoscope signals were compared with the roadset in a look up table and the road-associated muon charge was sent to the Level 2 board. The Level 2 trigger logic was implemented in a single board, receiving charge information from the top-half and bottom-half Level 1 boards and forming the logical combinations found in table 3.1.

The FPGA trigger decision was sent to the Trigger Supervisor where a common stop signal is issued to all Trigger Interface modules. After receiving the stop signal, each detector station halted data taking and read out data from an internal buffer going back a configurable amount of time. The trigger decision time, and TDC delay for the experiment, was 1 μ s. After data was recorded into the DAQ as detailed in sec.3.1, the trigger system and all detector readouts were reset for the next bunch of the proton beam. During the readout process, the TDCs in the FPGA trigger are halted and all inputs to the Trigger Supervisor are inhibited.

The trigger acceptance during SeaQuest preferentially selected the high-mass range of produced dimuons to reduce charmonium backgrounds in the primary analysis and to reject part of the mixed background. Many of the unassociated single muons which are misidentified as dimuons come from pion decays which tended to have lower single-track transverse momentum. False dimuons reconstructed from these unassociated single tracks tended to have low mass and were reduced by the

high-mass selection of the trigger [67]. A plot of the trigger acceptance in mass from ref. [67] is shown in fig. 3.2. The performance of the trigger was reported through

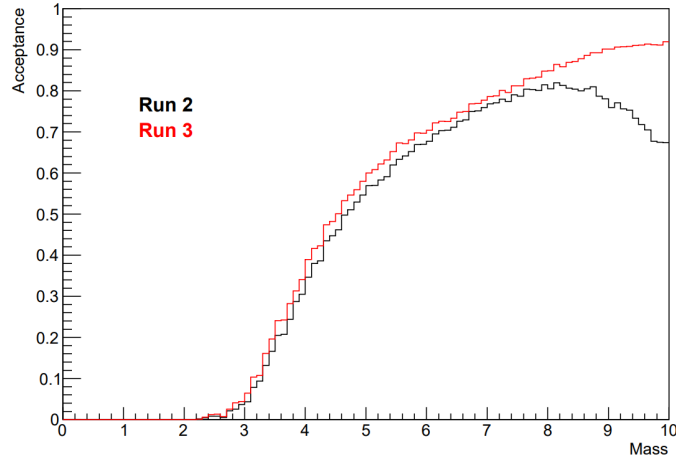


Figure 3.2: Trigger acceptance for the data used in this analysis, from ref. [67]. Reproduced as published, mass is in units of GeV/c^2 .

two metrics called “Logic Efficiency” and “Logic Purity” by ref. [67]. These names were chosen to clarify the difference between these values and what is typically meant by “efficiency” and “purity” in referring to the trigger’s capability to identify and accept events of interest. The “Logic” of these terms refers to the consistency of the trigger outputs with the hits recorded on its internal TDC. Any time the trigger records TDC hits corresponding to a trigger road, the expected trigger signal ought to be produced 100% of the time. Before Run 2, there were problems synchronizing the TDC hits with trigger outputs due to a difference in the 53MHz frequency of the beam and the 40MHz internal clock used in the trigger FPGA boards. After switching to using the 53MHz signal sent from the Accelerator Division as an external clock, the “Logic” efficiency and purity were found to be unity. Estimates of the conventional efficiency and purity (the signal acceptance and background rejection capabilities) of the trigger were made by a comparison with Monte Carlo and can be found in table 3.2 as reported in ref.[67]. The signal acceptance was calculated by comparing the FPGA 1 trigger acceptance to a hypothetical “all roads” trigger in

Data Taking Period	Trigger Roadset	Signal Acceptance	Background Acceptance
Run 2	57	59.76%	0.1833%
	59		
	62		
Run 3	67	62.95%	0.1852%
	70	62.45%	0.1775%

Table 3.2: Estimated signal and background acceptances for each roadset used in this analysis as published in [67]. Random data from Run 3 is used for the background estimate.

the Monte Carlo simulation. The background acceptance was computed in the same way, however data from the random trigger, NIM3, during Run 3 were used rather than simulation. Unfortunately, neither the signal nor background acceptances were published with error estimates.

3.3 Muon track Reconstruction with kTracker

After the Trigger has identified an event of interest and the data acquisition system has collected information from the detectors, the “kTracker” software package identifies and reconstructs muon tracks in each event. kTracker was developed by Kun Liu, a staff scientist at Los Alamos National Laboratory, and implements a Kalman filter to interpolate particle paths between each detector station. Once the positive and negative muon tracks have been reconstructed, a second Kalman filter is used to project them back through the magnetic field of FMag to determine their common vertex.

Several features of the SeaQuest experiment created challenges for muon track identification and reconstruction. Due to the high intensity of the beam, the average number of muons in the spectrometer was fifteen per event. Often, unassociated muons produced from physics interactions of the beam in the beam dump produced a false trigger. Identifying the detector information in two stations corresponding to the same muon grows combinatorially in complexity with the number of muon

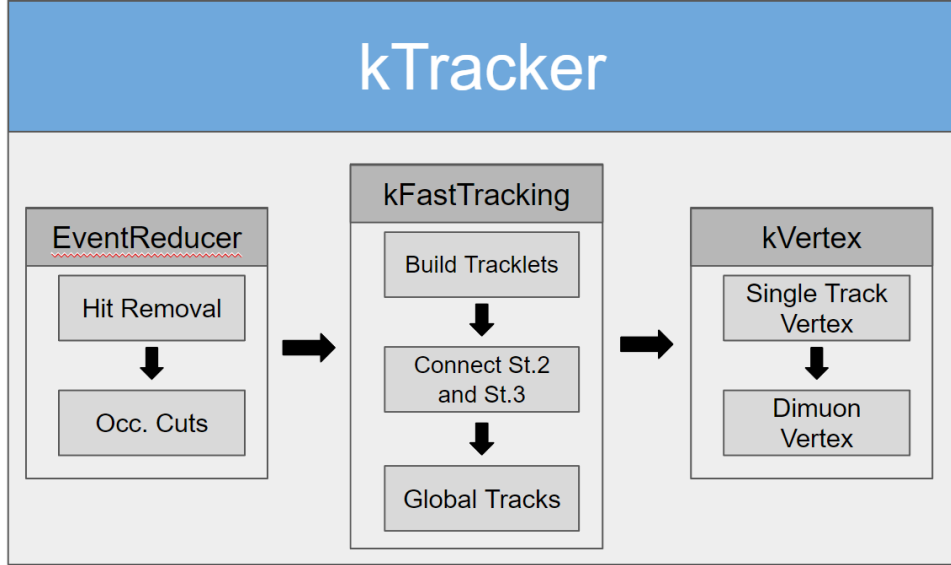


Figure 3.3: Data processing stages in the kTracker algorithm.

tracks, making analysis of data from intense beam bunches intractable. The iron core of FMag also presents difficulties, particularly in vertex reconstruction. Due to the sheer mass of iron the muons must traverse, there is a non-negligible deviation in their paths through FMag resulting from multiple scattering. Muons passing near the edges of KMag also experience the effects of field gradients. These complications make naive linear interpolation of tracks between stations poor and suggested a method which can incorporate models for multiple scattering or fringe fields. The Kalman filter provided an iterative approach to estimating muon tracks in stations 1-4 and for propagating tracks through FMag to determine the event vertex given a model for underlying sources of uncertainty. The algorithm is broken into three stages named EventReducer, kFastTracking, and kVertex shown in figure 3.3.

3.3.1 EventReducer

Before searching for muon tracks in the detector hit data, a series of selections are applied to remove extraneous hits, reducing the computation time and improving tracking results. All detector hits considered in tracking must be within a specified

time window, related to the expected arrival time of muons in the station and the beam arrival signal. Only the first hit on any single detector channel within the time window is considered, as reflections in detector readouts had been observed in early data taking. Data from the x -position measuring hodoscopes are compared with the trigger roadset to verify the trigger logic. All hodoscope hits that are not in the roadset are removed.

Hits in chambers are treated with special care and noisy “clusters”, groups of hits in neighboring wires likely arising from cosmic ray muons and secondary electron emission, are removed. Any set of three or more adjacent wire hits are removed immediately; while for pairs of neighboring wire hits, only the earliest hit is kept. The total number of hits in the chambers, hodoscopes, and proportional tubes is also

Detector	Maximum Occupancy
DC1.1	350
DC1.2	350
DC2	170
DC3m	140
DC3p	140
Station 1 X Hodoscopes	15
Station 2 X Hodoscopes	10
Station 3 X Hodoscopes	10
Station 4 X Hodoscopes	10
Proportional Tubes	300

Table 3.3: Maximum occupancy selections on each detector during the EventReducer.

used in data selection before tracking. A complete list of detector occupancy limits is provided in table 3.3. If the event passes occupancy checks after all hit removal is complete, the final selection imposes a maximum of five possible muon tracks. The surviving track candidates are further refined by track finding.

3.3.2 kFastTracking

After selections have been applied on the detector hits, they are extrapolated into continuous muon tracks from station 1-4. The process begins by identifying pairs of hits in the station 2 and station 3 chambers. In each chamber, hits in the X plane are associated with hits in the U and V stereo angle planes to form “local triplets”. A search is performed for a hit on wires in the U plane lying in a 20 cm window around the initial hit in the X plane. A smaller search window of 5 cm around identified U wires is sufficient to constrain the hit search in V . The procedure for local triplet identification is shown in fig. 3.4 in the X, Y plane transverse to the beam line. Drift distance information is not yet considered in the triplet fit and multiple triplets can share hits. Triplets are then loosely checked to ensure they point to a hit in the X hodoscopes in their station and point back to the target.

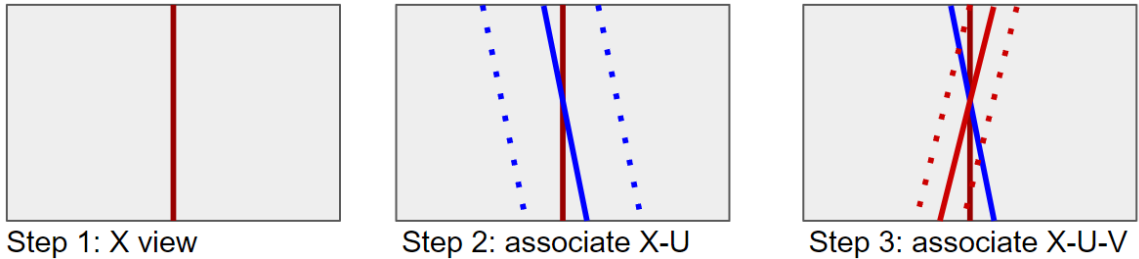


Figure 3.4: Cartoon showing local triplet formation in kFastTracking, with solid lines representing hit wires and dotted lines showing the search window for the next hit. First, a hit wire, colored red, is found in the X plane. Then a search is performed in the search window shown in blue in the U plane. Finally, a smaller search window, shown in red, is used to look for a matching hit in the V plane.

Triplets in station 2 and 3 are then combined to form “tracklets”. To reduce the number of hit combinations checked, rough selections are made on the tracklet slopes and whether the tracklet points back to the target and towards valid hits in station 4 proportional tubes. A simple χ^2 fit is performed on the remaining combinations and another selection is made to remove unlikely tracklets. The tracklets are then

extended to station 4, defining a region where a similar search is made for matching tracklets between the proportional tube planes. Multiple scattering in the 1 m iron absorber between is accounted for and introduces an uncertainty of 0.118 mrad/GeV [71] in the angle of the muon track between station 3 and 4. Tracklets deflected by more than 30 mrad in the absorber are discarded.

After confirming tracklets between station 2 and 3 via the station 4 proportional tubes, they are projected back through the magnetic field of KMag, using the sagitta ratio to define a central value and search window no greater than ± 5 cm for hits in station 1. This process also determines the momentum of the muon from the measured bend in the muon track and the known magnetic field of KMag and is further detailed in reference [71]. These hits are grouped into local triplets in station 1 and connected to the tracklets to form muon tracks through the spectrometer. The Kalman filter is applied to the resulting tracks to refine the track information, especially tracklets from station 2 to 3 which are not straight lines due to the fringe fields of KMag.

3.3.3 kVertex

Refined tracks from station 1-4 must be projected back to the target to identify the interaction vertex, requiring a model of the FMag magnetic field. The field is treated as a perfect dipole without fringes, sliced into segments along the beamline. Each step between segments is divided into a first and second half, applying energy loss corrected by total path length, with an intermediate transverse momentum kick from the field. Past FMag, the origin is chosen to be the distance of closest approach between the track and the beamline. A second Kalman filter is employed to refine the final vertex position following an algorithm inherited from a vertex fitter [72] developed for the CBM experiment at The GSI Helmholtz Centre for Heavy Ion Research in Germany.

3.4 SpinQuest Trigger and Tracking Upgrades

The SpinQuest experiment, E1039, aims to provide the first measurement of the sea-quark Sivers function via the Drell-Yan process. SpinQuest will make use of the SeaQuest spectrometer and data acquisition systems with minimal changes. A new, polarized target has been constructed to replace the SeaQuest target and a pair of new hodoscope planes have been added in stations 1 and 3 with finer spatial resolution. Finally, an upgraded trigger system and improved tracking have been installed and await future data taking. From 2019 until the present, my primary responsibility has been to serve as the FPGA trigger expert for the SpinQuest experiment. I spent a substantial portion of my effort testing the SpinQuest trigger system, developing live monitoring tools, and installing an improved trigger test stand in the experimental hall. I also independently developed a multithreaded extension of the kTracker program to meet online monitoring time constraints to provide real-time tracking for SpinQuest data taking. In this section, I detail my contributions to the upgraded trigger and tracking systems for the SpinQuest experiment.

3.4.1 SpinQuest Trigger System

The SpinQuest trigger system retains the core ideas and hardware of the SeaQuest system. Monte Carlo simulation is used to determine a set of most likely paths signals take through the spectrometer, referred to in the collaboration as a “roadset”. CAEN v1495 FPGA boards implement this roadset as a series of lookup tables and the primary logic looks for muons of opposite charges in opposite halves of the detector. By 2019, when I inherited the system, the SeaQuest trigger logic had been disassembled and the hardware was a cluttered mess of cables. I led the development of a trigger test stand to revive the SeaQuest trigger, installed the test stand in the experimental hall along with a new roadset for SpinQuest data taking, and implemented a buffering scheme to match the improved TDC buffering scheme discussed in chapter 2. The

new system is cleaner, more automated, and easier to test.

SeaQuest utilized a total of nine FPGA boards to implement the trigger logic. Four of these boards were used to monitor the horizontal, Y , hodoscopes, but their information was not meaningfully included in the trigger logic. Because the bend plane of FMag and KMag are in the horizontal, X , direction, the Y hodoscopes offered little predictive power in identifying interesting events. After Run 6 data taking was completed, several short experimental runs attempted to improve the trigger results by including the Y hodoscopes with little success. The Y hodoscope path was removed from the trigger, reducing the hardware components by half.

The five remaining FPGA boards were placed into a VME crate along with a Motorola MVME5500 VME processor which was connected to a computer by Ethernet cable. A library of driver functions were written in the C programming language and compiled for the VXWorks operating system which runs on the MVME5500. The driver functions map hardware memory on the FPGA boards into the computer's virtual memory, abstracting transfers over the VME backplane into conventional C-style memory accesses. A series of control registers in the FPGA firmware could then be written into by the computer to change the trigger state, readout trigger memory, and reset the trigger logic. A 40 MHz clock was provided by the V1495 boards, but the test stand utilized a 53 MHz clock generated by NIM modules to match the RF timing of the beam sent from the Accelerator Division, which will eventually be the system clock during data taking.

3.4.1.1 SpinQuest Trigger Test Stand

Development of the trigger test stand started from simple reads and writes to registers on the Level 0 board. Once I had confirmed the hardware of each of the boards by reading a dedicated register provided by the manufacturer, I used NIM modules to generate a 1 kHz test pulse to emulate detector input. With these inputs,

I was able to identify and test each unique input channel in the Level 0 trigger TDC. I also enabled the Level 0 pass-through used in standard data taking and confirmed the output mapping of the Level 0 boards. After verifying all hardware and firmware for the Level 0 boards, I connected the two Level 1 boards and tested their hardware and firmware. Using a python script I developed, trigger roads are converted into bit-wise patterns emulating roads matching the hodoscope mapping in Level 1 and then programmed into dedicated memory inside of the Level 0 boards. To verify the implementation of the trigger firmware, two sets of patterns were generated. First, a pattern of pure roads was programmed to ensure that the trigger fired on all elements of the roadset. Second, the pure roads were randomly modified by random removal or adding of non-road hits to ensure the trigger would only generate a signal when a road was properly identified. After tuning the system timings, the trigger firmware passed these tests with 100% accuracy. Finally, the Level 2 trigger board was placed into the system and had its hardware and firmware checked with the same method as Level 0 and 1. Emulated roads from the roadset were generated in Level 0, produced the correct muon charge information in Level 1, and the information from the top and bottom halves were assessed in Level 2, with final triggers recorded by a visual scaler. This procedure guaranteed that the system worked, but only provided the total efficiency during early tests. To properly align hodoscope channels in time, a more precise test stand was required to provide per-road trigger information. While ensuring the integrity of the trigger firmware and hardware, the roadset tests were coordinated by hand, with special driver functions sent via the command line. To test all 100,000 combinations of top and bottom roads and identify timing problems in individual input channels, an automated test stand was created. A second VME crate was added to the trigger test stand, serving as a Read Out Controller called 'Roc 6', in a standalone DAQ running CODA. Along with an MVME processor, the second crate contained a single VME scaler board which could be read over

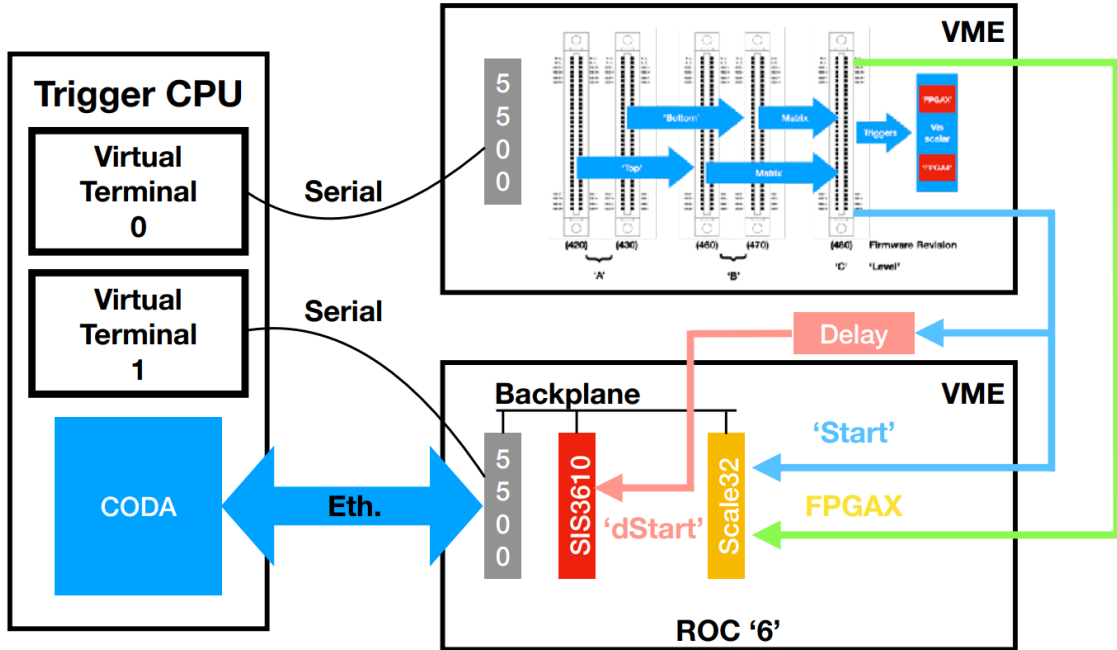


Figure 3.5: A cartoon showing the SpinQuest trigger teststand.

the backplane and a SIS3610 IO board, developed by Struck Innovative Systems for DESY in Hamburg, Germany, which simply raises interrupts on the VME backplane to initiate readout of the scaler. Both crates were controlled by a single computer which organized the trigger test, shown in the cartoon of fig. 3.5. A 'start' signal is initiated by the computer at the beginning of the firmware test which resets the trigger system and clears the scaler count. The same 'start' signal is delayed 800 ns to match the delay in the trigger logic and acts as a 'stop' signal to all systems. The pattern memory allowed a maximum of 10 roads to be tested in any one 'batch' of the test, identifying each 'start' signal with a maximum of 10 triggers. The output of the trigger system was sent to the scaler in the test ROC, which recorded all five of the FPGA trigger outputs on independent channels between the 'start' and 'stop' signals. When the SIS3610 in the test VME receives 'stop' it raised a VME interrupt which prompted readout of the scaler by CODA. This data is read by a custom C program and analyzed using the ROOT software package to identify any potential

firmware problems or channel timing mismatches.

3.4.1.2 Installation of the Trigger

After the trigger hardware and firmware was verified, the trigger and test stand were installed in the experimental hall and tested on cosmic rays. Both VME crates were brought down into the NM4 experimental area at Fermilab and connected to hodoscope channels in groups of sixteen. An estimate of the cable delay from each hodoscope station was made based on the cable length and measured by reflection on an oscilloscope. This estimate was used to set the initial per-channel delays in the FPGA system and refined by sending 1 kHz pulses over hodoscope channels in each station from a common source and examining the FPGA TDC data. Finally, the timing was aligned for cosmic rays by examining TDC data in triggered events from real hodoscope signals. The fine-alignment procedure is only repeated after new firmware is uploaded to the trigger or major changes occur during data taking, e.g. detector movement, changes in beam conditions, etc. A software package was eventually developed by my colleague, Ievgen Lahvrukin, to automatically determine the optimal per-channel detector alignment during data taking. The results of the automatic alignment process are shown in fig. 3.6. The time distributions are wider for cosmic rays than for the upcoming bunched proton beam, so the timing adjustment will be more precise during data taking. To test the trigger using cosmic rays, a simplified cosmic ray muon trigger roadset was developed to match the logic of diagnostic NIM triggers available at the time. The cosmic ray roadset identifies the coincidence of a hit in station 2 with a hit in station 4. A full list of the trigger logic for cosmics is shown in table 3.4. A simple comparison of trigger rates showed less than 1% difference between the FGPA and NIM triggers.

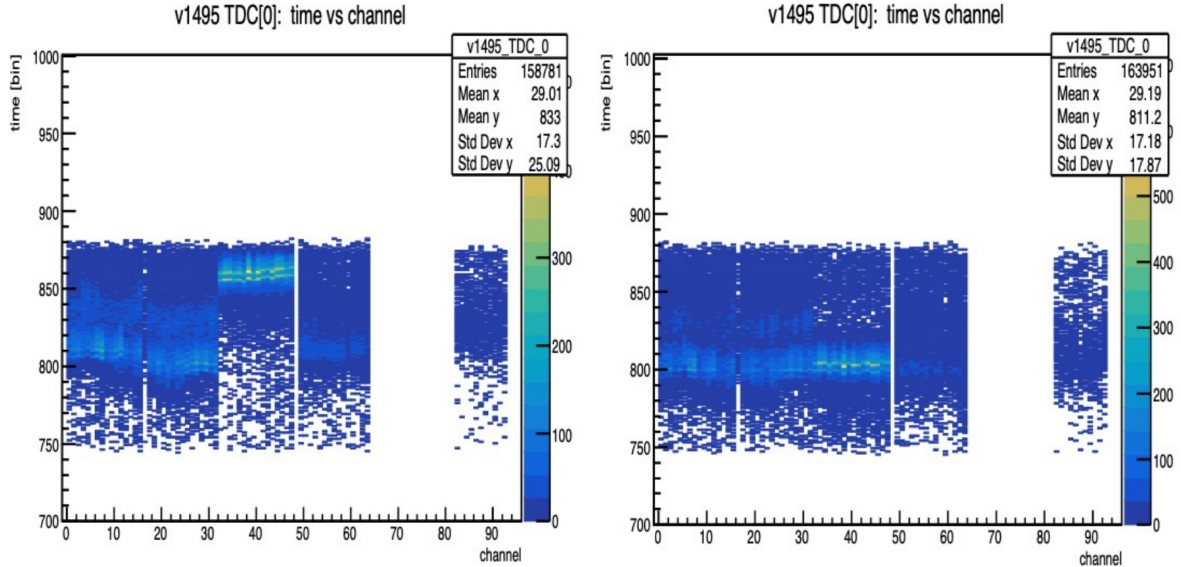


Figure 3.6: (Left) Two-dimensional histogram showing the frequency of TDC hits, with time in the vertical direction and input channel in the horizontal and an initial time delay of zero. A bright horizontal line should be observed when the channel timings are correctly aligned. (Right) The same histogram after the automatic alignment process has completed and an identifiable horizontal line is apparent.

3.4.2 A Multithreaded Extension of kTracker

While kTracker performed well for the offline analysis at SeaQuest, it was not fast enough to reconstruct a meaningful number of tracks during live data taking. I developed a multithreaded extension to the kTracker algorithm to parallelize computation of events, with the goal of an order of magnitude gain in track throughput, to serve as an online reconstruction platform for live track monitoring during SpinQuest data taking. A proposal for funding was approved and development of the project at Fermilab was supported through the Universities Research Association Visiting Scholars Program. First, a test model was developed on a personal laptop to demonstrate a simple analysis of detector data on parallel threads. Then, a demonstration of a parallel processing implementation of kTracker was shown at the Quarks2Cosmos conference in 2021. In the following months, a commercial machine with thirty-two

Cosmic Ray Trigger	Requirements
FPGA 1	Any hit in H2 and any hit in H4
FPGA 2	Any hit in the top of H2 and the top of H4
FPGA 3	Any hit in the top of H2 and the bottom of H4
FPGA 4	Any hit in the bottom of H2 and the top of H4
FPGA 5	Any hit in the bottom of H2 and the bottom of H4

Table 3.4: Cosmic ray FPGA trigger logic used for data taking while awaiting beam.

cores was purchased, installed, and tested at Fermilab on SeaQuest data. Output results were compared with results from the original kTracker for correctness. Final results from the full machine were shown at the APS DNP conference in October 2021.

3.4.2.1 Parallelizing Per-Event Processing

The multithreaded algorithm implemented the main-replica paradigm, which is discussed in great detail under the outdated name ‘master-slave’ in ref. [73]. A ‘main’ class, kScheduler, coordinates all working ‘replica’ threads, creating them when new jobs are necessary and collecting their outputs and deleting them after jobs are complete. For kTracker, and more generally in many physics analyses, the basic data path is simple. Data is read from disk on a per-event basis, a, typically, per-event analysis procedure is applied to the data, and the extracted physics information is then written to disk as illustrated in fig. 3.7. This suggests three kinds of thread jobs in the main-replica paradigm. In kScheduler, these are the fReaderThread, fWorkerThread, and fReaperThread. fReader is responsible for reading in physics events from disk, appending some job-specific meta data, and then dynamically balancing load by finding free CPU cores where the analysis can be performed. fWorker performs the analysis and in general this can be any kind of physics analysis. In this particular case, fWorker is simply a wrapper for underlying kTracker classes that can handle metadata requirements. Finally, the fReaper thread is responsible for collecting completed job information from fWorkers, writing data out based on metadata

indicators which summarize the results of tracking, and killing completed fWorker threads.

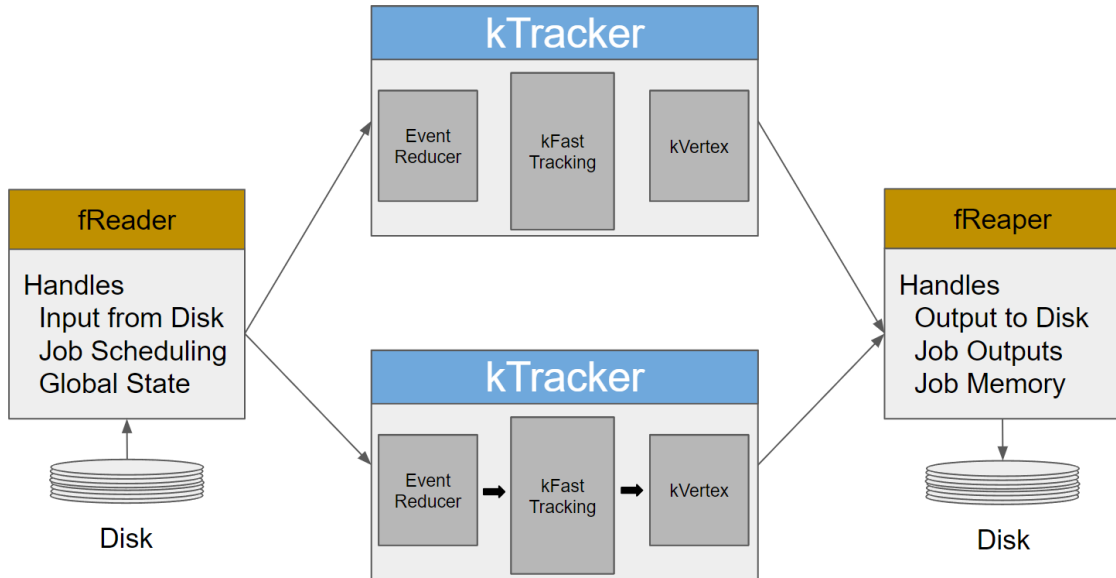


Figure 3.7: Data flow in the multithreaded tracking algorithm. fReader handles memory inputs from the disk and schedules multiple instances of the kTracker software on free computer cores as they become available. fReaper collects each completed tracking instance, deleting the associated working thread and writing the results to disk.

3.4.2.2 Software and Synchronization

Because the kTracker library is implemented in the ROOT data analysis framework, the best possible choice for a multithreaded approach was to use the TThreads library provided in ROOT. TThreads uses the underlying, system-dependant implementation of the posix pthreads library and provides hooks for all important functions and synchronization primitives. ROOT maintains a large quantity of global state variables, such as name lists or graphics lists, and attempting to synchronize every memory access from an external pthreads library would be nearly impossible. Each of the fReader, fWorker, and fReaper threads were implemented as TThread classes.

The TThreads interface was useful, allowing me to write my own class methods for reading and writing data, while also directly referencing kTracker classes, data structures, and methods. This was essential to developing a robust system, as any change or update to kTracker has no effect on the parallelization scheme, allowing the system to stay up to date without any additional labor.

To protect the integrity of data as it passes through the analysis framework, a synchronization scheme is necessary to prevent threads from simultaneously working on the same region of memory. The TMutex (mutual exclusion) class provides locks called 'mutex's which can be placed on regions of data to only allow a single thread to access the data at any time. When a thread attempts to access protected data, it first tries to acquire the mutex. If it cannot do so because another thread is currently performing operations on the data, the accessing thread is put to sleep by the system scheduler until control of the mutex is relinquished. This simultaneously prevents threads from accessing each others data at the same time, while also saving system resources because sleeping threads are not constantly polling to see if the mutex is available. For this project, the TSemaphore class provided an underlying synchronization primitive from which a series of synchronous queues were constructed. A semaphore is a mutex protected integer, $N < N_{max}$, with atomic update operations called 'put' and 'fetch' which increment and decrement N , respectively. When a thread attempts to 'put' the semaphore, it first acquires the mutex on N and determines whether $N + 1 < N_{max}$. If $N = N_{max}$, the thread sleeps until a 'fetch' decrements N . Otherwise, N is incremented by 1 and the mutex is relinquished. The 'fetch' operation works identically, but determines whether $N - 1 > 0$.

To see how semaphores can be used to form a synchronous queue, it is instructive to examine the data path from fReaderThread to fWorkerThread. Given an input first-in first-out buffer of size N acting as a queue, we would like the fReaderThread to read events from the disk and place them into the queue whenever a free space is

available. At the same time, we would like any free `fWorkerThread` with an available CPU core to take a job from the queue whenever a space is filled. Because the system scheduler is free to choose which threads to assign, it cannot be assumed that the `fReaderThread` exists or any jobs have been placed in the queue before an `fWorkerThread` arrives asking for work. To avoid a NULL memory access or buffer overflow, it is important that the `fWorkerThread` sleeps until a job is available if it finds an empty queue and the `fReaderThread` must sleep until a new job space is available upon finding a full queue. The `TSemaphore` provides precisely the solution that is needed. A semaphore of size N is initialized with a value of '0' before the `fReader` or `fWorker` threads, which are now required to 'put' and 'fetch' respectively before accessing the queue. If an `fWorker` thread is scheduled before the `fReader` has a chance to fill the queue, it will attempt to 'fetch' from the semaphore which has a value of 0, resulting in the `fWorkerThread` sleeping until the queue begins to fill. On the other hand, if the `fReader` thread is later attempting to put job data on a full queue, it will try to 'put' on the semaphore which has a value of N , resulting in the `fReader` sleeping. Whenever a 'put' or 'fetch' is successful, all sleeping threads waiting on the opposite operation ('fetch' or 'put') are awoken with equal probability to be chosen first by the scheduler. This solution is valid for an arbitrary number of writers or readers of the queue.

The synchronous queue is used to protect data as it traverses every level of the analysis pipeline. The `fReaderThread` writes to a synchronous queue that the `fWorkers` read from and in turn the `fWorker` threads write to an output queue that is read by the `fReaper` thread. The queues are also used as circular buffers during the tracking stage. Because it is expensive to instantiate and delete the large analysis classes which perform the core steps of `kTracker`, they are initialized only once at the beginning of tracking and deleted only once at the end. These expensive classes include the `eventReducer` and `kFastTracking`, which maintain their own internal state for each

internal step of tracking. To guarantee the validity of data at each step, these analysis classes are imbued with a sense of ownership and have their access protected by a circular buffer. When an fWorker has acquired event data and job metadata from the fReader, it attempts to access a synchronous queue where a number of eventReducer instances have been initialized. When the fWorker successfully acquires ownership of an eventReducer, it loads the analysis class with the event data and runs the analysis on a free CPU core. When the analysis is complete, the fWorker thread reads out the processed data and resets the analysis variables in the eventReducer before replacing it in the circular buffer. Tracking is completed in an identical process with a circular buffer of kFastTracker classes. A cartoon of the process is shown in fig. 3.8.

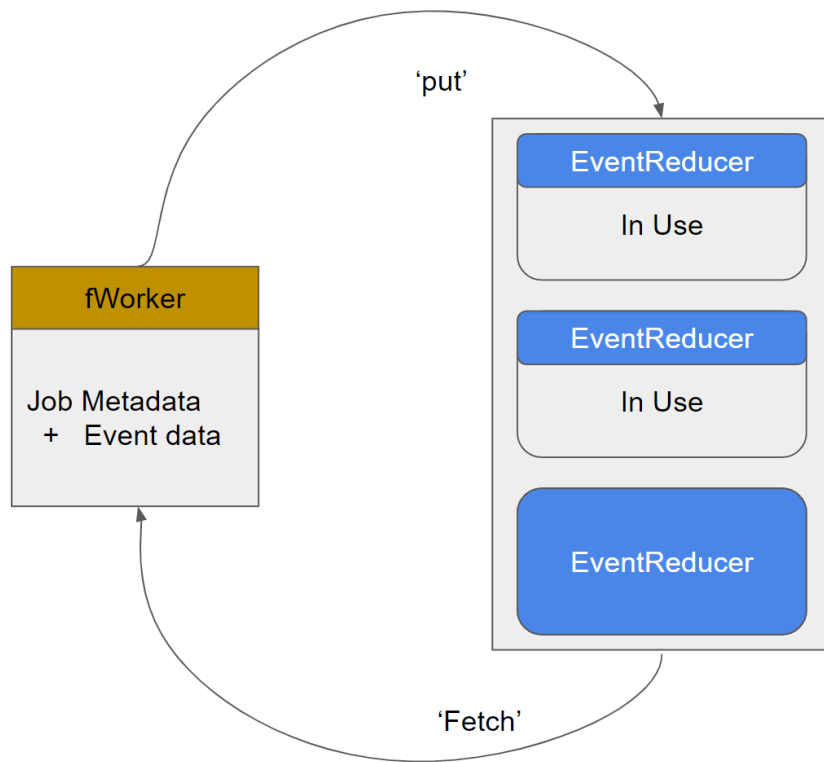


Figure 3.8: A cartoon showing a single fWorker thread attempting to access the circular buffer of eventReducers via synchronous queue operations, 'put' and 'fetch'. Two of the EventReducers are in use by workers, but a third is available and will be acquired by the fWorker thread on 'fetch' and later returned with 'put'

After tracking has been completed, the fReaper collects the processed event data

from the fWorkers through a final synchronous queue. fReaper collects data from fWorker threads and resets their job metadata before either returning them to work on the input queue or terminating them when no more events remain in the file. Ideally, threads are terminated even if there are jobs in the input queue as long as there are sufficient threads waiting to process them. Once the fReader thread has reached the end of the input stream, it generates a number of 'poison pills' equal to the total number of worker threads. The 'poison pills' are special, empty events with a unique marker in the job metadata that instructs fWorkers to skip analysis steps and signals the fReaper to kill a marked fWorker thread. After all fWorkers are terminated, the fReaper thread finishes writing any events in its buffer, closes all input and output files, terminates the fReaper thread, and finally terminates itself. The kScheduler, which has been waiting on all threads to terminate, writes a summary of the analysis for users and exits.

3.4.2.3 Performance and Hardware

An initial model of the multithreaded algorithm was developed on my personal, four-core, laptop. SeaQuest data from Run 2 were tracked using the single-threaded kTracker program used during SeaQuest data taking and the same data were tracked using a four-threaded implementation with the same underlying kTracker classes and methods to measure the performance of the system. All programs can be broken into a fixed-time component, primarily comprised of time reading or writing to disk, and a parallelizable component, which is any independent calculation on a computer core. Because the size of events at SeaQuest are small, on the order of a few hundred kilobytes, the read-in and write-out times are smaller than the tracking time for an event. Therefore, a good parallelization scheme ought to scale tracking times as $1/N$, where N is the number of computer cores. Initial results from the laptop model are shown in fig. 3.9, where it is clear that the performance is nearly ideal. Many

consumer-available machines provide up to thirty-two cores, promising well more than the order of magnitude improvement in throughput originally targeted as a project goal.

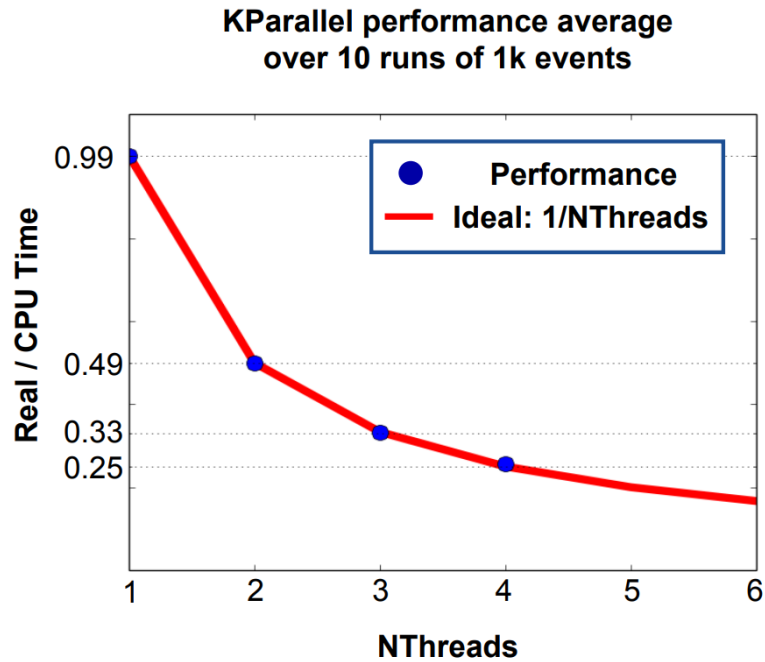


Figure 3.9: Ratio of wall-clock time to the computation time as a function of threads in the multithreaded tracking algorithm the four core laptop model.

A machine was purchased from Dell, through the University of Michigan, with thirty-two cores split between two primary computer chips connected by a shared motherboard. Computation is provided by dual Intel Xeon Silver 4216 server CPUs, each of which run 16 cores at 2.1GHz. 128Gb of RAM is used to buffer event data in local memory for faster computation. A 1TB hard drive serves as an initial buffer for output results and two Gigabit Ethernet ports are used to connect the machine to the local network that supports primary SeaQuest and SpinQuest data storage. When the beam arrives, events will be read into the machine, processed, and track information will be displayed for data-takers, allowing data quality monitoring just a few minutes after physics events inside of the detector. The machine was installed at Fermilab in the summer of 2021 and connected to the Event DAQ. The performance

of the machine was tested with the same procedure as the laptop model. The ratio of wall-clock time to computation time as a function of working threads is shown in fig. 3.10. The same $1/N$ behavior is observed, but does not give a full picture of the performance of the machine. For larger numbers of threads, the wall-clock to computation time strictly follows $1/N$, but the total computation time increases slightly, due to the cost of waking and scheduling large numbers of threads, as seen in fig. 3.11. This means that at full capacity, the thirty-two thread machine provides a factor of thirty improvement in track throughput, well over the project requirements.

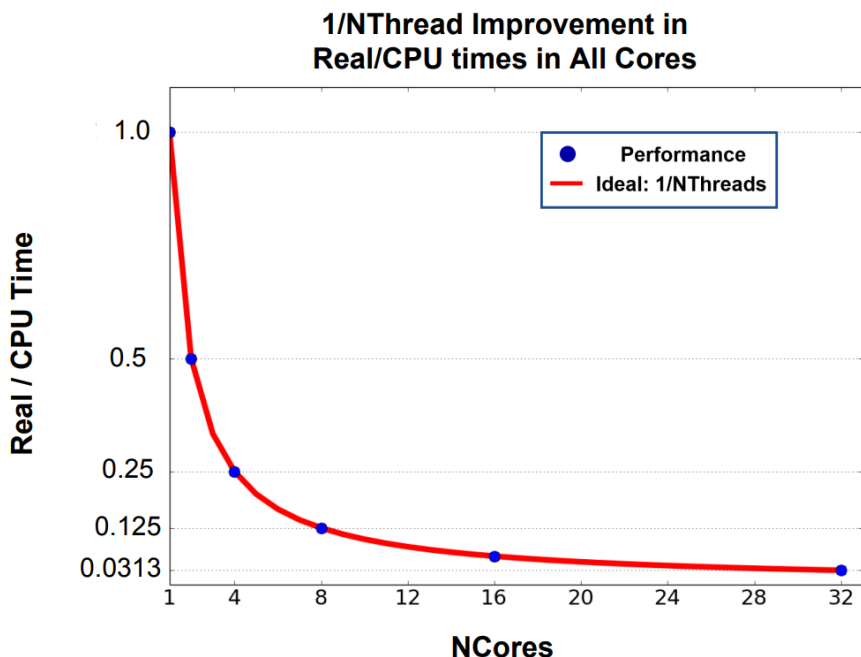


Figure 3.10: Ratio of wall-clock time to the computation time as a function of threads in the multithreaded tracking algorithm in the desktop installation in all thirty two cores.

3.4.2.4 Integration at SpinQuest

Currently, the machine detailed in sec. 3.4.2.3 is installed at Fermilab as the primary reconstruction tool for online data quality monitoring. It is worth noting that there is a concurrent effort at University of Mississippi to develop a parallelized

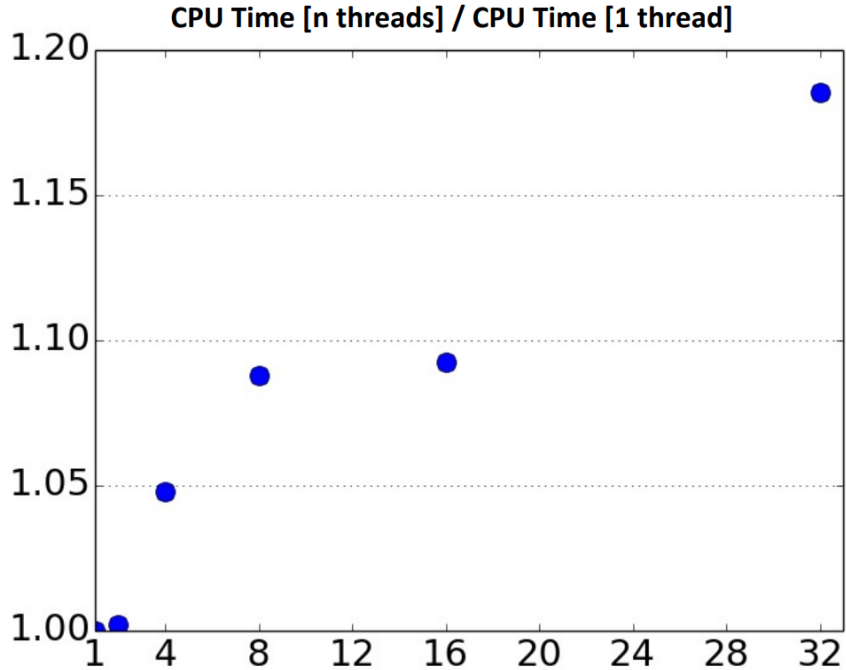


Figure 3.11: Ratio of computation time in N threads to a single thread showing a maximum computation time 20% longer than the single thread case, though the wall clock time is still strictly 1/32 of this value.

implementation of kTracker using graphics processing units. If this effort succeeds before data taking in the next year, it is likely that the difference in CPU and GPU processing will allow for another order of magnitude in performance improvement from the GPU team. In this case, the CPU-based machine will be a central part of the analysis after data taking.

The integration of the CPU based multithreaded algorithm at SpinQuest was accomplished with substantial input from Kenichi Nakano, a research scientist at University of Virginia. An SQL server is used to maintain the tracking status of data from each 4.5 second spill from the beam. The multithreaded tracking algorithm is called on each spill of data and the output is recorded and posted for data monitoring. A flowchart of the current data processing scheme is provided in fig. 3.12. When the trigger is received, the DAQ writes all detector data for the event in the typical format, using the 'SRawEvent' class. Simultaneously, a data status indicator is written to

the “spill ready” database indicating that the event information is ready for tracking. A daemon polls the spill ready database every 10s, fetching event data when new spill data has been posted. Finally, the daemon invokes the multithreaded tracking algorithm on the per-spill data, writing the standard 'SRecEvent' data class used in SeaQuest and SpinQuest analysis. Though data from cosmic rays are difficult to track, the data path has been tested with ongoing cosmic ray data taking. When SpinQuest receives beam in the near future, the system will be tested with real data.

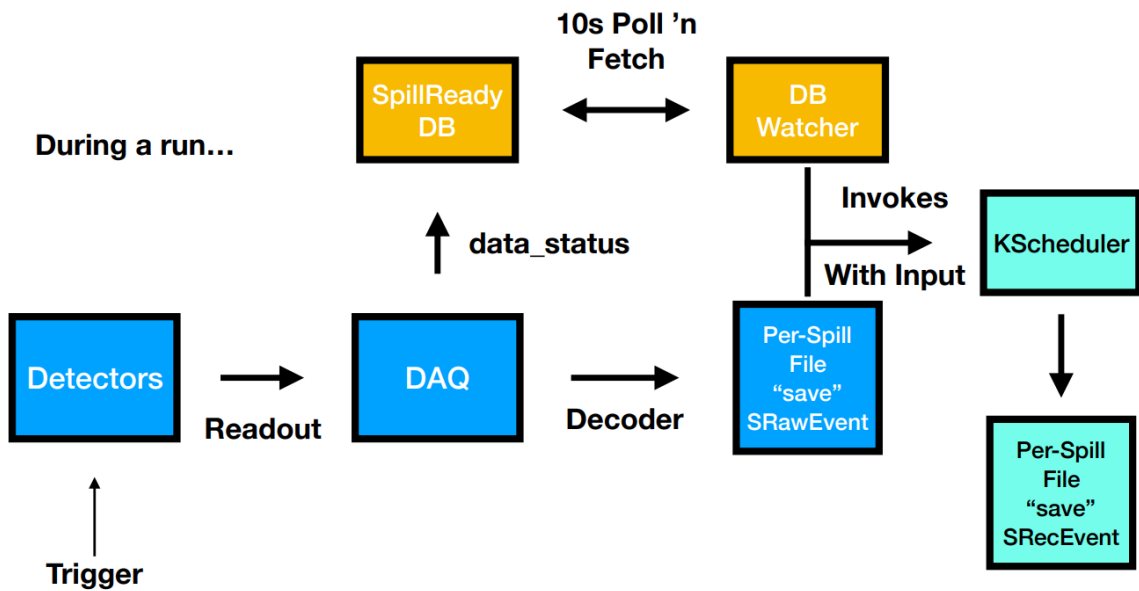


Figure 3.12: Flowchart showing the automatic process by which the multithreaded tracking algorithm is applied to data each spill.

Chapter IV

Data Analysis

In this analysis, data from Runs 2-3 are used, covering roadsets 57, 59, 62, 67, and 70. A full list of run dates and roadsets is presented in table 4.1. The J/Ψ suppression is studied, both as functions of x_F and p_T and integrated over these variables, through the production ratio on nuclear targets of nuclear mass, A , to that of deuterium: $R_{pA} = \frac{2}{A}\sigma_{pA}/\sigma_{pd}$. In the integrated analysis, the per-nucleon charmonium production cross section is assumed to be related to the nuclear cross section by $\sigma_{pA} = \sigma_{pd}A^\alpha$ and an extracted value of α is reported for both hydrogen and deuterium. In this analysis, the primary physics observables to extract are the production cross sections, σ_{pA} and σ_{pd} , which are simply the total number, or yields, of J/Ψ particles produced during data taking, weighted by some physical and detector-dependent variables. The total yield of J/Ψ particles is determined by using the `TFractionFitter` class, provided by ROOT. `TFractionFitter` scales and fits finite Monte Carlo data samples to a given data set to determine their relative contributions. The yields are then corrected for the efficiency of tracking software and the spectrometer acceptance. In this section, details are provided on how the `TFractionFitter` is used to determine J/Ψ yields, the selection of dimuon events in SeaQuest data, and the calculation of the R_{pA} ratio in SeaQuest data. Finally, the SeaQuest J/Ψ data are compared with theory predictions from ref. [46].

Data Set	Roadset	Dates
Run 2	Roadset 57	06/25/2014 - 08/20/2014
	Roadset 59	08/20/2014 - 09/03/2014
Run 3	Roadset 62	11/08/2014 - 01/14/2015
	Roadset 67	01/25/2015 - 06/19/2015
	Roadset 70	06/19/2016 - 07/03/2015

Table 4.1: A table showing the dates and roadsets associated with Run 2 and 3 data.

4.1 Extracting J/Ψ and Ψ' Yields in SeaQuest Data

To determine the production cross sections for the J/Ψ and Ψ' at SeaQuest, we must determine which fraction of reconstructed dimuons were produced from the decay of light charmonia. In this analysis, the TFractionFitter analysis class from the ROOT software package was used and is explained in great detail in ref. [74]. All dimuon data passing the data selections in sec. 4.2 are plotted as a histogram as a function the invariant mass of the reconstructed pair. A set of Monte Carlo simulations are used to produce similar histograms for dimuons arising from all the various processes that can produce them at SeaQuest. The contributing processes are Drell-Yan, dimuon events arising from interactions of the beam and the target container, J/Ψ' , Ψ' , and a “mixed” background that emulates the combinatoric background generated by single muons passing through the detector which might be misidentified as real dimuon pairs. Details on the construction of the Monte Carlo samples are given in sec. 4.3.

The TFractionFitter class fits Monte Carlo shapes to the data, determining each of their relative proportions, while propagating uncertainty arising from finite Monte Carlo samples. Due to the mixing process described in sec. 4.3 that is needed to produce realistic Monte Carlo samples for SeaQuest, it is critical to consider this uncertainty due to the relatively small size of the background samples, particularly for the mixed background.

We are given a set of binned data, $\{d_1, d_2, \dots, d_n\}$, where d_i is the number of

measured events in bin i . In each bin, $f_i(P_1, P_2, \dots, P_m)$ is the predicted number of events, which is a function of the proportions, P_j , and numbers, a_{ji} , of events from Monte Carlo source j as

$$f_i = N_D \sum_{j=1}^m P_j a_{ji} / N_j, \quad (4.1)$$

where N_D is the total number of the data sample, $N_D = \sum_{i=1}^n d_i$, and N_j is the total number in the Monte Carlo source j , $N_j = \sum_{i=1}^n a_{ji}$. The P_j , being the proportions of each contributor, must sum to unity. Writing $p_j = N_D P_j / N_j$, eq. 4.1 becomes

$$f_i = \sum_{j=1}^m p_j a_{ji}, \quad (4.2)$$

and the p_j can be estimated by maximizing the logarithm of the likelihood function

$$\ln \mathcal{L} = \sum_{i=1}^n d_i \ln f_i - f_i, \quad (4.3)$$

which is often referred to as a ‘‘binned maximum likelihood’’ fit. However, as ref. [74] notes, this method does not account for statistical fluctuations in the a_{ji} arising from the finite size of the Monte Carlo samples. Instead, eq. 4.2, is modified to

$$f_i = \sum_{j=1}^m p_j A_{ji}, \quad (4.4)$$

which reflects uncertainty in the source by writing an unknown expected number of events, A_{ji} , rather than the fixed quantity a_{ji} . The likelihood function, eq. 4.3, is also modified to maximise the combined probability of the observed d_i and observed a_{ji} and written as

$$\ln \mathcal{L} = \sum_{i=1}^n d_i \ln f_i - f_i + \sum_{i=1}^n \sum_{j=1}^m a_{ji} \ln A_{ji} - A_{ji}. \quad (4.5)$$

Now the p_j and A_{ji} estimates can be determined by maximising this likelihood while

incorporating the finite Monte Carlo statistics. On face, this is an intractable maximization problem in $m \times (n + 1)$ variables, but ref. [74] points out that it can be simplified. Differentiating eq. 4.5 with respect to the p_j and A_{ji} and setting them to zero generates two sets of equations:

$$\sum_{i=1}^n \frac{d_i A_{ji}}{f_i} - A_{ji} = 0 \text{ for all } j \quad (4.6)$$

and

$$\frac{d_i p_j}{f_i} - p_j + \frac{a_{ji}}{A_{ji}} - 1 = 0 \text{ for all } i, j. \quad (4.7)$$

Rewriting eq. 4.7 as

$$1 - \frac{d_i}{f_i} = \frac{1}{p_j} \left(\frac{a_{ji}}{A_{ji}} - 1 \right), \quad (4.8)$$

we note that the left hand side depends only on i and write

$$t_i = 1 - \frac{d_i}{f_i}, \quad (4.9)$$

such that the right hand side becomes

$$A_{ji} = \frac{a_{ji}}{1 + p_j t_i}, \quad (4.10)$$

which is a notable simplification. In any set of p_j , the $n \times m$ unknown A_{ji} are entirely constrained by the n unknowns, t_i which are given by eq. 4.9. For filled bins with non-zero d_i ,

$$\frac{d_i}{1 - t_i} = f_i = \sum_j p_j A_{ji} = \sum_j \frac{p_j a_{ji}}{1 + p_j t_i} \quad (4.11)$$

are the n equations, with the definition of A_{ji} given in eq. 4.10, which when satisfied also satisfy all $m \times n$ equations 4.7. Then, the m values, p_j , are determined by solving the m equations 4.6 and the appropriate A_{ji} are found by solving the n equations 4.11. These equations are not coupled and depend only on the number of events in any

given bin. By taking an initial value of $t_i = 0$, the equations are readily solved by Newton's method in only a few iterations.

Fortunately, this argument is also extended to weighted Monte Carlo samples, which are used at SeaQuest and described in sec. 4.4. With weights, w_{ji} , the predicted number of events in each bin is modified and eq. 4.4 becomes

$$f_i = \sum_{j=1}^m p_j w_{ji} A_{ji}, \quad (4.12)$$

while the likelihood remains unchanged because there is no uncertainty associated with the weights. The m equations 4.6 are modified to become

$$\sum_{i=1}^n \left(\frac{d_i}{f_i} - 1 \right) w_{ji} A_{ji} = 0 \text{ for all } j \quad (4.13)$$

and the n equations 4.11 become

$$\frac{d_i}{1 - t_i} = f_i = \sum_j \frac{p_j w_{ji} a_{ji}}{1 + p_j w_{ji} t_i} \quad (4.14)$$

and are solved using the same methods as the unweighted case. This assumes that the weight for all events from a given source in a given bin are equal to w_{ji} . This assumption may be violated if the variation in the weight factor is large in a single bin or if the weight factor depends on other kinematic variables which are integrated out during binning. It is a concern that in the SeaQuest Monte Carlo samples, the weights are functions of kinematic variables other than mass, where the binning and fitting actually takes place. It is known that for the J/Ψ and Ψ' , there is a coupled dependence of the Feynman- x , $x_F = x_1 - x_2$, and the transverse momentum, p_T . In this analysis, the Monte Carlo simulation is too sparse for a full two-dimensional fit in x_F and p_T and the same p_T based reweighting is applied across all values of x_F . More FPGA4 trigger data would allow for a larger mixed Monte Carlo sample and

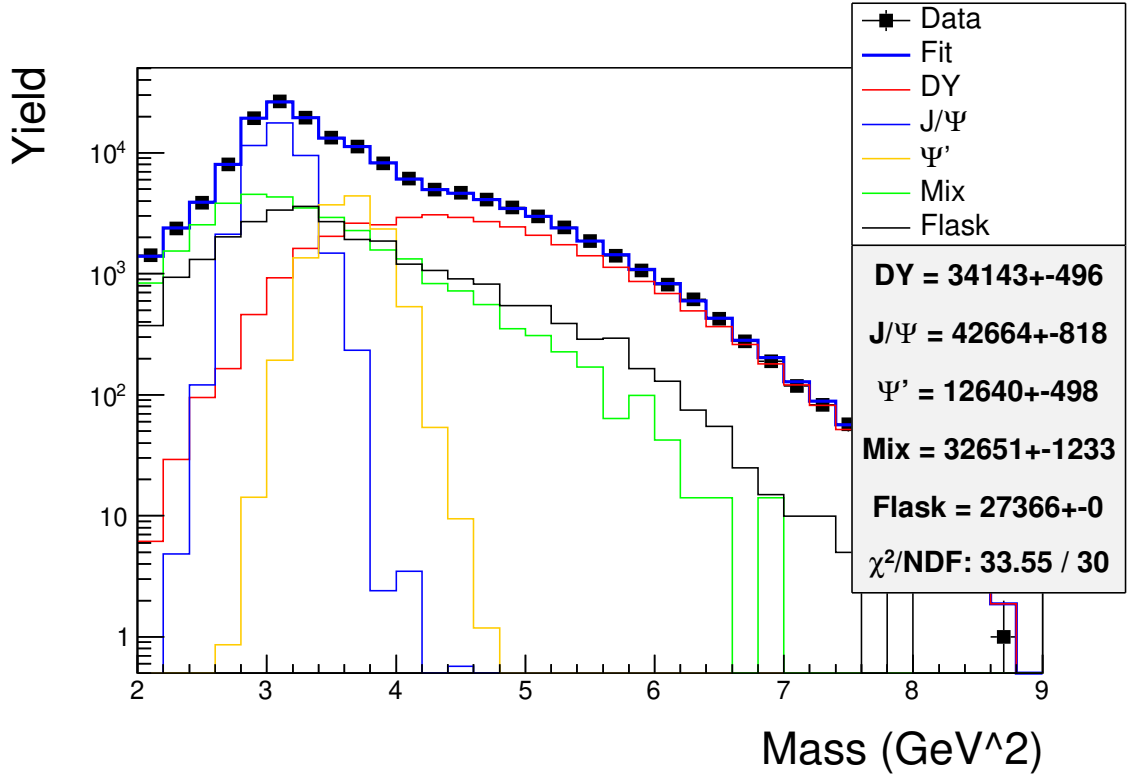


Figure 4.1: The mass-fit results of TFractionFitter, showing data from the liquid hydrogen target along with the scaled Monte Carlo samples which comprise it. The integrated yields are shown for each component and used in the cross section ratio calculation.

an improvement to this analysis with a two-dimensional binned fit in both p_T and x_F . An example mass-fit plot is presented in fig. 4.1 showing the results for the liquid hydrogen target data as well as the scaled Monte Carlo components. The total yield of each component is corrected by the tracking efficiency and detector acceptance before being used in the calculation of the cross section ratio. For the binned calculation, the data is first projected into the corresponding kinematic bin in x_F or p_T and then the mass-fit is performed in each bin. As a result, the bins chosen in sec. 4.8 are uneven and chosen to have roughly even statistics so that the mass-fits are comparable. All mass-fits and yields for the unbinned analysis are presented in appendix A.5, while the binned mass-fits are presented in appendix A.6.

4.2 Data Selections

After physics events have been identified and their information determined by kTracker, the dimuon data are subjected to a final set of selections. These data selections have been chosen to reduce noise and select for interesting dimuon events. In this analysis, the same data selections are used as in ref. [45]. Details in how these selections were determined can be found in refs. [45, 67, 75, 76]. The selections are divided amongst “spill-level” cuts, “event-level” cuts, track cuts, dimuon cuts, and finally whether the event most likely came from the target or the beam dump.

Spill-level selections are applied to each set of spill data and shown in table 4.2. Each quantity in the table must exist precisely once per spill. The “TargetPos” variable selects which target position was used for the data taking, “TSGo” is the total number of triggers received by the trigger supervisor across all trigger types, and the total number of accepted and inhibited FPGA1 triggers are given by “AcceptedFPGA1” and “AfterInhFPGA1” respectively. “G2SEM” is the proton intensity measured by the SEM detector at the G2 position in the beamline, discussed in sec. 2.1. “QIESum” is the total spill intensity summed by the BIM which was also introduced in sec. 2.1. “Inhibit” is the intensity sum of buckets that were vetoed by the QIE inhibit signal, while “busy” is the total intensity sum from buckets vetoed by the trigger supervisor inhibit busy signal. The only event-level cut is to confirm that the event was produced by the primary physics trigger, FPGA 1. Track cuts are applied to each single track in the reconstructed dimuon pairs and shown in table 4.3. Each track is required to correspond to a road within the roadset, have a sufficiently large number of chamber hits, and a low-enough χ^2/NDF . Finally, the tracks must have a distance of closest approach to the beamline within some range of the target and dump. A final selection was made on the longitudinal momentum of a track under a certain number of hits, selected to reduce the random background in the high dimuon mass range, according to ref. [77]. Dimuon cuts are applied to the reconstructed dimuons

Variable	Roadset 57 & 59	Roadset 62 & 67
TargetPos	1 - 7	1-7
TSGo	1000 - 8000	100 - 6000
AcceptedFPGA1	1000 - 8000	100 - 6000
AfterInhFPGA1	1000 - 30000	100 - 10000
AccetpedFPGA1 / AfterInhFPGA1	0.2 - 0.9	0.2 - 1.05
G2SEM	2e12 - 1e13	2e12 - 1e13
QIESum	4e10 - 1e12	4e10 - 1e12
Inhibit	4e9 - 1e11	4e9 - 2e11
Busy	4e9 - 1e11	4e9 - 1e11
Duty Factor	15-60	10-60

Table 4.2: Spill-level cuts applied to SeaQuest data, from ref. [77]. For a detailed description of each variable, see text.

Variable	Selection
Road ID	In the Roadset
Number of Chamber Hits	>14
Reduced χ^2	<5
Track Vertex position along Beamline	(-400 - 200) (cm)
pz1 with more than 18 chamber hits	>18 (GeV)

Table 4.3: Track-level cuts applied to SeaQuest data during track reconstruction.

Variable	Selection
Track Separation	(-250 - 250)
χ^2 of dimuon vertex	<15
X position of dimuon vertex	(-2 - 2)
Y position of dimuon vertex	(-2 - 2)
Z position of dimuon vertex	(-300 - 200)
X momentum at dimuon vertex	(-3 - 3)
Y momentum at dimuon vertex	(-3 - 3)
Z momentum at dimuon vertex	(30 - 120)
X momentum at mu+	>0
X momentum at mu-	<0
x_B	(0 - 1)
x_T	(0 - 1)
x_F	(-1 - 1)

Table 4.4: Dimuon selections applied to reconstructed dimuon pairs in SeaQuest data.

and are shown in table 4.4. “Track separation” is the difference along the beamline of the vertices for the μ^+ and μ^- and the dimuon χ^2 gives a metric for evaluating how well the two tracks converge to a single vertex. These selections target associated muon tracks most likely to form a true dimuon pair. Selection on the position of the dimuon vertex in x, y , and z guarantees the dimuon was produced in the target or dump. Reference [77] notes that a Monte Carlo study was used to determine the selections on x, y , and z momenta at the dimuon vertex. In particular, it was found that true dimuons under a certain momentum are bent out of the spectrometer acceptance by FMag and KMag and that the multiple scattering effects of traversing FMag’s iron core are enhanced for low momentum muons, substantially increasing uncertainty in the vertex position estimate. The reconstructed z -momentum is required to be less than the 120 GeV of the proton beam. Selections on the x -momenta of the μ^+ and μ^- remove tracks with incorrect polarity which would be bent out of spectrometer acceptance, rather than into it, by the the magnets. Finally, sanity checks are made on the kinematic variables, x_B , x_T , and x_F . The target and dump separation is determined from the reconstructed track’s closest approach to the beam line and the specific values are shown in table 4.5. A Monte Carlo study was per-

Variable	Selection
$\chi_{\text{Dump}}^2 - \chi_{\text{Target}}^2$	>10
Z position of dimuon vertex	$(-300 - 60)$

Table 4.5: Target and dump separation requirements for SeaQuest data. Nontrivial overlap of dimuons originating in the dump and the target is shown in fig. 4.2, motivating the selection.

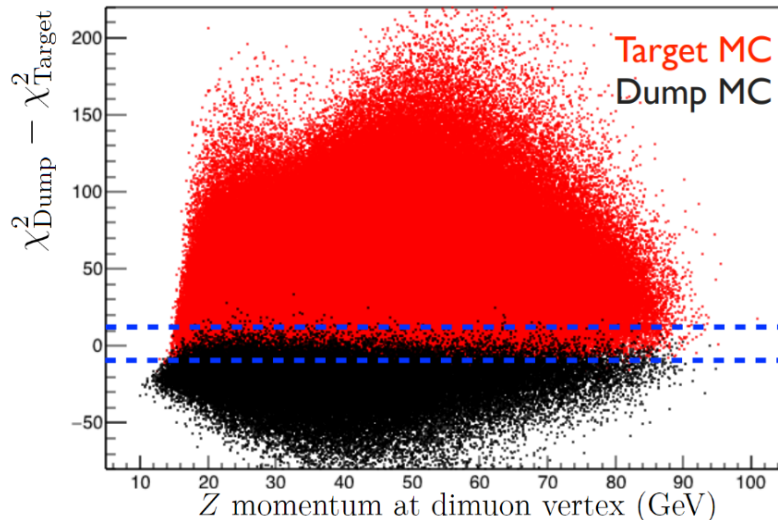


Figure 4.2: Selection on χ^2 of finding the track vertex in the target or dump from ref. [76]. Dotted blue lines show a nontrivial overlap region which is avoided by the selection.

formed to determine how well the tracking separates events originating in the target compared with the beam dump. Selections were chosen to unambiguously separate target and dump dimuons, though it is worth noting their non-trivial overlap as seen in fig. 4.2. An effort is currently underway to incorporate information from two new hodoscope stations to incorporate target and dump separation information into the FPGA trigger for the upcoming SpinQuest experiment.

4.3 Monte Carlo Simulation

Two different Monte Carlo simulations were developed and used during the SeaQuest experiment. The FastMC program was adopted from the E866 experiment at Fermilab and provided quick, but inaccurate results, during commissioning and the first

data taking. A Geant4 based simulation, GMC, was developed to provide more detailed simulation information on the effects of multiple scattering in FMag, fringe fields measured at the edges of KMag, and secondary emissions of muons passing through the spectrometer. Drell-Yan events were generated using a flat, equal-probability distribution in mass from 1 - 10 GeV and Feynman-x from $-1 < x_F < 1$. The transverse momentum, p_T , distribution was generated from the phenomenological Kaplan form of ref. [78]. It was later noticed that the parameters of ref. [78] were from J/Ψ and Ψ' data produced from an 800 GeV beam and did not properly match the data measured at SeaQuest. As a result, the Monte Carlo data used in this analysis were reweighted to correct the p_T distributions. This procedure is detailed in sec. 4.4. The dimuon origin along the beamline was chosen according to distributions based on beam attenuation. After the event has been generated, it is assigned a weight proportional to the leading order cross section. The calculation of the leading order cross section utilized PDF sets from the CTEQ-TEA collaboration from ref. [79]. The J/Ψ and Ψ' are produced with their precise mass values of 3.097 GeV and 3.686 GeV, with p_T distributions from ref. [78].

After the muon pairs are generated, they are propagated through the SeaQuest detector by Geant4. Simulated detector information is passed to kTracker to produce a set of reconstruction data for the Monte Carlo events. During the tracking process, a “realization” method is applied to the data to simulate the effects of chamber resolution and efficiency. All chambers are assigned a flat efficiency of 94% and 6% of wire chamber hits are randomly erased from the simulation. A convolution with a Gaussian of width 0.04 cm is applied to the remaining hits. The resulting files contain both the Monte Carlo “truth” information, as well as reconstructed information indistinguishable from real data. These files are colloquially referred to as “clean” Monte Carlo, containing only the tracks from a true dimuon pair and secondaries. The clean files are then embedded with random hits from NIM3 data. At first, the motivation

for embedding was to study kTracker’s performance against a noisy background, but the TFractionFitter method also relies upon realistic background Monte Carlo samples to fit data and extract the process yields. The embedded files are colloquially referred to as “messy” Monte Carlo.

The NIM3 trigger was a “random” data trigger that sampled the background at SeaQuest, generated by a 7.5 kHz signal which was not associated with the beam RF timing. This provided an unbiased sample of the average background occupancy rates in the various detectors in the spectrometer. It had been observed, and reported in ref. [80], that a typical signal event from the FPGA1 trigger had a higher average detector occupancy than NIM3 events. Therefore, a weighting scheme gave higher weights to high intensity NIM3 events during the selection of hits for embedding. The ratio of FPGA1 events to NIM3 events were plotted as a function of the chamber 1 occupancy, $D1$, and normalized to generate a probability distribution for inclusion of NIM3 events of a given occupancy. A plot of the ratio published in ref. [80] is shown in fig. 4.3. It is worth noting that the normalization was not correctly chosen for a probability distribution: the peak value, rather than the total integral, was chosen to be unity. In addition, the standard analysis cuts exclude the $D1 > 400$ region. However, the distribution’s shape is correct. After selecting NIM3 events according to the distribution of fig. 4.3, their hits are added to an FPGA 1 event to perform the embedding.

4.4 Monte Carlo p_T Reweighting

Shivangi Prasad was the first to note a significant difference between the p_T distributions observed in SeaQuest data and those used in the Monte Carlo simulations in ref. [81]. Ching Him Leung also extended the reweighing to the J/Ψ and Ψ' in

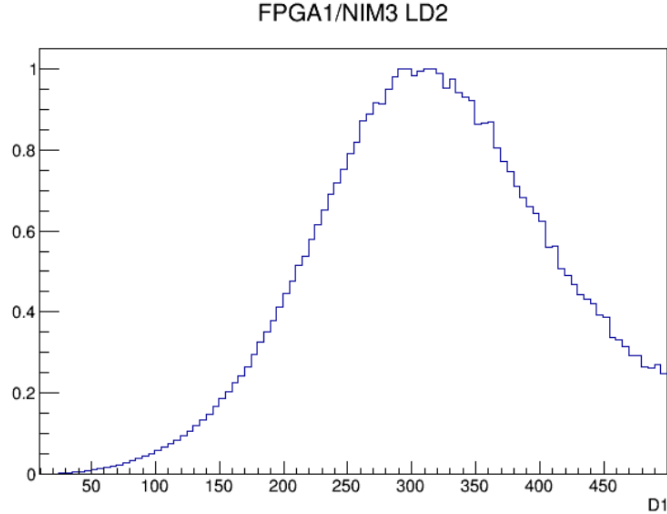


Figure 4.3: Probability distribution used to select NIM3 events as a function of chamber 1 occupancy, D1, reproduced as published in ref. [76]. An incorrect normalization is shown, but the shape is correct.

ref. [82]. A phenomenological “Kaplan” form is used from ref. [78], written as

$$\frac{d\sigma}{dp_T} \propto \frac{p_T}{\left(1 + \frac{p_T^2}{p_1^2}\right)^6}, \quad (4.15)$$

where p_1 is a tune-able parameter controlling the width of the distribution. The values used in the SeaQuest Monte Carlo were $p_1^{DY} = 2.8$ for Drell-Yan and $p_1^{\text{charm}} = 3.0$ for both the J/Ψ and Ψ' . These values were taken from an analysis of 800 GeV proton scattering data from the Fermilab Tevatron and the E866 experiment, published in ref. [78]. It is likely that the SeaQuest data, using a 120 GeV beam, requires an updated value of p_1 to best match the data. In this section, I present my independent analysis of the p_T reweighting factors for the Drell-Yan and charmonia distributions that are used in the calculations of sec. 4.8. Updated values of p_1 are found to be close to 2 for Drell-Yan and close to 2.5 for each of the J/Ψ and Ψ' .

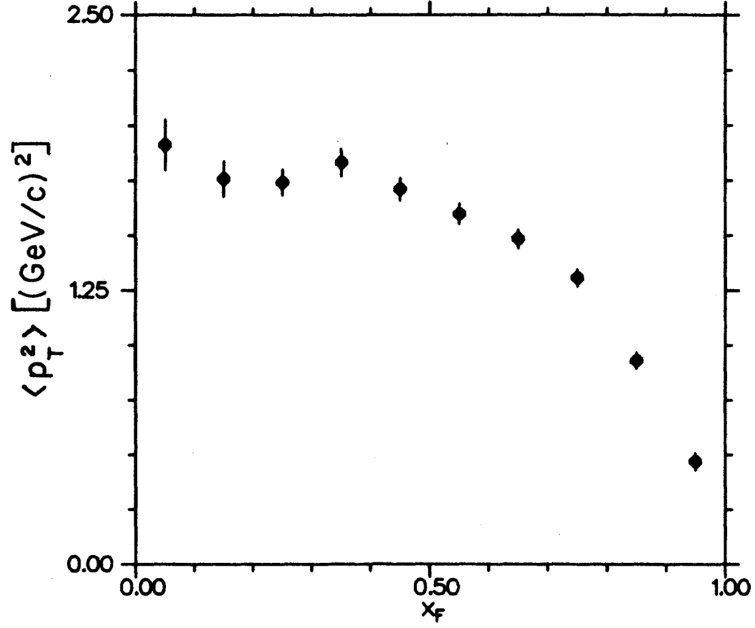


Figure 4.4: p_T , x_F dependence observed in E615 pion-induced Drell-Yan dimuons. Figure reproduced as published in ref. [83].

4.4.1 Drell-Yan MC

It had been observed at previous Drell-Yan experiments conducted at Fermilab that the average p_T^2 had a dependence on x_F . Results from E615 pion-induced Drell-Yan demonstrating this effect can be seen in fig. 4.4 from ref. [83]. Because of this dependence of the p_T distribution, and therefore the correct p_1 value for Monte Carlo events, the Drell-Yan data is divided into three separate x_F bins before the reweighting is computed. In each bin, the normalized empty flask background yield is subtracted and the Drell-Yan dimuons are plotted against p_T^2 and fit with the Kaplan form,

$$\frac{d\sigma}{dp_t} \propto \frac{1}{(1 + \frac{p_T^2}{p_1^2})^6}. \quad (4.16)$$

The choice to fit in p_T or p_T^2 ought not matter and for the Drell-Yan analysis, this has been conventionally done in p_T^2 for comparison inside the collaboration. The Drell-Yan yield is then corrected by the spectrometer acceptance which can be calculated

xF Bin Number	Range
1	$-0.1 < x_F \leq 0.3$
2	$0.3 < x_F \leq 0.6$
3	$0.6 < x_F < 0.95$

Table 4.6: x_F bins used in the Drell-Yan Monte Carlo reweighting.

by dividing the clean Monte Carlo by the 4pi Monte Carlo, which are discussed in sec. 4.3. This acceptance corrected yield is fit to the Kaplan form, from which p_1 is determined for each x_F bin. This process is repeated for each target. The x_F bins used in this analysis are presented in table 4.6. The fits across each x_F bin are shown for the hydrogen target in appendix A.1 in fig. A.1, deuterium in fig A.2, iron in fig. A.4, carbon in fig. A.3, and tungsten in fig. A.5. Typical values of p_1 for Drell-Yan determined by the Kaplan fit of SeaQuest data are near 2.0, while the original value used in the Monte Carlo generator, taken from fits to E866 data at 800 GeV, was 2.8. For each target the three extracted values of p_1 are plotted against the average x_F of each bin and a linear fit is performed to determine $p_1(x_F)$. The results for the liquid hydrogen target are shown as an example in fig. 4.5. The results for all targets are shown in appendix A.2. After p_1 is determined, the reweighting factor, which is multiplied into the Monte Carlo weights to correct for the change in distribution, must be computed. The initial reweighting factor suggested by ref. [81] was written as

$$\text{reweight}(x_F) = \frac{(1 + \frac{p_T^2}{2.8^2})^6}{(1 + \frac{p_T^2}{(p_1(x_F))^2})^2} \frac{2.8^2}{(p_1(x_F))^2} \quad (4.17)$$

until it was updated by the consideration that a maximum cutoff value of p_T must be imposed on the Monte Carlo by ref. [84]. The maximum constraint on p_T is set by

$$(p_T^{\text{max}})^2 = \frac{s}{4} \left(1 - \frac{m^2}{s}\right)^2 (1 - (x'_F)^2), \quad (4.18)$$

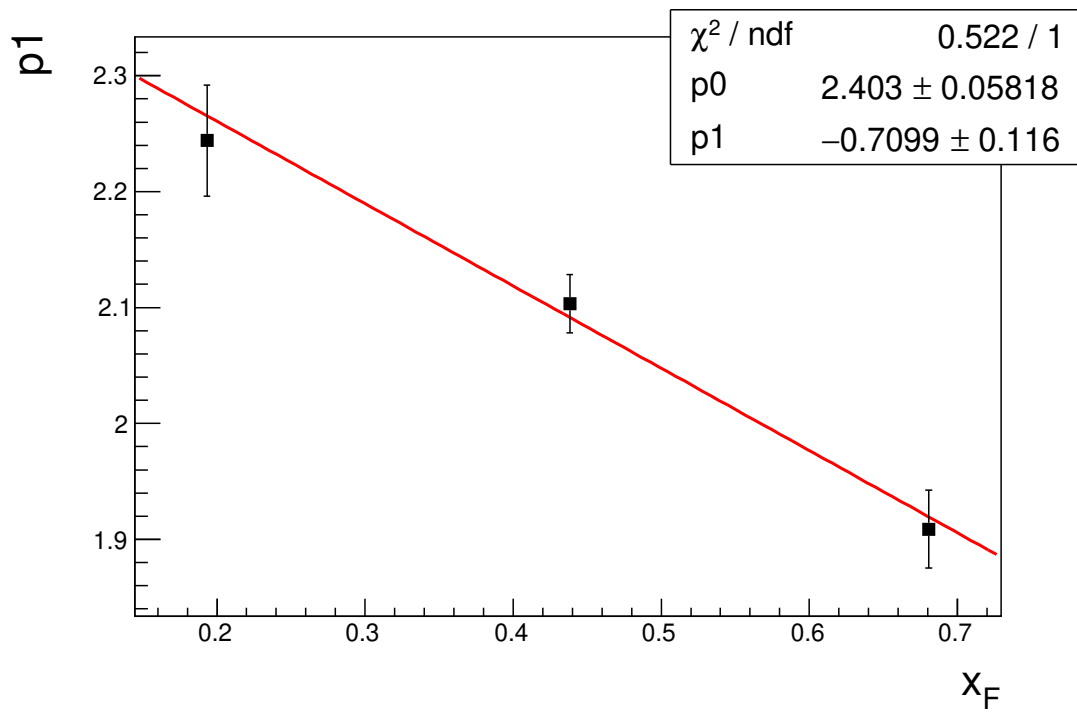


Figure 4.5: Parameter p_1 , used in the Drell-Yan Monte Carlo reweighting, as a linear interpolation in x_F for the liquid hydrogen target. In the information box, p0 and p1 are distinct from $p_1(x_F)$, and represent the parameters of the linear fit.

where

$$x'_F = \frac{2P_L}{\sqrt{s}(1 - m^2/s)}, \quad (4.19)$$

in which $\sqrt{s} = E_{CM}$ is the center of mass energy and P_L is the longitudinal momentum of the dimuon pair. Integrating up to the p_T^{\max} cutoff introduces a corrective factor to eq. 4.17, becoming

$$\text{reweight}(x_F) = \frac{\left(1 + \frac{p_T^2}{2.8^2}\right)^6}{\left(1 + \frac{p_T^2}{(p_1(x_F))^2}\right)^2} \frac{2.8^2}{(p_1(x_F))^2} \frac{1 - \left(1 + \frac{(p_T^{\max}(m, x_F))^2}{2.8^2}\right)^{-5}}{1 - \left(1 + \frac{(p_T^{\max}(m, x_F))^2}{(p_1(x_F))^2}\right)^{-5}}. \quad (4.20)$$

Looping over each event in the 4pi, messy, and clean Drell-Yan Monte Carlo samples, the event x_F is used to compute p_1 from the linear interpolation and eq. 4.20 is evaluated and multiplied into the event weight.

4.4.2 J/Ψ and Ψ' MC

The J/Ψ and Ψ' reweighting is more challenging, due to the small fraction of charmonia in the SeaQuest data. The charmonia are also generated in the simulation according to eq. 4.15, with a value of $p_1 = 3.0$, compared with the Drell-Yan value of 2.8. Because the charmonia make up a small fraction of the data, a naive estimate of the reweighting factor cannot be performed from the whole data set. Instead, the charmonia yields must be computed from the mass-fitting procedure of sec. 4.1, which itself depends on the reweighted Monte Carlo data. An iterative approach is taken: using the default p_1 value to perform the binned mass-fit in p_T , the obtained yields are then fit with the Kaplan form and an initial value of $p_1^{(0)}$ is determined. The charm Monte Carlo is reweighed using $p_1^{(0)}$ and the process is repeated. The mass-fitting procedure is only reliable for sufficiently large statistics, preventing the same kind of x_F binned analysis used in the Drell-Yan case, so a unique value of p_1 , integrated over x_F , is applied for each of the J/Ψ and Ψ' respectively. It is found that p_1 converges after a single iteration, though the Kaplan form is not an ideal

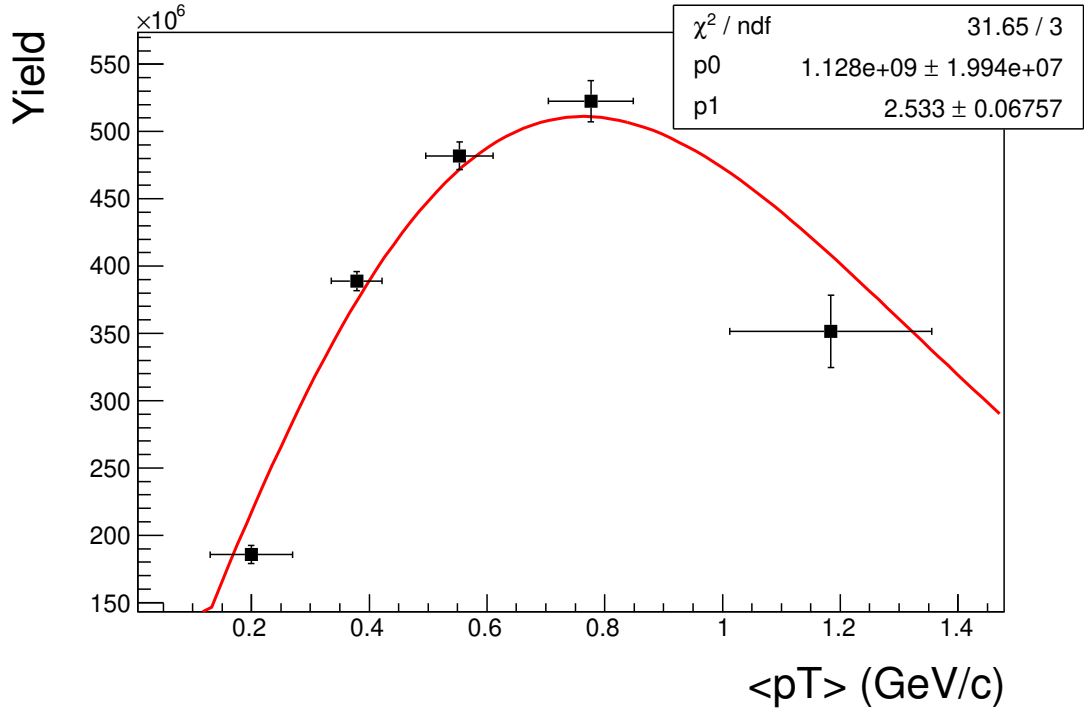


Figure 4.6: J/Ψ yield from liquid hydrogen target, plotted in p_T and fit with Kaplan form to extract parameter p_1 .

descriptor and provides poor fits. The results for the J/Ψ Kaplan fit for the liquid hydrogen target is shown in fig. 4.6. The results for Ψ' and the rest of the targets are shown in appendix A.3. The horizontal error bars were not considered in the fit due to a known problem in the fitting procedure used in ROOT, but are included in the plot and represent the standard deviation in each p_T bin. Most importantly, in this analysis, the cross section ratios, $R_{pA}^{(D/H)}$, are not meaningfully sensitive to the re-weighting scheme as the effects cancel in the yield ratios. Even the effect on raw yields from different values of the reweighting factor are small, leading to differences in yields negligible compared with the statistical errors. An estimate of the systematic error introduced by the process can be made by taking the difference in the final cross section ratios computed with the lower and upper bounds on the reweighting factor, but is typically less than 0.5 percent.

4.5 Mixed Background Emulation

The remaining contribution needed for TFractionFitter to determine process yields is a sample of the combinatoric background at SeaQuest. The combinatoric, “mixed” background, arises from the false identification of unassociated single muon tracks as true dimuon pairs by kTracker. There are a number of processes which produce these extraneous muons, such as the decay of kaons and pions, which can be produced in nuclear interactions of the beam with the target, or Drell-Yan dimuons produced in the beam dump. A full simulation of the combinatoric background was attempted, but proved too expensive to produce large samples on a feasible time scale. Instead, a data-driven approach was adopted to extract tracks from real data and mix them to emulate the combinatoric background. Pile-up of true physics events in single RF buckets, such as Drell-Yan or charmonium production in the target, was exceedingly rare at SeaQuest, and therefore single muon tracks were chosen for mixing rather than dimuon tracks. The SeaQuest track mixing method utilized single tracks recorded by the FPGA4 trigger as part of simulation data tracking in kTracker. Due to the high prescale factor applied to FPGA4, it was necessary to identify and compile tracks across a large number of data files. The “/analysis_tools/eventSelector.cxx” script provided in the kTracker library performs the sorting. Once compiled, the tracks are sorted by charge, target, and upper or lower half of spectrometer where they were detected. Mixing is performed via a “sliding” method, looping over all positive tracks in the top half of the detector and pairing them with a negative track in the bottom half from the next event and the same is done for the opposite polarity. The event offset value was controllable as part of the mixed background generation. It had been noted that it was difficult to assign a notion of intensity to the events generated using this method. It is possible that there are differences in the emulated background when mixing tracks of varying occupancies together, so only events of similar occupancy were mixed. The FPGA4 based mixed background produced by Jason Dove is one

of two used in this analysis. The New Mexico State University group, headed by Stephen Pate, Abinash Pun, and Forhad Hossein are currently engaged in an effort to develop a novel track mixing method for the SpinQuest experiment, which will soon be published in JINST and is currently available in ref. [85]. The new method does not use FPGA4 data and instead uses tracks from normal data tacking runs. In addition, the new method naturally produces the correct normalization and special focus was placed on correctly choosing tracks based on the occupancy of station 1, which had only been loosely considered in the mix of ref. [80]. Additionally, the group has produced the mixed background in such a way as to guarantee that the embedded tracks do not produce signals which can be misidentified by kTracker as proper dimuons. The NMSU mixed background is the second emulated combinatoric background used in this study. Because the backgrounds are produced by completely different methods, the difference in the resulting cross section ratio is used to estimate the systematic uncertainty introduced by emulated background choice.

4.6 Chamber Occupancy Effects on kTracker 'Efficiency'

It was understood that the kTracker software would become less efficient at higher detector occupancy, as it would become intractable to connect matching hits in station 2 and 3 in a high-noise background. There were several studies of the appropriate method to estimate the efficiency of kTracker, such as those presented in refs. [82, 86, 87]. The method used in the primary physics analysis printed in ref. [45] is to compute the ratio of messy to clean Monte Carlo events as a function of occupancy in each of the stations. While the efficiency can be estimated, in principal, by studying the occupancy in any of the stations, it has been conventional in SeaQuest analysis to choose the station 1 occupancy, $D1$. Due to the embedded hits in the messy Monte Carlo sample, it is possible for kTracker to incorrectly reconstruct dimuon pairs which do not exist in the clean sample. This occasionally results in a ratio greater than unity,

meaning that the metric is not, strictly speaking, an 'efficiency'. However, this effect is only observed in data with lower D1 occupancy, and almost all data falls into a region less than unity, so the value is often referred to as 'efficiency' within the collaboration. An example of the tracking efficiency, estimated with the J/Ψ Monte Carlo and deuterium target data, in each of stations 1, 2, and 3 is provided in fig. 4.7. The data is fit with a simple line with one parameter, p_0 , as the primary SeaQuest analysis has always assumed the tracking efficiency goes to unity as the intensity goes to zero. Because the average intensity of the beam was the same for each target material, but the target materials were of different thicknesses, each target data has a slightly different average D1 occupancy. There is a correction in the calculation of the cross section ratios $R_{pa}^{D/H}$ arising from the ratios of tracking efficiencies for each target. In the analysis, the yields are correct by a factor of $1/\varepsilon_{\text{track}}$, where $\varepsilon_{\text{track}}$ is the tracking efficiency, computed for each particle, target, and kinematic bin by the average D1 value of the binning. An estimate of the systematic uncertainty introduced by the process can be estimated by computing the difference in the cross section ratios, $R_{pA}^{D/H}$, evaluated with the central value of p_0 compared with its upper and lower limits, presented in sec. 4.9.

4.7 Acceptance Corrections

The SeaQuest spectrometer covers a small solid angle downstream of the target and is only capable of detecting a fraction of dimuons from Drell-Yan or charmonium decay. This inefficiency is referred to as the spectrometer acceptance. The acceptance is defined as the ratio of accepted events of interest and the total number of produced events of interest. To evaluate the acceptance, the 4pi Monte Carlo sample is used as an estimate of the total produced dimuons, while the clean Monte Carlo serves as an estimate of the accepted dimuons. In this analysis, the M027 Monte Carlo samples produced by Kei Nagai were normalized with respect to each other. This means that

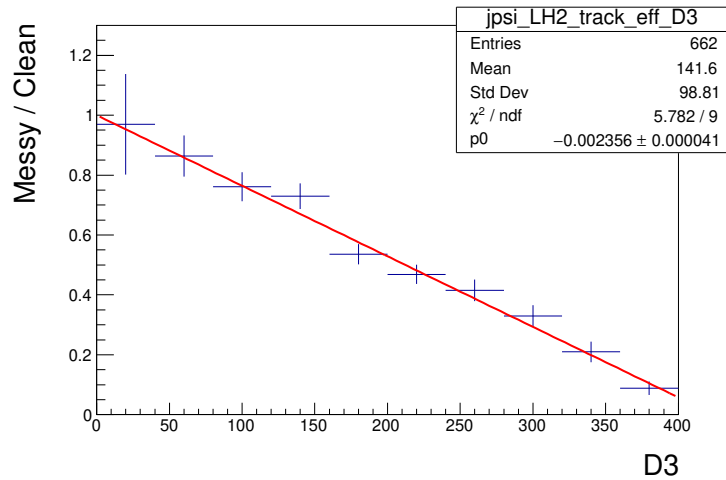
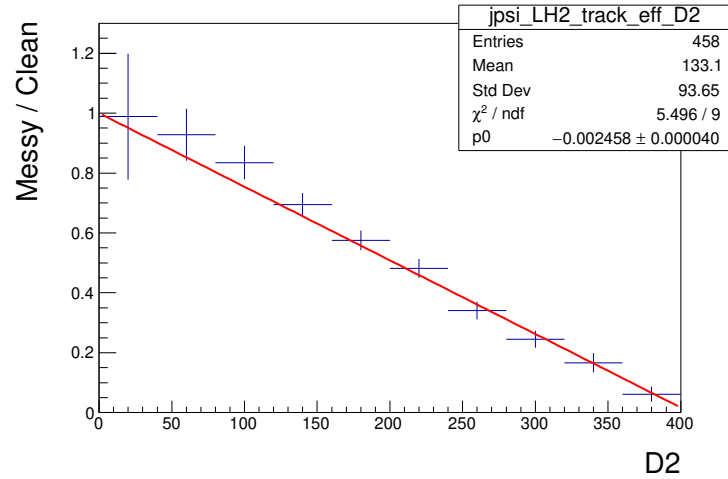
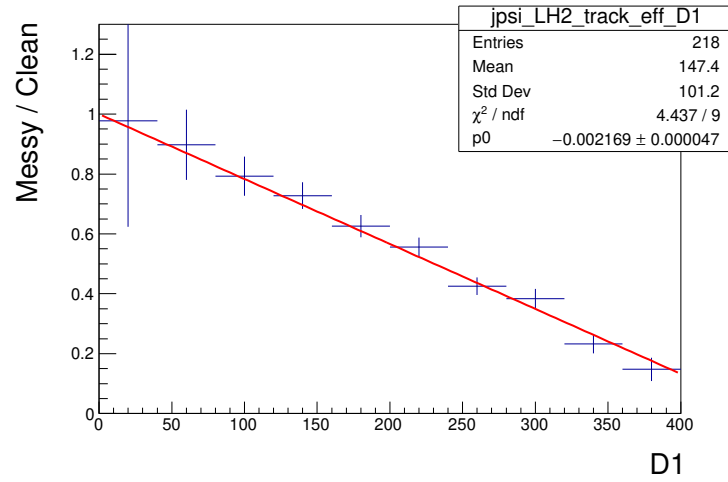


Figure 4.7: kTracker efficiency for the J/Ψ as a function of chamber occupancy in stations 1, 2, and 3 for the liquid hydrogen target. The efficiency is computed as a ratio of messy and clean Monte Carlo samples. The efficiency as a function of D1 occupancy is chosen to correct the yields for all processes.

the clean Monte Carlo sample is the subset of 4pi which successfully made it through the detector simulation. No additional normalization is required and the acceptance can be calculated by dividing the 4pi sample by the clean one. It is worth noting that the lengths of each of the solid target samples were chosen so as to have the closest possible detector acceptance, and in fact this acceptance has been assumed to cancel in previous cross section ratio calculations. In this work, the acceptance is explicitly calculated and used to correct the process yields used to compute the cross section ratio.

The acceptance calculations used in this analysis were performed for each of the Drell-Yan, J/Ψ , and Ψ' Monte Carlo samples and for each target and kinematic bin. The results for the J/Ψ in p_T are shown in fig. 4.8. All acceptance results for Drell-Yan, J/Ψ , and Ψ' can be found for both x_F and p_T in appendix A.4. Acceptance was calculated as a function of x_F and p_T and used for the binned analysis results. Ratios of the acceptances of the solid targets to the liquid ones appear in the calculation of the cross section ratios, $R_{pA}^{D/H}$, so the absolute value is less important than the relative values. There are differences observed in the p_T and x_F acceptances for the Drell-Yan Monte Carlo samples, with the liquid hydrogen target being roughly 1σ lower than the rest of the target data, particularly in p_T . The liquid deuterium target has results much closer to those for the solid targets, and the resulting uncertainty should be smaller in R_{pA}^D than R_{pA}^H . The differences amongst target acceptances are much smaller for the charmonia data, with the largest difference observed in the lowest p_T bin of the J/Ψ data. The absolute values for acceptance are similar across all possible dimuon production mechanisms, within a few percent of each other.

4.8 R_{pA} Results

The results for the R_{pA} cross section ratios are given in this section. There are two analyses performed. The first is an unbinned analysis, integrated over all Feynman- x

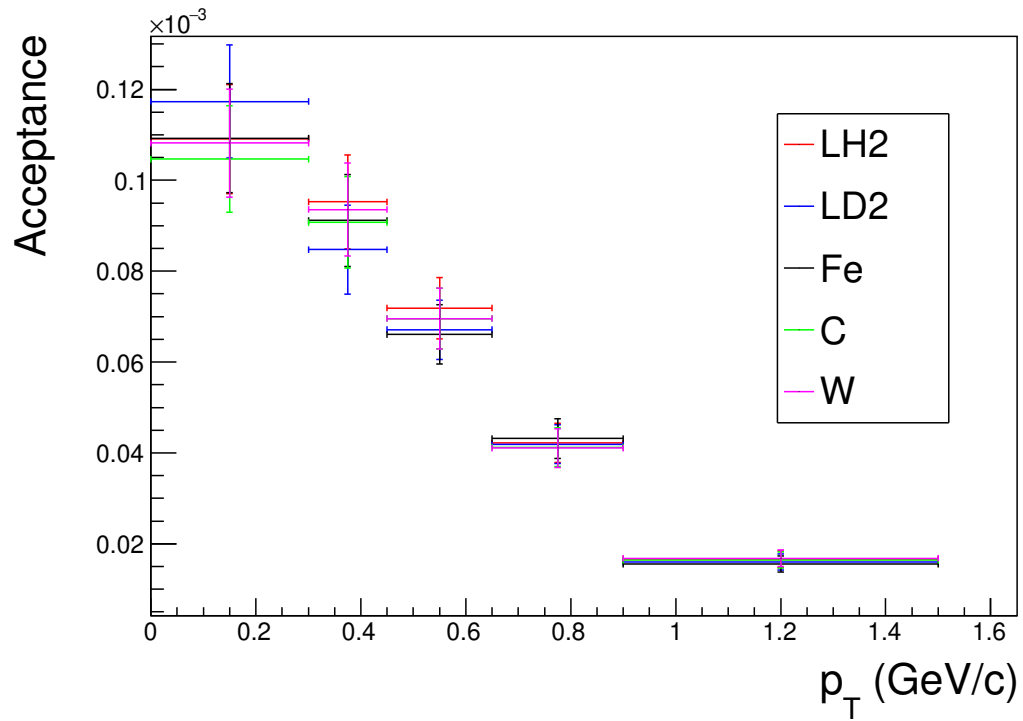


Figure 4.8: Acceptance results for J/Ψ in p_T for all targets. Small differences between targets are observed, particularly in the lowest bin, which are included in the cross section ratio calculation.

and transverse momentum. The second is a binned analysis with results given for the ratio as a function of Feynman- x and separately as a function of transverse momentum. The central values of each cross section ratio were determined using the reweighting factors found in sec. 4.4, the central values of the kTracker efficiency fits in sec. 4.6, the acceptances of sec. 4.7, and the FPGA4 mixed background from Jason Dove used in the primary SeaQuest analysis. Once again, the R_{pA} ratio is defined as

$$R_{pA}^H = \frac{1}{A} \frac{\sigma_{pA}}{\sigma_{pp}} \quad (4.21)$$

for the hydrogen target and

$$R_{pA}^D = \frac{2}{A} \frac{\sigma_{pA}}{\sigma_{pd}} \quad (4.22)$$

for the deuterium target, noting the factor of two difference arising from the greater atomic mass of deuterium. The two cross sections, σ_{pA} and $\sigma_{p(p/d)}$, must be determined experimentally. Generically, the experimental cross section is the number of scattering events divided by the densities of colliding particles and the cross sectional area of the interaction. At SeaQuest, the cross section may be written as

$$\sigma_{pA} = \frac{Y_A M_A}{T_A^A N_A P_A A_A \varepsilon_A}, \quad (4.23)$$

where Y_A is the event yield on target A , M_A is the atomic mass of the target, T_A^A is the thickness of target material inside of the target (important for the hydrogen contamination in the deuterium target), N_A is Avogadro's number, P_A is the number of protons on target, A_A is the attenuation of the proton beam on target A , and ε_A is the combined geometric and reconstruction efficiencies on target A . Plugging this into eq. 4.21, the ratio is

$$R_{pA}^H = \frac{1}{M_H} \frac{Y_A}{Y_H} \frac{T_H^H}{T_A^A} \frac{A_H}{A_A} \frac{P_H}{P_A} \frac{\varepsilon_H}{\varepsilon_A}, \quad (4.24)$$

Sample Number	Bottle Number	Source	Analysis Date	Composition
1	53	Fermilab	4/12/18	95.6% D, 4.4% H; ca 92% D2 and 8% HD gases
2	113	Fermilab	4/12/18	96% D, 4% H; ca 93% D2 and 7% HD gases
3	53	Fermilab	4/12/18	Air, container developed a leak
4	127	Matheson	4/12/18	Half air, remaining 99.7 D2% and 0.7% H gases
5	2	Matheson	4/12/18	Test sample
6	N/A	Matheson	7/28/16	Mostly air, remaining 99.3% D and 0.7% H gases
7	N/A	Matheson	5/28/17	99.8% D, 0.2% H; ca 99.6% D2 and 0.4% HD gases

Table 4.7: Results of target gas analysis from ref. [88] showing a small fraction of hydrogen contamination in the deuterium targets used in data taking Run 2 and 3.

which is a ratio of yields from the targets weighed by some physical constants. Equation 4.24 is used to compute R_{pA} for both the J/Ψ and Ψ' , substituting in the appropriate particle yields.

The cross section ratio analysis for the deuterium target was complicated by contamination from hydrogen in the data used in this analysis. After the data taking was completed, an analysis of the target gas compositions was made and presented in ref. [88]. Table 4.7 shows the results of the analysis and the composition of gas used in the various target gas supplies. In this analysis, data from Run 2 and 3 are used corresponding to samples 1 and 2 from table 4.7. The Matheson gas was introduced during Run 3 starting from data taking period 14652, which is outside of the scope of this analysis. The recommended composition of 95.8 +/- 0.2% D and 4.2 +/- 0.2% H presented in ref. [88] are used for this analysis.

The effect of the target contamination is handled in this analysis in the same way as the primary SeaQuest analysis published in ref. [45]. The experimental deuterium cross section, σ_{pd} , is modified with a small term weighed by the hydrogen cross section, σ_{pp} to account for the contamination. Writing the deuterium cross section as

$$\sigma_{pd} = \frac{Y_D M_D}{T_D^D P_D A_D N_D \epsilon_D} - \sigma_{pp} \frac{T_H^D P_D A_D N_D \epsilon_D}{M_H} \frac{M_D}{T_D^D P_D A_D N_D \epsilon_D}, \quad (4.25)$$

we can insert eq. 4.23 for σ_{pp} and plug σ_{pd} into eq. 4.22 to get

$$R_{pA}^D = \frac{2}{M_D} \frac{\langle T_D^D \rangle}{T_A^A} \left[\frac{Y_A / (P_A A_A \varepsilon_A)}{Y_D / (P_D A_D \varepsilon_D) - \frac{\langle T_H^D \rangle}{T_H^D} Y_H / (P_H A_H \varepsilon_H)} \right]. \quad (4.26)$$

While the cross section ratio for hydrogen depends only on the ratio of yields on the hydrogen and comparison target, eq. 4.26 shows that the cross section ratio for deuterium also requires the hydrogen data to correct for the contamination. In addition, the thicknesses in the deuterium target, T_D^D and T_H^D , take on their average value for the small differences in contamination between deuterium samples 1 and 2. The quantities T_H^H , T_H^D , and T_D^D , were computed by Don Geesaman in ref. [88] using the results of the target gas analysis in table. 4.7. The proton attenuation values for each target, A_A , were computed by the method suggested in ref. [88] and evaluating the integral

$$\int_0^L dl \exp\left\{-\frac{l}{\lambda}\right\} = \lambda \left(1 - \exp\left\{-\frac{L}{\lambda}\right\}\right), \quad (4.27)$$

where L is the length of the target material, and λ is the interaction length of the material. The atomic masses are taken from ref. [89]. A full list of the non-yield values used in this analysis are presented in table. 4.8. Each of eq. 4.24 and eq. 4.26 assume that the chamber detector efficiencies cancel in the ratio. The efficiencies for each target, ε_A , are the combined acceptance and reconstruction efficiencies, $\varepsilon_A = \varepsilon_{\text{Accept}} * \varepsilon_{\text{Track}}$, and depend on each process, target, and bin in x_F and p_T in the binned analysis.

Statistical uncertainties are propagated to the cross section ratio by evaluating $\partial R_{pA}^{(D/H)} / \partial Y_X$, where X counts over all contributing yields, before summing in quadrature. For the hydrogen ratio these are computed from eq. 4.24 as

$$\frac{\partial R_{pA}^H}{\partial Y_A} = \frac{1}{M_H} \frac{1}{Y_H} \left[\frac{T_H^H}{T_A^A} \frac{A_H}{A_A} \frac{P_H}{P_A} \frac{\varepsilon_H}{\varepsilon_A} \right] \quad (4.28)$$

Variable	Value
M_H	1.008 g * mol ⁻¹
M_D	2.014 g * mol ⁻¹
M_C	12.01 g * mol ⁻¹
M_{Fe}	55.84 g * mol ⁻¹
M_W	183.8 g * mol ⁻¹
A_H	0.966
A_D	0.945
A_C	0.966
A_{Fe}	0.945
A_W	0.954
T_H^H	3.597 gm/cm ²
T_H^D	0.173 gm/cm ²
T_D^D	7.89 gm/cm ²

Table 4.8: Constant values used to calculate the cross section ratios, $R_{pA}^{(D/H)}$, in this analysis.

for the uncertainty in yield from target A ; and

$$\frac{\partial R_{pA}^H}{\partial Y_H} = -\frac{1}{M_H} \frac{T_H^H Y_A}{T_A^A P_A A_A \varepsilon_A} \frac{P_H A_H \varepsilon_H}{Y_H^2} = -\frac{1}{A_A Y_H} \frac{\sigma_{pA}}{\sigma_{pp}} \quad (4.29)$$

for the uncertainty in yield from the hydrogen target. These are summed in quadrature to give the final uncertainty on R_{pA}^H ,

$$\sigma_{R^H} = \sqrt{\left(\frac{\partial R_{pA}^H}{\partial Y_A} \sigma_A\right)^2 + \left(\frac{\partial R_{pA}^H}{\partial Y_H} \sigma_H\right)^2}. \quad (4.30)$$

The same derivatives are taken to determine the errors on the deuterium ratio, defining $\xi_i \equiv P_i A_i \varepsilon_i$ for notational simplicity:

$$\frac{\partial R_{pA}^D}{\partial Y_A} = \frac{2}{M_D} \frac{T_D^D}{T_A^A} \left[\frac{1/\xi_A}{Y_D/\xi_D - \frac{T_D^D}{T_H^D} Y_H/\xi_H} \right], \quad (4.31)$$

$$\frac{\partial R_{pA}^D}{\partial Y_D} = -\frac{2}{M_D} \frac{T_D^D}{T_A^A} \frac{\xi_D}{\xi_A} Y_A \left[Y_D - \frac{T_D^D}{T_H^D} \frac{\xi_D}{\xi_H} Y_H \right]^{-2}, \quad (4.32)$$

and

$$\frac{\partial R_{pA}^D}{\partial Y_H} = \frac{2}{M_D} \frac{T_D^D}{T_A^A} \frac{T_H^D}{T_H^H} \frac{Y_A}{\xi_A \xi_H} \left[\frac{Y_D}{\xi_D} - \frac{T_H^D}{T_H^H} \frac{Y_H}{\xi_H} \right]^{-2}. \quad (4.33)$$

With error on R_{pA}^D :

$$\sigma_{R^D} = \sqrt{\left(\frac{\partial R_{pA}^D}{\partial Y_A} \sigma_A \right)^2 + \left(\frac{\partial R_{pA}^D}{\partial Y_D} \sigma_D \right)^2 + \left(\frac{\partial R_{pA}^D}{\partial Y_H} \sigma_H \right)^2}. \quad (4.34)$$

The yields are determined from the TFractionFitter algorithm described in sec. 4.1.

4.9 Systematic Sources of Uncertainty

There are three primary systematic sources of uncertainty in this analysis. First, the choice of emulated mixed background could affect the mass-fitting procedure, resulting in a change in particle yields. In the unbinned analysis, the uncertainty is estimated by computing α in A^α using two different emulated backgrounds generated through distinct methods. The mixed backgrounds generated by Jason Dove and the NMSU group are used to compute α and the difference is used to estimate the systematic uncertainty. In the binned analysis, the difference in the cross section ratio in each bin is used to estimate the uncertainty. Second, the effect of chamber occupancy on the results of kTracker reconstruction introduces a reweighing parameter proportional to the 'efficiency' of kTracker as a function of D1. This efficiency value is calculated from a linear fit and an estimate of the systematic uncertainty is made by evaluating the cross section ratios with the upper and lower bounds on the slope of the fit. Finally, the reweighing of the Monte Carlo p_T distributions is considered by taking the upper and lower bounds on the Kaplan fit parameter, $p1$. The mixed background and kTracker efficiency are entirely uncorrelated errors and are summed in quadrature. The Monte Carlo reweighing scheme depends entirely on the results of the mass-fit which in turn depends on both the mixed background choice and the

kTracker efficiency results. The corrections from reweighting end up being small, but the uncertainty is estimated as if it is maximally anti-correlated with the other errors and is added to the total systematic uncertainty linearly.

4.10 Unbinned Results

The unbinned analysis studies the cross section ratios, $R_{PA}^{(D/H)}$, as a function of the atomic mass of the target, A . Previous fits to the cross section ratio have assumed that the per nucleon cross section is proportional to the per-nucleus cross section as

$$\sigma_{pA} = \sigma_{pd}A^\alpha. \quad (4.35)$$

The mass-fit plots used to determine the yields are shown in appendix A.5. The results for the cross section ratio for the hydrogen target data are presented for the J/Ψ and Ψ' in fig. 4.9 along with the data and fit from the E772 experiment published in ref. [54]. A value of $\alpha_H = 0.883 \pm 0.004(\text{stat.}) \pm 0.005(\text{sys.})$, plotted in red, is determined by referencing eq. 4.35 and using a fit of the form

$$R_{pA}^H = A^{(\alpha-1)}, \quad (4.36)$$

compared with the E772 value of $\alpha_H = 0.92$ which is plotted in black. Reference [54] notes that Eq. 4.35 is not necessarily valid and that data from ref. [90] had previously seemed to violate it. The cross section ratio for carbon determined in this analysis is close to the E772 value, while the iron and tungsten values are smaller than previously observed. Because the tungsten has such a large atomic mass, it provides significant leverage in the exponential fit, resulting in the smaller value for α_H seen in the SeaQuest data. Worth pointing out is the absence of the notable correlation of the Ψ' data with the J/Ψ data which had been observed at E772. The Ψ' in this

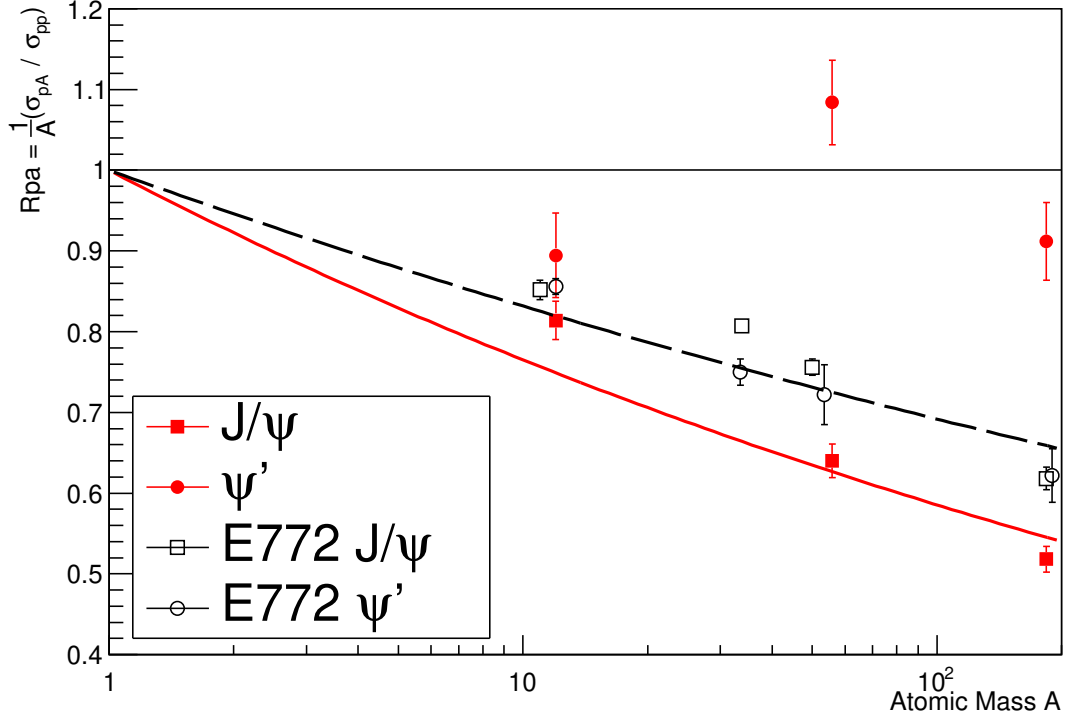


Figure 4.9: R_{pA} results for the hydrogen target in red, compared to E772 results in black from ref. [54]. The exponential fit, corresponding to $\alpha = 0.883$, is shown as a red curve for the J/Ψ , while the E772 value of $\alpha = 0.92$ used to describe both the J/Ψ and Ψ' is shown in dotted black. While the J/Ψ and Ψ' suppression is similar in the E772 data, the SeaQuest Ψ' ratio is consistent with unity.

analysis is consistent with a ratio of unity, similar to the Drell-Yan data observed at E772. The results for the cross section ratio for the deuterium target data are presented for the J/Ψ and Ψ' in fig. 4.10 alongside the hydrogen data from ref. [90]. A value of $\alpha_D = 0.877 \pm 0.004(\text{stat.}) \pm 0.003(\text{sys.})$ is determined by the exponential fit of eq. 4.36. The cross section ratio for carbon is again similar to the E772 values, while the iron and tungsten values bring the overall fit for α_D lower. The data from E772 shown here is not from a deuterium target, so it is not expected that the values are the same and E772 did not report a value of α_D . Again, the Ψ' ratio is consistent with unity.

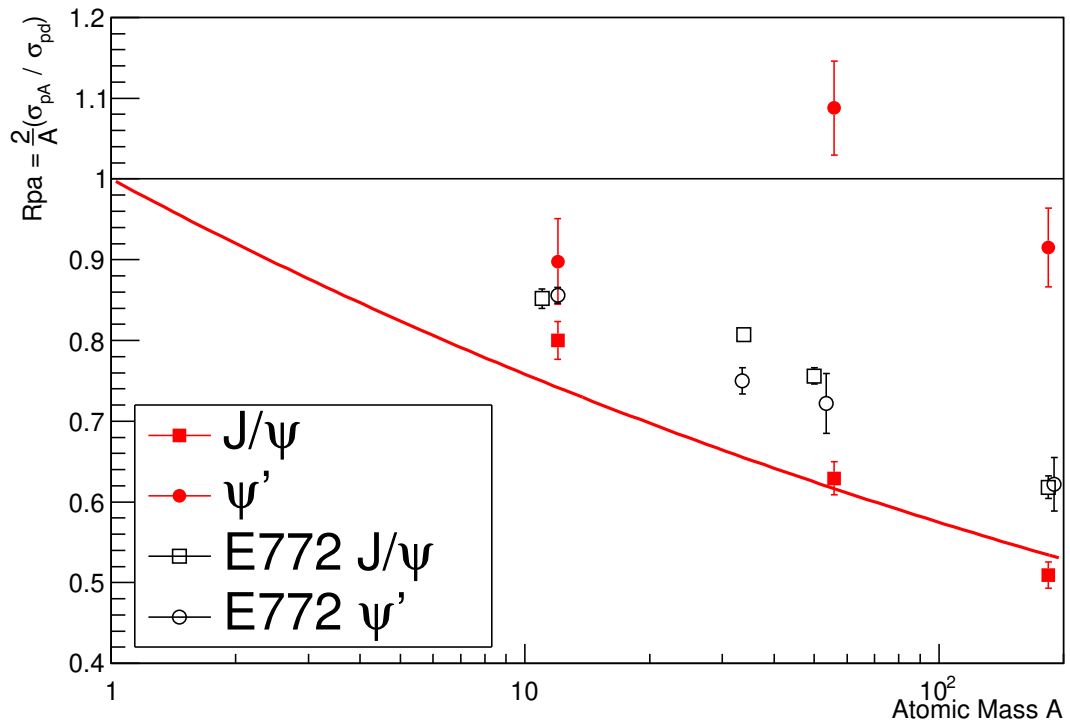


Figure 4.10: R_{pA} results for the deuterium target in red, compared to hydrogen results reported by E772 in black from ref. [54]. The exponential fit, corresponding to $\alpha = 0.877$, is shown as a red curve for the J/Ψ . While the J/Ψ and Ψ' suppression is similar in the E772 data, the SeaQuest Ψ' ratio is consistent with unity.

4.11 Binned Results in p_T and x_F

The binned analysis studies the cross section ratios, $R_{PA}^{(D/H)}$, per target, as a function of either the Feynman- x , x_F , or the transverse momentum, p_T . With more dedicated data taking and a trigger optimized for charmonia, an improved analysis could have been simultaneously performed in both dimensions, but the data from SeaQuest is too sparse. It had been observed by the E772 collaboration in ref. [54] that the cross section ratio tended to increase in p_T , an effect known as “ p_T broadening”, while decreasing in x_F . A similar effect is observed in the SeaQuest data, but the uncertainties for many targets make many results inconclusive. A future improvement would be the inclusion of the Run 5 and 6 data which would increase the data by a factor of two. A comparison of the J/Ψ results with theory predictions from ref. [46] is given in sec. 4.12. There are no predictions for the Drell-Yan or Ψ' available for the SeaQuest kinematic range, but the results for all processes are reported in appendix A.6. The p_T and x_F bins in this analysis are presented in table. 4.9. All mass-fits used to determine yields are presented in appendix A.6. The systematic errors computed for each bin in the binned fits are presented in appendix A.7. The errors are written as δp_{mix} , for the difference in the mixed backgrounds, δp_{trk}^+ , for evaluating the upper bound on the tracking efficiency, δp_{trk}^- , for evaluating the lower bound on the tracking efficiency, δp_{k1}^+ , for evaluating the upper bound on the Kaplan p_1 parameter, and δp_{k1}^- , for evaluating the lower bound on the Kaplan p_1 parameter. The total systematic uncertainty, δp_{tot} , is obtained by summing the uncorrelated errors in quadrature and the correlated error linearly. Hence, $\delta p_{\text{tot}} = \sqrt{(\delta p_{\text{mix}})^2 + (\delta p_{\text{trk}}^+)^2 + (\delta p_{\text{trk}}^-)^2} + |\delta p_{k1}^+| + |\delta p_{k1}^-|$, as the tracking efficiency and mixed background are independent but the reweighting is entirely correlated with each of the others. In all plots, the red error bars represent statistical error and the black bars represent the combined systematic and statistical errors, summed in quadrature.

Bin	p_T Selection	x_F Selection
0	0.0 – 0.3 GeV	0.4 – 0.6
1	0.3 – 0.45 GeV	0.6 – 0.65
2	0.45 – 0.65 GeV	0.65 – 0.7
3	0.65 – 0.9 GeV	0.7 – 0.77
4	0.9 – 1.5 GeV	0.77 – 0.95

Table 4.9: x_F and p_T bins used in the analysis.

4.12 Comparison with Theory

Predictions for J/Ψ suppression at SeaQuest have been made by Ramona Vogt in both p_T and x_F . Vogt notes that SeaQuest’s coverage in x_F is of particular interest in setting limits on the intrinsic charm content of the proton wavefunction (the $c\bar{c}$ distributions). The A dependence of the J/Ψ cross section ratio had previously been used to determine an effective nuclear absorption cross section and it had been assumed that deviations of α from unity had solely been accounted for by nuclear absorption. Data from experiments such as E615 and E772 have revealed a dependence of α on p_T and x_F which cannot be explained simply by nuclear absorption. Various cold nuclear matter effects contribute to this dependence including the modification of the parton distributions in nucleons in a nucleus relative to free nucleons, energy loss and p_t broadening from multiple scattering of the scattering particle as it traverses the nucleus, and absorption. Reference [46] notes that models which only include cold nuclear matter effects struggle to describe the x_F and p_T data. The NA3 collaboration had proposed to divide the J/Ψ production into “hard” and “diffractive” parts corresponding to cold nuclear matter effects evaluated with pQCD and the intrinsic charm components of the proton wavefunction respectively. A second term is added to Eq. 4.35, becoming

$$\frac{d\sigma_{pA}}{dx_F} = A^{\alpha'} \frac{d\sigma_h}{dx_F} + A^\beta \frac{d\sigma_d}{dx_F}, \quad (4.37)$$

where σ_h is the hard component and σ_d is the diffractive component. NA3 reported values of $\alpha' = 0.97$ and $\beta = 0.71$ in ref. [83]. Due to the large charm quark mass, it is

expected that intrinsic $c\bar{c}$ pairs carry a substantial fraction of the proton longitudinal momentum, contributing most significantly at large x_F , where the perturbative charm is observed to decrease strongly. For this reason, the SeaQuest data is of particular interest in understanding the intrinsic charm contribution, due to its acceptance at large x_F . In ref. [46], the Color Evaporation Model, detailed in ref. [91], is used to predict the J/Ψ production and cross section ratios in x_F and p_T at SeaQuest kinematics. Model predictions are made with increasing complexity and number of considered effects. The primary modifications to the pQCD results considered are the nuclear modification of parton densities, absorption by nucleons, and transverse momentum broadening. Finally, the contribution of the intrinsic charm is added to the model predictions. In this section, a brief discussion of the theory predictions is presented and comparisons with the results of this analysis are shown. Note that a full set of model predictions is published in ref. [46] and only a few are presented in sec. 4.12.6 for comparison.

4.12.1 J/Ψ in the Color Evaporation Model

In the Color Evaporation Model, it is assumed that some fraction of $c\bar{c}$ pairs, F_C with mass less than that of the D meson production threshold will go on mass shell as a J/Ψ , such that

$$\sigma_{\text{CEM}}(pp) = F_C \sum_{i,j} \int_{4m^2}^{4m_H^2} ds \int dx_1 dx_2 F_i^P(x_1, \mu_F^2, k_{T_1}) F_j^P(x_2, \mu_F^2, k_{T_2}) \hat{\sigma}_{ij}(\hat{s}, \mu_F^2, \mu_R^2), \quad (4.38)$$

where $F_{i,j}^P$ are parton densities, i and j count over the gg , $q\bar{q}$, and $q(\bar{q})g$ charmonium production channels shown in fig. 1.4, and $\hat{\sigma}_{ij}(\hat{s}, \mu_F^2, \mu_R^2)$ is the parton level cross section for initial state i, j calculated at factorization scale μ_F and renormalized at scale μ_R . The parton densities include intrinsic transverse momentum, k_T , and are assumed to be related to the normal parton densities in collinear factorization by the

relationship

$$F^P(x, \mu_F^2, k_T) = f^p(x, \mu_F^2)G_p(k_T), \quad (4.39)$$

where $f^p(x, \mu_F^2)$ are the typical parton distributions and $G_p(k_T)$ contains the intrinsic transverse momentum dependence. All predictions utilize the CT10 proton parton densities [92] to compute the parton densities. At leading order in the Color Evaporation Model, the J/Ψ p_T is zero, so the p_T predictions are made at next-to-leading order, while the x_F predictions are at leading order in the strong coupling α_s .

4.12.2 Nuclear Modification of Parton Densities

It is well known that the parton distributions of nucleons bound in a nucleus differ from those of free nucleons. The effect has been studied in deep inelastic scattering experiments, but leptonic probes only measure the charged components of the proton structure, leaving modifications of gluon densities to inference through evolution of parton densities in scale and momentum sum rules. At large momentum fractions, $x > 0.3$, a deficit is observed in the nucleus compared to the free nucleon, known as the EMC effect as it had been observed by the European Muon Collaboration [93]. There is also a deficit at low momentum fractions, $x < 0.03$, known as nuclear shadowing. In the intermediate x region, there is an enhancement called anti-shadowing. Typically, the nuclear parton density effects are parameterized in x , μ_F , and A such that the k_T dependent distributions of Eq. 4.38 are replaced by

$$f_j^A(x_2, \mu_F^2) = R_j(x_2, \mu_F^2, A)f_j^p(x_2, \mu_F^2). \quad (4.40)$$

The predictions in ref. [46] use the EPPS16 parameterizations at next-to-leading order in α_s , which have been published in ref. [94].

4.12.3 Absorption by the Nucleus

In $p + A$ collisions, it is possible that the $c\bar{c}$ produced in the parton scattering interacts with other nucleons in the nucleus, becoming disassociated or absorbed by the nuclear medium before fully hadronizing. This effect had previously been studied by Vogt in ref. [95] and the effect of nuclear absorption alone can be expressed as

$$\begin{aligned}\sigma_{pA} &= \sigma_{pN} S_A^{\text{abs}} = \sigma_{pN} \int d^2b \int_{-\text{inf}}^{\text{inf}} dz \rho_A(b, z) S^{\text{abs}}(b) \\ &= \sigma_{pN} \int d^2b \int_{-\text{inf}}^{\text{inf}} dz \rho_A(b, z) \exp\left\{-\int_z^{\text{inf}} dz' \rho_A(b, z') \sigma_{\text{abs}}(z' - z)\right\},\end{aligned}$$

where b is the impact parameter, z is the $c\bar{c}$ production location, $\rho_A(b, z)$ is the nuclear density distribution, $S^{\text{abs}}(b)$ is the nuclear absorption survival probability, and $\sigma_{\text{abs}}(z' - z)$ is the nuclear absorption cross section. The absorption cross section is assumed to be constant in the predictions, though it is written as a function of the path length through the nucleus. Vogt uses a value of $7 \leq \sigma_{\text{abs}} \leq 9$ mb, which had been determined for the 120 GeV proton beam at SeaQuest.

4.12.4 k_T Broadening

In the Color Evaporation Model, it is necessary to add an intrinsic broadening of the transverse momentum, k_T , of the produced $c\bar{c}$ pairs to keep the p_T distribution finite in the $p_T \rightarrow 0$ limit. In the calculations presented in ref. [46], a Gaussian blur is applied to the final state $c\bar{c}$. Effectively, the intrinsic k_T effects of Eq. 4.39 are modified and the factors $G_p(k_T)$ for the partons are replaced by

$$g_p(k_T) = G_p(k_{T_1})G_p(k_{T_2}), \quad (4.41)$$

where the Gaussian blur is implemented as

$$g_p(k_T) = \frac{1}{\pi \langle k_T^2 \rangle_p} \exp(-k_T^2 / \langle k_T^2 \rangle_p). \quad (4.42)$$

It is expected that the presence of the nuclear medium produces additional multiple scattering and therefore a larger intrinsic k_T broadening is required to model $p + A$ collisions than $p + p$ collisions, known as the Cronin effect [96]. The broadening in a nucleus relative to a free nucleon can be written as

$$\langle k_T^2 \rangle_A = \langle k_T^2 \rangle_p + \delta k_T^2, \quad (4.43)$$

where the additional second term is given by

$$\delta k_T^2 = (\langle \nu \rangle - 1) \Delta^2(\mu), \quad (4.44)$$

which depends on the number of collisions besides the first, $(\langle \nu \rangle - 1)$ and has strength $\Delta^2(\mu)$, which depends upon the interaction scale. In ref. [46], the average values used for the carbon, iron, and tungsten targets are $\delta k_T^2 = 0.1, 0.25,$ and 0.39 GeV^2 respectively. Generally, the k_T broadening suggests that the cross section ratios should be reduced at low p_T and enhanced at higher p_T .

4.12.5 Intrinsic Charm Contributions

Reference [46] notes that the wave function of the proton can be expressed in QCD as a superposition of Fock state fluctuations in the proton base state, $|uud\rangle$, containing intrinsic $q\bar{q}$ pairs, such as $|uudc\bar{c}\rangle$. The frame-independent probability distribution of the 5-particle Fock state for the intrinsic charm in the proton is given

by

$$dP_{ic\bar{5}} = P_{ic\bar{5}}^0 N_5 \int dx_1 \dots dx_5 \int dk_{x1} \dots dk_{x5} \int dk_{y1} \dots dk_{y5} \frac{\delta(1 - \sum_{i=1}^5 x_i) \delta(\sum_{i=1}^5 k_{xi}) \delta(\sum_{i=1}^5 k_{yi})}{(m_p^2 - \sum_{i=1}^5 (\hat{m}_i^2/x_i))^2}, \quad (4.45)$$

where $i = 1, 2, 3$ sums over the light quarks (u,u,d) and $i = 4, 5$ sums over the charm quarks c and \bar{c} respectively. N_5 is a constant normalizing the $|uudc\bar{c}\rangle$ probability to unity, while $P_{ic\bar{5}}^0$ scales the normalized probability to the assumed intrinsic charm content of the proton. While Eq. 4.45 has been considered for the x_F distribution, the J/Ψ p_T distribution calculated in ref. [46] is the first to be computed from a 5-particle Fock state approach. To evaluate the p_T distributions, the delta functions, $\delta(p_T - k_{xc} - k_{x\bar{c}})$ and $\delta(k_{yc} + k_{y\bar{c}})$ are inserted into Eq. 4.45 and it is assumed for simplicity that the transverse momentum component of the J/Ψ is only along the x direction. A full description of the calculation and results is provided in ref. [46] and the reader is encouraged to read a detailed review of other intrinsic charm models, such as meson-cloud models, presented in ref. [97]. A more recent review of the current state of theory of intrinsic heavy quark states by Brodsky and collaborators can be found ref. [98].

4.12.6 Comparison With SeaQuest R_{pA} Results

The theory predictions for R_{pA} are given for the nuclear PDF effects alone, nuclear PDF effects with k_T broadening, nuclear PDF effects with absorption, and the combined results of all of these effects. In addition, predictions are made including the results from the Fock state analysis of the proton intrinsic charm. In this section, the SeaQuest results of this analysis are compared only with the results for all combined nuclear effects and the additional intrinsic charm predictions for legibility. In

all plots, the red error bars represent statistical errors and the combined statistical and systematic error, summed in quadrature, is shown in black. The results for the p_T analysis are shown in fig. 4.11 for the carbon and fig. 4.12 and fig. 4.13 for iron and tungsten respectively, while the results for x_F are shown for carbon in fig. 4.14 and for iron and tungsten in fig. 4.15 and fig. 4.16. In each plot, the magenta, cyan, and black are predictions including all nuclear effects and the enhanced nuclear k_T broadening effect. Magenta represents a production probability of 0.1% for intrinsic charm, while the cyan and black predictions represent 0.31% and 1%, respectively. The predictions are binned as in ref. [75], but are reproduced as published in ref. [46] and placed with bin centers, rather than bin averages. The theory values correspond to the central values of the EPPS16 nuclear parton distribution parameterizations.

4.13 Discussion

In the unbinned analysis, there are some notable differences from the previous E772 results. The values of α for both the hydrogen and deuterium targets are lower than that found by E772. The primary difference between the experiments is the energy of the proton beam. E772 used an 800 GeV beam, while SeaQuest used the Main Injector Proton Beam at 120 GeV. From the work of refs. [46, 95], this difference in energy changes the primary production channel of the J/Ψ and Ψ' . At higher energies, charmonium production is dominated by gluon-gluon fusion, but at SeaQuest energies charmonium has a large quark-antiquark annihilation contribution. As a result, the in-going effects of the cold nuclear media may be similar to Drell-Yan, which is driven entirely by quark-antiquark annihilation, where no suppression was observed by E772. The clearest difference between these results and those of E772 is the behavior of the Ψ' . The E772 data showed J/Ψ and Ψ' suppression of equal magnitude. While the E906 data also shows a suppression in J/Ψ production, the

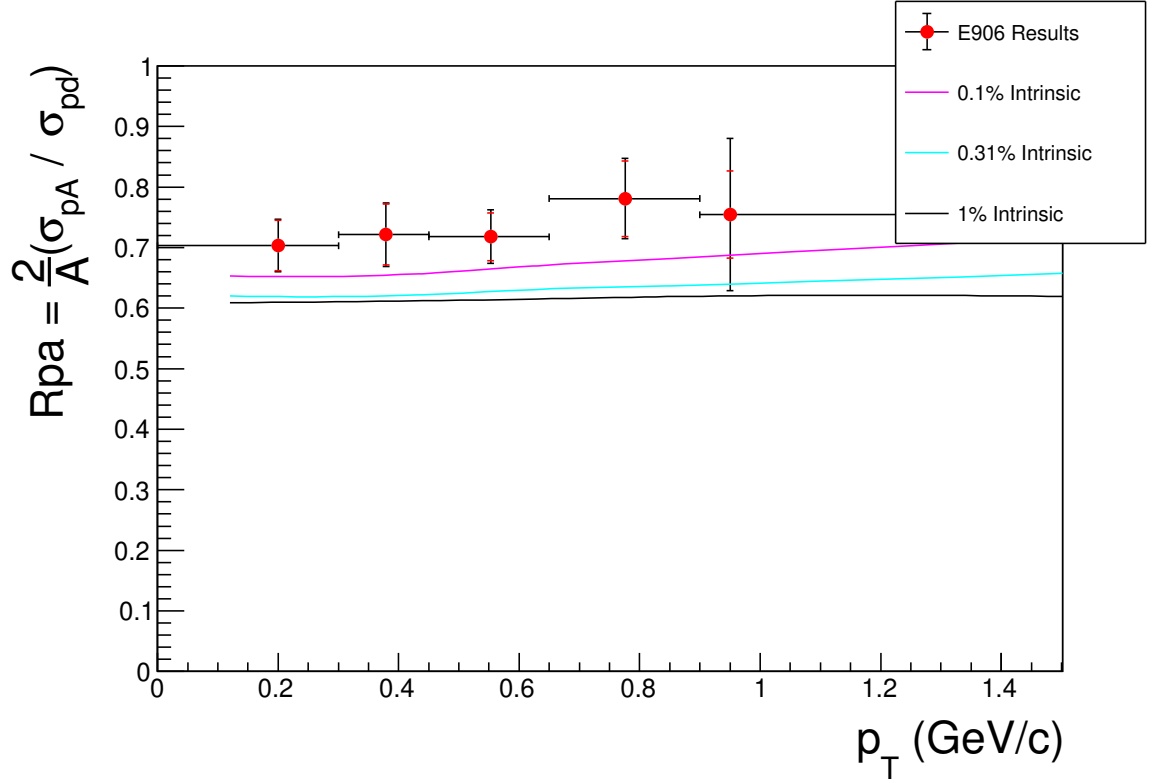


Figure 4.11: R_{pA} results of this analysis compared to the predictions of ref. [46] for J/Ψ from the carbon target, binned in p_T . Horizontal errors represent bin widths, with markers placed at bin averages. Red error bars represent statistical error and the combined statistical and systematic error is shown in black. The magenta, cyan, and black curves include all nuclear effects, including enhanced nuclear k_T broadening, and correspond to a 0.1%, 0.31%, and 1% probability for intrinsic charm production, respectively. Prediction values are placed at bin centers rather than averages and use central values of the EPPS16 nPDF set.

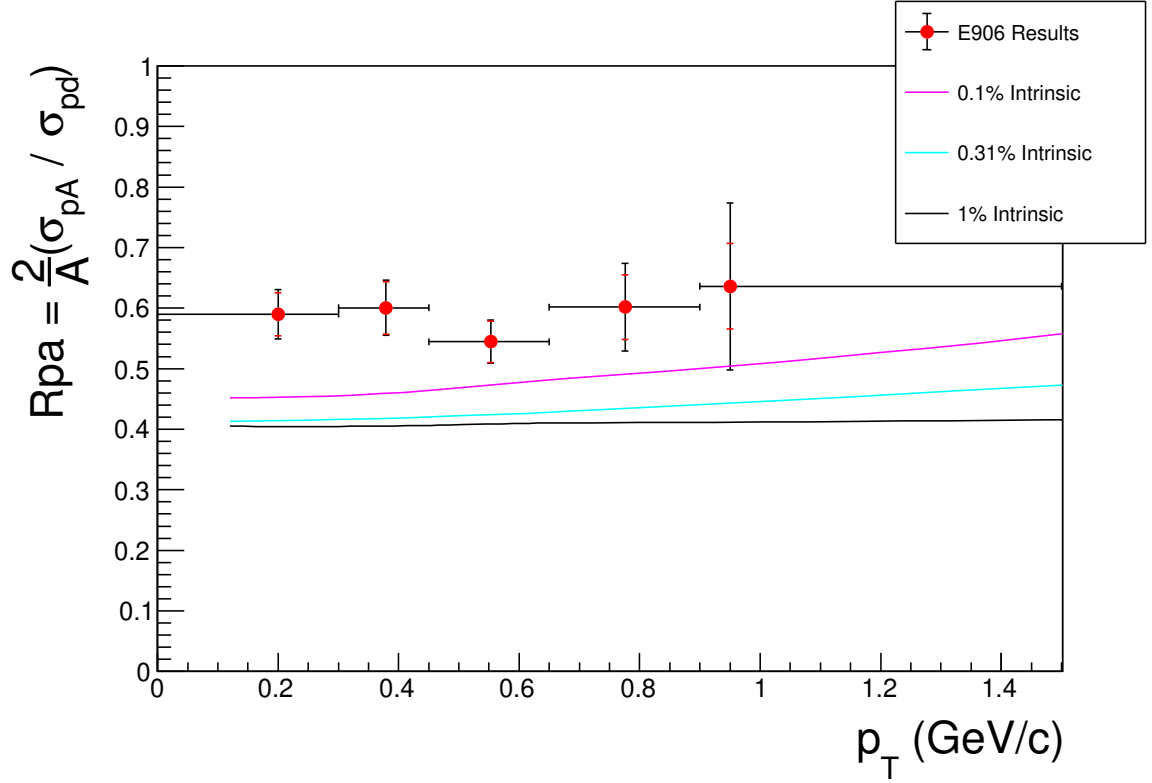


Figure 4.12: R_{pA} results of this analysis compared to the predictions of ref. [46] for J/Ψ from the iron target, binned in p_T . Horizontal errors represent bin widths, with markers placed at bin averages. Red error bars represent statistical error and the combined statistical and systematic error is shown in black. The magenta, cyan, and black curves include all nuclear effects, including enhanced nuclear k_T broadening, and correspond to a 0.1%, 0.31%, and 1% probability for intrinsic charm production, respectively. Prediction values are placed at bin centers rather than averages and use central values of the EPPS16 nPDF set.

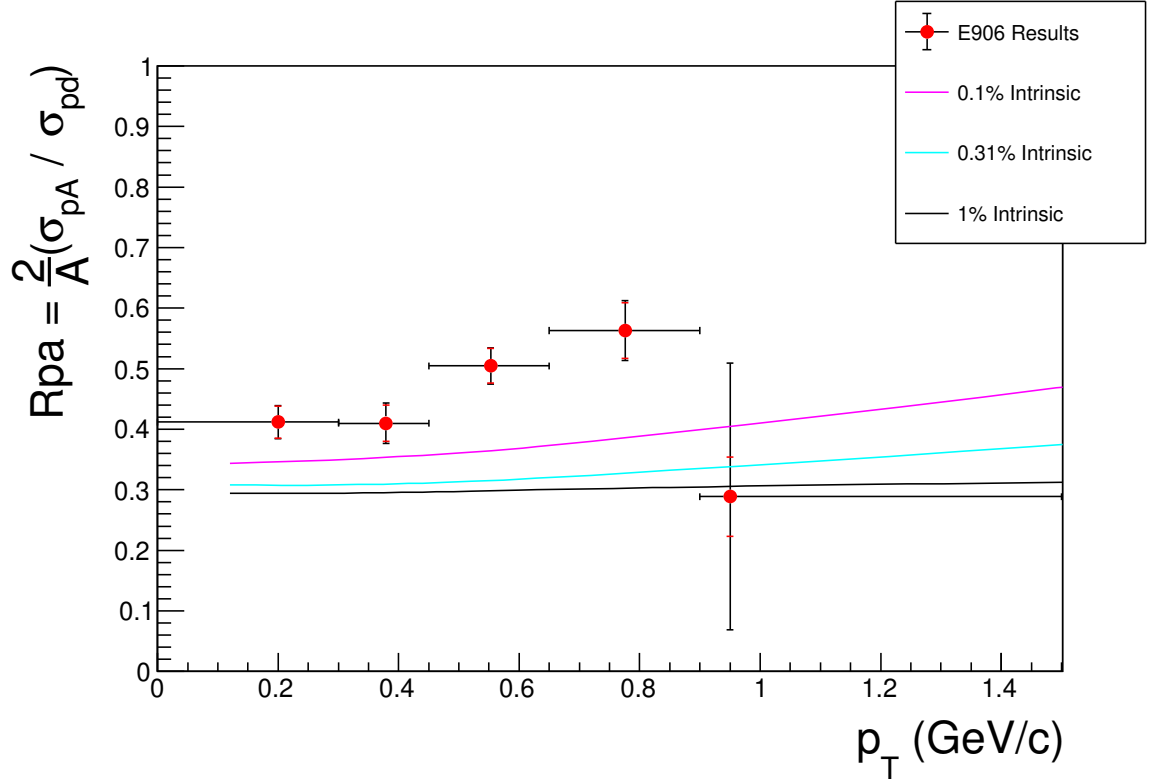


Figure 4.13: R_{pA} results of this analysis compared to the predictions of ref. [46] for J/Ψ from the tungsten target, binned in p_T . Horizontal errors represent bin widths, with markers placed at bin averages. Red error bars represent statistical error and the combined statistical and systematic error is shown in black. The magenta, cyan, and black curves include all nuclear effects, including enhanced nuclear k_T broadening, and correspond to a 0.1%, 0.31%, and 1% probability for intrinsic charm production, respectively. Prediction values are placed at bin centers rather than averages and use central values of the EPPS16 nPDF set.

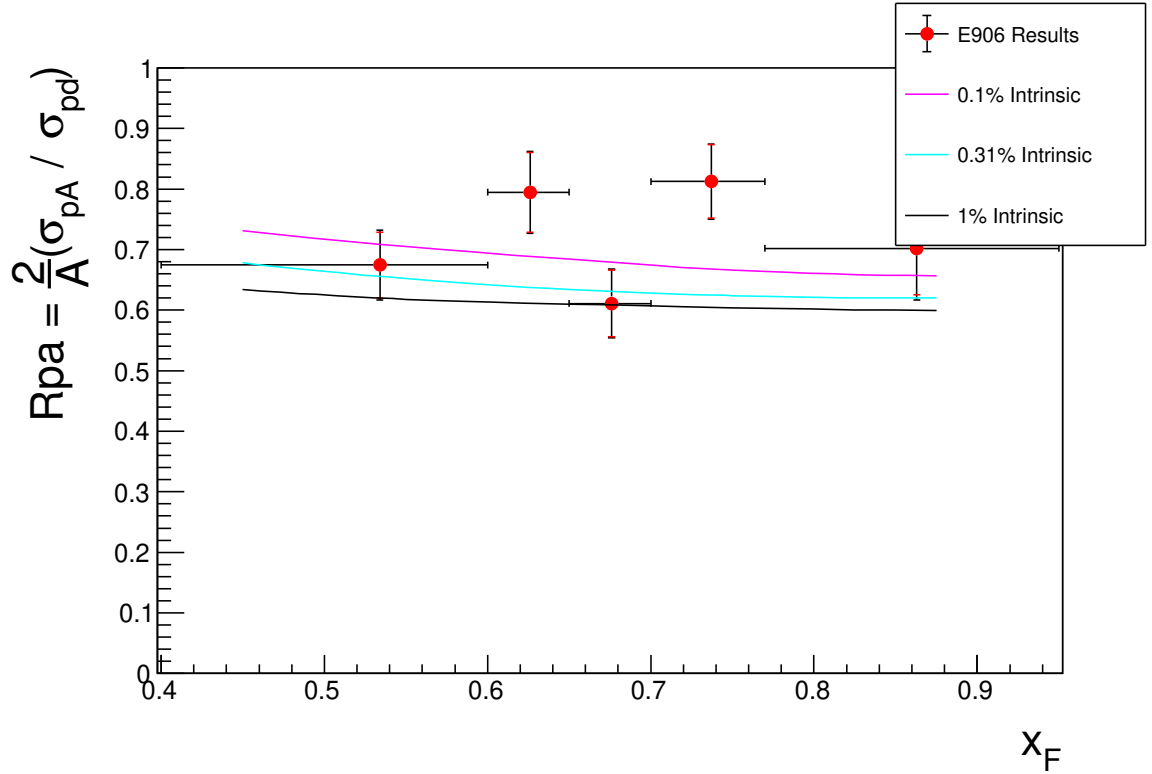


Figure 4.14: R_{pA} results of this analysis compared to the predictions of ref. [46] for J/Ψ from the carbon target, binned in x_F . Horizontal errors represent bin widths, with markers placed at bin averages. Red error bars represent statistical error and the combined statistical and systematic error is shown in black. The magenta, cyan, and black curves include all nuclear effects, including enhanced nuclear k_T broadening, and correspond to a 0.1%, 0.31%, and 1% probability for intrinsic charm production, respectively. Prediction values are placed at bin centers rather than averages and use central values of the EPPS16 nPDF set.

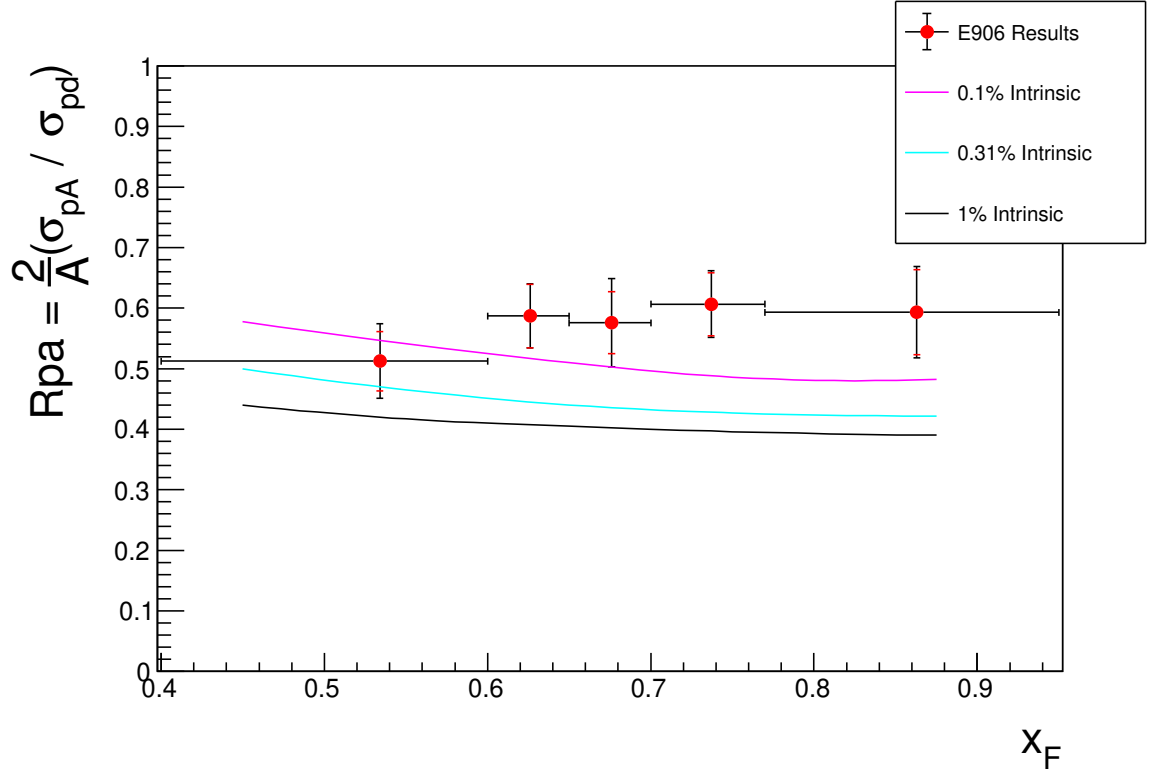


Figure 4.15: R_{pA} results of this analysis compared to the predictions of ref. [46] for J/Ψ from the iron target, binned in x_F . Horizontal errors represent bin widths, with markers placed at bin averages. Red error bars represent statistical error and the combined statistical and systematic error is shown in black. The magenta, cyan, and black curves include all nuclear effects, including enhanced nuclear k_T broadening, and correspond to a 0.1%, 0.31%, and 1% probability for intrinsic charm production, respectively. Prediction values are placed at bin centers rather than averages and use central values of the EPPS16 nPDF set.

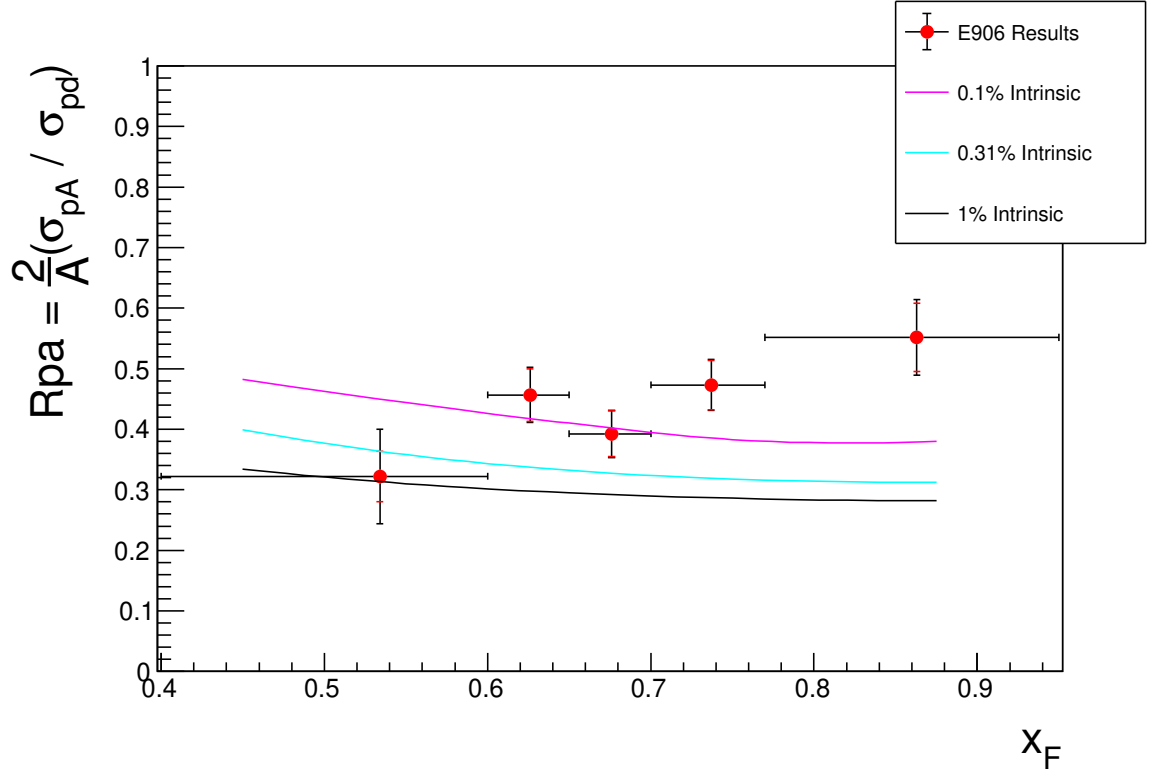


Figure 4.16: R_{pA} results of this analysis compared to the predictions of ref. [46] for J/Ψ from the tungsten target, binned in x_F . Horizontal errors represent bin widths, with markers placed at bin averages. Red error bars represent statistical error and blue error bars represent the systematic errors and the combined error is shown in black. The magenta, cyan, and black curves include all nuclear effects, including enhanced nuclear k_T broadening, and correspond to a 0.1%, 0.31%, and 1% probability for intrinsic charm production, respectively. Prediction values are placed at bin centers rather than averages and use central values of the EPPS16 nPDF set.

Ψ' production is consistent with being constant as a function of atomic mass. These results could hint at the difference in ingoing and outgoing sources of suppression observed at E866 and SeaQuest energies.

In the binned analysis, the data demonstrates less suppression than expected for intrinsic charm production possibilities between 0.1% and 1% from ref. [46]. In the p_T analysis, the results are typically 1–2 σ larger than expected. The data is in better agreement with theory predictions presented in ref. [46] with a small or negligible nuclear absorption cross section. There is also a notable difference in the x_F binned analysis. Across all targets, theory predictions suggest a fall off in the cross section ratio at higher x_F , but this effect is not observed in the SeaQuest data. While the carbon and iron data are, perhaps, consistent with being constant in x_F , the tungsten results hint at a possible enhancement in the cross section at higher x_F values. The data and theory do not differ by more than 2σ in the highest x_F bin. However, part of the motivation to study the J/Ψ at SeaQuest is the relatively large acceptance at high x_F compared to collider experiments and these data cover the kinematic range with the least experimental input for modeling.

Chapter V

Conclusions

5.1 Summary

For the majority of my research time, I worked on the E1039 / SpinQuest experiment as the on-call FPGA trigger expert. During the development period of the SpinQuest experiment, the FPGA trigger system from E906 was updated with a new roadset and a buffered readout system, along with an automatic timing system. A full testbench has been developed and installed onsite in the experimental hall, capable of installing and testing a new roadset, remotely, in less than 20 minutes. The performances of the FPGA boards used in the trigger system were characterized and the trigger is currently taking data with a special roadset optimized for cosmic ray data taking and comparison with the NIM trigger. The system is ready for commissioning and will hopefully be used in the near future.

A multi-threaded extension to the kTracker algorithm was also developed during the SpinQuest development period. The software utilizes the ROOT TThread library to assign multiple instances of the kTracker algorithm to run on multiple CPU cores in parallel. A model was developed on a four core laptop, showing the expected time scaling of $1/N_{\text{cores}}$, before a thirty-two core machine was purchased from Dell and installed onsite at Fermilab. The machine demonstrates a $30\times$ improvement in tracking throughput and will serve as an online reconstruction station during SpinQuest data

taking as well as a primary machine in the offline analysis. The algorithm was tested on SeaQuest data and compared with the single threaded implementation for correctness. A mySQL based database system, developed by Kenichi Nakano, automatically invokes the tracking algorithm on new spill data during data acquisition.

Originally, the proposed goal of my research was to study the Sivvers asymmetry at SpinQuest, but several challenges have delayed data taking. The Covid-19 pandemic prevented substantial on-site work during a crucial time period for target installation for most of 2020. In addition, Fermilab has increased its safety requirements to match DOE standards during the development of the experiment. While data taking was planned for this year, there are two remaining safety reviews before SpinQuest can take data. A target safety review for the new, polarized target and a review of the beam-line must be completed in conjunction with Fermilab. Unfortunately, the collaboration was not able to coordinate the reviews with Fermilab before the summer shut down, likely delaying commissioning to early next year. As a result, I received permission from the SeaQuest collaboration to utilize their data for the analysis presented here, which has been my focus for the last year.

The Drell-Yan, J/Ψ , and Ψ' production cross section ratios for carbon, iron, and tungsten targets, compared with hydrogen and deuterium targets, have been studied using the 120 GeV Main Injector Proton Beam at Fermi National Accelerator Laboratory as part of the E906 / SeaQuest experiment. The `TFractionFitter` class provided by ROOT was employed to calculate the particle yields. I was also used to propagate the statistical uncertainty associated with the data-driven Monte Carlo samples generated by the collaboration. The standard data selections used in the SeaQuest Nature paper were applied to the data. The process yields were then corrected by the efficiency of the SeaQuest tracking algorithm and geometric acceptance of the spectrometer. Two independent sets of data-driven background samples were used in the yield extraction. The background sample used in the Nature paper, produced by

Jason Dove, was used to calculate the central values in this analysis. The New Mexico State University background sample was used to estimate the systematic uncertainty introduced by the choice of background sample. It is found that the background sample choice is a dominant contributor to the systematic error. A limited amount of SeaQuest data is available to produce new, larger mixed background samples, which would reduce the systematic uncertainty.

The cross section ratios, $R_{pA}^{D/H}$ have been reported as a function of the target atomic mass and compared with results from the E772 experiment. E772 observed a comparable suppression for the J/Ψ and Ψ' using an 800 GeV proton beam and a Drell-Yan ratio consistent with unity. The E906 data shows a suppression of the J/Ψ with similar magnitude to that observed at E772, but the Ψ' production appears to be consistent with unity across all studied targets. The predictions of ref. [46] suggest that charmonia production at E772 energies is dominated by the gluon-gluon fusion cross section, while the quark-antiquark annihilation channel becomes a significant contributor at SeaQuest energies. The cold nuclear media interacts with both the ingoing partons during charmonium production and the outgoing, hadronizing $c\bar{c}$ pairs. At SeaQuest, it is more likely that the in-going particle is a quark or anti-quark, which interacts differently with the cold nuclear media, than a gluon. This difference in Ψ' results could point to a difference in the strength of ingoing and outgoing suppression sources at SeaQuest energy compared to the higher E772 energy.

The cross section ratios have also been reported as a function of transverse momentum, p_T , and Feynman-x, x_F . The deuterium ratio results are compared to the Color Evaporation Model predictions of ref. [46]. The predictions incorporate several effects of cold nuclear media, including the nuclear modification of parton densities, absorption by the nucleus, and p_T broadening from multiple scattering in the nuclear medium. Reference [46] also calculates effects arising from a possible intrinsic charm component of the proton by evaluation of the five particle Fock state, $|uudc\bar{c}\rangle$.

The data shows less suppression than theory predictions for intrinsic charm production probabilities between 0.1% – 1% in the studied transverse momentum range of $0.0 \leq p_T < 1.5$ GeV/c for all targets. The most notable difference between the data and the theory predictions appear in the Feynman-x data, studied in the range $0.4 \leq x_F < 0.95$. Across all targets, the theory predicts a falling cross section at higher x_F values. While the carbon target results are consistent with the theory prediction, the iron data does not feature a falling cross section and the tungsten data even suggests a slight enhancement in x_F . It is important to remember that while the theory predictions were made for SeaQuest kinematics, one of the motivations for studying the J/Ψ at SeaQuest is the large x_F coverage, as high x_F events often lie outside of the acceptance of collider experiments. The difference from theory and data is not more than 2σ in the highest bin of the tungsten results, but it also corresponds to a kinematic regime with the least available data for modeling. There are also several predictions in ref. [46] with different nuclear absorption cross sections which may match the SeaQuest data better.

The Drell-Yan cross section ratios were not compared with theory predictions and were not the primary focus of this analysis, but there are a few notable features in the data. A clear p_T broadening effect is observed across all targets, with most ratio values greater than unity and growing at higher p_T . In Feynman-x, the Drell-Yan data is largely consistent with being constant, though a slight downwards trend can be seen in the comparison of the hydrogen and tungsten target data.

5.2 Future Outlook

There are several possible improvements to this analysis which can be made in the future. First and foremost is the inclusion of more data. Runs 2 and 3 represent roughly 50% of the total usable SeaQuest data set and there is ongoing work within the collaboration to finish processing the Run 5 and 6 data. Run 1 data was primarily

aimed at commissioning the detector and used the DC3m chamber which was replaced by the DC3m.2 detector by Run 2. The Run 4 data saw similar changes in detector configurations with the replacement of DC1 by DC1.2 and the later re-inclusion of DC1, renamed to DC1.1, further downstream. The data in these runs is challenging to analyze and is omitted from the primary SeaQuest analysis. Inclusion of the Run 5 and 6 data would reduce the statistical errors of the study by $1/\sqrt{2}$. Furthermore, a new station, DC1.2 had been installed between run 3 and 5 and was designed to improve the detector acceptance at large x_F , where the theory is least constrained. Second, the largest source of systematic uncertainty in the analysis is the choice of mixed background sample. While both the FPGA4 and the NMSU background samples are produced with unique techniques, the total data available to draw tracks from is a shared and finite pool. Runs 5 and 6 provide more possible tracks to include in the mixing method and a larger background sample would help to reduce the systematic error of this study. Finally, it has been standard in the collaboration to combine data across roadsets when performing the yield extraction. While it is true that the roadsets show very similar distributions of kinematic variables, there are distinct changes in detector status and configuration from run to run. An improved analysis would ideally extract yields from each individual roadset, applying per-roadset corrections to the yields, before combining the results for the cross section ratio measurement. With more precision, the SeaQuest data could provide further insight into the relative strengths of nuclear absorption and a potential intrinsic charm contribution to the suppression of light charmonia by cold nuclear matter.

Appendix

Plots and Tables

A.1 p_T^2 Kaplan Fits for Drell-Yan

Kaplan fits used to reweight the Drell-Yan Monte Carlo in sec. 4.3 are presented in figs. A.1 to A.5.

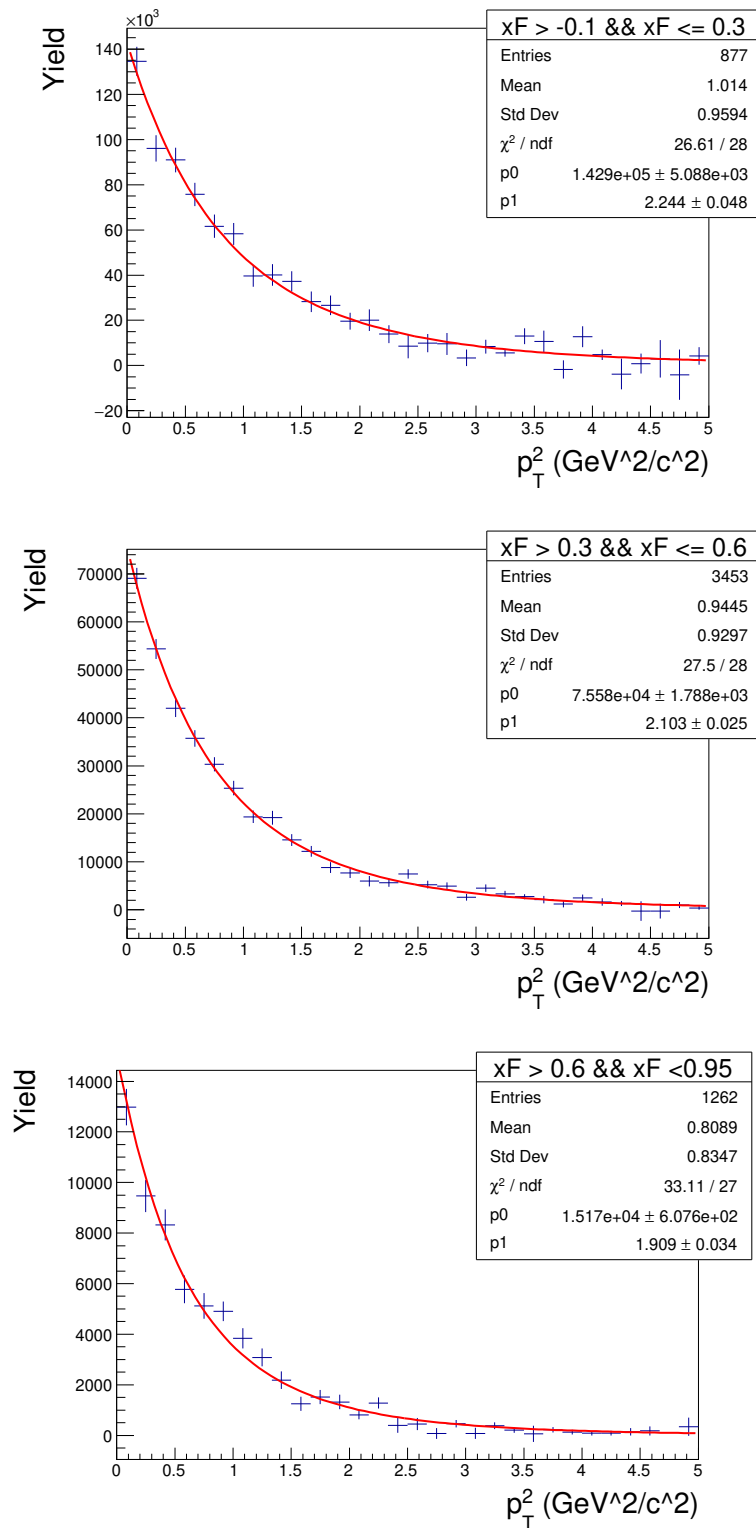


Figure A.1: Kaplan fit for Drell-Yan reweighting in increasing x_F bins, hydrogen target.

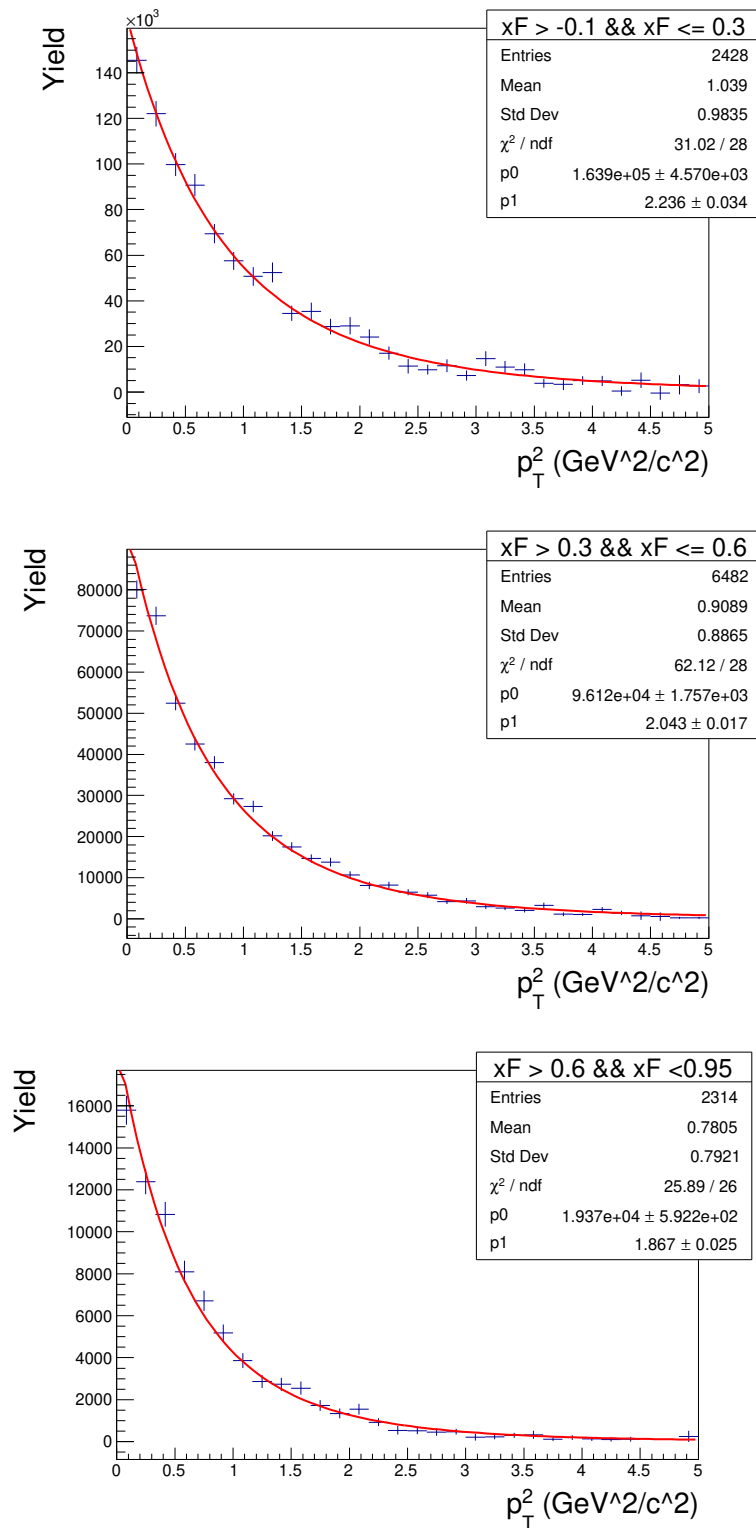


Figure A.2: Kaplan fit for Drell-Yan reweighting in increasing x_F bins, deuterium target.

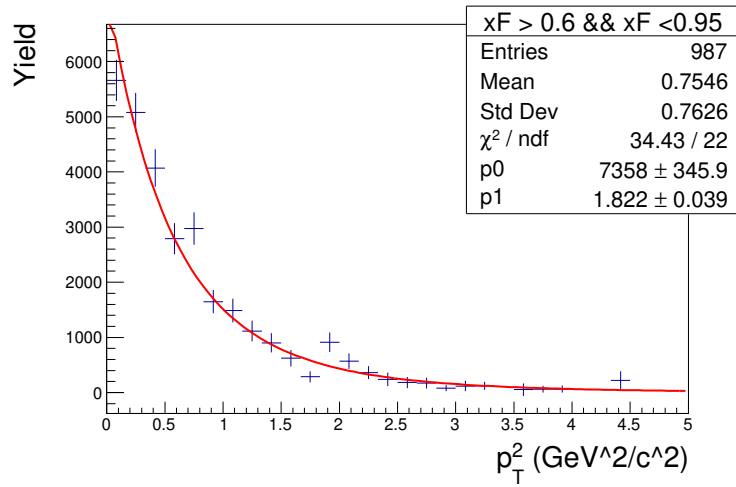
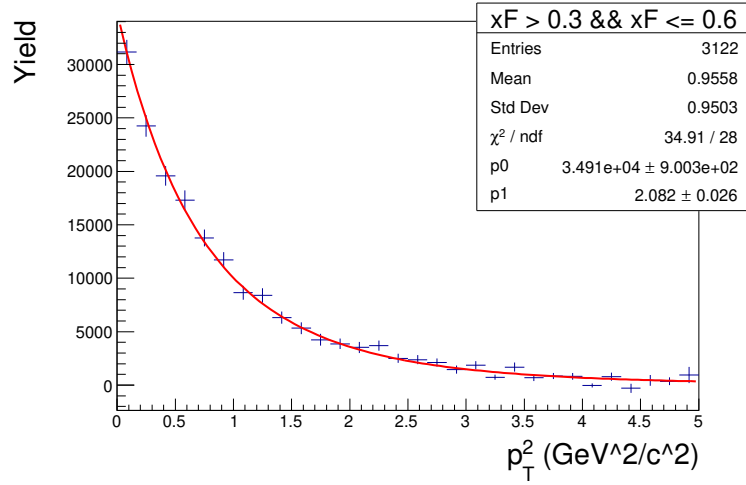
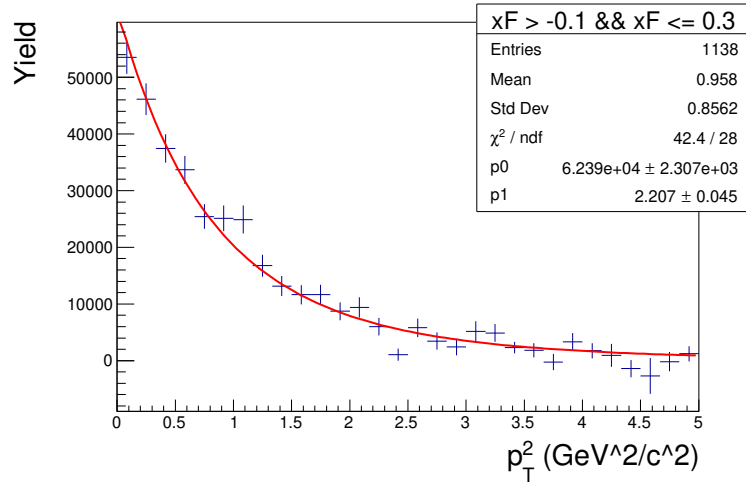


Figure A.3: Kaplan fit for Drell-Yan reweighting in increasing x_F bins, carbon target.

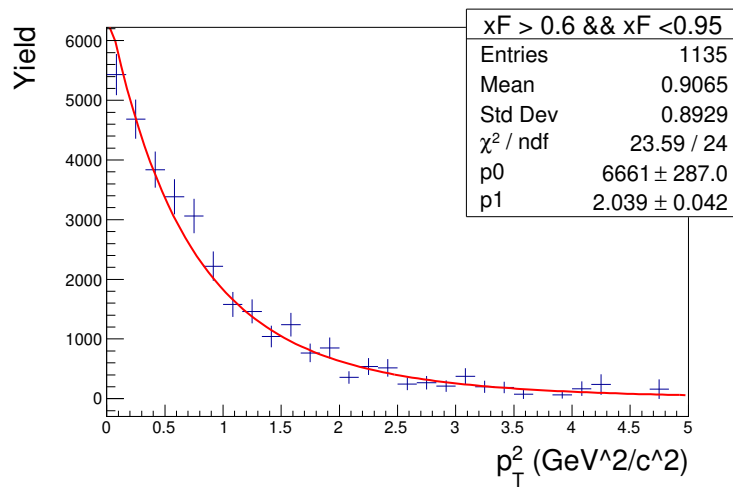
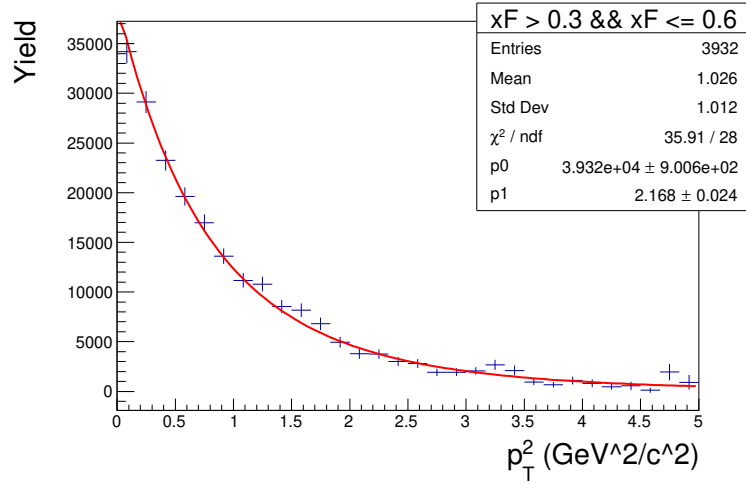
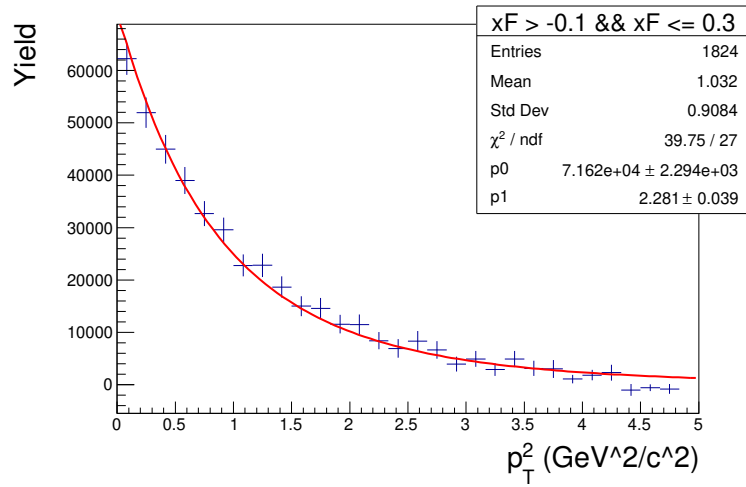


Figure A.4: Kaplan fit for Drell-Yan reweighting in increasing x_F bins, iron target.

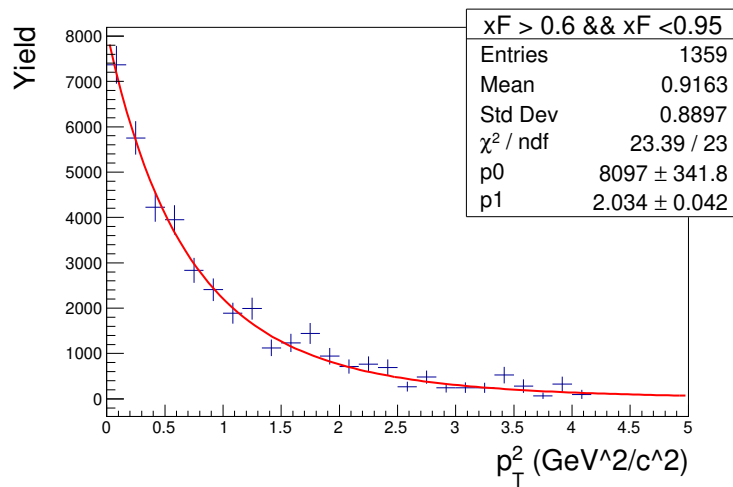
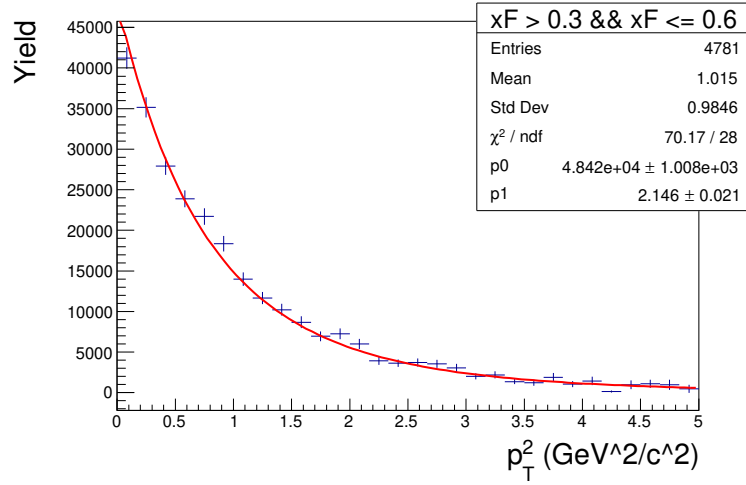
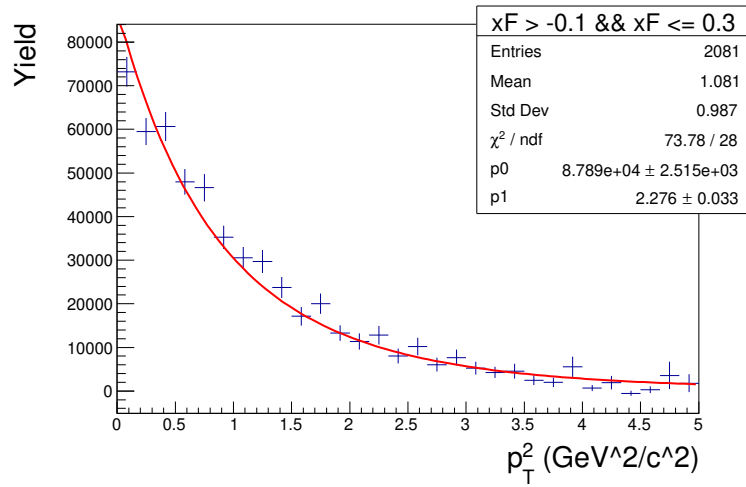


Figure A.5: Kaplan fit for Drell-Yan reweighting in increasing x_F bins, tungsten target.

A.2 Drell-Yan Kaplan $p_1(x_F)$

Plots of the Kaplan parameter, p_1 , as a function of Feynman- x are presented for the liquid targets in fig. A.7 and for the solid targets in fig. A.7.

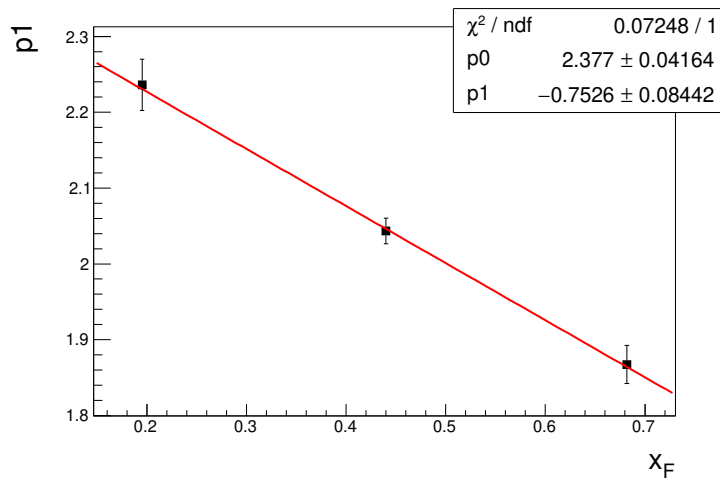
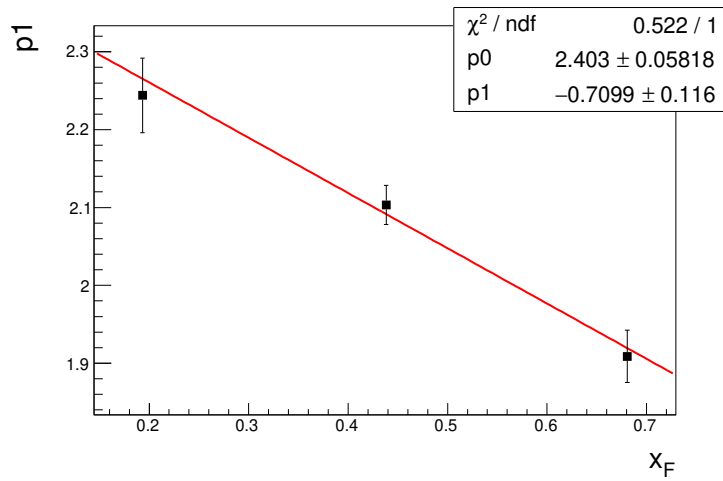


Figure A.6: Kaplan parameter p_1 as a linear interpolation in x_F used to reweight the Drell-Yan Monte Carlo. (Top) liquid hydrogen results (Bottom) liquid deuterium results.

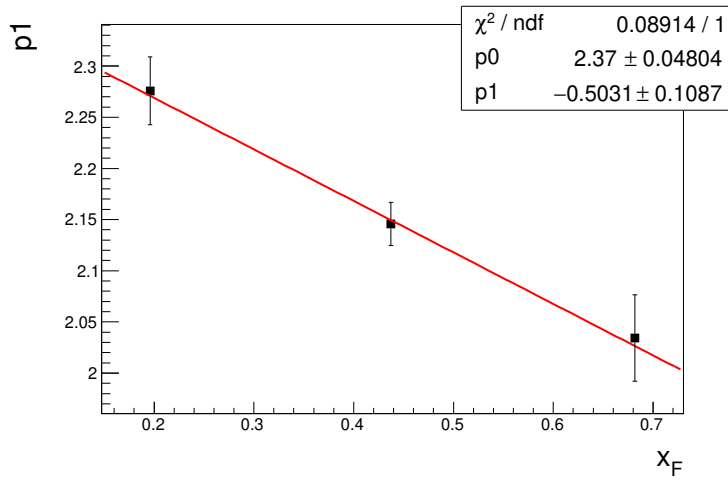
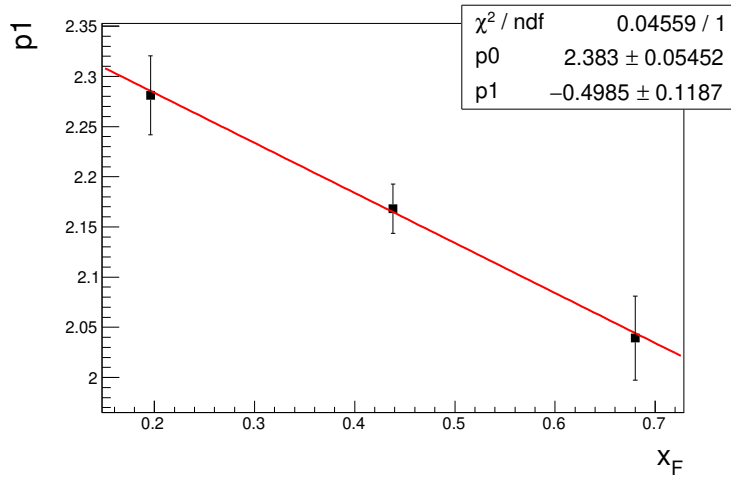
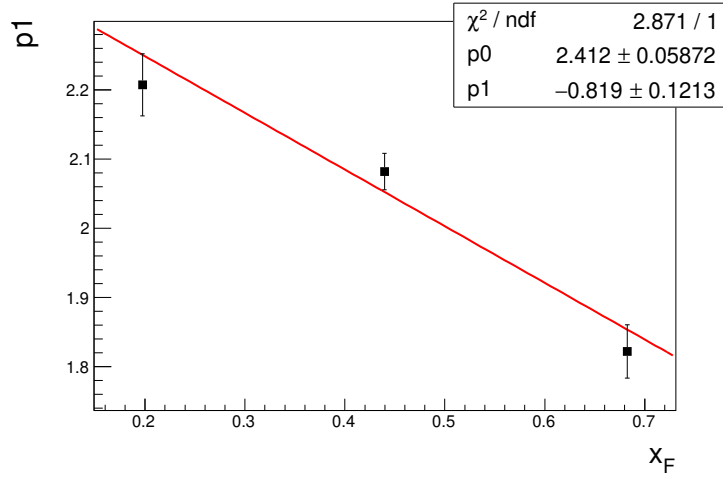


Figure A.7: Kaplan parameter p_1 as a linear interpolation in x_F used to reweight the Drell-Yan Monte Carlo. (Top) carbon results (Middle) iron results (Bottom) tungsten results.

A.3 p_T Kaplan Fits for J/Ψ and Ψ'

Kaplan fits used to reweight the J/Ψ and Ψ' Monte Carlo in sec. 4.3 are presented in figs. A.8 to A.11.

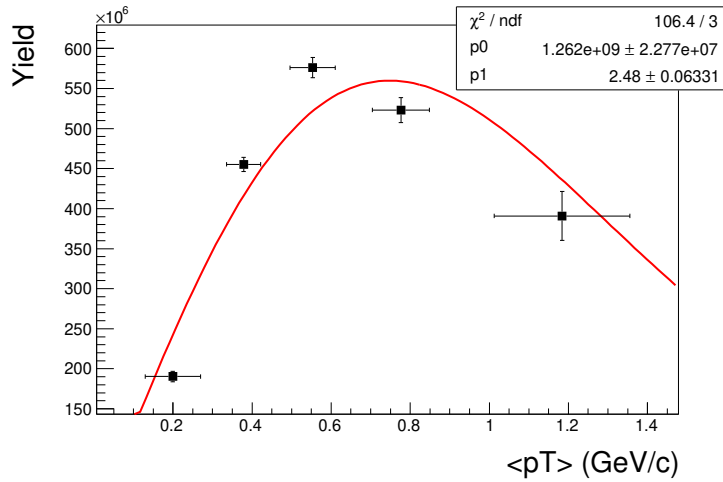
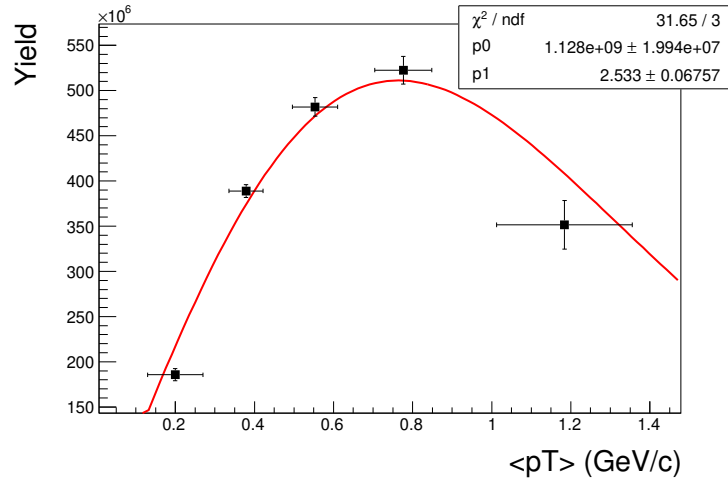


Figure A.8: Acceptance corrected J/Ψ yield, fit with the Kaplan form to determine p_1 , used in the Monte Carlo reweighting. (Top) liquid hydrogen results (Bottom) liquid deuterium results. Horizontal error bars are not considered in the fit and represent the standard deviation of each p_T bin.

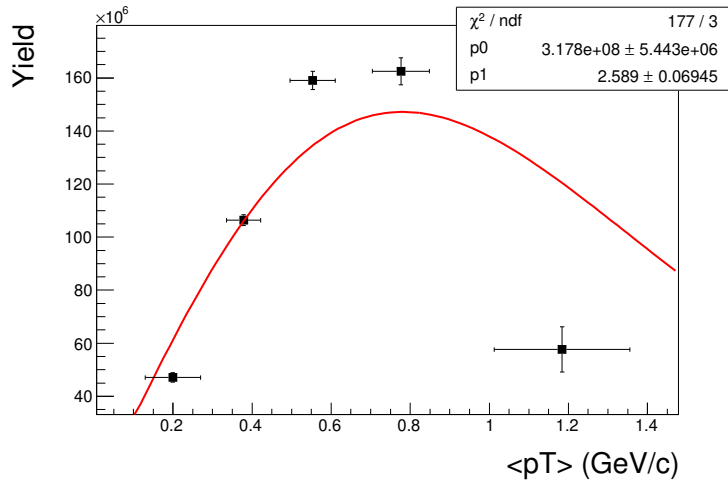
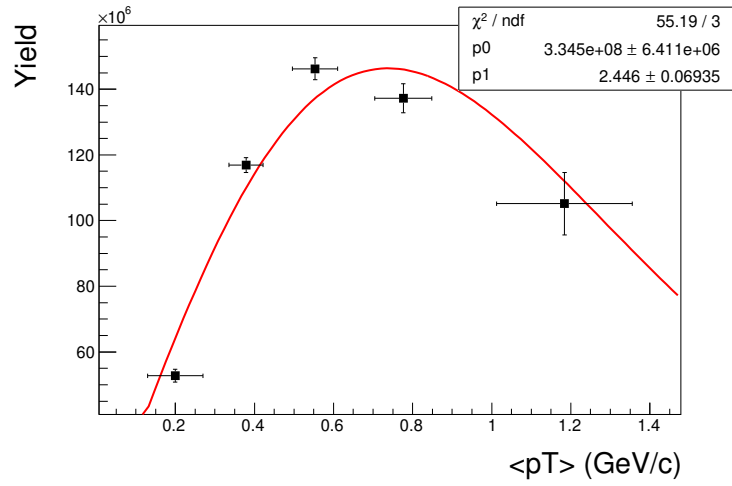
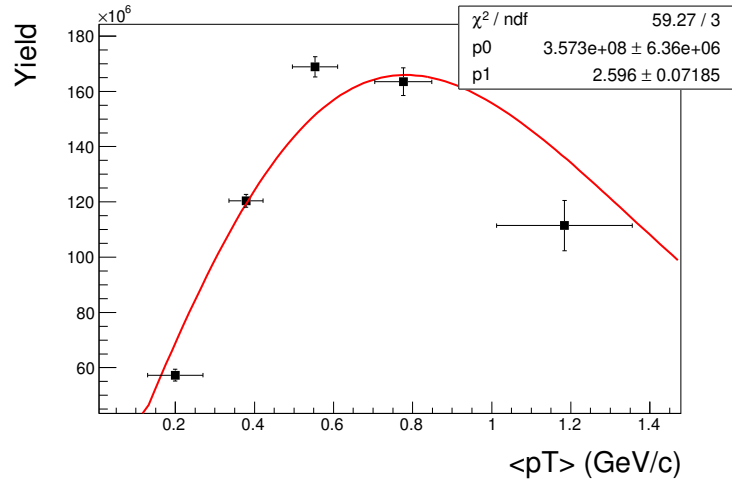


Figure A.9: Acceptance corrected J/Ψ yield, fit with the Kaplan form to determine p_1 , used in the Monte Carlo reweighting. (Top) carbon results (Middle) iron results (Bottom) tungsten results. Horizontal error bars are not considered in the fit and represent the standard deviation of each p_T bin.

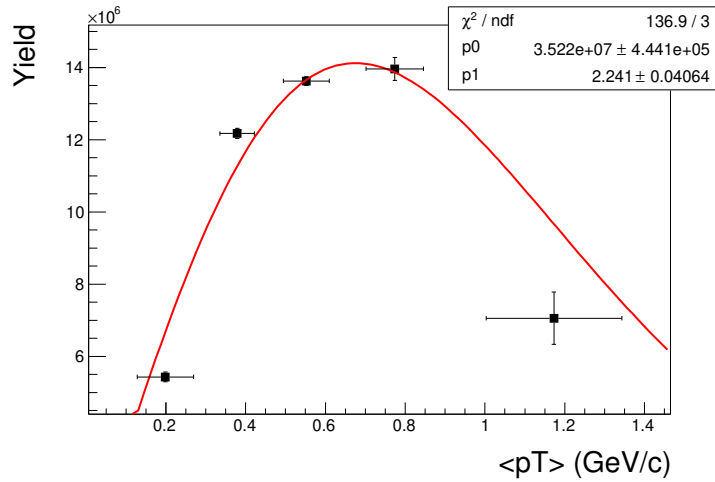
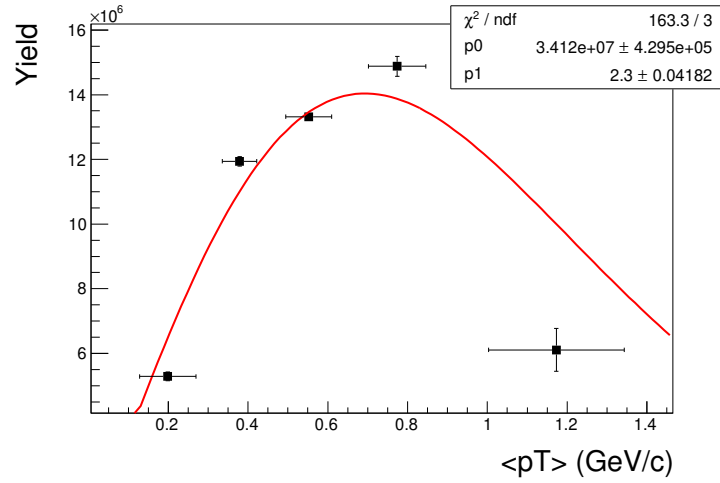


Figure A.10: Acceptance corrected Ψ' yield, fit with the Kaplan form to determine p_1 , used in the Monte Carlo reweighting. (Top) liquid hydrogen results (Bottom) liquid deuterium results. Horizontal error bars are not considered in the fit and represent the standard deviation of each p_T bin.

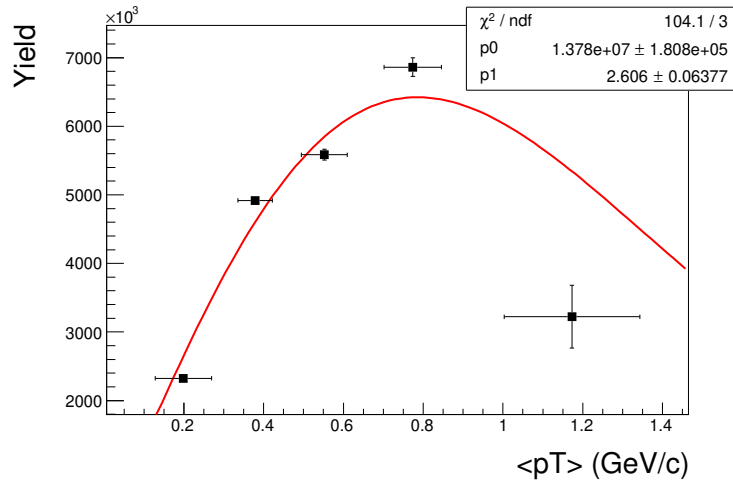
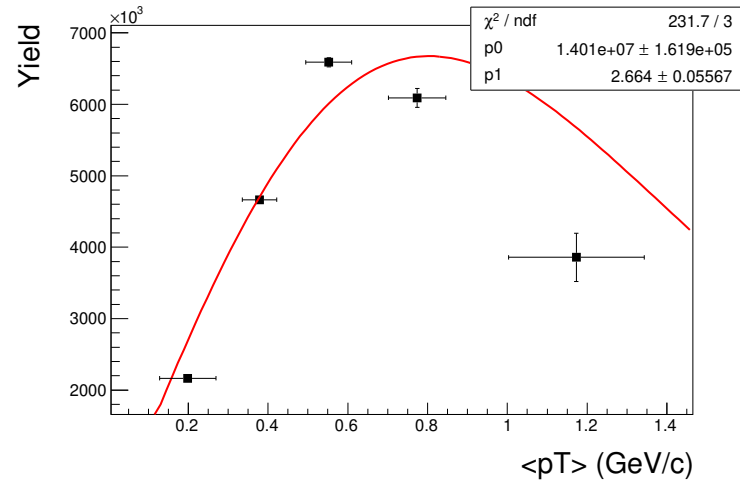
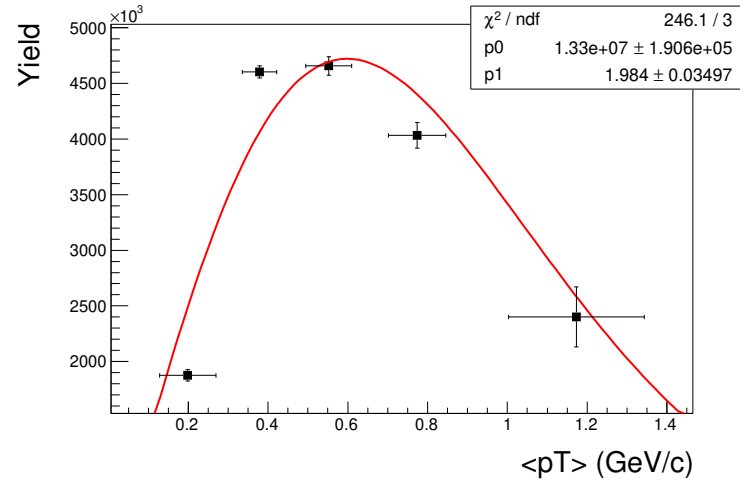


Figure A.11: Acceptance corrected Ψ' yield, fit with the Kaplan form to determine p_1 , used in the Monte Carlo reweighting. (Top) carbon results (Middle) iron results (Bottom) tungsten results. Horizontal error bars are not considered in the fit and represent the standard deviation of each p_T bin.

A.4 Acceptance Plots

The acceptance results for Drell-Yan are shown in fig. A.12, those for J/Ψ in fig. A.13, and those for Ψ' in fig. A.14.

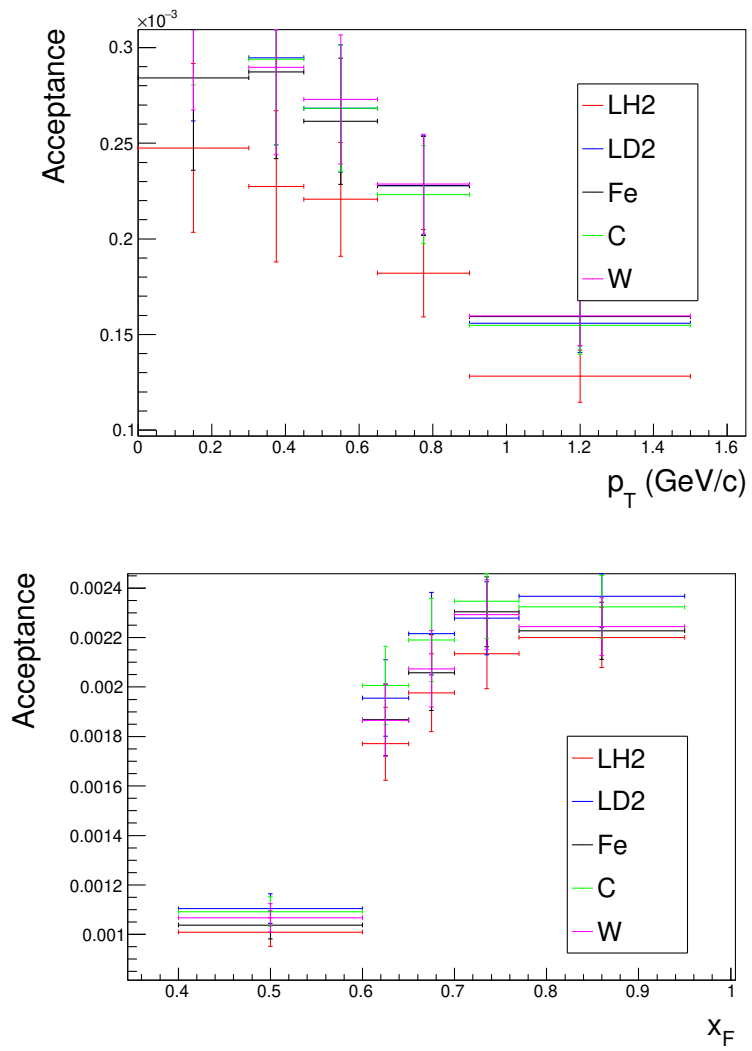


Figure A.12: (Top) Drell-Yan acceptance in p_T . (Bottom) The acceptance in x_F .

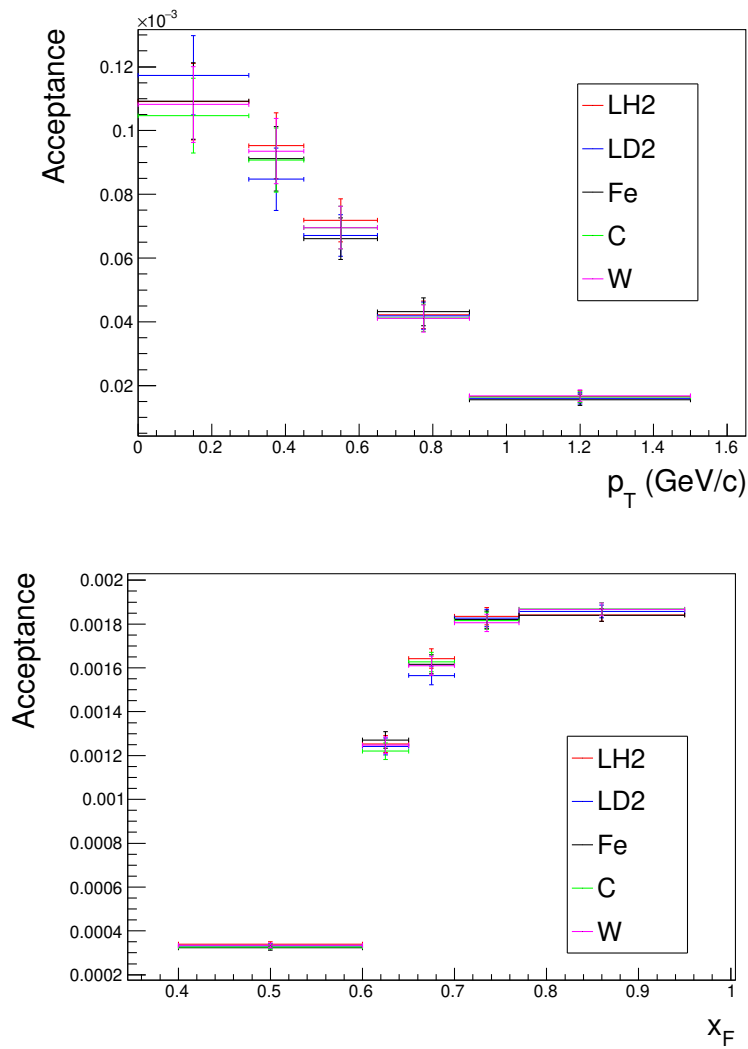


Figure A.13: (Top) J/Ψ acceptance in p_T . (Bottom) The acceptance in x_F .

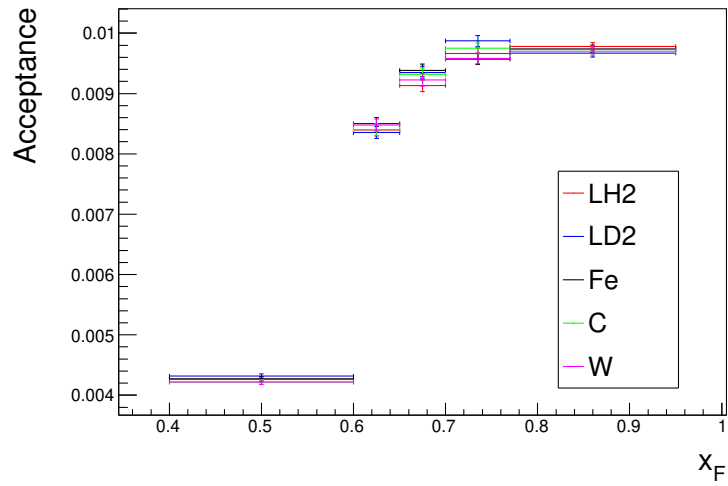
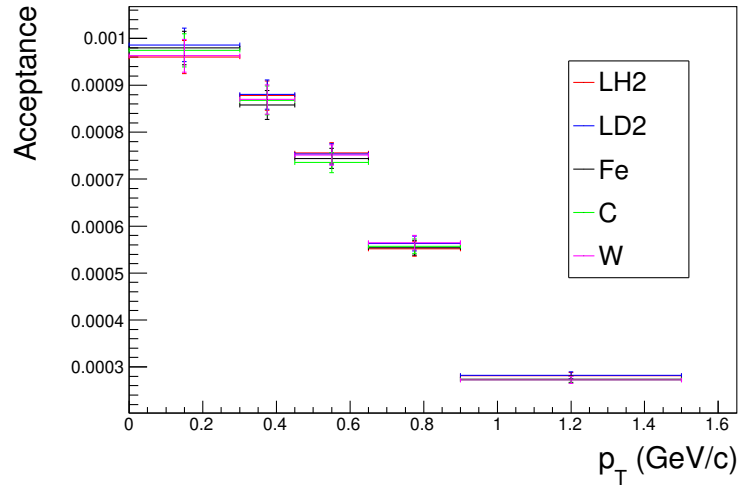


Figure A.14: (Top) Ψ' acceptance in p_T . (Bottom) The acceptance in x_F .

A.5 Unbinned Yields

The yields are determined according to sec. 4.1. The mass-fitting plots for the liquid targets are shown in fig. A.15 and for the solid targets in fig. A.16.

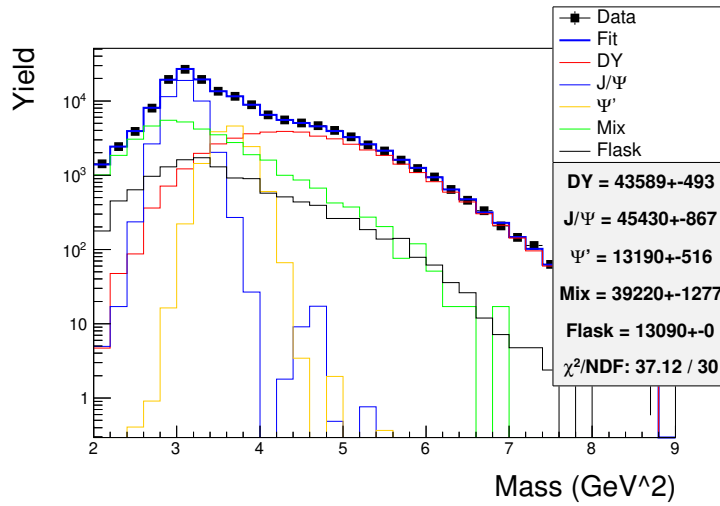
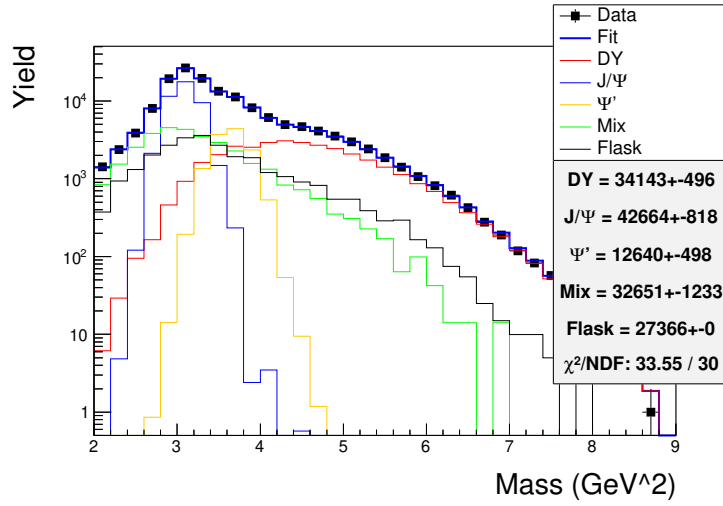


Figure A.15: Mass-fit plots and uncorrected yields for the unbinned data. (Top) hydrogen target (Bottom) deuterium target.

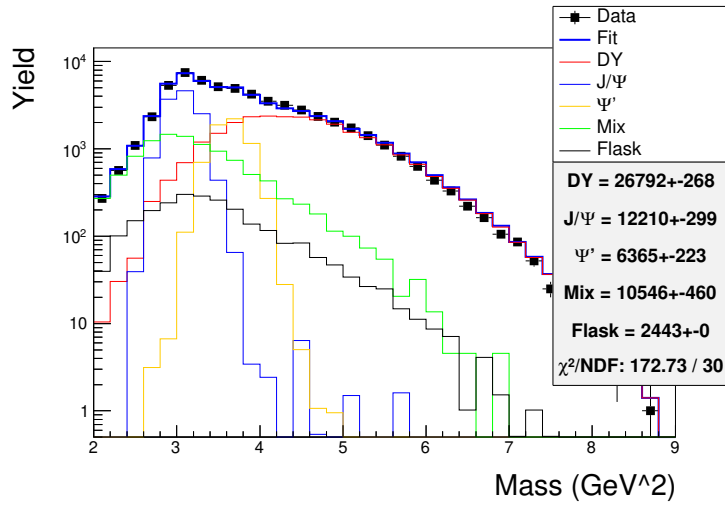
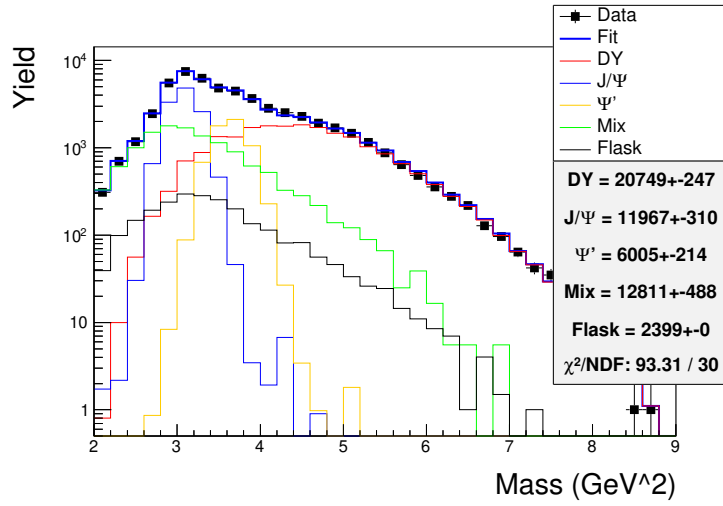
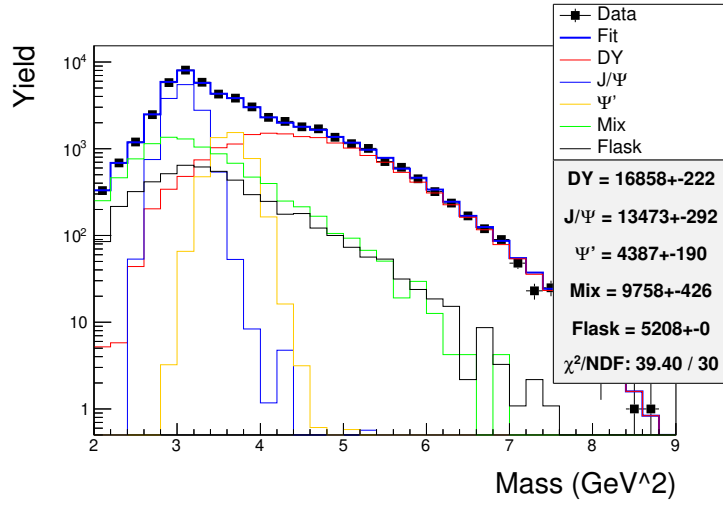


Figure A.16: Mass-fit plots and uncorrected yields for the unbinned data. (Top) carbon target (Middle) iron target (Bottom) tungsten target.

A.6 Binned Yields in p_T and x_F

The mass-fits and yields are presented in p_T bins for hydrogen in fig. A.17, for deuterium in fig. A.18, for carbon in fig. A.19, for iron in fig. A.20, and for tungsten in fig. A.21. The mass-fits and yields are presented in x_F bins for hydrogen in fig. A.22, for deuterium in fig. A.23, for carbon in fig. A.24, for iron in fig. A.25, and for tungsten in fig. A.26.

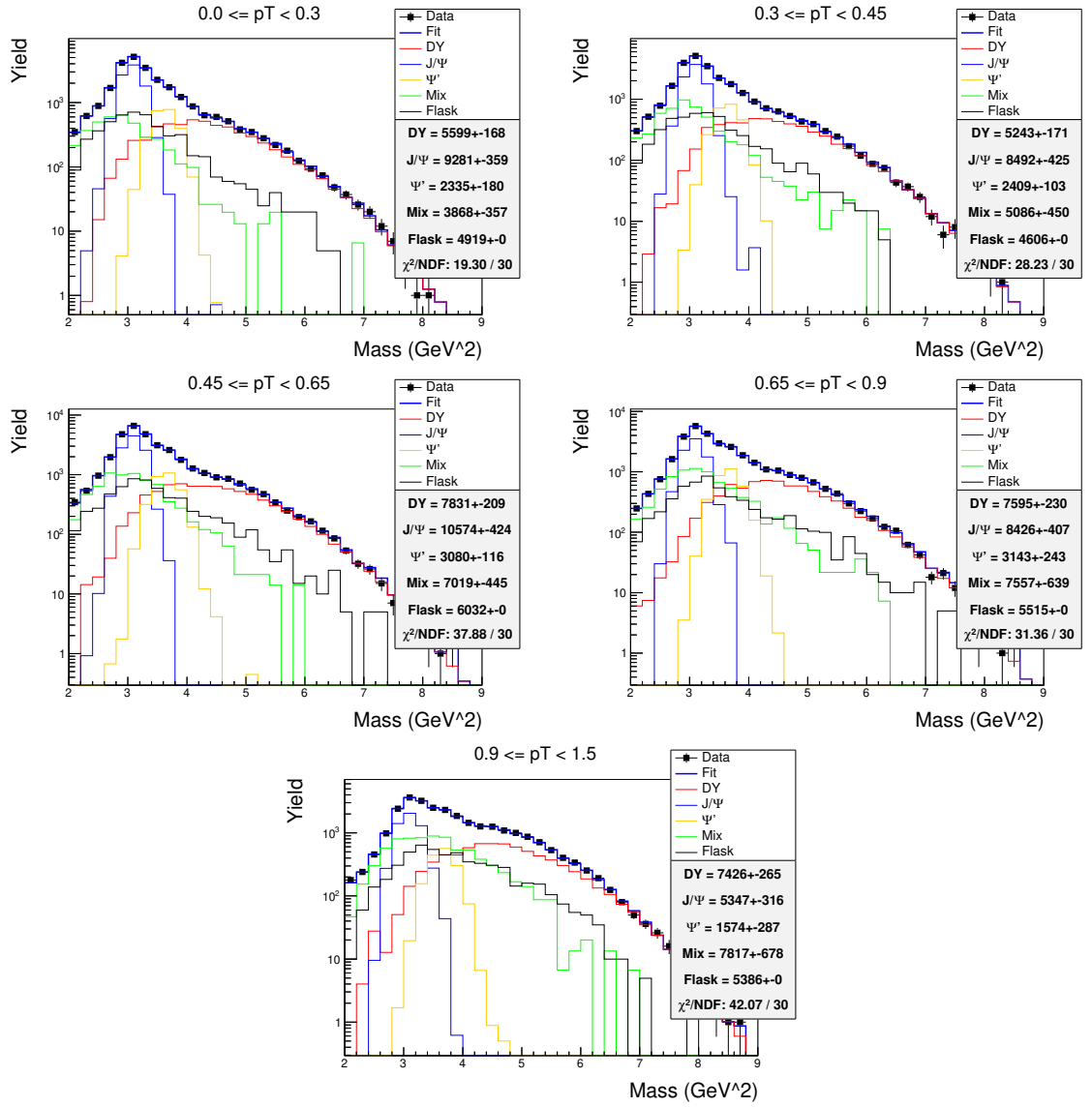


Figure A.17: Mass-fit plots for the p_T binned data, LH2 target.

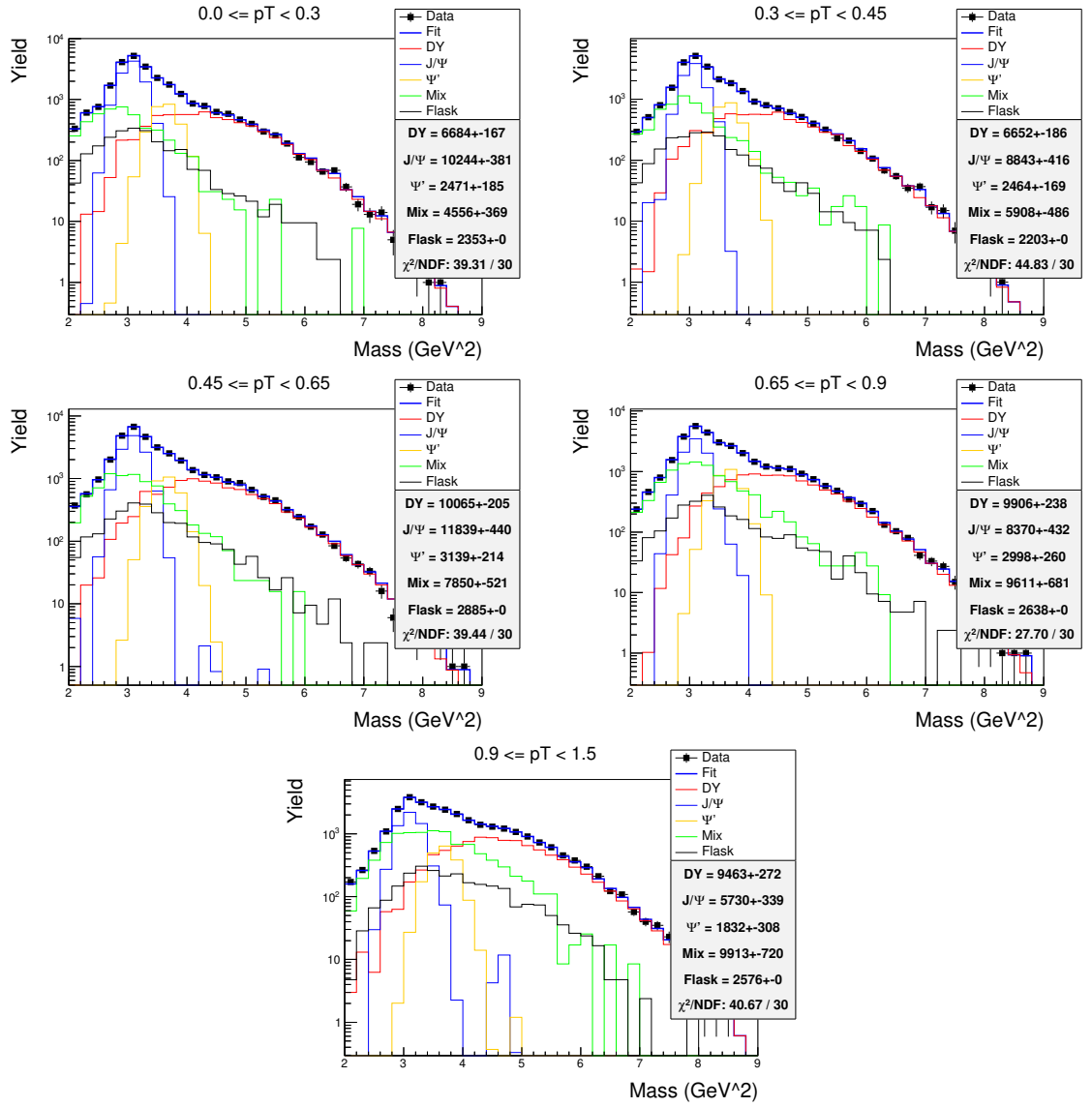


Figure A.18: Mass-fit plots for the p_T binned data, LD2 target.

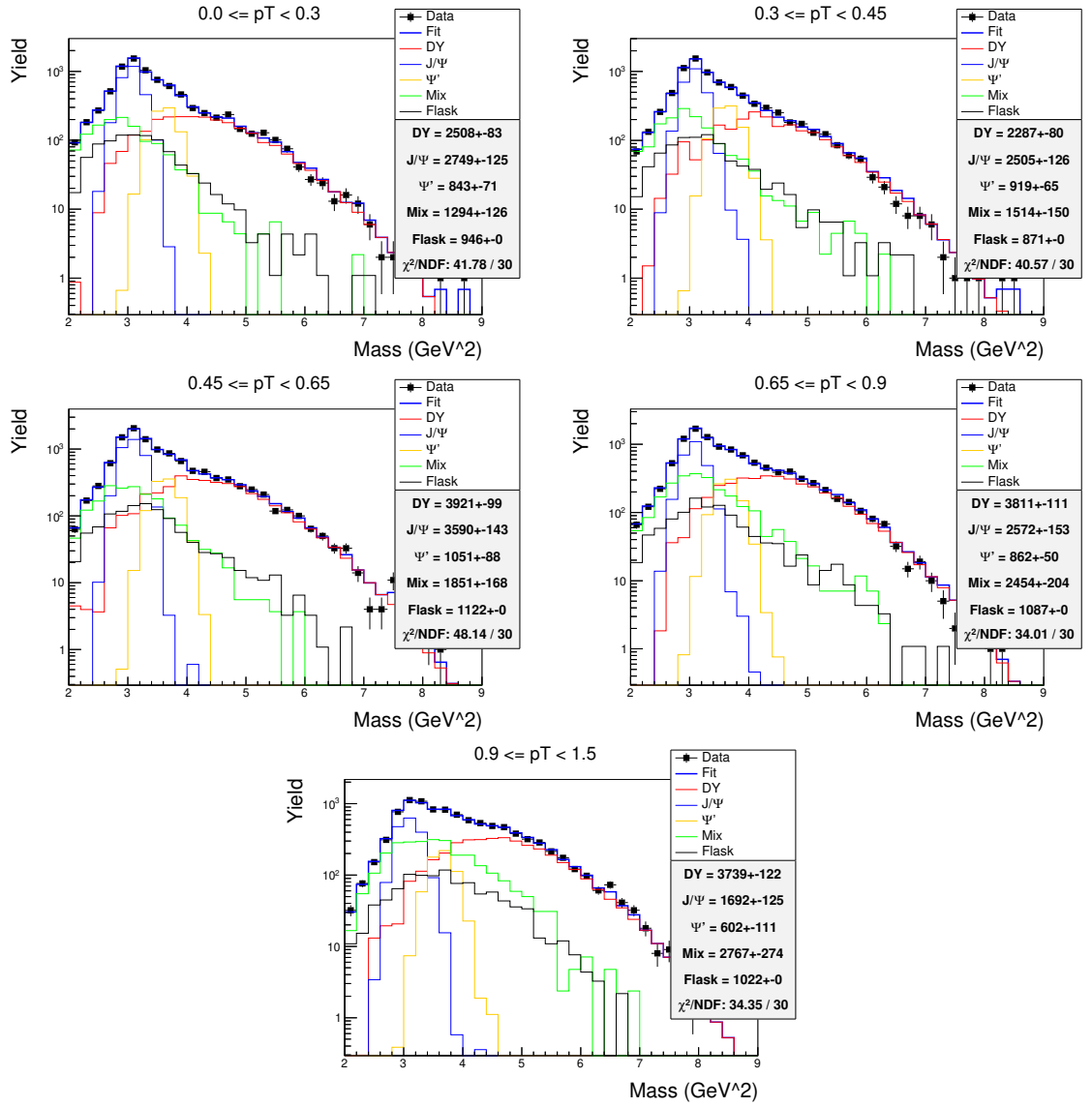


Figure A.19: Mass-fit plots for the p_T binned data, carbon target.

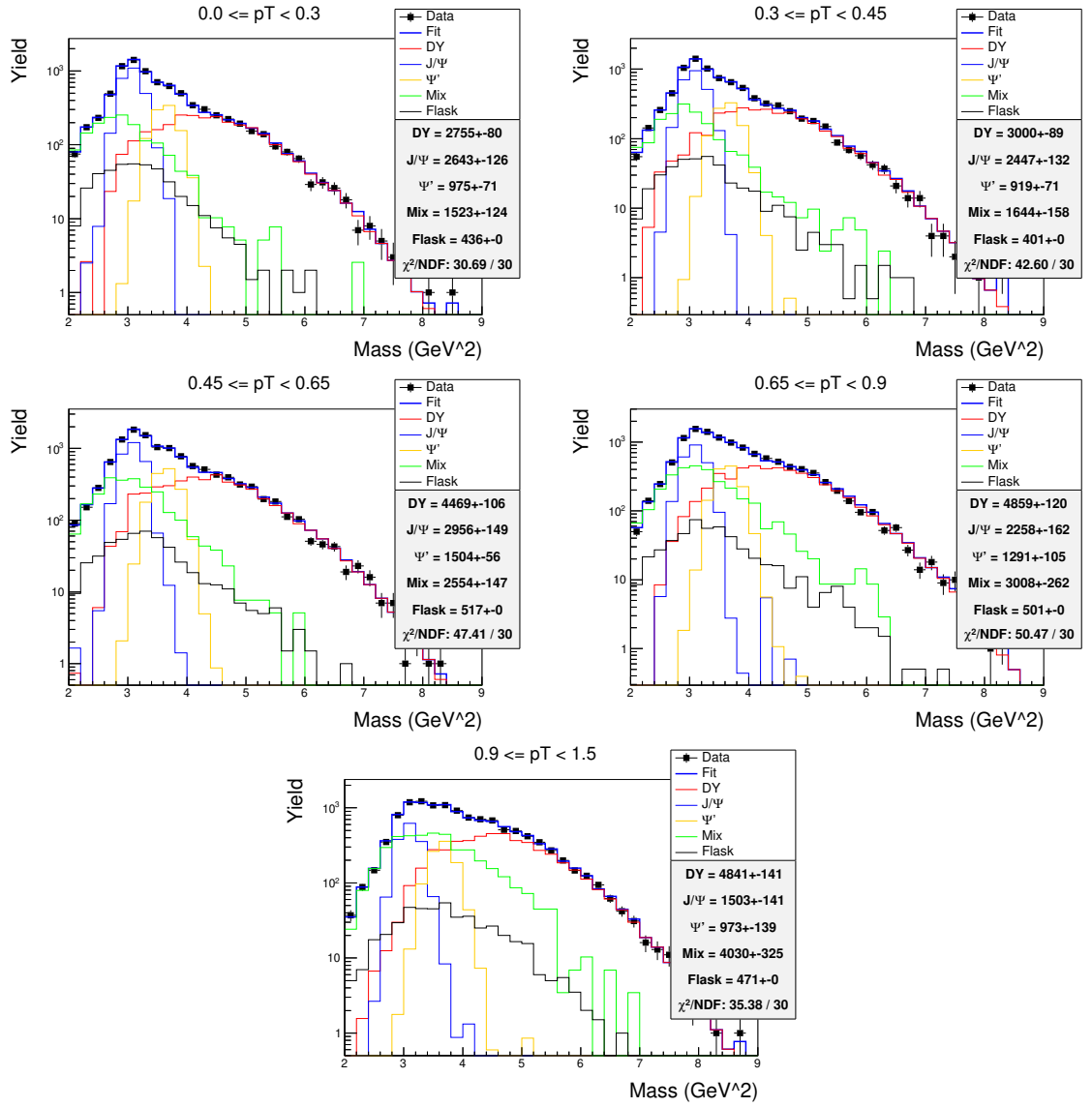


Figure A.20: Mass-fit plots for p_T binned data, iron target.

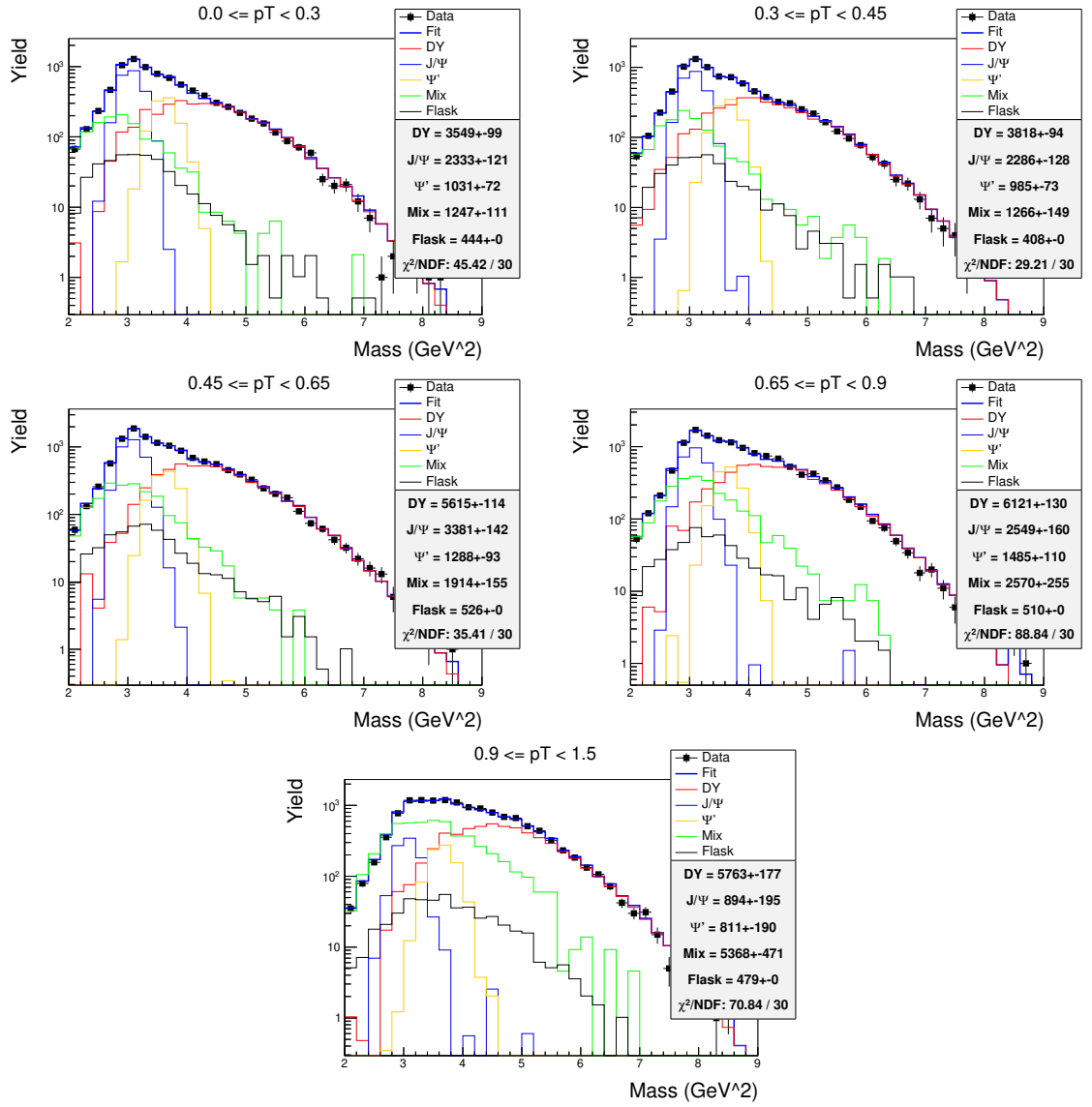


Figure A.21: Mass-fit plots for the p_T binned data, tungsten target.

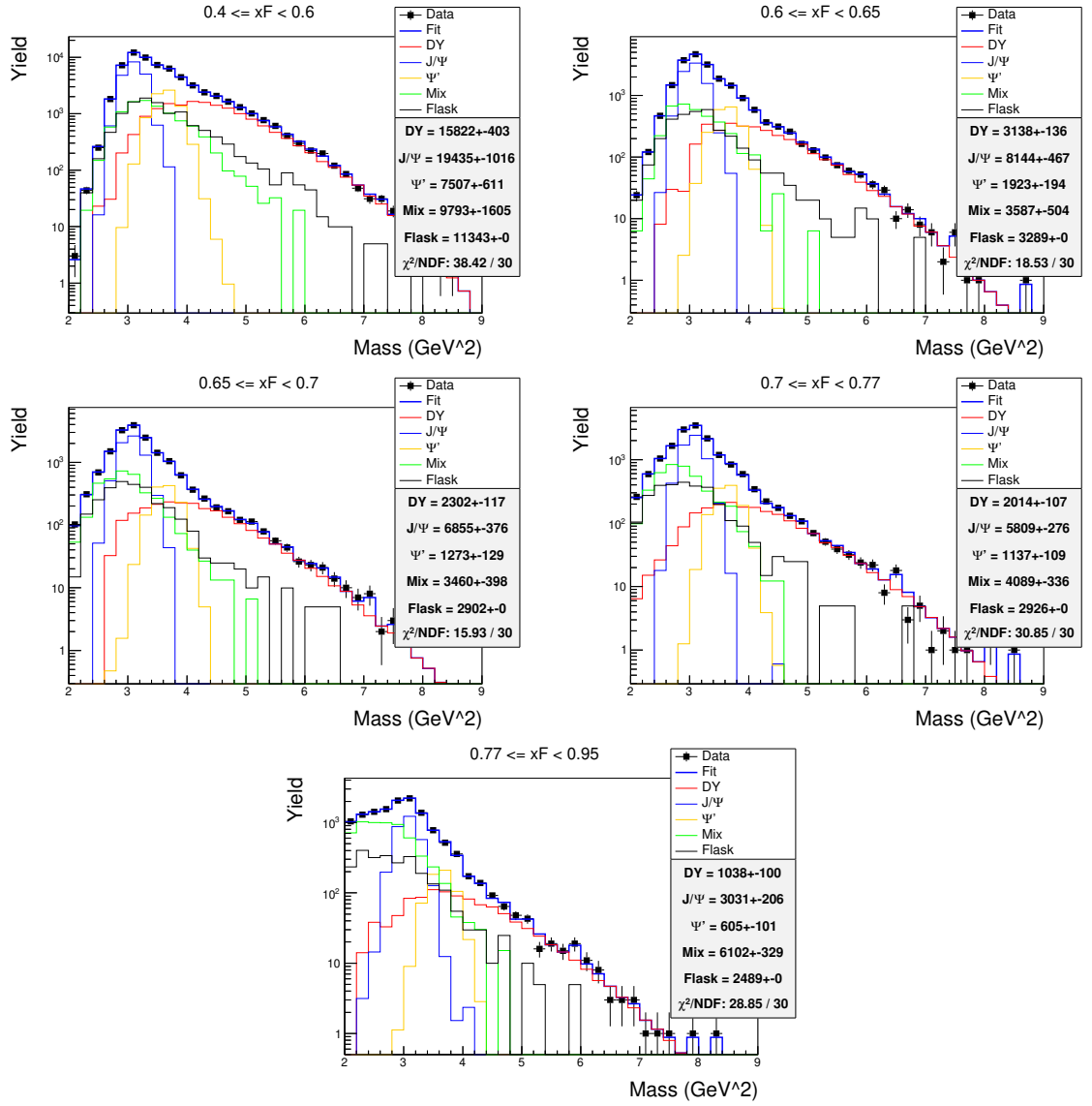


Figure A.22: Mass-fit plots for the x_F binned data, LH2 target.

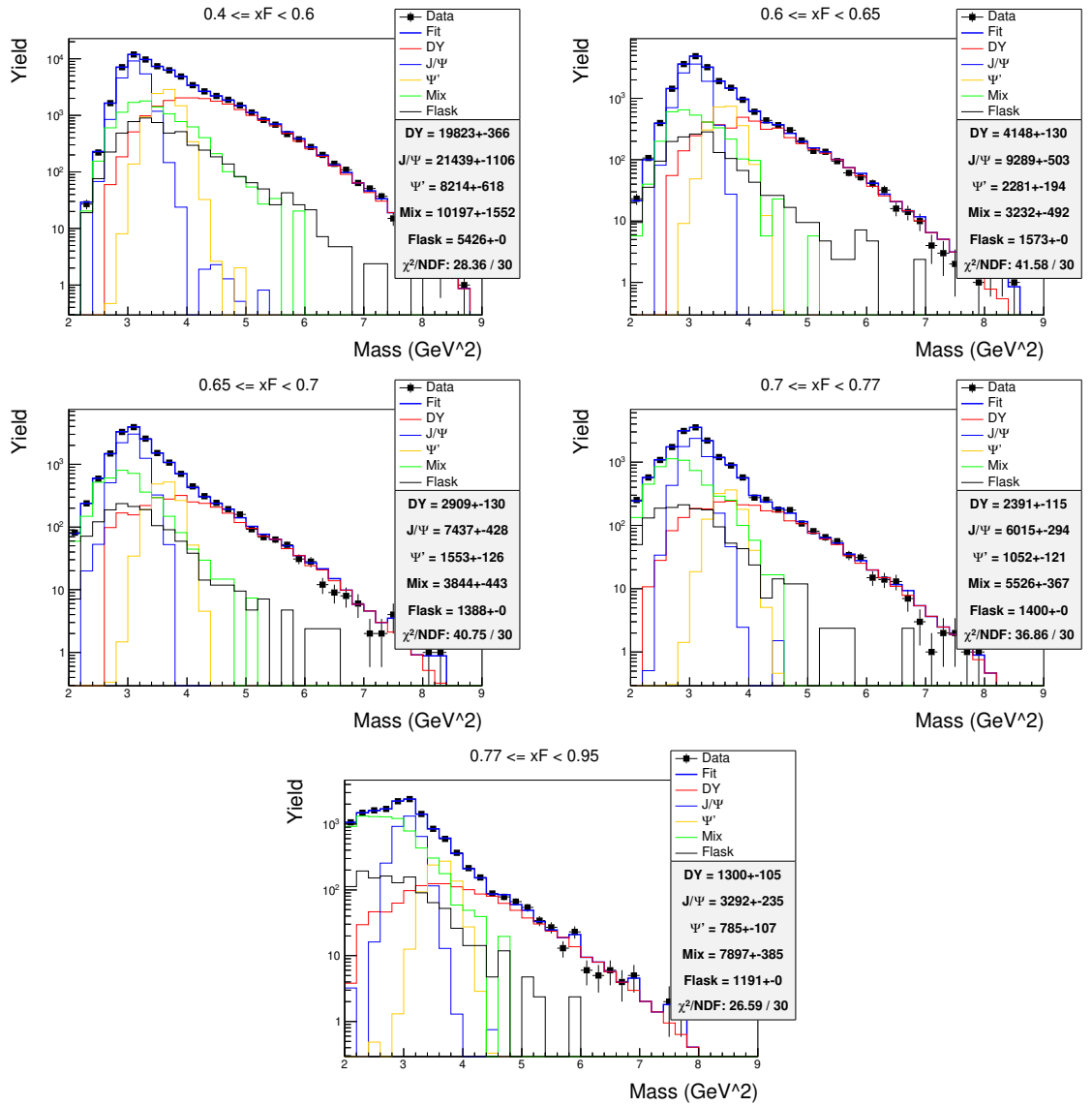


Figure A.23: Mass-fit plots for the x_F binned data, LD2 target

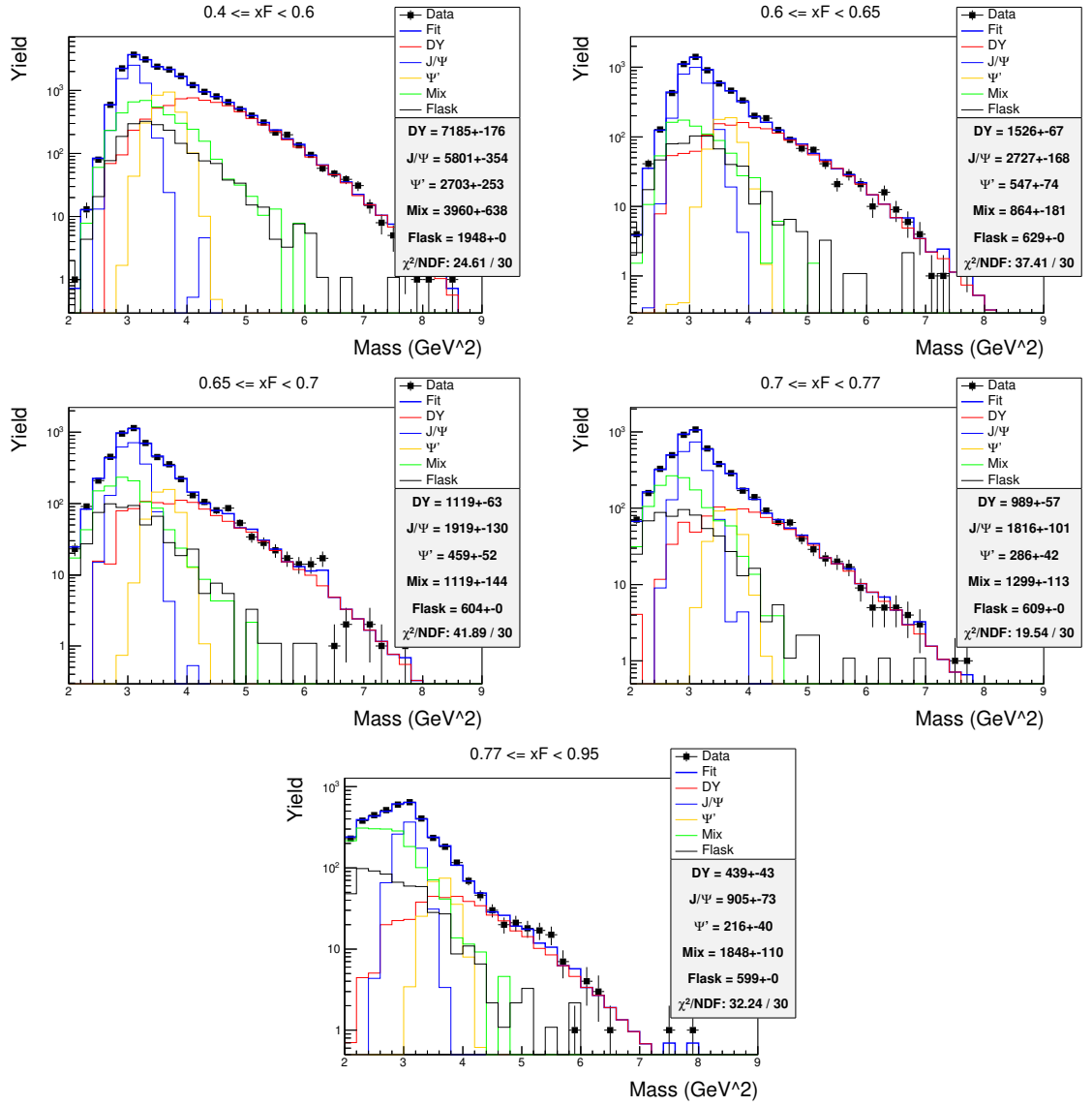


Figure A.24: Mass-fit plots for the x_F binned data, carbon target.

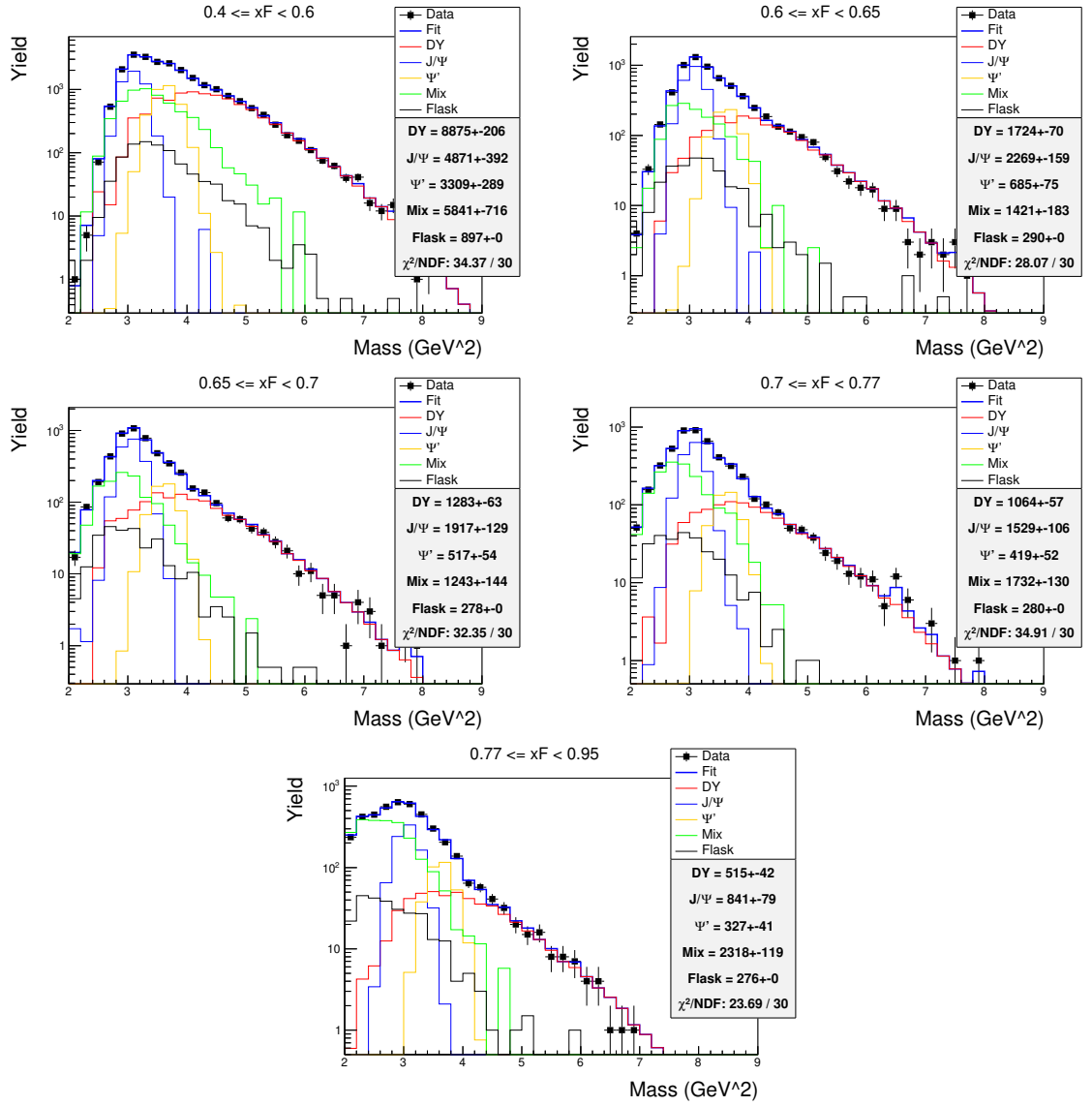


Figure A.25: Mass-fit plots for the x_F binned data, iron target.

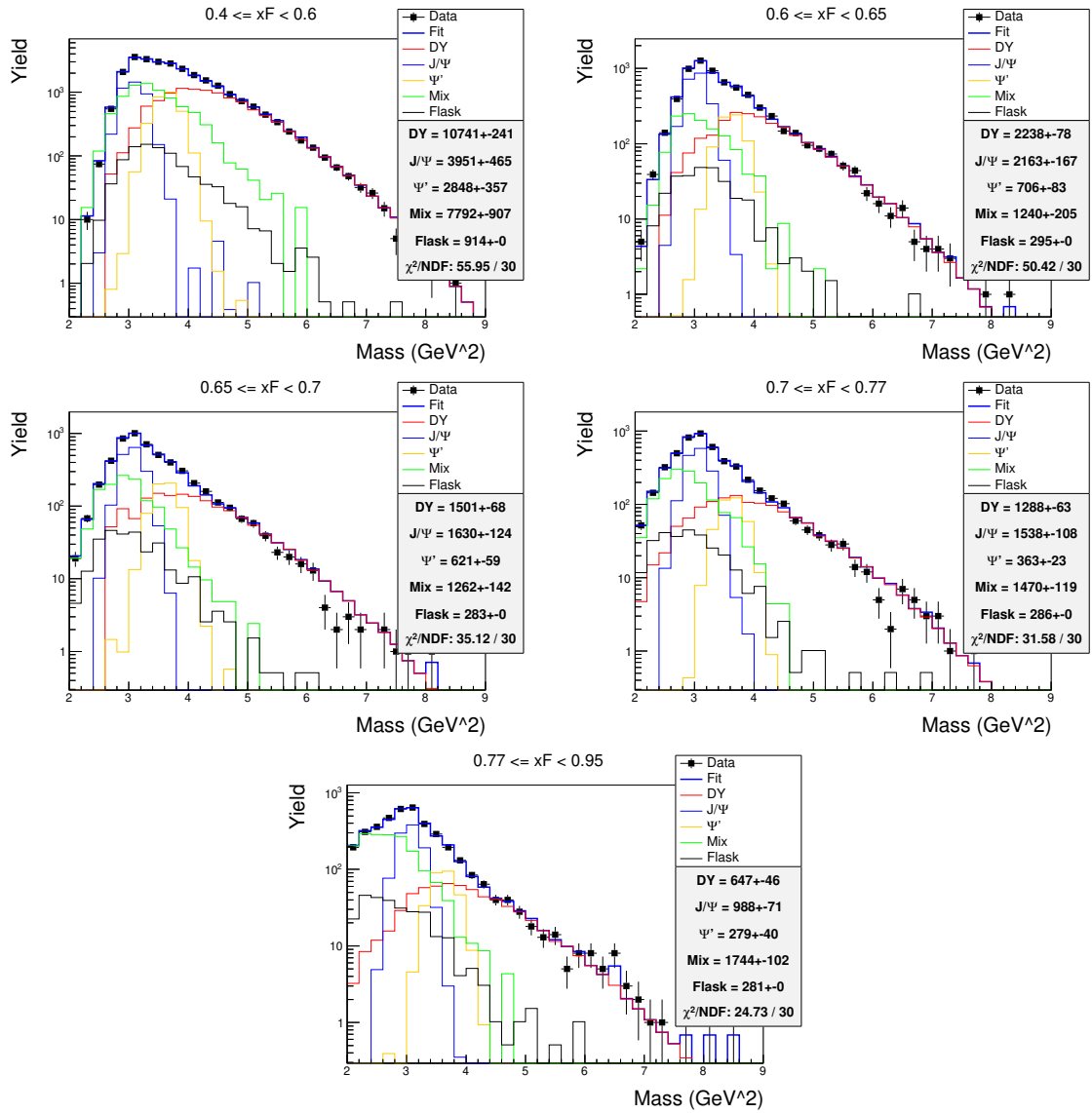


Figure A.26: Mass-fit plots for the x_F binned data, tungsten target.

A.7 Systematic Errors in Binned Fits

The systematic errors for each bin in the binned fits are presented in tables A.1 through A.36. First, the hydrogen cross section results are shown for Drell-Yan, J/Ψ , and Ψ' in x_F and p_T . Then the same order of results is shown for the deuterium cross section ratios. The errors are written as δp_{mix} , for the difference in the mixed backgrounds, δp_{trk}^+ , for evaluating the upper bound on the tracking efficiency, δp_{trk}^- , for evaluating the lower bound on the tracking efficiency, δp_{k1}^+ , for evaluating the upper bound on the Kaplan p_1 parameter, and δp_{k1}^- , for evaluating the lower bound on the Kaplan p_1 parameter. The total systematic uncertainty, δp_{tot} , is obtained by summing the uncorrelated errors in quadrature and the correlated error linearly. Hence, $\delta p_{\text{tot}} = \sqrt{(\delta p_{\text{mix}})^2 + (\delta p_{\text{trk}}^+)^2 + (\delta p_{\text{trk}}^-)^2} + |\delta p_{k1}^+| + |\delta p_{k1}^-|$, as the tracking efficiency and mixed background are independent but the reweighting is entirely correlated with each of the others.

x_F range	δp_{mix}	δp_{trk}^+	δp_{trk}^-	δp_{k1}^+	δp_{k1}^-	δ_{tot}
$0.400 \leq x_F < 0.600$	0.017	-0.000	0.000	-0.000	0.000	0.018
$0.600 \leq x_F < 0.650$	-0.024	-0.010	0.011	0.000	-0.000	0.029
$0.650 \leq x_F < 0.700$	-0.025	-0.064	0.066	0.000	-0.000	0.096
$0.700 \leq x_F < 0.770$	-0.005	0.005	-0.005	-0.000	0.000	0.009
$0.770 \leq x_F < 0.950$	-0.015	-0.042	0.044	-0.000	0.000	0.063

Table A.1: Systematic errors for each x_F bin in the Drell-Yan cross section ratio for carbon compared to the hydrogen target.

x_F range	δp_{mix}	δp_{trk}^+	δp_{trk}^-	δp_{k1}^+	δp_{k1}^-	δ_{tot}
$0.400 \leq x_F < 0.600$	-0.010	0.001	-0.001	-0.000	0.000	0.010
$0.600 \leq x_F < 0.650$	-0.004	0.006	-0.007	0.000	-0.000	0.010
$0.650 \leq x_F < 0.700$	-0.013	0.006	-0.007	0.000	-0.000	0.016
$0.700 \leq x_F < 0.770$	-0.027	0.026	-0.030	-0.000	0.000	0.048
$0.770 \leq x_F < 0.950$	-0.008	-0.002	0.002	-0.000	0.000	0.009

Table A.2: Systematic errors for each x_F bin in the Drell-Yan cross section ratio for iron compared to the hydrogen target.

x_F range	δp_{mix}	δp_{trk}^+	δp_{trk}^-	δp_{k1}^+	δp_{k1}^-	δ_{tot}
$0.400 \leq x_F < 0.600$	-0.025	-0.005	0.005	0.000	-0.000	0.026
$0.600 \leq x_F < 0.650$	-0.017	-0.010	0.011	0.000	-0.000	0.023
$0.650 \leq x_F < 0.700$	-0.019	-0.017	0.019	-0.000	0.000	0.032
$0.700 \leq x_F < 0.770$	-0.022	-0.003	0.003	-0.000	0.000	0.023
$0.770 \leq x_F < 0.950$	-0.050	-0.003	0.003	-0.000	0.000	0.051

Table A.3: Systematic errors for each x_F bin in the Drell-Yan cross section ratio for tungsten compared to the hydrogen target.

x_F range	δp_{mix}	δp_{trk}^+	δp_{trk}^-	δp_{k1}^+	δp_{k1}^-	δ_{tot}
$0.400 \leq x_F < 0.600$	0.026	-0.008	0.009	-0.001	0.001	0.029
$0.600 \leq x_F < 0.650$	0.033	-0.009	0.010	0.002	-0.002	0.038
$0.650 \leq x_F < 0.700$	-0.019	-0.004	0.005	0.000	-0.000	0.020
$0.700 \leq x_F < 0.770$	0.006	-0.001	0.001	0.000	-0.000	0.007
$0.770 \leq x_F < 0.950$	-0.005	0.027	-0.030	-0.000	0.000	0.041

Table A.4: Systematic errors for each x_F bin in the J/Ψ cross section ratio for carbon compared to the hydrogen target.

x_F range	δp_{mix}	δp_{trk}^+	δp_{trk}^-	δp_{k1}^+	δp_{k1}^-	δ_{tot}
$0.400 \leq x_F < 0.600$	-0.033	-0.004	0.005	-0.000	0.000	0.034
$0.600 \leq x_F < 0.650$	0.023	-0.010	0.012	0.000	-0.001	0.029
$0.650 \leq x_F < 0.700$	-0.003	-0.040	0.041	0.000	-0.000	0.059
$0.700 \leq x_F < 0.770$	-0.021	-0.004	0.004	0.000	-0.000	0.022
$0.770 \leq x_F < 0.950$	-0.038	-0.000	0.000	0.000	-0.000	0.038

Table A.5: Systematic errors for each x_F bin in the J/Ψ cross section ratio for iron compared to the hydrogen target.

x_F range	δp_{mix}	δp_{trk}^+	δp_{trk}^-	δp_{k1}^+	δp_{k1}^-	δ_{tot}
$0.400 \leq x_F < 0.600$	-0.072	-0.003	0.004	0.000	-0.000	0.073
$0.600 \leq x_F < 0.650$	0.026	-0.008	0.009	0.000	-0.000	0.029
$0.650 \leq x_F < 0.700$	-0.009	-0.005	0.006	-0.000	0.000	0.012
$0.700 \leq x_F < 0.770$	-0.002	-0.005	0.006	0.000	-0.000	0.009
$0.770 \leq x_F < 0.950$	-0.008	0.019	-0.021	-0.000	0.000	0.029

Table A.6: Systematic errors for each x_F bin in the J/Ψ cross section ratio for tungsten compared to the hydrogen target.

x_F range	δp_{mix}	δp_{trk}^+	δp_{trk}^-	δp_{k1}^+	δp_{k1}^-	δ_{tot}
$0.400 \leq x_F < 0.600$	0.059	-0.001	0.001	-0.000	0.000	0.059
$0.600 \leq x_F < 0.650$	0.025	0.000	-0.000	0.000	-0.000	0.026
$0.650 \leq x_F < 0.700$	-0.014	-0.003	0.003	-0.000	0.000	0.016
$0.700 \leq x_F < 0.770$	-0.018	-0.001	0.001	-0.000	0.000	0.018
$0.770 \leq x_F < 0.950$	-0.005	-0.001	0.001	0.000	-0.000	0.005

Table A.7: Systematic errors for each x_F bin in the Ψ' cross section ratio for carbon compared to the hydrogen target.

x_F range	δp_{mix}	δp_{trk}^+	δp_{trk}^-	δp_{k1}^+	δp_{k1}^-	δ_{tot}
$0.400 \leq x_F < 0.600$	-0.016	-0.000	0.000	-0.001	0.001	0.019
$0.600 \leq x_F < 0.650$	0.044	0.003	-0.003	0.000	-0.000	0.045
$0.650 \leq x_F < 0.700$	0.009	-0.003	0.003	-0.001	0.002	0.013
$0.700 \leq x_F < 0.770$	-0.005	0.001	-0.001	-0.000	0.000	0.005
$0.770 \leq x_F < 0.950$	-0.070	0.001	-0.001	0.000	-0.000	0.071

Table A.8: Systematic errors for each x_F bin in the Ψ' cross section ratio for iron compared to the hydrogen target.

x_F range	δp_{mix}	δp_{trk}^+	δp_{trk}^-	δp_{k1}^+	δp_{k1}^-	δ_{tot}
$0.400 \leq x_F < 0.600$	-0.083	-0.002	0.002	0.000	-0.000	0.083
$0.600 \leq x_F < 0.650$	0.035	0.001	-0.001	-0.001	0.001	0.037
$0.650 \leq x_F < 0.700$	0.003	-0.004	0.005	-0.001	0.001	0.009
$0.700 \leq x_F < 0.770$	0.000	-0.001	0.002	-0.000	0.000	0.003
$0.770 \leq x_F < 0.950$	-0.047	-0.001	0.001	0.001	-0.001	0.048

Table A.9: Systematic errors for each x_F bin in the Ψ' cross section ratio for tungsten compared to the hydrogen target.

x_F range	δp_{mix}	δp_{trk}^+	δp_{trk}^-	δp_{k1}^+	δp_{k1}^-	δ_{tot}
$0.400 \leq x_F < 0.600$	0.009	-0.007	0.007	-0.000	0.000	0.014
$0.600 \leq x_F < 0.650$	-0.015	-0.011	0.013	0.000	-0.000	0.023
$0.650 \leq x_F < 0.700$	-0.002	0.001	-0.002	-0.000	0.000	0.003
$0.700 \leq x_F < 0.770$	0.009	0.038	-0.042	-0.000	0.000	0.057
$0.770 \leq x_F < 0.950$	0.043	0.002	-0.002	-0.000	0.000	0.044

Table A.10: Systematic errors for each x_F bin in the Drell-Yan cross section ratio for carbon compared to the deuterium target.

x_F range	δp_{mix}	δp_{trk}^+	δp_{trk}^-	δp_{k1}^+	δp_{k1}^-	δ_{tot}
$0.400 \leq x_F < 0.600$	-0.015	-0.007	0.008	-0.000	0.000	0.019
$0.600 \leq x_F < 0.650$	0.002	0.002	-0.002	0.000	-0.000	0.004
$0.650 \leq x_F < 0.700$	0.011	0.069	-0.081	-0.000	0.000	0.107
$0.700 \leq x_F < 0.770$	-0.011	0.058	-0.068	0.000	-0.000	0.090
$0.770 \leq x_F < 0.950$	0.056	0.040	-0.045	-0.000	0.000	0.082

Table A.11: Systematic errors for each x_F bin in the Drell-Yan cross section ratio for iron compared to the deuterium target.

x_F range	δp_{mix}	δp_{trk}^+	δp_{trk}^-	δp_{k1}^+	δp_{k1}^-	δ_{tot}
$0.400 \leq x_F < 0.600$	-0.028	-0.011	0.012	-0.000	0.000	0.033
$0.600 \leq x_F < 0.650$	-0.009	-0.011	0.013	-0.000	-0.000	0.019
$0.650 \leq x_F < 0.700$	0.004	0.043	-0.049	-0.000	0.000	0.066
$0.700 \leq x_F < 0.770$	-0.007	0.031	-0.035	0.000	-0.000	0.047
$0.770 \leq x_F < 0.950$	0.021	0.039	-0.043	-0.000	0.000	0.062

Table A.12: Systematic errors for each x_F bin in the Drell-Yan cross section ratio for tungsten compared to the deuterium target.

x_F range	δp_{mix}	δp_{trk}^+	δp_{trk}^-	δp_{k1}^+	δp_{k1}^-	δ_{tot}
$0.400 \leq x_F < 0.600$	0.013	-0.008	0.009	-0.001	0.001	0.019
$0.600 \leq x_F < 0.650$	0.012	0.003	-0.004	0.001	-0.001	0.015
$0.650 \leq x_F < 0.700$	-0.012	-0.006	0.006	-0.000	0.000	0.015
$0.700 \leq x_F < 0.770$	0.011	-0.001	0.001	0.000	-0.000	0.012
$0.770 \leq x_F < 0.950$	0.004	0.025	-0.027	-0.000	0.000	0.037

Table A.13: Systematic errors for each x_F bin in the J/Ψ cross section ratio for carbon compared to the deuterium target.

x_F range	δp_{mix}	δp_{trk}^+	δp_{trk}^-	δp_{k1}^+	δp_{k1}^-	δ_{tot}
$0.400 \leq x_F < 0.600$	-0.035	-0.004	0.005	-0.001	0.001	0.037
$0.600 \leq x_F < 0.650$	0.007	-0.001	0.002	0.000	-0.000	0.008
$0.650 \leq x_F < 0.700$	0.001	-0.036	0.037	0.000	-0.000	0.052
$0.700 \leq x_F < 0.770$	-0.016	-0.004	0.005	0.001	-0.001	0.018
$0.770 \leq x_F < 0.950$	-0.027	-0.000	0.000	-0.000	0.000	0.027

Table A.14: Systematic errors for each x_F bin in the J/Ψ cross section ratio for iron compared to the deuterium target.

x_F range	δp_{mix}	δp_{trk}^+	δp_{trk}^-	δp_{k1}^+	δp_{k1}^-	δ_{tot}
$0.400 \leq x_F < 0.600$	-0.066	-0.003	0.004	0.000	-0.000	0.066
$0.600 \leq x_F < 0.650$	0.013	-0.001	0.001	-0.000	0.000	0.013
$0.650 \leq x_F < 0.700$	-0.005	-0.006	0.006	-0.000	0.000	0.010
$0.700 \leq x_F < 0.770$	0.001	-0.005	0.006	0.000	-0.000	0.009
$0.770 \leq x_F < 0.950$	-0.001	0.017	-0.019	-0.000	0.000	0.026

Table A.15: Systematic errors for each x_F bin in the J/Ψ cross section ratio for tungsten compared to the deuterium target.

x_F range	δp_{mix}	δp_{trk}^+	δp_{trk}^-	δp_{k1}^+	δp_{k1}^-	δ_{tot}
$0.400 \leq x_F < 0.600$	0.040	-0.001	0.001	-0.001	0.001	0.042
$0.600 \leq x_F < 0.650$	0.010	-0.002	0.002	0.001	-0.001	0.012
$0.650 \leq x_F < 0.700$	-0.013	-0.001	0.001	0.001	-0.001	0.015
$0.700 \leq x_F < 0.770$	0.009	-0.002	0.002	-0.001	0.001	0.011
$0.770 \leq x_F < 0.950$	-0.042	-0.002	0.002	-0.000	0.000	0.042

Table A.16: Systematic errors for each x_F bin in the Ψ' cross section ratio for carbon compared to the deuterium target.

x_F range	δp_{mix}	δp_{trk}^+	δp_{trk}^-	δp_{k1}^+	δp_{k1}^-	δ_{tot}
$0.400 \leq x_F < 0.600$	-0.033	-0.001	0.001	-0.002	0.002	0.038
$0.600 \leq x_F < 0.650$	0.025	0.000	-0.000	0.001	-0.001	0.027
$0.650 \leq x_F < 0.700$	0.006	-0.001	0.001	-0.000	0.000	0.006
$0.700 \leq x_F < 0.770$	0.033	0.000	-0.000	-0.000	0.000	0.033
$0.770 \leq x_F < 0.950$	-0.109	-0.001	0.001	-0.000	0.000	0.109

Table A.17: Systematic errors for each x_F bin in the Ψ' cross section ratio for iron compared to the deuterium target.

x_F range	δp_{mix}	δp_{trk}^+	δp_{trk}^-	δp_{k1}^+	δp_{k1}^-	δ_{tot}
$0.400 \leq x_F < 0.600$	-0.091	-0.002	0.002	-0.001	0.001	0.092
$0.600 \leq x_F < 0.650$	0.019	-0.001	0.001	-0.000	0.000	0.020
$0.650 \leq x_F < 0.700$	0.001	-0.002	0.002	0.000	-0.000	0.004
$0.700 \leq x_F < 0.770$	0.026	-0.002	0.002	-0.000	0.000	0.026
$0.770 \leq x_F < 0.950$	-0.073	-0.002	0.002	0.000	-0.000	0.073

Table A.18: Systematic errors for each x_F bin in the Ψ' cross section ratio for tungsten compared to the deuterium target.

p_T range	δp_{mix}	δp_{trk}^+	δp_{trk}^-	δp_{k1}^+	δp_{k1}^-	δ_{tot}
$0.000 \leq p_T < 0.300$	-0.002	0.017	-0.019	0.000	-0.000	0.026
$0.300 \leq p_T < 0.450$	0.004	-0.009	0.010	-0.000	0.000	0.014
$0.450 \leq p_T < 0.650$	0.005	-0.003	0.003	0.000	-0.000	0.006
$0.650 \leq p_T < 0.900$	0.005	-0.001	0.001	-0.000	0.000	0.006
$0.900 \leq p_T < 1.500$	-0.015	-0.004	0.004	0.000	-0.000	0.017

Table A.19: Systematic errors for each p_T bin in the Drell-Yan cross section ratio for carbon compared to the hydrogen target.

p_T range	δp_{mix}	δp_{trk}^+	δp_{trk}^-	δp_{k1}^+	δp_{k1}^-	δ_{tot}
$0.000 \leq p_T < 0.300$	0.002	0.023	-0.027	-0.000	0.000	0.035
$0.300 \leq p_T < 0.450$	0.008	-0.005	0.006	0.000	-0.000	0.011
$0.450 \leq p_T < 0.650$	-0.001	-0.003	0.003	-0.000	0.000	0.004
$0.650 \leq p_T < 0.900$	0.012	0.005	-0.005	0.000	-0.000	0.015
$0.900 \leq p_T < 1.500$	-0.029	-0.002	0.002	-0.000	0.000	0.029

Table A.20: Systematic errors for each p_T bin in the Drell-Yan cross section ratio for iron compared to the hydrogen target.

p_T range	δp_{mix}	δp_{trk}^+	δp_{trk}^-	δp_{k1}^+	δp_{k1}^-	δ_{tot}
$0.000 \leq p_T < 0.300$	-0.001	-0.002	0.002	-0.000	-0.000	0.003
$0.300 \leq p_T < 0.450$	0.017	-0.017	0.019	0.000	-0.000	0.031
$0.450 \leq p_T < 0.650$	0.009	-0.003	0.004	-0.000	-0.000	0.010
$0.650 \leq p_T < 0.900$	0.020	0.005	-0.005	0.000	-0.000	0.021
$0.900 \leq p_T < 1.500$	-0.086	-0.004	0.005	0.000	-0.000	0.086

Table A.21: Systematic errors for each p_T bin in the Drell-Yan cross section ratio for tungsten compared to the hydrogen target.

p_T range	δp_{mix}	δp_{trk}^+	δp_{trk}^-	δp_{k1}^+	δp_{k1}^-	δ_{tot}
$0.000 \leq p_T < 0.300$	-0.002	-0.021	0.026	0.000	-0.000	0.034
$0.300 \leq p_T < 0.450$	0.010	0.002	-0.003	0.000	-0.000	0.011
$0.450 \leq p_T < 0.650$	0.008	-0.004	0.005	-0.000	0.000	0.010
$0.650 \leq p_T < 0.900$	-0.020	-0.004	0.005	-0.000	0.000	0.022
$0.900 \leq p_T < 1.500$	-0.041	0.014	-0.017	0.001	-0.001	0.049

Table A.22: Systematic errors for each p_T bin in the J/Ψ cross section ratio for carbon compared to the hydrogen target.

p_T range	δp_{mix}	δp_{trk}^+	δp_{trk}^-	δp_{k1}^+	δp_{k1}^-	δ_{tot}
$0.000 \leq p_T < 0.300$	-0.013	-0.038	0.043	0.000	-0.000	0.059
$0.300 \leq p_T < 0.450$	0.001	-0.002	0.003	0.000	-0.000	0.004
$0.450 \leq p_T < 0.650$	-0.010	0.003	-0.004	0.000	-0.000	0.011
$0.650 \leq p_T < 0.900$	-0.025	-0.022	0.025	-0.001	0.001	0.043
$0.900 \leq p_T < 1.500$	-0.096	0.015	-0.019	0.000	-0.000	0.099

Table A.23: Systematic errors for each p_T bin in the J/Ψ cross section ratio for iron compared to the hydrogen target.

p_T range	δp_{mix}	δp_{trk}^+	δp_{trk}^-	δp_{k1}^+	δp_{k1}^-	δ_{tot}
$0.000 \leq p_T < 0.300$	-0.007	-0.018	0.021	0.000	-0.000	0.029
$0.300 \leq p_T < 0.450$	0.005	-0.005	0.006	0.000	-0.000	0.010
$0.450 \leq p_T < 0.650$	0.005	0.002	-0.003	-0.000	0.000	0.006
$0.650 \leq p_T < 0.900$	-0.013	-0.003	0.003	0.000	-0.000	0.014
$0.900 \leq p_T < 1.500$	-0.237	-0.002	0.003	0.001	-0.001	0.238

Table A.24: Systematic errors for each p_T bin in the J/Ψ cross section ratio for tungsten compared to the hydrogen target.

p_T range	δp_{mix}	δp_{trk}^+	δp_{trk}^-	δp_{k1}^+	δp_{k1}^-	δ_{tot}
$0.000 \leq p_T < 0.300$	0.006	0.004	-0.004	0.000	-0.000	0.009
$0.300 \leq p_T < 0.450$	0.009	0.011	-0.012	-0.000	0.000	0.019
$0.450 \leq p_T < 0.650$	0.013	0.006	-0.006	0.000	-0.000	0.016
$0.650 \leq p_T < 0.900$	-0.014	-0.004	0.004	-0.000	0.000	0.016
$0.900 \leq p_T < 1.500$	-0.023	-0.002	0.002	0.000	-0.000	0.024

Table A.25: Systematic errors for each p_T bin in the Ψ' cross section ratio for carbon compared to the hydrogen target.

p_T range	δp_{mix}	δp_{trk}^+	δp_{trk}^-	δp_{k1}^+	δp_{k1}^-	δ_{tot}
$0.000 \leq p_T < 0.300$	0.003	-0.002	0.002	0.000	-0.000	0.005
$0.300 \leq p_T < 0.450$	0.012	0.008	-0.008	-0.000	0.000	0.017
$0.450 \leq p_T < 0.650$	0.023	0.007	-0.007	0.000	-0.000	0.026
$0.650 \leq p_T < 0.900$	0.004	-0.003	0.004	-0.000	0.000	0.007
$0.900 \leq p_T < 1.500$	-0.016	-0.004	0.005	-0.001	0.001	0.018

Table A.26: Systematic errors for each p_T bin in the Ψ' cross section ratio for iron compared to the hydrogen target.

p_T range	δp_{mix}	δp_{trk}^+	δp_{trk}^-	δp_{k1}^+	δp_{k1}^-	δ_{tot}
$0.000 \leq p_T < 0.300$	-0.001	-0.010	0.011	0.000	-0.000	0.015
$0.300 \leq p_T < 0.450$	0.004	0.001	-0.001	-0.000	0.000	0.004
$0.450 \leq p_T < 0.650$	0.018	-0.001	0.002	0.000	-0.000	0.018
$0.650 \leq p_T < 0.900$	0.007	-0.006	0.006	-0.000	0.000	0.011
$0.900 \leq p_T < 1.500$	-0.406	0.001	-0.001	0.002	-0.002	0.410

Table A.27: Systematic errors for each p_T bin in the Ψ' cross section ratio for tungsten compared to the hydrogen target.

p_T range	δp_{mix}	δp_{trk}^+	δp_{trk}^-	δp_{k1}^+	δp_{k1}^-	δ_{tot}
$0.000 \leq p_T < 0.300$	-0.001	0.007	-0.008	0.000	-0.000	0.010
$0.300 \leq p_T < 0.450$	0.015	-0.012	0.013	0.000	-0.000	0.023
$0.450 \leq p_T < 0.650$	0.002	-0.001	0.002	-0.000	0.000	0.003
$0.650 \leq p_T < 0.900$	0.004	-0.010	0.011	-0.000	0.000	0.015
$0.900 \leq p_T < 1.500$	-0.023	-0.008	0.009	0.000	-0.000	0.026

Table A.28: Systematic errors for each p_T bin in the Drell-Yan cross section ratio for carbon compared to the deuterium target.

p_T range	δp_{mix}	δp_{trk}^+	δp_{trk}^-	δp_{k1}^+	δp_{k1}^-	δ_{tot}
$0.000 \leq p_T < 0.300$	0.004	0.011	-0.013	-0.000	0.000	0.018
$0.300 \leq p_T < 0.450$	0.021	-0.008	0.009	0.000	-0.000	0.025
$0.450 \leq p_T < 0.650$	-0.003	-0.001	0.001	-0.000	0.000	0.004
$0.650 \leq p_T < 0.900$	0.011	-0.006	0.006	0.000	-0.000	0.014
$0.900 \leq p_T < 1.500$	-0.037	-0.007	0.008	-0.000	0.000	0.039

Table A.29: Systematic errors for each p_T bin in the Drell-Yan cross section ratio for iron compared to the deuterium target.

p_T range	δp_{mix}	δp_{trk}^+	δp_{trk}^-	δp_{k1}^+	δp_{k1}^-	δ_{tot}
$0.000 \leq p_T < 0.300$	0.000	-0.014	0.016	0.000	-0.000	0.021
$0.300 \leq p_T < 0.450$	0.031	-0.020	0.023	0.000	-0.000	0.044
$0.450 \leq p_T < 0.650$	0.006	-0.002	0.002	-0.000	0.000	0.007
$0.650 \leq p_T < 0.900$	0.018	-0.006	0.006	0.000	-0.000	0.020
$0.900 \leq p_T < 1.500$	-0.092	-0.009	0.010	0.000	-0.000	0.093

Table A.30: Systematic errors for each p_T bin in the Drell-Yan cross section ratio for tungsten compared to the deuterium target.

p_T range	δp_{mix}	δp_{trk}^+	δp_{trk}^-	δp_{k1}^+	δp_{k1}^-	δ_{tot}
$0.000 \leq p_T < 0.300$	0.000	0.007	-0.009	-0.000	0.000	0.011
$0.300 \leq p_T < 0.450$	0.012	-0.005	0.007	0.000	-0.000	0.015
$0.450 \leq p_T < 0.650$	0.006	-0.012	0.014	-0.000	0.000	0.020
$0.650 \leq p_T < 0.900$	-0.006	-0.014	0.017	0.000	-0.000	0.023
$0.900 \leq p_T < 1.500$	-0.034	0.060	-0.075	0.001	-0.001	0.103

Table A.31: Systematic errors for each p_T bin in the J/Ψ cross section ratio for carbon compared to the deuterium target.

p_T range	δp_{mix}	δp_{trk}^+	δp_{trk}^-	δp_{k1}^+	δp_{k1}^-	δ_{tot}
$0.000 \leq p_T < 0.300$	-0.010	-0.011	0.012	-0.000	0.000	0.019
$0.300 \leq p_T < 0.450$	0.003	-0.008	0.010	0.000	-0.000	0.013
$0.450 \leq p_T < 0.650$	-0.008	-0.004	0.004	-0.000	0.000	0.010
$0.650 \leq p_T < 0.900$	-0.014	-0.030	0.034	-0.001	0.001	0.049
$0.900 \leq p_T < 1.500$	-0.082	0.053	-0.067	-0.000	0.000	0.119

Table A.32: Systematic errors for each p_T bin in the J/Ψ cross section ratio for iron compared to the deuterium target.

p_T range	δp_{mix}	δp_{trk}^+	δp_{trk}^-	δp_{k1}^+	δp_{k1}^-	δ_{tot}
$0.000 \leq p_T < 0.300$	-0.005	-0.000	0.000	-0.000	0.000	0.005
$0.300 \leq p_T < 0.450$	0.006	-0.009	0.010	0.000	-0.000	0.015
$0.450 \leq p_T < 0.650$	0.004	-0.004	0.005	-0.000	0.000	0.008
$0.650 \leq p_T < 0.900$	-0.003	-0.010	0.012	0.000	-0.000	0.017
$0.900 \leq p_T < 1.500$	-0.208	0.017	-0.019	0.000	-0.000	0.210

Table A.33: Systematic errors for each p_T bin in the J/Ψ cross section ratio for tungsten compared to the deuterium target.

p_T range	δp_{mix}	δp_{trk}^+	δp_{trk}^-	δp_{k1}^+	δp_{k1}^-	δ_{tot}
$0.000 \leq p_T < 0.300$	0.007	0.001	-0.001	-0.000	0.000	0.007
$0.300 \leq p_T < 0.450$	0.003	0.005	-0.005	-0.000	0.000	0.008
$0.450 \leq p_T < 0.650$	-0.001	0.006	-0.007	0.001	-0.001	0.011
$0.650 \leq p_T < 0.900$	0.000	-0.006	0.006	0.000	-0.000	0.009
$0.900 \leq p_T < 1.500$	-0.020	-0.000	0.000	0.000	-0.000	0.020

Table A.34: Systematic errors for each p_T bin in the Ψ' cross section ratio for carbon compared to the deuterium target.

p_T range	δp_{mix}	δp_{trk}^+	δp_{trk}^-	δp_{k1}^+	δp_{k1}^-	δ_{tot}
$0.000 \leq p_T < 0.300$	0.004	-0.005	0.006	-0.000	0.000	0.009
$0.300 \leq p_T < 0.450$	0.007	0.002	-0.002	-0.000	0.000	0.008
$0.450 \leq p_T < 0.650$	0.006	0.007	-0.008	0.001	-0.001	0.014
$0.650 \leq p_T < 0.900$	0.026	-0.005	0.006	0.000	-0.000	0.027
$0.900 \leq p_T < 1.500$	-0.014	-0.002	0.002	-0.001	0.001	0.016

Table A.35: Systematic errors for each p_T bin in the Ψ' cross section ratio for iron compared to the deuterium target.

p_T range	δp_{mix}	δp_{trk}^+	δp_{trk}^-	δp_{k1}^+	δp_{k1}^-	δ_{tot}
$0.000 \leq p_T < 0.300$	-0.000	-0.012	0.013	-0.000	0.000	0.018
$0.300 \leq p_T < 0.450$	-0.000	-0.004	0.004	0.000	-0.000	0.006
$0.450 \leq p_T < 0.650$	0.006	-0.001	0.001	0.001	-0.001	0.008
$0.650 \leq p_T < 0.900$	0.027	-0.008	0.008	0.000	-0.000	0.030
$0.900 \leq p_T < 1.500$	-0.350	0.002	-0.003	0.001	-0.002	0.353

Table A.36: Systematic errors for each p_T bin in the Ψ' cross section ratio for tungsten compared to the deuterium target.

A.8 R_{pA} in p_T and x_F

The results for the binned analysis in x_F for the hydrogen data are shown for Drell-Yan, J/Ψ , and Ψ' in fig. A.27, fig. A.28, and fig. A.29 respectively. The deuterium data are shown for Drell-Yan, J/Ψ , and Ψ' in fig. A.30, fig. A.31, and fig. A.32 respectively. The results for the binned analysis in p_T for the hydrogen data are shown for Drell-Yan, J/Ψ , and Ψ' in fig. A.33, fig. A.34, and fig. A.35 respectively. The deuterium data are shown for Drell-Yan, J/Ψ , and Ψ' in fig. A.36, fig. A.37, and fig. A.38 respectively.

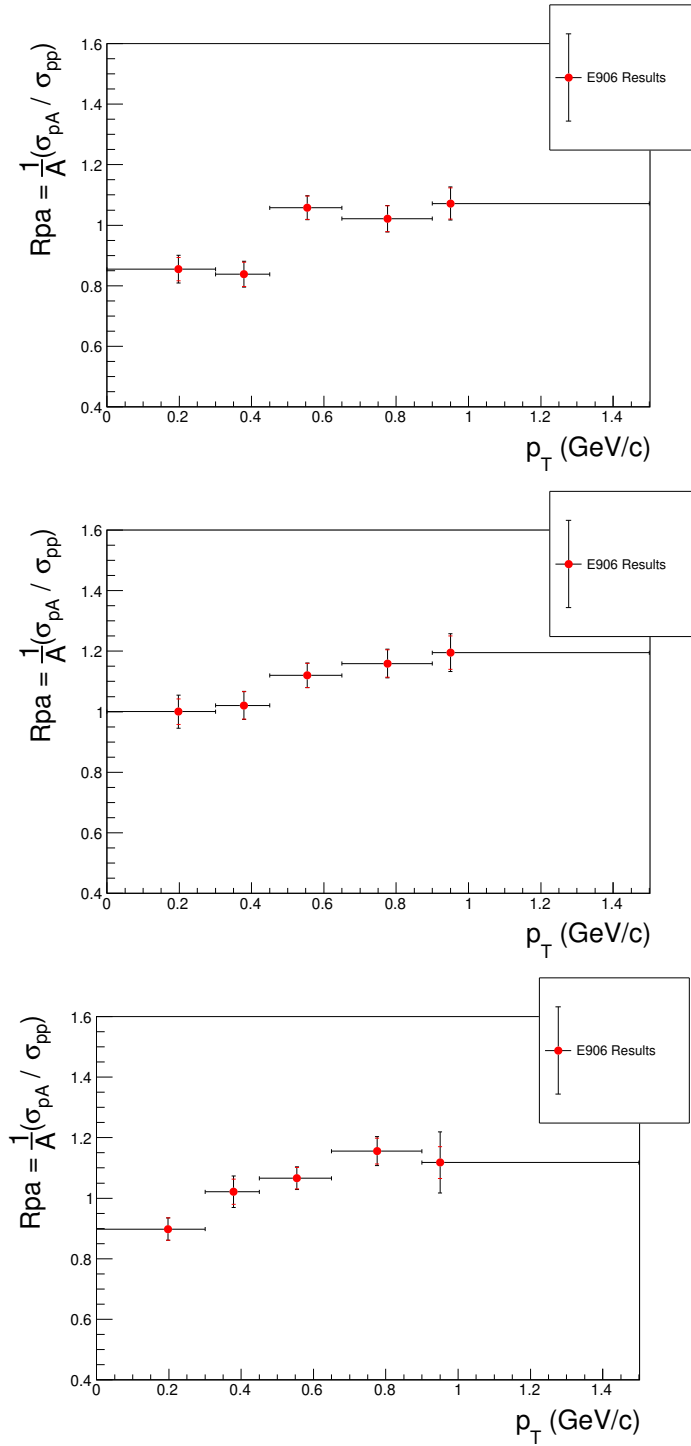


Figure A.27: R_{pA} for Drell-Yan from the hydrogen target, binned in p_T . (Top) results for carbon. (Middle) results for iron. (Bottom) results for tungsten. Horizontal error bars represent bin widths and markers are placed at bin averages. Red errors represent statistical uncertainty and black error bars represent the combined systematic and statistical error, summed in quadrature. A clear p_T broadening effect is observed.

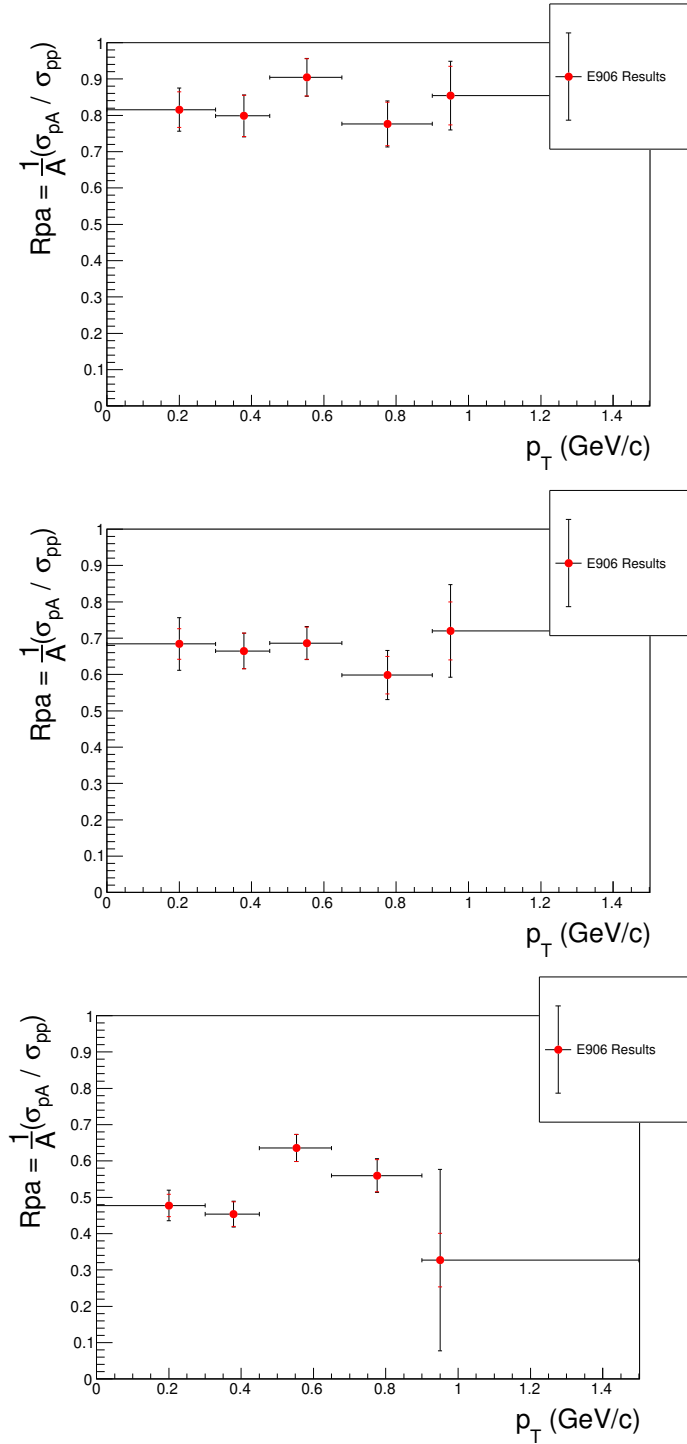


Figure A.28: R_{pA} for J/Ψ from the hydrogen target, binned in p_T . (Top) results for carbon. (Middle) results for iron. (Bottom) results for tungsten. Horizontal error bars represent bin widths and markers are placed at bin averages. Red errors represent statistical uncertainty and black error bars represent the combined systematic and statistical error, summed in quadrature.

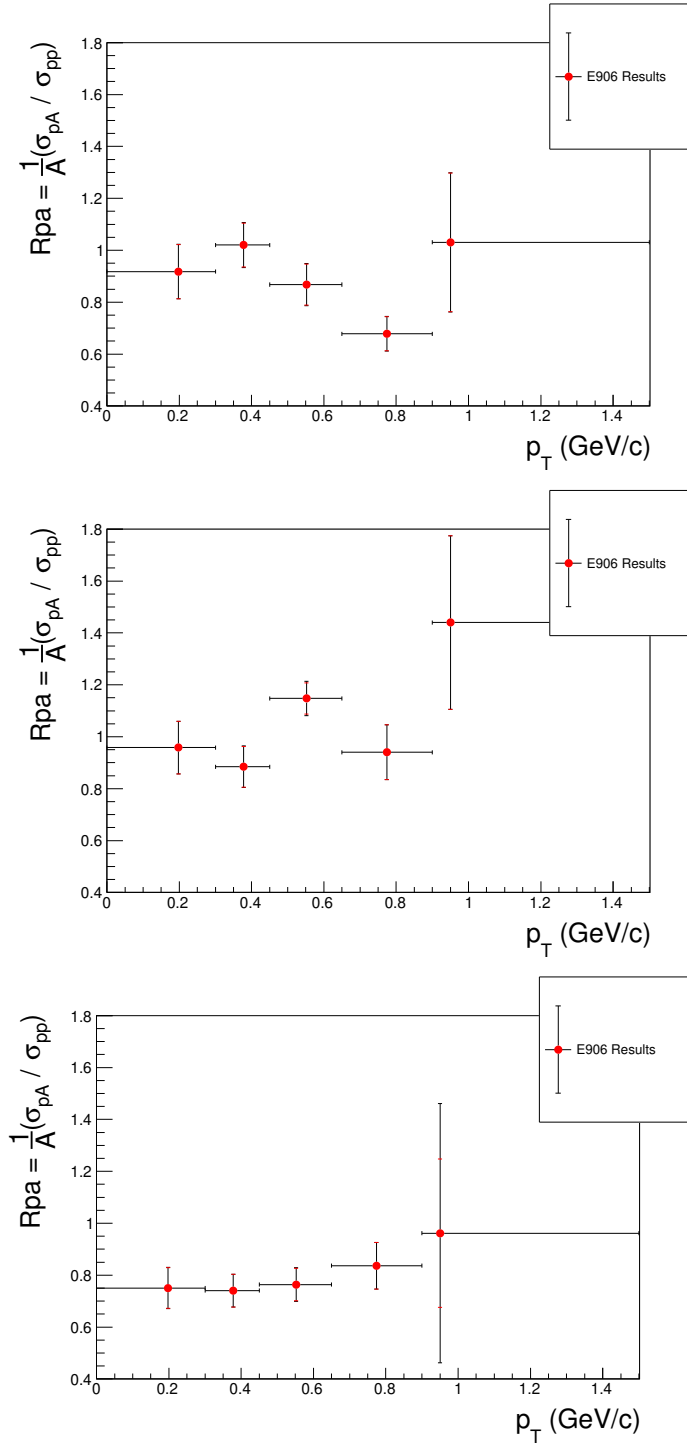


Figure A.29: R_{pA} for Ψ' from the hydrogen target, binned in p_T . (Top) results for carbon. (Middle) results for iron. (Bottom) results for tungsten. Horizontal error bars represent bin widths and markers are placed at bin averages. Red errors represent statistical uncertainty and black error bars represent the combined systematic and statistical error, summed in quadrature.

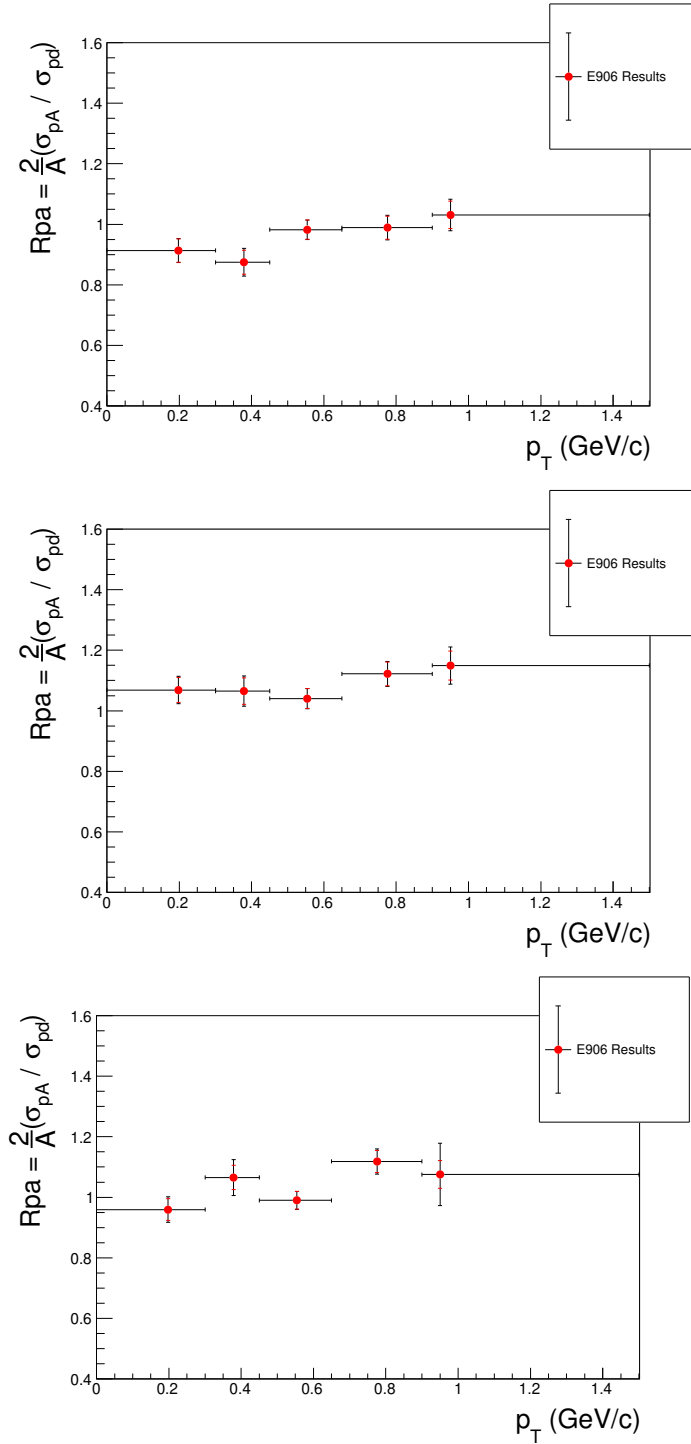


Figure A.30: R_{pA} for Drell-Yan from the deuterium target, binned in p_T . (Top) results for carbon. (Middle) results for iron. (Bottom) results for tungsten. Horizontal error bars represent bin widths and markers are placed at bin averages. Red errors represent statistical uncertainty and black error bars represent the combined systematic and statistical error, summed in quadrature.

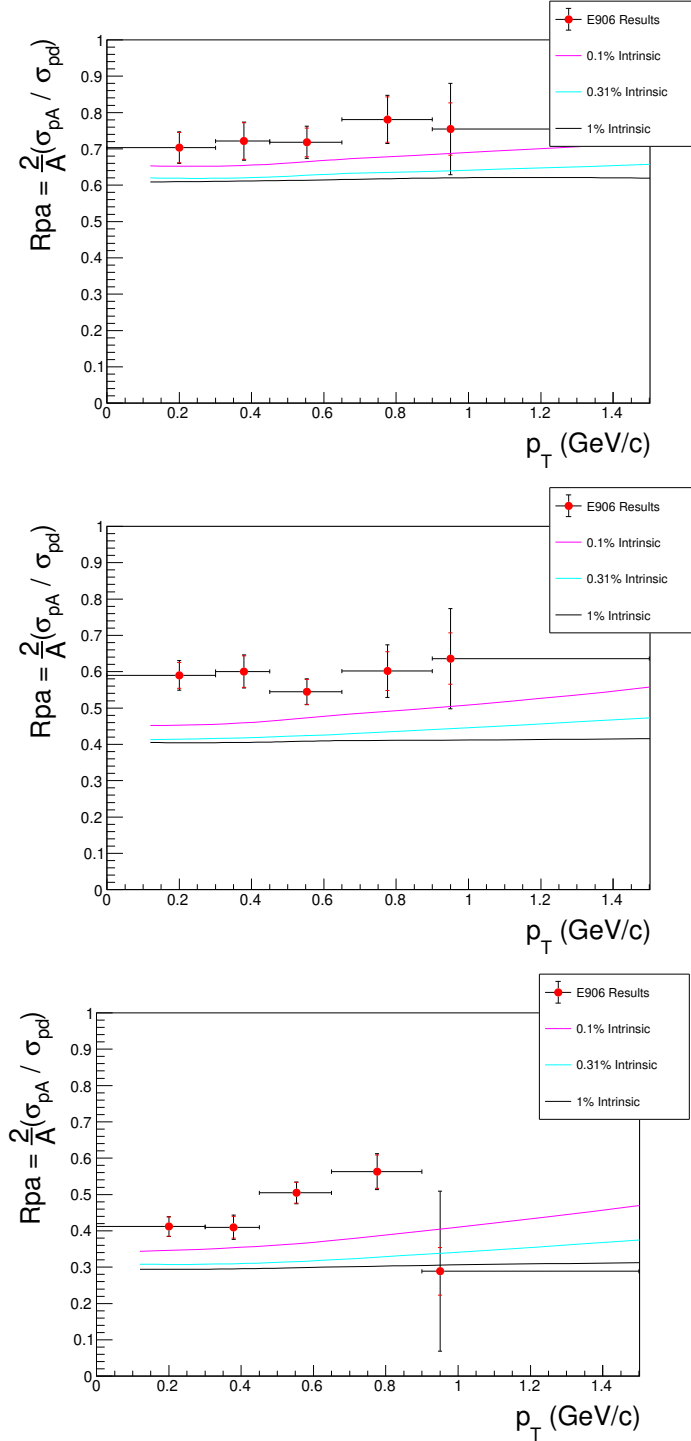


Figure A.31: R_{pA} for J/Ψ from the deuterium target, binned in p_T . (Top) results for carbon. (Middle) results for iron. (Bottom) results for tungsten. Horizontal error bars represent bin widths and markers are placed at bin averages. Red errors represent statistical uncertainty and black error bars represent the combined systematic and statistical error, summed in quadrature. Theory curves from ref. [46] are overlaid for the 0.01%, 0.31%, and 1% intrinsic charm production probabilities respectively.

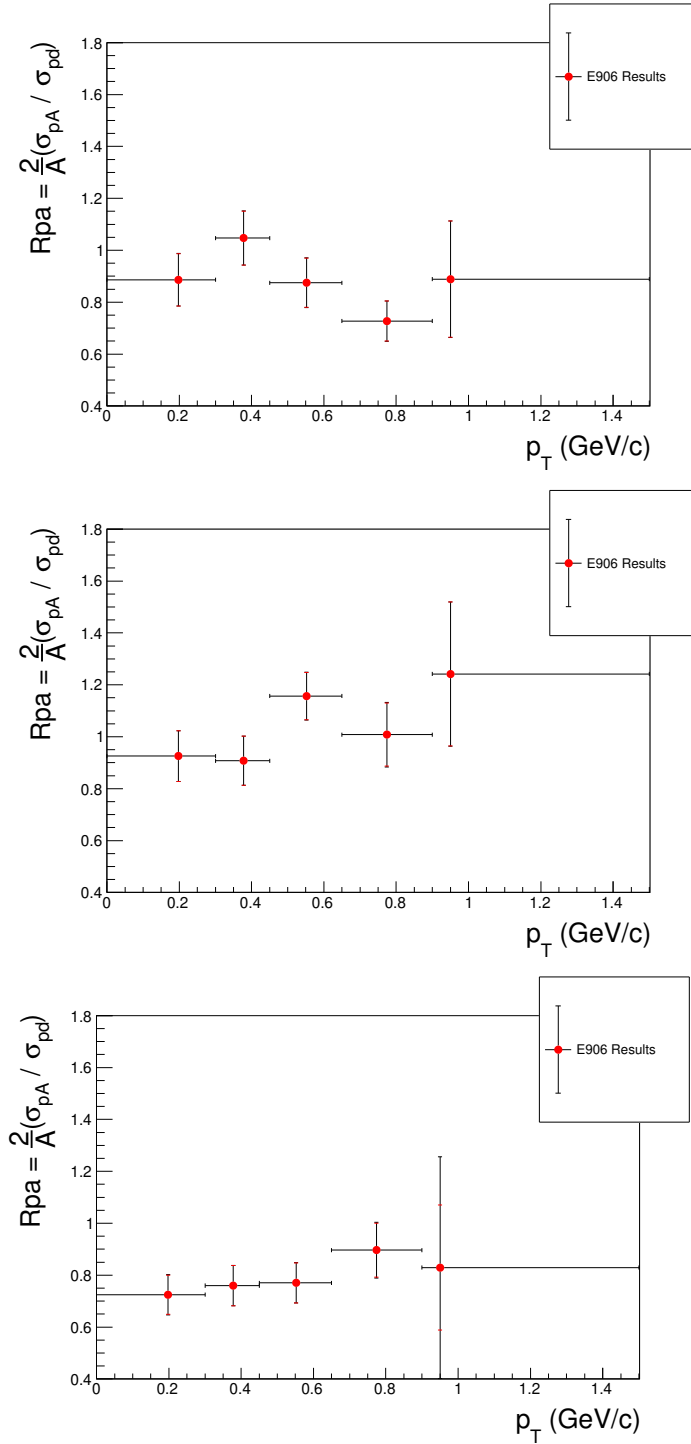


Figure A.32: R_{pA} for Ψ' from the deuterium target, binned in p_T . (Top) results for carbon. (Middle) results for iron. (Bottom) results for tungsten. Horizontal error bars represent bin widths and markers are placed at bin averages. Red errors represent statistical uncertainty and black error bars represent the combined systematic and statistical error, summed in quadrature.

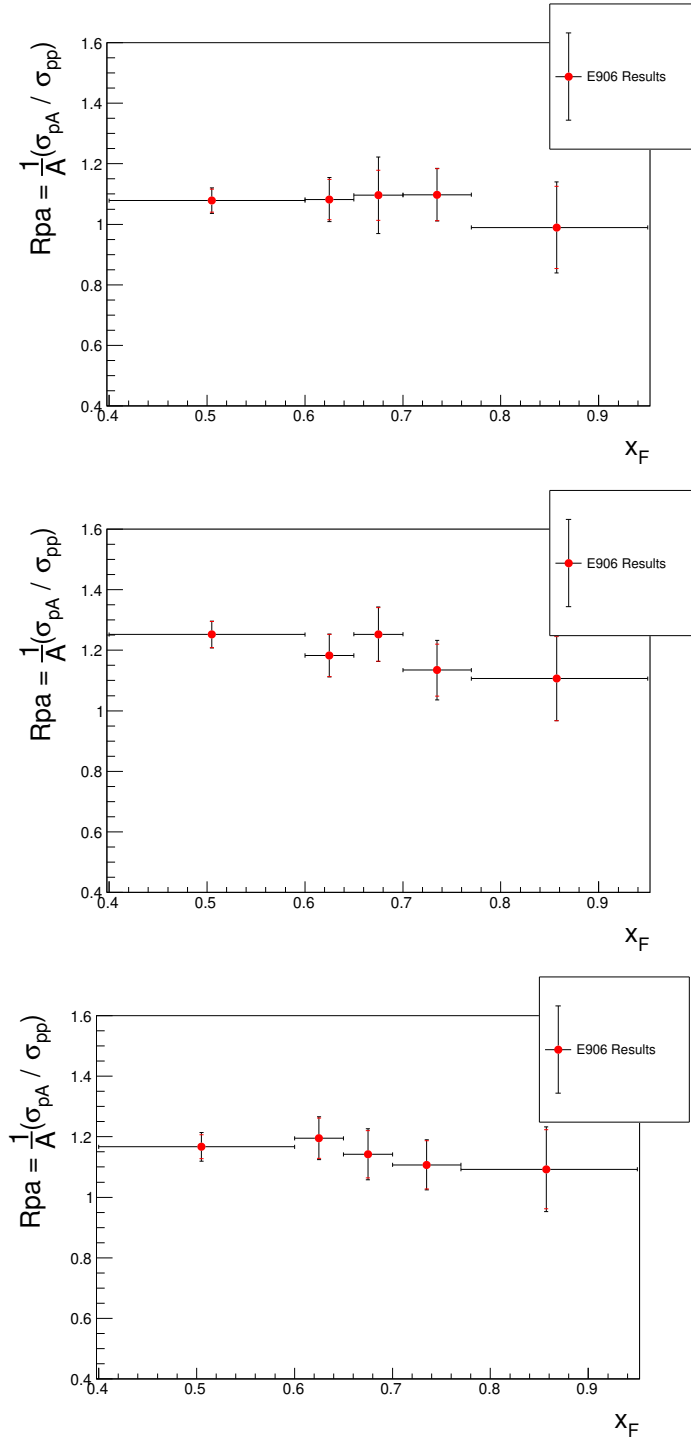


Figure A.33: R_{pA} for Drell-Yan from the hydrogen target, binned in x_F . (Top) results for carbon. (Middle) results for iron. (Bottom) results for tungsten. Horizontal error bars represent bin widths and markers are placed at bin averages. Red errors represent statistical uncertainty and black error bars represent the combined systematic and statistical error, summed in quadrature.

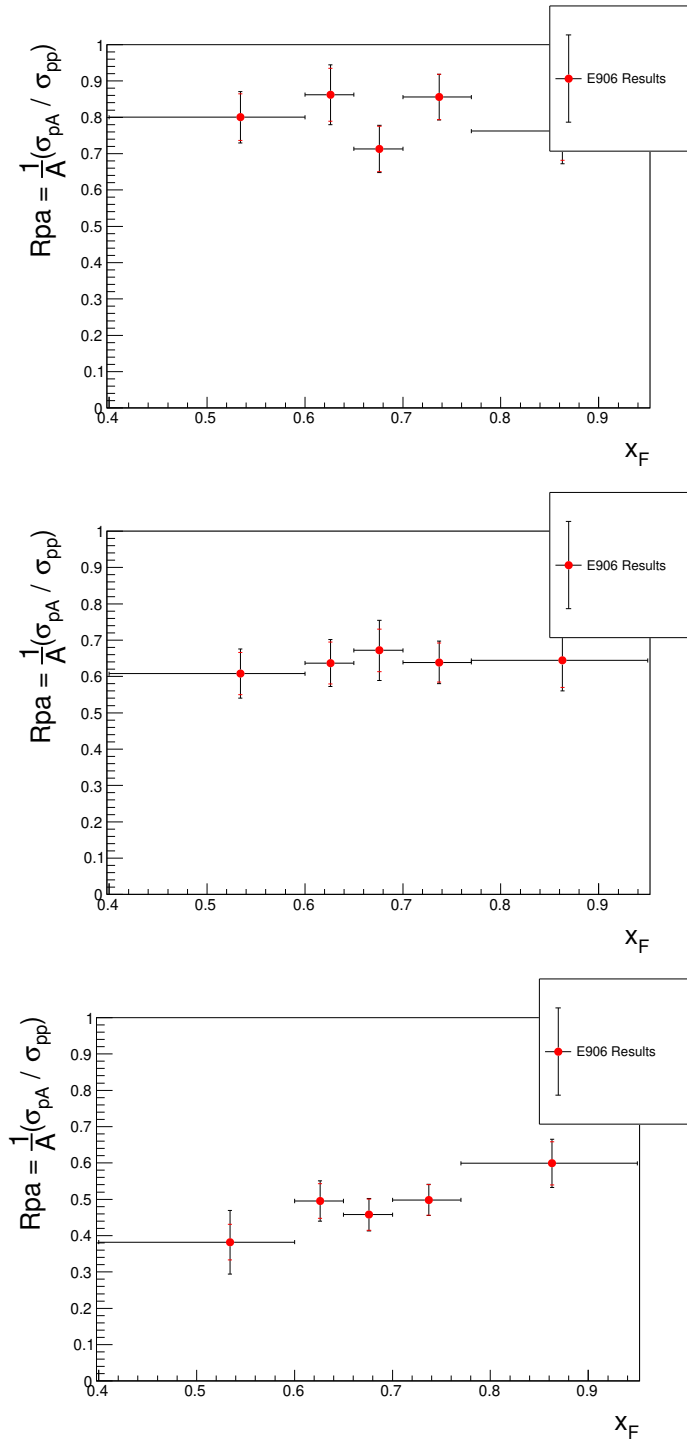


Figure A.34: R_{pA} for J/Ψ from the hydrogen target, binned in x_F . (Top) results for carbon. (Middle) results for iron. (Bottom) results for tungsten. Horizontal error bars represent bin widths and markers are placed at bin averages. Red errors represent statistical uncertainty and black error bars represent the combined systematic and statistical error, summed in quadrature.

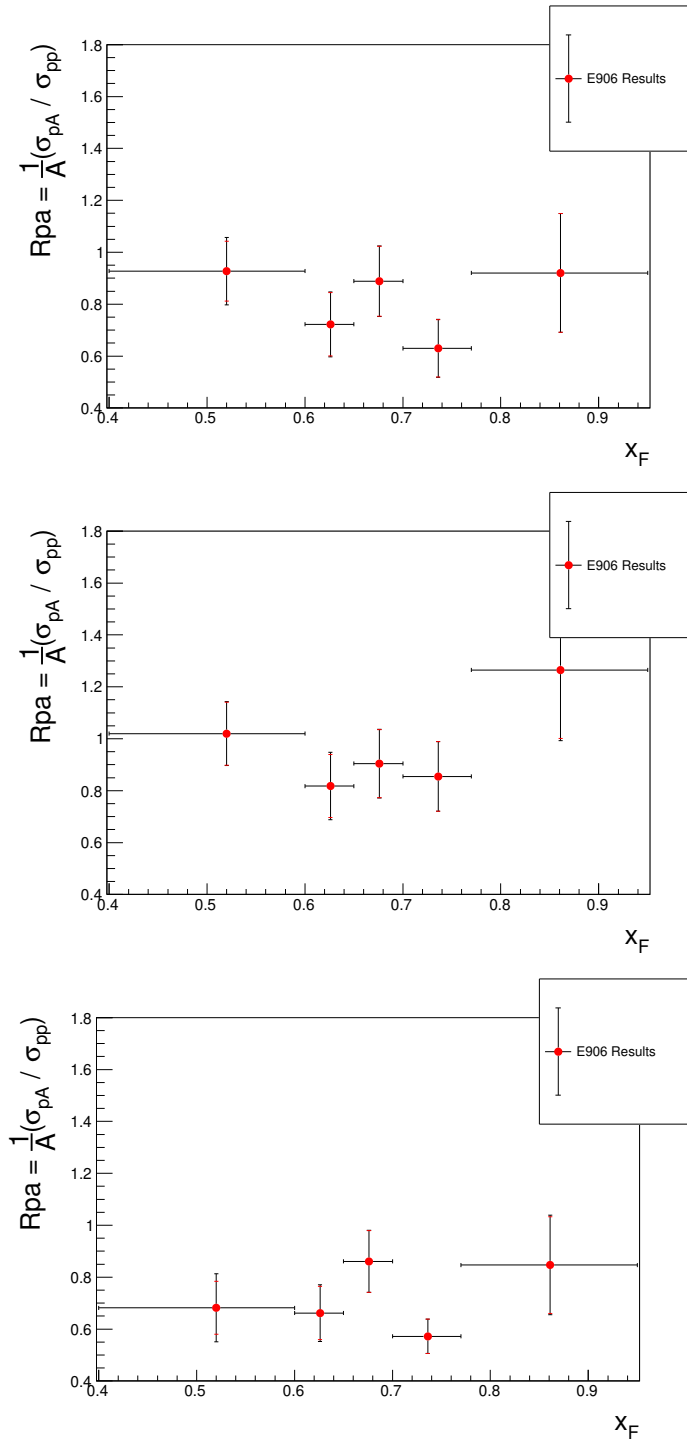


Figure A.35: R_{pA} for Ψ' from the hydrogen target, binned in x_F . (Top) results for carbon. (Middle) results for iron. (Bottom) results for tungsten. Horizontal error bars represent bin widths and markers are placed at bin averages. Red errors represent statistical uncertainty and black error bars represent the combined systematic and statistical error, summed in quadrature.

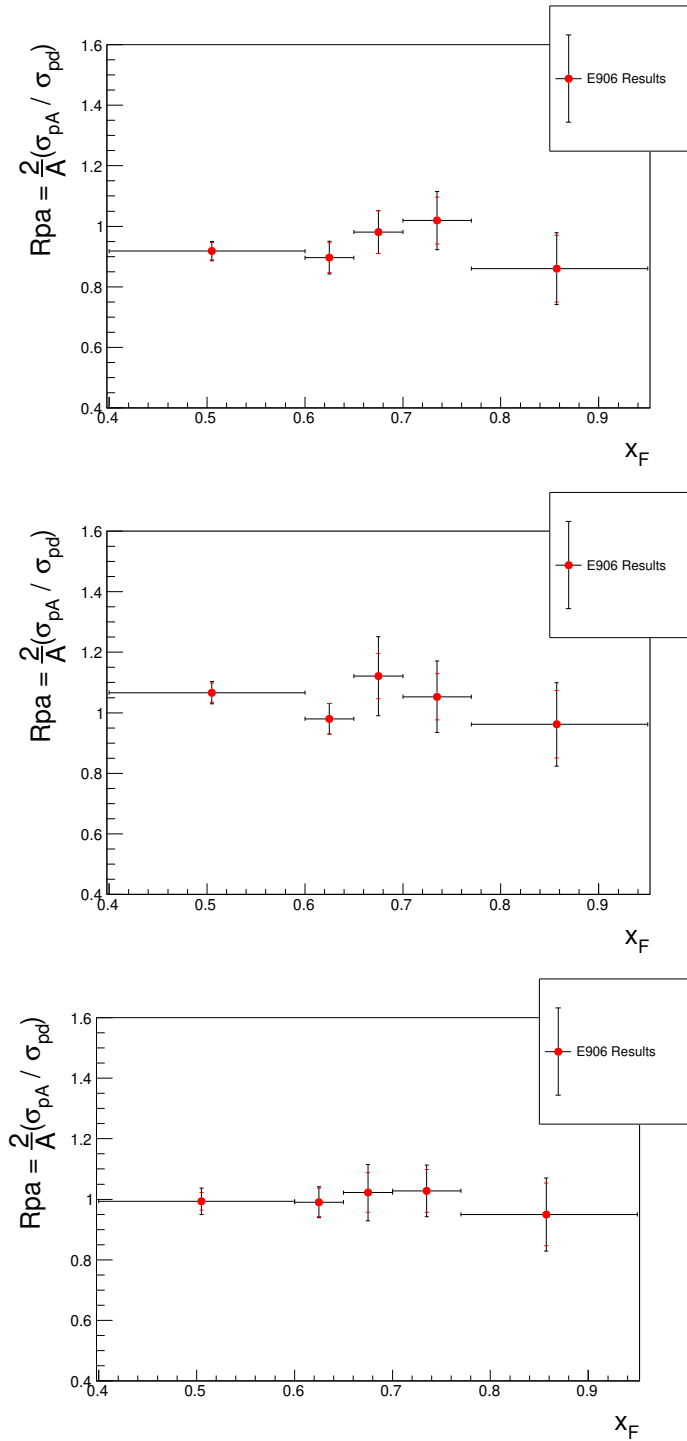


Figure A.36: R_{pA} for Drell-Yan from the deuterium target, binned in x_F . (Top) results for carbon. (Middle) results for iron. (Bottom) results for tungsten. Horizontal error bars represent bin widths and markers are placed at bin averages. Red errors represent statistical uncertainty and black error bars represent the combined systematic and statistical error, summed in quadrature.

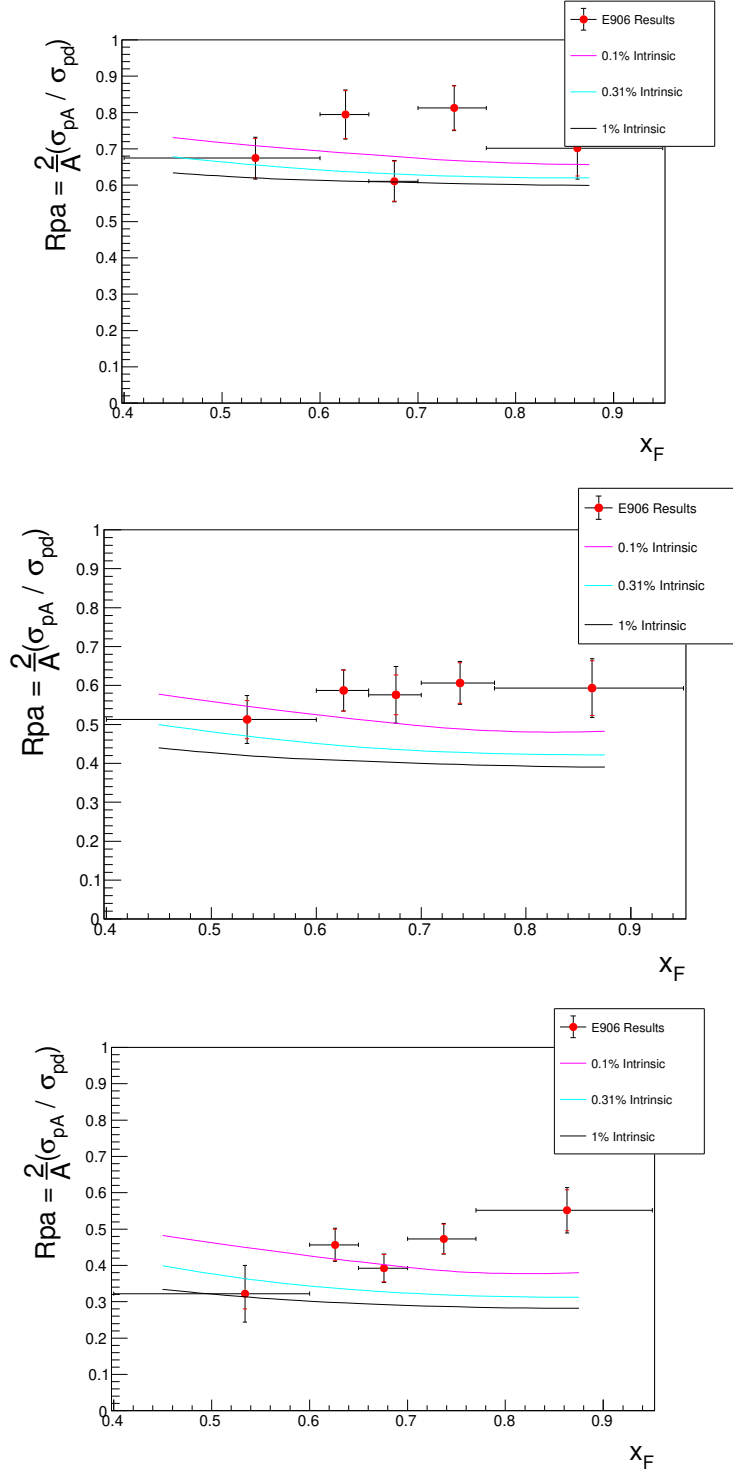


Figure A.37: R_{pA} for J/Ψ from the deuterium target, binned in x_F . (Top) results for carbon. (Middle) results for iron. (Bottom) results for tungsten. Horizontal error bars represent bin widths and markers are placed at bin averages. Red errors represent statistical uncertainty and black error bars represent the combined systematic and statistical error, summed in quadrature. Theory curves from ref. [46] are overlaid for the 0.01%, 0.31%, and 1% intrinsic charm production probabilities respectively.

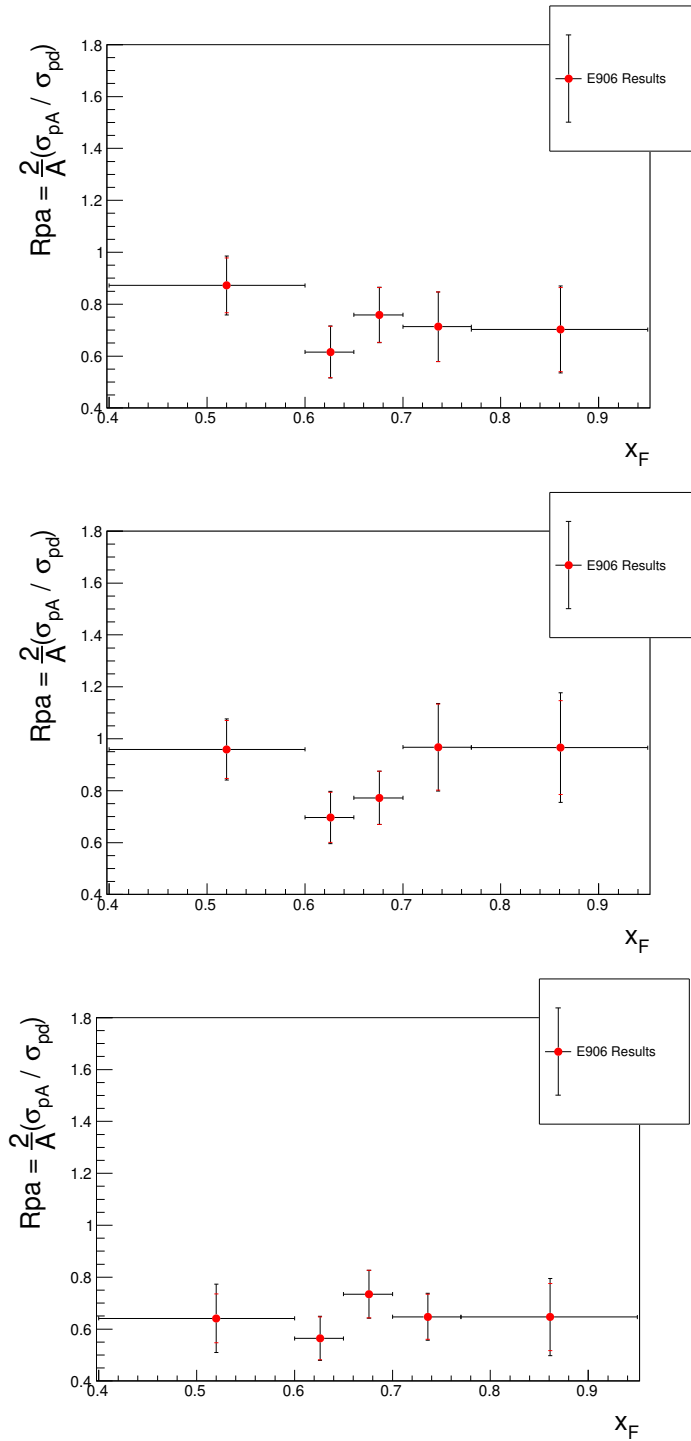


Figure A.38: R_{pA} for Ψ' from the deuterium target, binned in x_F . (Top) results for carbon. (Middle) results for iron. (Bottom) results for tungsten. Horizontal error bars represent bin widths and markers are placed at bin averages. Red errors represent statistical uncertainty and black error bars represent the combined systematic and statistical error, summed in quadrature.

A.9 Overview of Analysis Software

In this section I provide an overview of the software layout of the analysis for interested parties who have access to the machines at Fermilab. The data presented in this analysis is processed through a series of ROOT macros hosted on the "seaquest" disk hosted at Fermilab and accessed through the common machine, "seaquestgpvm01". All of the software relevant to the analysis can be found in my personal directory under /seaquest/users/nwuerfel/thesis_work. There are four primary components to the analysis: massfit, pT_reweight, acceptance, and nuclear_modification. Each is stored in a directory of the same name. All data used in the analysis can be found in /seaquest/users/nwuerfel/thesis_work/datafiles, where the primary experiment data from roadsets 57, 59, 62, 67, and 70 are stored in a common data file and events can be identified with their respective roadsets by the "runID" field. Inside of the /massfit/ directory, there are several macros to facilitate the process of applying the TFractionFitter to the data to extract the contributing yields of each physics process. First, a series of selections are made on the data, listed in sec. 4.2, via the macro "applyCuts.C". In addition to applying selections, the data is also projected into several Feynman- x and transverse momentum bins at this point. The macro "drawAllDist.C" generates mass plots which show the contribution of each of the data bins to the total, unbinned data set, along with the shape of the data before and after the selections of "applyCuts.C" have been applied. "fitComponents.C" performs massfits on unbinned data as well as each individual bin of the data and writes the process yields and uncertainties to a human readable text file. These yields are later read by the code which computes the cross section ratio from them.

The /pT_reweight/ directory contains all macros required to correct the transverse momentum distributions of the Drell-Yan, J/Ψ , and Ψ' . The original transverse momentum distributions in the SeaQuest Monte Carlo were generated from phenomenological fits to data previously taken with an 800 GeV proton beam. It is

known that the distributions are a function of scale and a correction is expected for the 120 GeV beam used at SeaQuest. Further motivation and details of the process are provided in sec. 4.4. The reweighting of the Drell-Yan Monte Carlo is separate from that of the charmonia, but the method is similar for each process. The original Monte Carlo samples with the incorrect distributions are used as a first-order estimate and the particle yields are extracted from the massfit method. The yields are fit with the same phenomenological form, with a parameter allowed to float. A reweighting value is computed from the fit value of this parameter and applied to the Monte Carlo as a first-pass at reweighting. The process is iterated to provide the best possible parameter to describe the transverse momentum distributions in the SeaQuest data. "firstAcceptance.C" computes the acceptance of the Drell-Yan Monte Carlo and produces a set of acceptance histograms which are saved to the /first_acc_results/ directory. "fitKaplan.C" uses these acceptance histograms to correct the Drell-Yan Monte Carlo data and then fits the data using the phenomenological Kaplan fit from ref. [78]. The data is fit in three separate Feynman- x bins and a linear fit is made to produce a linear interpolation for the Kaplan fit parameter, p1, as a function of x_F . "dyreweightData.C" runs through the Drell-Yan Monte Carlo data, determining a value of p1 for each event based on the x_F value and applying the appropriate reweighting factor to the event, producing a reweighted Monte Carlo file, containing all data fields of the original along with a new field "ReWeight". "charmAcceptance.C" performs a similar calculation of the charmonia acceptances and "makeCharmYieldPlots.C" fits the acceptance corrected Monte Carlo data to determine values of p1 for each of the J/Ψ and Ψ' . There is insufficient charmonia data to produce an interpolation of p1 in x_F , so a single p1 value, averaged over the x_F distribution of the J/Ψ or Ψ' , is applied to the respective Monte Carlos by "charmReweightAfterFit.C".

The /acceptance/ directory contains all macros required to compute the acceptance corrections for each target in x_F and p_T . "binAndCut.C" applies selections to

the Monte Carlo data and "drawAllCuts.C" shows the relative contribution of each bin to the total data. "calcDrawAcc.C" computes the ratio of "clean" Monte Carlo events, which pass through simulated detector geometry, to "4pi" Monte Carlo events which need not pass through the spectrometer. This gives an estimate of the total efficiency of the spectrometer, measuring the fraction of total dimuon events produced in the target which pass through and are measured by the detector. "plotAcc.C" formats the acceptance results for each target and produces a final plot comparing the acceptances across all possible targets. Because the final results of this analysis are cross section ratios, the acceptance effects should be small and only the ratio of acceptances of various targets becomes relevant. Previous analyses of charmonium data at SeaQuest have tended to neglect the acceptance effect as small. Finally, the /nuclear_modification/ directory contains the macros which compute the cross section ratios, $R_{pA}^{H/D}$, and extract a value of α . "calcAttenuation.C" computes the proton beam attenuation on each of the different targets, and the resulting values are used in the cross section ratio calculation. "calcNuclearCSR.C" computes both the unbinned and binned cross section ratios across all targets and dimensions. "jpsipComparisonReal.C" compares the results of the unbinned analysis with the E772 results and fits the data on a lin-log scale to extract a value of α for each process.

Bibliography

- [1] Niels Bohr. “I. On the constitution of atoms and molecules”. In: *The London, Edinburgh, and Dublin Philosophical Magazine and Journal of Science* 26.151 (1913), pp. 1–25.
- [2] G. Zweig. “An SU(3) model for strong interaction symmetry and its breaking. Version 2”. In: *DEVELOPMENTS IN THE QUARK THEORY OF HADRONS. VOL. 1. 1964 - 1978*. Ed. by D. B. Lichtenberg and Simon Peter Rosen. 1964, pp. 22–101.
- [3] Murray Gell-Mann. “A Schematic Model of Baryons and Mesons”. In: *Phys. Lett.* 8 (1964), pp. 214–215. DOI: 10.1016/S0031-9163(64)92001-3.
- [4] B.J. Björken and S.L. Glashow. “Elementary particles and SU(4)”. In: *Physics Letters* 11.3 (1964), pp. 255–257. ISSN: 0031-9163. DOI: [https://doi.org/10.1016/0031-9163\(64\)90433-0](https://doi.org/10.1016/0031-9163(64)90433-0). URL: <https://www.sciencedirect.com/science/article/pii/0031916364904330>.
- [5] O. W. Greenberg. “Spin and Unitary-Spin Independence in a Paraquark Model of Baryons and Mesons”. In: *Phys. Rev. Lett.* 13 (20 1964), pp. 598–602. DOI: 10.1103/PhysRevLett.13.598. URL: <https://link.aps.org/doi/10.1103/PhysRevLett.13.598>.

- [6] M. Y. Han and Y. Nambu. “Three-Triplet Model with Double SU(3) Symmetry”. In: *Phys. Rev.* 139 (4B 1965), B1006–B1010. DOI: 10.1103/PhysRev.139.B1006. URL: <https://link.aps.org/doi/10.1103/PhysRev.139.B1006>.
- [7] J. D. Bjorken. “CURRENT ALGEBRA AT SMALL DISTANCES”. In: *Conf. Proc. C 670717* (1967), pp. 55–81.
- [8] R. P. Feynman. “The behavior of hadron collisions at extreme energies”. In: *Conf. Proc. C 690905* (1969), pp. 237–258.
- [9] S. L. Glashow, J. Iliopoulos, and L. Maiani. “Weak Interactions with Lepton-Hadron Symmetry”. In: *Phys. Rev. D* 2 (7 1970), pp. 1285–1292. DOI: 10.1103/PhysRevD.2.1285. URL: <https://link.aps.org/doi/10.1103/PhysRevD.2.1285>.
- [10] Makoto Kobayashi and Toshihide Maskawa. “CP-Violation in the Renormalizable Theory of Weak Interaction”. In: *Progress of Theoretical Physics* 49.2 (1973), pp. 652–657. ISSN: 0033-068X. DOI: 10.1143/PTP.49.652. eprint: <https://academic.oup.com/ptp/article-pdf/49/2/652/5257692/49-2-652.pdf>. URL: <https://doi.org/10.1143/PTP.49.652>.
- [11] E. Ambler et al. “Further Experiments on β Decay of Polarized Nuclei”. In: *Phys. Rev.* 106 (6 1957), pp. 1361–1363. DOI: 10.1103/PhysRev.106.1361. URL: <https://link.aps.org/doi/10.1103/PhysRev.106.1361>.
- [12] B Richter. “Total hadron cross section, new particles, and muon electron events in e^+e^- annihilation at SPEAR”. In: (1976). URL: <https://www.osti.gov/biblio/5184400>.
- [13] J. J. Aubert et al. “Experimental Observation of a Heavy Particle J ”. In: *Phys. Rev. Lett.* 33 (23 1974), pp. 1404–1406. DOI: 10.1103/PhysRevLett.33.1404. URL: <https://link.aps.org/doi/10.1103/PhysRevLett.33.1404>.

- [14] S. W. Herb et al. “Observation of a Dimuon Resonance at 9.5 GeV in 400-GeV Proton-Nucleus Collisions”. In: *Phys. Rev. Lett.* 39 (5 1977), pp. 252–255. DOI: 10.1103/PhysRevLett.39.252. URL: <https://link.aps.org/doi/10.1103/PhysRevLett.39.252>.
- [15] Sau Lan Wu. “e+ e- Physics at PETRA: The First 5-Years”. In: *Phys. Rept.* 107 (1984), pp. 59–324. DOI: 10.1016/0370-1573(84)90033-4.
- [16] F. Abe et al. “Observation of Top Quark Production in $\bar{p}p$ Collisions with the Collider Detector at Fermilab”. In: *Phys. Rev. Lett.* 74 (14 1995), pp. 2626–2631. DOI: 10.1103/PhysRevLett.74.2626. URL: <https://link.aps.org/doi/10.1103/PhysRevLett.74.2626>.
- [17] S. Abachi et al. “Observation of the Top Quark”. In: *Phys. Rev. Lett.* 74 (14 1995), pp. 2632–2637. DOI: 10.1103/PhysRevLett.74.2632. URL: <https://link.aps.org/doi/10.1103/PhysRevLett.74.2632>.
- [18] C. N. Yang and R. L. Mills. “Conservation of Isotopic Spin and Isotopic Gauge Invariance”. In: *Phys. Rev.* 96 (1 1954), pp. 191–195. DOI: 10.1103/PhysRev.96.191. URL: <https://link.aps.org/doi/10.1103/PhysRev.96.191>.
- [19] H. Fritzsch, M. Gell-Mann, and H. Leutwyler. “Advantages of the color octet gluon picture”. In: *Physics Letters B* 47.4 (1973), pp. 365–368. ISSN: 0370-2693. DOI: [https://doi.org/10.1016/0370-2693\(73\)90625-4](https://doi.org/10.1016/0370-2693(73)90625-4). URL: <https://www.sciencedirect.com/science/article/pii/0370269373906254>.
- [20] Michael Edward Peskin and Daniel V. Schroeder. *An Introduction to Quantum Field Theory*. Reading, USA: Addison-Wesley (1995) 842 p. Westview Press, 1995.
- [21] Gerard 't Hooft. “Renormalizable Lagrangians for Massive Yang-Mills Fields”. In: *Nucl. Phys. B* 35 (1971). Ed. by J. C. Taylor, pp. 167–188. DOI: 10.1016/0550-3213(71)90139-8.

- [22] David J. Gross and Frank Wilczek. “Ultraviolet Behavior of Non-Abelian Gauge Theories”. In: *Phys. Rev. Lett.* 30 (26 1973), pp. 1343–1346. DOI: 10.1103/PhysRevLett.30.1343. URL: <https://link.aps.org/doi/10.1103/PhysRevLett.30.1343>.
- [23] H. David Politzer. “Reliable Perturbative Results for Strong Interactions?” In: *Phys. Rev. Lett.* 30 (26 1973), pp. 1346–1349. DOI: 10.1103/PhysRevLett.30.1346. URL: <https://link.aps.org/doi/10.1103/PhysRevLett.30.1346>.
- [24] Sidney Coleman and David J. Gross. “Price of Asymptotic Freedom”. In: *Phys. Rev. Lett.* 31 (13 1973), pp. 851–854. DOI: 10.1103/PhysRevLett.31.851. URL: <https://link.aps.org/doi/10.1103/PhysRevLett.31.851>.
- [25] L.D. Faddeev and V.N. Popov. “Feynman diagrams for the Yang-Mills field”. In: *Physics Letters B* 25.1 (1967), pp. 29–30. ISSN: 0370-2693. DOI: [https://doi.org/10.1016/0370-2693\(67\)90067-6](https://doi.org/10.1016/0370-2693(67)90067-6). URL: <https://www.sciencedirect.com/science/article/pii/0370269367900676>.
- [26] Stephen L. Adler and Wu-Ki Tung. “Breakdown of Asymptotic Sum Rules in Perturbation Theory”. In: *Phys. Rev. Lett.* 22 (18 1969), pp. 978–981. DOI: 10.1103/PhysRevLett.22.978. URL: <https://link.aps.org/doi/10.1103/PhysRevLett.22.978>.
- [27] R. Jackiw and G. Preparata. “Probes for the Constituents of the Electromagnetic Current and Anomalous Commutators”. In: *Phys. Rev. Lett.* 22 (18 1969), pp. 975–977. DOI: 10.1103/PhysRevLett.22.975. URL: <https://link.aps.org/doi/10.1103/PhysRevLett.22.975>.
- [28] R. Jaffe. “One Theorist’s Perspective on Four Eras of Electron-Proton Scattering”. In: (1998).
- [29] John C. Collins, Davison E. Soper, and George Sterman. *Factorization of Hard Processes in QCD*. 2004. arXiv: hep-ph/0409313 [hep-ph].

- [30] Sidney D. Drell and Tung-Mow Yan. “Massive Lepton-Pair Production in Hadron-Hadron Collisions at High Energies”. In: *Phys. Rev. Lett.* 25 (5 1970), pp. 316–320. DOI: 10.1103/PhysRevLett.25.316. URL: <https://link.aps.org/doi/10.1103/PhysRevLett.25.316>.
- [31] Pavel M. Nadolsky et al. “Implications of CTEQ global analysis for collider observables”. In: *Physical Review D* 78.1 (2008). DOI: 10.1103/physrevd.78.013004. URL: <https://doi.org/10.1103/PhysRevD.78.013004>.
- [32] A. D. Martin et al. “Parton distributions for the LHC”. In: *The European Physical Journal C* 63.2 (2009), pp. 189–285. DOI: 10.1140/epjc/s10052-009-1072-5. URL: <https://doi.org/10.1140/epjc/s10052-009-1072-5>.
- [33] M. Glück, P. Jimenez-Delgado, and E. Reya. “Dynamical parton distributions of the nucleon and very small-x physics”. In: *The European Physical Journal C* 53.3 (2007), pp. 355–366. DOI: 10.1140/epjc/s10052-007-0462-9. URL: <https://doi.org/10.1140/epjc/s10052-007-0462-9>.
- [34] Richard D. Ball et al. “A first unbiased global NLO determination of parton distributions and their uncertainties”. In: *Nuclear Physics B* 838.1-2 (2010), pp. 136–206. DOI: 10.1016/j.nuclphysb.2010.05.008. URL: <https://doi.org/10.1016/j.nuclphysb.2010.05.008>.
- [35] Xiang Gao et al. “Unpolarized proton PDF at NNLO from lattice QCD with physical quark masses”. In: *Physical Review D* 107.7 (2023). DOI: 10.1103/physrevd.107.074509. URL: <https://doi.org/10.1103/PhysRevD.107.074509>.
- [36] John C. Collins and Davison E. Soper. “Parton Distribution and Decay Functions”. In: *Nucl. Phys. B* 194 (1982), pp. 445–492. DOI: 10.1016/0550-3213(82)90021-9.

- [37] Davison E. Soper. “Parton distribution functions”. In: *Nuclear Physics B - Proceedings Supplements* 53.1-3 (1997), pp. 69–80. DOI: 10.1016/s0920-5632(96)00600-7. URL: <https://doi.org/10.10162Fs0920-563228962900600-7>.
- [38] V. N. Gribov and L. N. Lipatov. “Deep inelastic e p scattering in perturbation theory”. In: *Sov. J. Nucl. Phys.* 15 (1972), pp. 438–450.
- [39] Guido Altarelli and G. Parisi. “Asymptotic Freedom in Parton Language”. In: *Nucl. Phys. B* 126 (1977), pp. 298–318. DOI: 10.1016/0550-3213(77)90384-4.
- [40] Yuri L. Dokshitzer. “Calculation of the Structure Functions for Deep Inelastic Scattering and e+ e- Annihilation by Perturbation Theory in Quantum Chromodynamics.” In: *Sov. Phys. JETP* 46 (1977), pp. 641–653.
- [41] E. Rondio. “New results on the F2 and R on the proton and the deuteron from NMC”. In: *Nucl. Phys. B Proc. Suppl.* 54 (1997). Ed. by Stephan Narison, pp. 139–143. DOI: 10.1016/S0920-5632(97)00029-7.
- [42] A Abreu, A Baldit, and C Barrière. “Study of the isospin breaking in the light quark sea from the Drell-Yan process”. In: *Phys. Lett. B* 256 (1991), 258–264 (Annexed article). URL: <https://cds.cern.ch/record/295487>.
- [43] J. C. Peng et al. “asymmetry and the origin of the nucleon sea”. In: *Physical Review D* 58.9 (1998). DOI: 10.1103/physrevd.58.092004. URL: <https://doi.org/10.11032Fphysrevd.58.092004>.
- [44] K Ackerstaff et al. “Flavor asymmetry of the light quark sea from semi-inclusive deep-inelastic scattering”. In: *Physical Review Letters* 81.25 (1998), p. 5519.
- [45] J. Dove et al. “The asymmetry of antimatter in the proton”. In: *Nature* 590.7847 (2021), pp. 561–565. DOI: 10.1038/s41586-021-03282-z. URL: <https://doi.org/10.10382Fs41586-021-03282-z>.

- [46] R. Vogt. “Limits on intrinsic charm production from the SeaQuest experiment”. In: *Physical Review C* 103.3 (2021). DOI: 10.1103/physrevc.103.035204. URL: <https://doi.org/10.1103/physrevc.103.035204>.
- [47] S.J. Brodsky et al. “The intrinsic charm of the proton”. In: *Physics Letters B* 93.4 (1980), pp. 451–455. ISSN: 0370-2693. DOI: [https://doi.org/10.1016/0370-2693\(80\)90364-0](https://doi.org/10.1016/0370-2693(80)90364-0). URL: <https://www.sciencedirect.com/science/article/pii/0370269380903640>.
- [48] S. J. Brodsky, C. Peterson, and N. Sakai. “Intrinsic heavy-quark states”. In: *Phys. Rev. D* 23 (11 1981), pp. 2745–2757. DOI: 10.1103/PhysRevD.23.2745. URL: <https://link.aps.org/doi/10.1103/PhysRevD.23.2745>.
- [49] M. Agnello et al. *Study of hard and electromagnetic processes at CERN-SPS energies: an investigation of the high- $\mu_{\mathbf{B}}$ region of the QCD phase diagram with NA60+*. 2018. arXiv: 1812.07948 [nucl-ex].
- [50] L. Massacrier et al. *Feasibility studies for quarkonium production at a fixed-target experiment using the LHC proton and lead beams (AFTER@LHC)*. 2015. arXiv: 1504.05145 [hep-ex].
- [51] R. Aaij et al. “First Measurement of Charm Production in its Fixed-Target Configuration at the LHC”. In: *Physical Review Letters* 122.13 (2019). DOI: 10.1103/physrevlett.122.132002. URL: <https://doi.org/10.1103/physrevlett.122.132002>.
- [52] J. Badier et al. “Experimental J/psi Hadronic Production from 150-GeV/c to 280-GeV/c”. In: *Z. Phys. C* 20 (1983), p. 101. DOI: 10.1007/BF01573213.
- [53] C. Baglin et al. “The production of J Ψ in 200 GeV/nucleon oxygen-uranium interactions”. In: *Physics Letters B* 220.3 (1989), pp. 471–478. ISSN: 0370-2693. DOI: [https://doi.org/10.1016/0370-2693\(89\)90905-2](https://doi.org/10.1016/0370-2693(89)90905-2). URL: <https://www.sciencedirect.com/science/article/pii/0370269389909052>.

- [54] D. M. Alde et al. “A dependence of J/ψ and ψ' production at 800 GeV/c”. In: *Phys. Rev. Lett.* 66 (2 1991), pp. 133–136. DOI: 10.1103/PhysRevLett.66.133. URL: <https://link.aps.org/doi/10.1103/PhysRevLett.66.133>.
- [55] T. Matsui and H. Satz. “ J/ψ suppression by quark-gluon plasma formation”. In: *Physics Letters B* 178.4 (1986), pp. 416–422. ISSN: 0370-2693. DOI: [https://doi.org/10.1016/0370-2693\(86\)91404-8](https://doi.org/10.1016/0370-2693(86)91404-8). URL: <https://www.sciencedirect.com/science/article/pii/0370269386914048>.
- [56] B. Povh and J. Hüfner. “Geometric interpretation of hadron-proton total cross sections and a determination of hadronic radii”. In: *Phys. Rev. Lett.* 58 (16 1987), pp. 1612–1615. DOI: 10.1103/PhysRevLett.58.1612. URL: <https://link.aps.org/doi/10.1103/PhysRevLett.58.1612>.
- [57] M. J. Leitch et al. “Nuclear effects on heavy quark production results from Fermilab experiments E772 and E789.” In: *Nucl. Phys. A* 544 (1992). Ed. by T. C. Awes et al., pp. 197C–207C. DOI: 10.1016/0375-9474(92)90574-4.
- [58] Michele Arneodo. “Nuclear effects in structure functions”. In: *Physics Reports* 240.5 (1994), pp. 301–393. ISSN: 0370-1573. DOI: [https://doi.org/10.1016/0370-1573\(94\)90048-5](https://doi.org/10.1016/0370-1573(94)90048-5). URL: <https://www.sciencedirect.com/science/article/pii/0370157394900485>.
- [59] Francois Arleo and Stéphane Peigné. “ J/ψ Suppression in p - A Collisions from Parton Energy Loss in Cold QCD Matter”. In: *Phys. Rev. Lett.* 109 (12 2012), p. 122301. DOI: 10.1103/PhysRevLett.109.122301. URL: <https://link.aps.org/doi/10.1103/PhysRevLett.109.122301>.
- [60] Stanley J. Brodsky and Paul Hoyer. “The Nucleus as a Color Filter in QCD Decays: Hadroproduction in Nuclei”. In: *Phys. Rev. Lett.* 63 (1989), p. 1566. DOI: 10.1103/PhysRevLett.63.1566.

- [61] Helmut Satz. *A Brief History of J/Psi Suppression*. 1998. arXiv: hep-ph/9806319 [hep-ph].
- [62] SeaQuest Collaboration et al. *The SeaQuest Spectrometer at Fermilab*. 2019. arXiv: 1706.09990 [physics.ins-det].
- [63] K. Akerstaff et al. “The HERMES Spectrometer”. In: *Nuclear Instruments and Methods in Physics Research Section A: Accelerators, Spectrometers, Detectors and Associated Equipment* 417.2 (1998), pp. 230–265. ISSN: 0168-9002. DOI: [https://doi.org/10.1016/S0168-9002\(98\)00769-4](https://doi.org/10.1016/S0168-9002(98)00769-4). URL: <https://www.sciencedirect.com/science/article/pii/S0168900298007694>.
- [64] C. Morris et al. “Tomographic Imaging with Cosmic Ray Muons”. In: *Science & Global Security* 16 (2008). DOI: 10.1080/08929880802335758.
- [65] Shiuan-Hal Shiu et al. “FPGA-based trigger system for the Fermilab SeaQuest experimentz”. In: *Nucl. Instrum. Meth. A* 802 (2015), pp. 82–88. DOI: 10.1016/j.nima.2015.09.001. arXiv: 1509.04864 [physics.ins-det].
- [66] Thomas Jefferson National Accelerator Facility Data Aquisition Support Group. *CODA documentation website*. URL: <https://coda.jlab.org/drupal>.
- [67] Randall Evan McClellan. “Angular Distributions of High-Mass Dilepton Production in Hadron Collisions”. PhD thesis. Illinois U., Urbana, 2016. DOI: 10.2172/1294516.
- [68] J. Allison et al. “Recent developments in Geant4”. In: *Nuclear Instruments and Methods in Physics Research Section A: Accelerators, Spectrometers, Detectors and Associated Equipment* 835 (2016), pp. 186–225. ISSN: 0168-9002. DOI: <https://doi.org/10.1016/j.nima.2016.06.125>. URL: <https://www.sciencedirect.com/science/article/pii/S0168900216306957>.
- [69] J. Allison et al. “Geant4 developments and applications”. In: *IEEE Transactions on Nuclear Science* 53.1 (2006), pp. 270–278. DOI: 10.1109/TNS.2006.869826.

- [70] S. Agostinelli et al. “Geant4—a simulation toolkit”. In: *Nuclear Instruments and Methods in Physics Research Section A: Accelerators, Spectrometers, Detectors and Associated Equipment* 506.3 (2003), pp. 250–303. ISSN: 0168-9002. DOI: [https://doi.org/10.1016/S0168-9002\(03\)01368-8](https://doi.org/10.1016/S0168-9002(03)01368-8). URL: <https://www.sciencedirect.com/science/article/pii/S0168900203013688>.
- [71] K. Liu. *kTracker Walkthrough*. 2015. eprint: seaquest - docdb - 1283. URL: https://seaquest-docdb.fnal.gov/cgi-bin/sso/RetrieveFile?docid=1283&filename=kTracker_Collaboration_20140212.pdf&version=1.
- [72] S. Gorbunov and I. Kisel. *Primary vertex fit based on the Kalman filter*. 2006. eprint: CBM-SOFT-note-2006-001. URL: <https://www.star.bnl.gov/~bouchet/KFParticle/DOC-2006-Jan-19-1.pdf>.
- [73] Timothy G. Mattson, Beverly A. Sanders, and Berna L. Massingill. “Patterns for parallel programming”. In: 2004.
- [74] Roger Barlow and Christine Beeston. “Fitting using finite Monte Carlo samples”. In: *Computer Physics Communications* 77.2 (1993), pp. 219–228. ISSN: 0010-4655. DOI: [https://doi.org/10.1016/0010-4655\(93\)90005-W](https://doi.org/10.1016/0010-4655(93)90005-W). URL: <https://www.sciencedirect.com/science/article/pii/001046559390005W>.
- [75] Catherine Ayuso. “Nuclear Modification of J/Ψ and Drell-Yan Production at the E906/SeaQuest Experiment”. PhD thesis. Michigan U., 2020. DOI: 10.2172/1637630.
- [76] K. Liu. *First draft of recommended analysis cuts for R005 production*. 2015. eprint: seaquest - docdb - 1487. URL: <https://seaquest-docdb.fnal.gov/cgi-bin/sso/RetrieveFile?docid=1487>.
- [77] Po-Ju Lin. “Measurement of Quark Energy Loss in Cold Nuclear Matter at Fermilab E906/SeaQuest”. PhD thesis. Colorado U., 2017. DOI: 10.2172/1398791.

- [78] M. H. Schub et al. “Measurement of J/ψ and ψ' production in 800 GeV/c proton-gold collisions”. In: *Phys. Rev. D* 52 (3 1995), pp. 1307–1315. DOI: 10.1103/PhysRevD.52.1307. URL: <https://link.aps.org/doi/10.1103/PhysRevD.52.1307>.
- [79] CTEQ collaboration. *CT14 Parton Distribution Functions website*. 2015. URL: <http://hep.pa.msu.edu/cteq/public/>.
- [80] Jason Dove. “Probing the Flavor Dependence of Proton’s Light-Quark Sea In the SeaQuest Experiment at Fermilab”. PhD thesis. Illinois at Urbana-Champaign U., 2020.
- [81] Shivangi Prasad. *p_T reweighting*. 2021. eprint: seaquest-docdb-9294. URL: https://seaquest-docdb.fnal.gov/cgi-bin/sso/RetrieveFile?docid=9294&filename=pT_reweighting.pdf&version=1.
- [82] Ching Him Leung. *J/Ψ cross section ratio analysis note*. 2020. eprint: seaquest-docdb-8537. URL: https://seaquest-docdb.fnal.gov/cgi-bin/sso/RetrieveFile?docid=8537&filename=JPsi_analysis_note_v3.pdf&version=4.
- [83] J. S. Conway et al. “Experimental study of muon pairs produced by 252-GeV pions on tungsten”. In: *Phys. Rev. D* 39 (1 1989), pp. 92–122. DOI: 10.1103/PhysRevD.39.92. URL: <https://link.aps.org/doi/10.1103/PhysRevD.39.92>.
- [84] Ching Him Leung. *$P_{Tmaxcut}$* . 2021. eprint: seaquest-docdb-9292. URL: <https://seaquest-docdb.fnal.gov/cgi-bin/sso/RetrieveFile?docid=9292>.
- [85] S. F. Pate et al. *Estimation of Combinatoric Background in SeaQuest using an Event-Mixing Method*. 2023. arXiv: 2302.04152 [hep-ex].

- [86] Kei Nagai. “Recent Measurement of Flavor Asymmetry of Antiquarks in the Proton by Drell-Yan Experiment SeaQuest at Fermilab”. PhD thesis. Tokyo Institute of Technology, 2017.
- [87] Kei Nagai. *Definition of kTracker Efficiency*. 2018. eprint: seaquest-docdb-3590. URL: <https://seaquest-docdb.fnal.gov/cgi-bin/sso/RetrieveFile?docid=3590>.
- [88] Donald Geesaman. *Handling the Liquid Target Contamination and Densities V7*. 2022. eprint: seaquest-docdb-4993. URL: <https://seaquest-docdb.fnal.gov/cgi-bin/sso/RetrieveFile?docid=4993>.
- [89] R. L. Workman et al. “Review of Particle Physics”. In: *PTEP* 2022 (2022), p. 083C01. DOI: 10.1093/ptep/ptac097.
- [90] S. Katsanevas et al. “Nuclear-Target Effects in $\frac{J}{\psi}$ Production in 125-GeV/c Antiproton and π^- Interactions”. In: *Phys. Rev. Lett.* 60 (21 1988), pp. 2121–2124. DOI: 10.1103/PhysRevLett.60.2121. URL: <https://link.aps.org/doi/10.1103/PhysRevLett.60.2121>.
- [91] R. GAVAI et al. “QUARKONIUM PRODUCTION IN HADRONIC COLLISIONS”. In: *International Journal of Modern Physics A* 10.20n21 (1995), pp. 3043–3070. DOI: 10.1142/s0217751x95001443. URL: <https://doi.org/10.1142/s0217751x95001443>.
- [92] Hung-Liang Lai et al. “New parton distributions for collider physics”. In: *Phys. Rev. D* 82 (7 2010), p. 074024. DOI: 10.1103/PhysRevD.82.074024. URL: <https://link.aps.org/doi/10.1103/PhysRevD.82.074024>.
- [93] Jean-Jacques Aubert et al. “The ratio of the nucleon structure functions F_2^N for iron and deuterium”. In: *Phys. Lett. B* 123 (1983), pp. 275–278. DOI: 10.1016/0370-2693(83)90437-9. URL: <https://cds.cern.ch/record/142300>.

- [94] Kari J. Eskola et al. “EPPS16: nuclear parton distributions with LHC data”. In: *The European Physical Journal C* 77.3 (2017). DOI: 10.1140/epjc/s10052-017-4725-9. URL: <https://doi.org/10.1140%2Fepjc%2Fs10052-017-4725-9>.
- [95] R. Vogt. “J/ production and suppression” This work was supported in part by the Director, Office of Energy Research, Division of Nuclear Physics of the Office of High Energy and Nuclear Physics of the U.S. Department of Energy under Contract Number DE-AC03-76SF00098.” In: *Physics Reports* 310.4 (1999), pp. 197–260. ISSN: 0370-1573. DOI: [https://doi.org/10.1016/S0370-1573\(98\)00074-X](https://doi.org/10.1016/S0370-1573(98)00074-X). URL: <https://www.sciencedirect.com/science/article/pii/S037015739800074X>.
- [96] J. W. Cronin et al. “Production of hadrons at large transverse momentum at 200, 300, and 400 GeV”. In: *Phys. Rev. D* 11 (11 June 1975), pp. 3105–3123. DOI: 10.1103/PhysRevD.11.3105. URL: <https://link.aps.org/doi/10.1103/PhysRevD.11.3105>.
- [97] S. J. Brodsky et al. “A Review of the Intrinsic Heavy Quark Content of the Nucleon”. In: *Advances in High Energy Physics* 2015 (2015), pp. 1–12. DOI: 10.1155/2015/231547. URL: <https://doi.org/10.1155%2F2015%2F231547>.
- [98] S. J. Brodsky et al. “Novel Heavy-Quark Physics Phenomena”. In: *Prog. Part. Nucl. Phys.* 114 (2020), p. 103802. DOI: 10.1016/j.pnnp.2020.103802. arXiv: 2006.09443 [hep-ph].